RADIATION CHEMISTRY BY SOFT X-RAY SPECTROMICROSCOPY

By

Jian Wang, M.Sc.

A Thesis

Submitted to the School of Graduate Studies

in Partial Fulfillment of the Requirements

for the Degree of

Doctor of Philosophy

McMaster University

© Jian Wang, February 2008

DOCTOR OF PHILOSOPHY (2008) McMaster University
(Chemistry) Hamilton, Ontario

TITLE: Radiation Chemistry by Soft X-ray Spectromicroscopy

AUTHOR: Jian Wang, M.Sc. (Nanjing University)

SUPERVISOR: Professor Adam P. Hitchcock

NUMBER OF PAGES: XX, 246

ABSTRACT

This thesis presents the qualitative and quantitative determination of soft X-ray damage to selected polymer materials, including poly(methyl methacrylate) (PMMA), polyacrylonitrile (PAN), poly(ethyl cyanoacrylate) (PECA), poly(propylene carbonate) (PPC), poly(ethylene carbonate) (PEC), polyethylene terephthalate (PET), polystyrene (PS), and fibrinogen (Fg) by a scanning transmission X-ray microscope (STXM), and by a X-ray photoemission electron microscope (X-PEEM) for PMMA, PS and Fg. NEXAFS spectroscopy at C 1s, N 1s and O 1s edges was used to study the radiation chemistry of these polymers. The damage rate in terms of the critical dose is determined by the quantitative methodology developed in this thesis. The results show that not only radiation chemistry, but also damage rate is rather different among these polymers.

Chemically selective soft X-ray damage and patterning by STXM was explored and investigated in six different polymer systems: a PMMA/PAN bilayer film, a PMMA-*blend*-PAN micro phase-separated film, a poly(MMA-*co*-AN) copolymer film, a PECA homopolymer film, and two trilayer films, i.e. PMMA/PPC/PAN and PMMA/PEC/PAN. A high level of chemically selective damage was only achieved for layered polymer systems. Although the overall thickness of the bilayer and trilayer samples is much smaller than the damage spread range, the interface between the layers appears to very effectively block the damage transfer from one layer to the other. Full color patterning with the best spatial resolution to date of ~ 150 nm was achieved. A simulation program was developed to predict the patterning results with semi-quantitative accuracy.

ACKNOWLEDGEMENTS

I would like to express my great thanks to my supervisor, Dr. Adam Hitchcock, for his excellent guidance, encouragement and endless support through the past five years. His passion for science, critical thinking, scientific integrity, breadth of knowledge and hard working attitude impressed me so much. The work experience in Dr. Hitchcock's group has become one of my most valuable wealth in my life. He also gave me the opportunity to get into the X-ray Spectromicroscopy field and provided me the most exciting project in the group, radiation chemistry.

I would also like to thank my supervisory committee members, Dr. Peter Kruse and Dr. Gillian Goward, for their research advice, suggestions and support, especially when I switched to the current PhD project.

Special thanks to Dr. Harald Stöver for educating me on polymer chemistry and many helpful discussions with him on polymer reaction mechanisms. He is so generous to share his samples, chemicals and lab. His group members, Nick, Jafar, are so kind to me.

I'm grateful for the current and past group members, Dr. Glyn Cooper, Dr. Jay Dynes, Dr. Martin Obst, Hua Jiang, Jeffrey Li, Ebrihim Najafi, Bonnie Leung, Karen Lam; Dr. Daniel Hernandez-Cruz, Dr. Göran Johansson, Dr. Cassia Turci, Dr. Cynthia Morin, Dr. Li Li, Dr. Sherry Zhang, Dr. Antonio Guerra, Peter Brodersen, Jacob Stewart-Ornstein, Eric Christensen, Saurabh S. Chitnis, Stephanie Hanhan, Jerome Cuny, Padraic Foley, David Tulumello, for their assistance and cooperation in the lab during the past five years. It's such a wonderful experience to work with these great guys. Special thanks to Glyn when the ISEELS machine broke down he could always provide immediate help;

to Daniel and Göran for helping the STXM experiments in ALS; to Cynthia for collaboration on the X-PEEM/STXM damage paper; to Peter and Jacob for helping the work on the surface machine.

Many thanks to Advanced Light Source beamline scientists: Dr. David Kilcoyne and Dr. Tolek Tyliszczak of STXM 5.3.2; Dr. Andreas Scholl and Dr. Andrew Doran of X-PEEM 7.3.1.1, for their technical support and expert maintenance of the instruments. Special thanks to superman Tolek. He coded the pattern generation program so quickly and it works very well.

Thanks to other McMaster collaborators: Dr. Kari Dalnoki-Veress and his group for allowing me to use his lab; Dr. Gianluigi Botton for collaboration on TEM radiation damage; and Marcia West for superb microtomy and TEM damage.

Thanks to all the people in McMaster Chemistry community and all my friends for all the great times we had together.

Finally I would like to thank my families for their eternal support and love. My wife Caroline is helping me through the hardest times in my life. My son Richard has brought me so much fun although I have to spend some time playing with him during the busy thesis writing period. My mother, my brother and my sister continuously encouraged me to do my best to achieve my goals. This thesis is dedicated to all of them.

TABLE OF CONTENTS

Descriptive Note ii
Abstract iii
Acknowledgements iv
Table of Contents vi
List of Figures x
List of Tables xiv
List of Abbreviations and Symbols xvi

Chapter 1 Introduction **1**
1.1 Overview of thesis 1
1.2 Ionizing radiation damage 4
1.2.1 Types of ionizing radiation 4
1.2.2 The fields of ionizing radiation damage . . . 7
1.3 Effects of soft X-ray induced radiation damage . . . 10
1.3.1 Physical effects 11
1.3.2 Chemical effects 13
1.3.3 Radiation effects on living species 17
1.4 Qualitative and quantitative characterization of soft X-ray radiation damage 18
1.5 Significance of this work to soft X-ray radiation damage to polymers 28
1.6 Outline of the thesis 30

Chapter 2 Methods **32**
2.1 Synchrotron radiation 32
2.2 NEXAFS 37
2.2.1 Theory of X-ray absorption 38
2.2.2 Detection techniques 40
2.2.3 NEXAFS spectroscopy 44
2.2.3.1 NEXAFS spectroscopic features . . . 44
2.2.3.2 Chemical sensitivity 46
2.3 Introduction to X-ray microscopy 49
2.3.1 Full field X-ray microscopy 50
2.3.2 Scanning X-ray microscopy 50
2.4 STXM principles and instrumentation 52
2.4.1 STXM principles 52
2.4.2 STXM instrumentation 55
2.4.2.1 STXM beamline 5.3.2 55
2.4.2.2 STXM microscope 57
2.5 X-PEEM principles and instrumentation 62
2.5.1 X-PEEM principles 62
2.5.2 X-PEEM instrumentation 64
2.5.2.1 X-PEEM beamline 7.3.1.1 64

2.5.2.2 X-PEEM microscope 65

Chapter 3 Experimental 70
3.1 STXM data acquisition 70
3.1.1 Single energy images 70
3.1.2 Point scans 72
3.1.3 Linescan spectra 74
3.1.4 Image sequences (stacks) 76
3.1.5 Pattern generation 78
3.2 Quantitative dose-damage analysis in STXM . . . 81
3.3 Chemically selective patterning of multilayer polymer systems by STXM 87
3.3.1 Experimental approach 87
3.3.2 Simulations: ChemLith 91
3.4 X-PEEM data acquisition 97
3.4.1 Single energy images 98
3.4.2 Spectra 100
3.4.3 Image sequences (stacks) 102
3.5 Quantitative dose-damage analysis in X-PEEM . . . 103
3.5.1 Determination of the absolute I_0 profile . . . 104
3.5.2 Photon flux in the measured region 106
3.5.3 Critical dose 108
3.6 Sample preparation 111
3.6.1 STXM sample preparation 111
3.6.1.1 Spin coating 111
3.6.1.2 Solvent casting 114
3.6.1.3 Microtomy 114
3.6.2 X-PEEM sample preparation 115
3.6.2.1 Spin coating 115
3.6.2.2 HF-etched Si wafer 115
3.6.3 Characterization of samples 116
3.6.3.1 Optical microscope 116
3.6.3.2 Atomic Force Microscopy 117
3.6.3.3 Transmission Electron Microscopy . . . 118

Chapter 4 Characterization of polymer radiation damage . . 120
4.1 Introduction 120
4.2 NEXAFS of radiation damaged non-aromatic polymers and kinetics 122
4.2.1 Chemistry change without mass loss 122
4.2.2 Chemistry change with small mass loss . . . 129
4.2.3 Chemistry change with large mass loss . . . 136
4.3 NEXAFS of radiation damaged aromatic polymers and kinetics . 141
4.4 Discussion 146

Chapter 5 Characterization of polymer radiation damage in X-PEEM and comparison with STXM . . . 155
5.1 Introduction 157
5.2 Experimental 159
5.2.1 Sample preparation 159
5.2.1.1 PMMA and PS 159
5.2.1.2 Protein samples for X-PEEM and STXM . . 159
5.2.1.3 HF-etched Si - X-PEEM Io substrate . . . 160
5.2.2 X-PEEM 160
5.2.3 STXM 161
5.3 Quantitative dose-damage results 162
5.3.1 X-PEEM sampling depth 162
5.3.2 PMMA - radiation damage in X-PEEM . . . 164
5.3.3 PMMA - radiation damage in STXM 167
5.3.4 Dose-damage relationships for PMMA, PS and Fg in X-PEEM and STXM 169
5.4 Chemical changes from radiation damage as probed by NEXAFS . 173
5.5 Recommended procedures for X-ray microscopy studies of radiation sensitive samples 178
5.6 Summary 179

Chapter 6 Chemically selective soft X-ray patterning of single-layer and bilayer polymer films 183
6.1 Introduction 184
6.2 Experimental 185
6.2.1 Sample preparation 185
6.2.2 STXM 186
6.3 Results 187
6.3.1 Radiation damage for PMMA and PAN . . . 187
6.3.2 Chemically selective radiation damage . . . 188
6.3.3 Chemically selective patterning 189
6.4 Discussion 190
6.4.1 What causes the spread of damage beyond the size of the X-ray beam? 190
6.4.2 What is the role of the interface in preventing spread of damage between the layers? 192

Chapter 7 Chemically selective soft X-ray patterning of trilayer polymer films 194
7.1 Introduction 195
7.2 Experimental section 196
7.2.1 Sample preparation 196
7.2.2 STXM 196
7.3 Simulation of chemically selective patterning in multilayer polymer

systems 196
7.4 Results 197
7.4.1 NEXAFS spectra and critical doses for PMMA, PAN, PPC, and PEC 197
7.4.2 Chemically selective patterning for PMMA/PPC/PAN trilayer 198
7.4.3 Chemically Selective Patterning of a PMMA/PEC/PAN trilayer 200
7.5 Discussion 202

Chapter 8 Summary and future work 204
8.1 Summary 204
8.2 Original contributions of this thesis 208
8.3 Future work 208
8.3.1 Understanding the polymer interface effect . . . 208
8.3.2 Understanding radiation damage mechanisms . . 210
8.3.3 Anti-contamination in STXM 212
8.3.4 Further improvement of chemical patterning in multi-layer polymer films 215
8.3.5 Further improvement of simulations 216
8.3.6 Extension to more organic materials 216
8.3.7 Potential applications 217

References 218

Appendices 237
A.1 STXM damage of hexaphenylbenzene (Ph_6Bz) . . . 237
A.2 Unpublished radiation damage results and literature results . . 240
B.1 Publications 241
B.2 Conference presentations and contributions 242
C Software packages used for this thesis 245

LIST OF FIGURES

Chapter 1

Fig. 1.1 Inelastic mean free path in solids as a function of the electron kinetic energy 6
Fig. 1.2 Timescale of soft X-ray damage to organic materials . 11

Chapter 2

Fig. 2.1 Radiation patterns of electrons in a circular orbit . . 33
Fig. 2.2 Schematic of the two main approaches used for synchrotron light generation 35
Fig. 2.3 Two detection techniques of recording NEXAFS spectra . 40
Fig. 2.4 Energy diagram and the C1s NEXAFS spectrum of polystyrene 46
Fig. 2.5 NEXAFS spectra of a series of non-aromatic polymers . 47
Fig. 2.6 Schematic geometry of a zone plate and the focusing scheme of a STXM with a plane wave illumination of X-rays . . 53
Fig. 2.7 The layout of beamline 5.3.2 for polymer STXM at the ALS 55
Fig. 2.8 The ALS beamline 5.3.2 polymer STXM . . . 59
Fig. 2.9 The optimal distance between any two of the zone plate, the OSA and the sample as a function of photon energy for the ALS STXM 5.3.2 61
Fig. 2.10 The ALS STXM 5.3.2 detector for transmitted soft X-rays . 62
Fig. 2.11 The layout of beamline 7.3.1.1 for X-PEEM at the ALS . 64
Fig. 2.12 The ALS PEEM2 at beamline 7.3.1.1 . . . 67

Chapter 3

Fig. 3.1 STXM images of a micro phase-separated polymer film, PMMA-*blend*-PAN, at three energies . . . 71
Fig. 3.2 Point scan of a multilayer polymer film fabricated from microtomed PMMA and PAN single layer films . . 73
Fig. 3.3 Line scan of a spun coated multilayer polymer film, PMMA/PUR/PAN 75
Fig. 3.4 Screen shot of the STXM_control scan definition panel set up for a STXM image sequence 76
Fig. 3.5 Image sequence of a micro phase-separated polymer film, PMMA-*blend*-PAN 77
Fig. 3.6 STXM pattern generation for polymer films . . . 80
Fig. 3.7 Screen shots of Excel^{TM} worksheet for STXM dose-damage analysis 84
Fig. 3.8 STXM dose-damage analysis of radiation damage in PMMA 86
Fig. 3.9 TEM image and STXM chemical mapping of the cross section of a bilayer polymer system, i.e. PMMA/PAN, which was embedded in epoxy resin and microtomed 89

Fig. 3.10 Screen shots of **ChemLith** for the patterning of a PMMA/PPC/PAN trilayer using exposure at the three photon energies indicated 92-93
Fig. 3.11 Visual display using *aXis2000* of the predicted patterns for the best exposure protocol in terms of optimizer for a PMMA/PPC/PAN trilayer, compared with experimental results 94
Fig. 3.12 X-PEEM image at 288.5 eV of sample PMMA/Si . . 98
Fig. 3.13 PEEM2 FOV as a function of voltages . . . 100
Fig. 3.14 Raw X-PEEM spectrum of PMMA/Si and the spectrum after normalization to the I_0 spectrum of an HF-etched Si wafer with Ti filter in 101
Fig. 3.15 X-PEEM image sequence of sample PMMA/Si . . 102
Fig. 3.16 X-PEEM I_0 spectra and determined absolute photon flux . 105
Fig. 3.17 X-PEEM images used to determine the photon flux in a measured sample region 107
Fig. 3.18 X-PEEM beam spot shape as a function of photon energy on a PMMA/Si sample 107
Fig. 3.19 X-PEEM dose-damage analysis of radiation damage in PMMA/Si 110
Fig. 3.20 Setup of the vacuum oven 113
Fig. 3.21 VLM images of STXM samples 116
Fig. 3.22 AFM image of a PMMA/PAN bilayer film on a cover glass slide scratched by a sharp tweezer tip 118
Fig. 3.23 STXM image at 288.2 eV of a PET film, which was damaged by TEM at two series of spots with designated exposure times and beam current density 119

Chapter 4

Fig. 4.1 Near edge X-ray absorption fine structure (NEXAFS) spectra of undamaged and damaged PAN 122
Fig. 4.2 Proposed mechanisms of soft X-ray damage to PAN . 126
Fig. 4.3 NEXAFS spectra of undamaged and damaged PAN compared to inner shell electron energy loss spectra (ISEELS) of gas phase pyridine 126
Fig. 4.4 Plots of the normalized optical density at 286.8 and 285.1 eV as a function of radiation dose for PAN 127
Fig. 4.5 NEXAFS spectra of undamaged and radiation damaged PECA 130
Fig. 4.6 Plots of the fraction of elemental mass remaining as a function of radiation dose for PECA and PPC 132
Fig. 4.7 Proposed mechanisms of soft X-ray damage to PECA . 133
Fig. 4.8 STXM damage of PECA 134
Fig. 4.9 NEXAFS spectra of undamaged and radiation damaged PPC 136
Fig. 4.10 NEXAFS spectra of undamaged and completely radiation damaged PEC 138
Fig. 4.11 Possible created species of soft X-ray damage to PPC and PEC 139

Fig. 4.12 Plots of the normalized optical density at 290.4 and 300 eV as a function of radiation dose for PPC 140
Fig. 4.13 NEXAFS spectra of undamaged and two series of radiation damaged PET 142
Fig. 4.14 Possible structures due to main chain scission in soft X-ray damaged PET 144
Fig. 4.15 STXM damage of PET 145
Fig. 4.16 Plots of the normalized optical density at 288.5 eV of $\pi^*_{C=O}$ as a function of radiation dose for dry and wet PMMA . 147
Fig. 4.17 Plots of the linearized version of the dose-damage data fit to equation 4.2 to determine the critical dose for PPC . . 151
Fig. 4.18 Comparison of critical doses of the ester group in PLA, PMMA and PET, and critical doses of the nitrile group in PAN and PECA 153

Chapter 5
Fig. 5.1 X-PEEM signal intensity at 285 eV and 282 eV as a function of the thickness of a spun cast polystyrene (PS) film on a native oxide silicon substrate. 163
Fig. 5.2 Sequence of C 1s spectra of PMMA recorded by X-PEEM with a reduced flux on the same area 164
Fig. 5.3 X-PEEM damage of PMMA 165
Fig. 5.4 STXM damage of PMMA 168
Fig. 5.5 Damage versus dose curves for PMMA, PS and Fg derived from X-PEEM spectral measurements at the C 1s, N 1s and O 1s edges 170
Fig. 5.6 Damage versus dose curves for PMMA, PS and Fg derived from STXM damage pattern spectral measurements at the C 1s edge 172
Fig. 5.7 Changes with radiation damage in the C 1s spectra recorded by STXM for PMMA, PS and Fg 174
Fig. 5.8 Changes with radiation damage in the N 1s spectra of Fg, and in the O1s spectra of PMMA and Fg recorded by STXM . 175
Fig. 5.9 Proposed reactions for radiation damage of PMMA, PS and Fg 177

Chapter 6
Fig. 6.1 C 1s near-edge X-ray absorption fine structure (NEXAFS) spectra of undamaged and damaged PMMA and PAN . . 187
Fig. 6.2 C 1s absolute linear absorption NEXAFS spectra of PMMA-*on*-PAN bilayer, poly(MMA-*co*-AN) and PECA . 188
Fig. 6.3 Optical density images of radiation damage of PMMA/PAN bilayer, poly(MMA-*co*-AN) and PECA . . . 189
Fig. 6.4 Evaluation of radical migration in a PMMA-blend-PAN microphase-separated film 190
Fig. 6.5 Demonstration of chemically selective patterning for PMMA/PAN bilayer and PECA 191
Fig. 6.6 Effect of environment (vacuum versus one-third atmosphere of

helium) on the line width with adjusted same dose for vacuum and helium for both PMMA and PAN . . . 192
Fig. 6.7 Diagram emphasizing the critical role of the interface in achieving chemically selective patterning by minimizing radical migration between layers 192

Chapter 7
Fig. 7.1 C 1s NEXAFS spectra of PMMA, PAN, PPC, and PEC . 197
Fig. 7.2 Damage versus dose curves for PMMA, PAN, PPC, and PEC derived from STXM measurements at the C 1s edge . . 198
Fig. 7.3 Simulations and experimental results for chemically selective patterning of PMMA/PPC/PAN and PMMA/PEC/PAN trilayers 199
Fig. 7.4 Demonstration of chemically selective patterning of the LBNL logo into PMMA/PPC/PAN and PMMA/PEC/PAN trilayers 199
Fig. 7.5 Chemically selective patterning of a PMMA/PEC/PAN trilayer 201
Fig. 7.6 Comparison of chemically selective patterning of a PMMA/PEC/PAN trilayer and its reverse . . . 201

Chapter 8
Fig. 8.1 Photograph of the in-vacuum liquid nitrogen cold trap . 213
Fig. 8.2 Plots of the integrated areal optical density of carbon as a function of radiation exposure 213
Fig. 8.3 Schemes to protect polymer films from photodeposition . 214

Appendices
Fig. A.1 C 1s NEXAFS spectra of undamaged and radiation damaged Ph_6Bz 237
Fig.A.2 STXM damage of Ph_6Bz 238

LIST OF TABLES

Chapter 1

Table 1.1 Energy and penetration ranges of common ionizing radiation sources 5
Table 1.2 Selected references (books, review articles and research papers) for ionizing radiation damage to different kinds of materials 8
Table 1.3 Some biological effects of ionizing radiation damage . 17
Table 1.4 Techniques to characterize soft X-ray damage of organic materials 19-20
Table 1.5 STXM characterization of soft X-ray damage in polymers . 20

Chapter 2

Table 2.1 Energies of C 1s → π* transitions of a series of non-aromatic Polymers 48
Table 2.2 Trade-off of slits sizes with flux, energy and spatial resolution 57
Table 2.3 Locations and properties of current STXM microscopes . 58
Table 2.4 Locations and properties of selected PEEM microscopes . 66
Table 2.5 Comparison of ALS STXM and X-PEEM . . . 69

Chapter 3

Table 3.1 **ChemLith** simulation procedure and input parameters for trilayer systems 95-96
Table 3.2 Comparison of radiation dose in STXM and X-PEEM for an image sequence 102
Table 3.3 Polymer film samples with selected preparation conditions for STXM and X-PEEM measurements 112

Chapter 4

Table 4.1 The major NEXAFS features of undamaged PAN, PECA, PPC, PEC and PET polymers and new features created in the damaged Polymers 123
Table 4.2 Photon energies and normalized infinite optical densities used to monitor and quantify chemistry changes and mass loss for PAN, PECA, PPC, PEC and PET polymers 128
Table 4.3 Photon energies used to quantify soft X-ray damage rate and determined critical doses for PMMA, PAN, PECA, PPC, PEC, PET, Fg and PS polymers 152

Chapter 5

Table 5.1 Reproducibility of dose - damage data from X-PEEM measurements on PMMA with various dose rates . . 166
Table 5.2 Critical doses for radiation damage of PMMA, PS and Fg at C 1s, N 1s and O 1s edges as determined by X-PEEM . 166
Table 5.3 Critical doses for radiation damage of PMMA, PS and Fg as

determined by STXM 169

Chapter 7
Table 7.1 Solubility of selected polymers in selected solvents . . 196

Appendices
Table A.1 Photon energies used to damage and quantify soft X-ray damage rate and determined critical dose from unpublished work and from literature 240

LIST OF ABBREVIATIONS AND SYMBOLS

A	Absorbance
a	Dose in MGy (mega grays)
a_c	Critical Dose
AFM	Atomic Force Microscopy
ALS	Advanced Light Source
AOI	Area of Interest, region of a sample in X-PEEM
BESSY	Berliner Elektronenspeicherring-Gesellschaft für Synchrotronstrahlung
BM	Bend Magnet
BW	Bandwidth
c	Speed of Light in Vacuum
γ	Lorentz Factor
CCD	Charge-Coupled Device
CLS	Canadian Light Source
CXRO	Center for X-Ray Optics
δ	Polydispersity Index, M_w/M_n
Δr_n	Width of the Most Outer Zone (Nth) of a Zone Plate
$\Delta\phi$	Angular Spread of Synchrotron Radiation
D	Damage (optical density change, or peak area change)
DDI	Distilled Deionized Water
DME	1,2-Dimethoxyethane
DMF	Dimethylformamide
DNA	Deoxyribonucleic Acid
DSB	Double Strand Break
D_∞	Signal at Saturation Damage
ε	Detector Efficiency
EPR	Electron Paramagnetic Resonance
EPU	Elliptically Polarizing Undulators
EUV	Extreme Ultraviolet

F	Absorbed Flux
$F_{ph}(E)$	Photon Flux
FEL	Free-Electron Laser
f	Focal Length
$\langle f \vert$	Final Electronic State
Fg	Fibrinogen
FOV	Field of View
FWHM	Full Width at Half Maximum
θ	Angle
HFIP	Hexafluoro-2-propanol
HOMO	Highest Occupied Molecular Orbital
HPLC	High Performance Liquid Chromatography
I	Transmitted Photon Intensity (Flux) in STXM; Intensity in X-PEEM
$\vert i \rangle$	Initial Electronic State
IMFP	Inelastic Mean Free Path
IP	Ionization Potential
IRRAS	Infrared Reflection Absorption Spectroscopy
ISEELS	Inner Shell Electron Energy Loss Spectroscopy
I_0	Incident Photon Intensity (Flux)
KB	Kirkpatrick-Baez
λ	Wavelength of Light
L	Sampling Depth in X-PEEM
l	Sample Thickness
LBNL	Lawrence Berkeley National Laboratory
LEED	Low Energy Electron Diffraction
LUMO	Lowest Unoccupied Molecular Orbital
M or MW	Molecular Weight
μ	Energy Dependent Mass Absorption Coefficient
MALDI	Matrix-Assisted Laser Desorption/Ionization

Mb	Megabyte
MGy	Mega Grays
M_n	Number Average Molecular Weight
M_w	Weight Average Molecular Weight
NA	Numerical Aperture
NEXAFS	Near Edge X-Ray Absorption Fine Structure
NMR	Nuclear Magnetic Resonance
NSLS	National Synchrotron Light Source
NSRRC	National Synchrotron Radiation Research Center
OD	Optical Density
OD1	Optical Density per nm Thickness Material
OD_0	Initial Optical Density
OD_∞	Optical Density after Infinite Dose
OS	Oscillator Strength
OSA	Order Sorting Aperture
PAN	Polyacrylonitrile
PAY	Partial Auger Yield
PBD	Polybutadiene
PC	Polycarbonate
PDI	Polydispersity Index
PE	Polyethylene
PEC	Poly(ethylene carbonate)
PECA	Poly(ethyl cyanoacrylate)
PES	Poly(ethylene succinate)
PET	Poly(ethylene terephthalate)
PEY	Partial Electron Yield
$P_{if}(E)$	Transition Probability
PIY	Partial Ion Yield
PMA	Poly(methyl acrylate)

PMAA	Poly(methacrylic acid)
PMMA	Poly(methyl methacrylate)
PMT	Photomultiplier
POM	Particulate Organic Matter
PPC	Poly(propylene carbonate)
PPO	Poly(propylene oxide)
PS	Polystyrene
PtBA	Poly(*tert*-butyl acrylate)
PU	Polyurea; Polyurethane in ref. [CUA02]
PUR	Polyurethane
PVMK	Poly(vinyl methyl ketone)
MS	Mass Spectrometry
Q	Partial Photoionization Cross Section
RNA	Ribonucleic Acid
rpm	Revolution per Minute
ρ	Sample Density
$\rho_f(E)$	Energy Density of Final States
σ_a	Atomic Photoabsorption Cross Section
$\sigma_x(E)$	X-ray Absorption Cross Section
S	Patterning Selectivity
SAM	Self-Assembled Monolayer
SAXS	Small-Angle X-ray Scattering
SGM	Spherical Grating Monochromator
SIMS	Secondary Ion Mass Spectrometry
SLS	Swiss Light Source
S_{OD}	Integrated Optical Density
SPEM	Scanning Photoelectron Microscopy
SSB	Single Strand Break
SSRF	Shanghai Synchrotron Radiation Facility

SSRL	Stanford Synchrotron Radiation Laboratory
SSLS	Singapore Synchrotron Light Source
STXM	Scanning Transmission X-Ray Microscopy
T	Transmittance
t	Exposure Time
TCE	Trichloroethylene
TEM	Transmission Electron Microscopy
TEY	Total Electron Yield
TFY	Total Fluorescence Yield
TIY	Total Ion Yield
TOF	Time of Flight
TXM	Transmission X-Ray Microscopy
UHV	Ultra High Vacuum
UPS	Ultraviolet Photoelectron Spectroscopy
v	Particle's Velocity
$V(E,t)$	Electromagnetic Energy- and Time-Dependent Perturbation
VLM	Visible Light Microscope
Ω	Electron Emission Solid Angle
ω	Frequency
wt%	Weight Percent
XMCD	X-Ray Magnetic Circular Dichroism
XMLD	X-Ray Magnetic Linear Dichroism
X-PEEM	X-ray Photoemission Electron Microscopy
XPS	X-ray Photoelectron Spectroscopy
XRD	X-ray Diffraction
ZP	Fresnel Zone Plate

Chapter 1

Introduction

This chapter gives an overview of the thesis and an introduction to damage caused by ionizing radiation, particularly by soft X-rays. This is followed by a review of qualitative and quantitative methods to evaluate damage by soft X-rays. The significance and applications of this work to radiation damage of polymers are described. This chapter concludes with an outline of the whole thesis.

1.1 Overview of thesis

For about a century, synthetic polymers have made a huge impact on our daily lives. With further advances in the understanding of polymers, and with new applications being researched, polymers will play an even more important role in human society. Polymer degradation is an important research area in polymer science. Radiation damage of polymers induced by X-rays, particularly soft X-rays, is recently attracting growing attention, coincident with a significant increase in applications of synchrotron X-rays to the micro-analysis of organic materials and biological samples. In addition, with the wide usage of the intense third generation synchrotron sources, radiation damage caused by X-rays has been a concern for most of the analytical tools using synchrotron radiation. In modern soft X-ray microscopy, radiation damage of organic materials is a common and important phenomenon. A better understanding of the damage mechanisms and characterization of soft X-ray damage of polymers is not only of particular importance to guide procedures for meaningful X-ray microanalysis of macromolecules, but also of

fundamental significance in investigating more complicated radiation damage effects in larger biological systems, including those significant to the health of humans.

This thesis is motivated to gain a more complete understanding and a more accurate characterization of soft X-ray damage of several selected polymer materials. In addition, applications of this research are explored with pioneering results. Specifically, qualitative and quantitative characterization of X-ray damage to polymers were studied using modern synchrotron soft X-ray spectromicroscopic techniques, i.e. scanning transmission X-ray microscopy (STXM) [ASE98, AUT02] and X-ray photoemission electron microscopy (X-PEEM) [DGP&98, APD&99, B01]. The power of soft X-ray spectromicroscopy is to produce a three-dimensional data set (two-dimensional images as a function of photon energy), from which detailed chemical information can be extracted. In addition, STXM has a fine spatial resolution of ~ 30 nm and has an excellent spectral resolution of ~ 0.05 eV. These properties make STXM very suitable for both qualitative and quantitative radiation damage studies. X-PEEM has sensitivity to the surface and near surface. Thus, it can provide information about damage to the surface of the sample. Qualitative and quantitative damage evaluation is based on dose dependent changes in the near edge X-ray absorption fine structure (NEXAFS) spectroscopy of the polymers. NEXAFS not only has high elemental sensitivity, but also has high chemical sensitivity for a number of chemical bonding and functional groups. C 1s, N 1s and O 1s NEXAFS spectroscopy was used to study chemical changes caused by radiation damage, such as functional group destruction, new bond formation, fragment elimination (or mass loss), structural reorganization, etc. The quantitative approach of dose-damage evaluation of

polymers is composed of three major parts: (1) radiation dose evaluation for STXM and X-PEEM; (2) application of Beer-Lambert law for damage evaluation; and (3) mathematic fitting of the dose-damage data points to a model based on first-order kinetics [ZJL&95, RHA&97, A98, BJ02, CUA02]. The quantitative approach of this thesis carefully determined and evaluated many factors, such as mass loss, damage saturation level, error analysis, etc. In addition, a quantitative approach was developed for X-PEEM for the first time. Based on the qualitative and quantitative measurements, mechanisms of radiation damage to polymers were derived, such as radiation chemistry and damage spread beyond the X-ray irradiation spot probably via radical/ion migration.

Soft X-ray damage to polymers was developed as a tool in STXM for nanoscale, chemically selective, soft X-ray direct-write patterning. This application was developed based on a few key properties of polymer NEXAFS and radiation damage studies. In particular, polymers have selective absorption at different photon energies for different functional groups and chemical environments, and also have differential damage rates. Thus chemically selective damage is possible at these selective absorption energies. However, it was found that damage spread destroys the intrinsic absorption selectivity unless a layered polymer structure is used. The interface between layered polymers is very effective to restrict damage spread between different layers. Eventually, the chemically selective soft X-ray direct-write patterning (or lithography) was successfully demonstrated in bilayer and trilayer polymer systems with multi-wavelength patterns selectively written into each layer. In addition, a general procedure to simulate chemically selective patterning was developed and shown to be a useful tool in designing multilayer

"X-ray sensitive paper" with high contrast properties.

1.2 Ionizing radiation damage

1.2.1 Types of ionizing radiation

Radiation damage refers to the alteration of the properties of a material from exposure to an energy source, such as X-rays, γ-rays, charged particles, fission fragments in nuclear materials, neutrons etc. Radiation processes involving energy transfer to the target above the first ionization potential (IP) are known as ionizing radiation, while radiation at energies lower than the first IP is known as non-ionizing radiation. Ionizing radiation includes two major categories, electromagnetic radiation and particulate radiation [BC63, C83, MM85]. The minimum energy of ionizing radiation can be as low as a few electron volts (eV) depending on the properties of materials. This threshold corresponds to the first IP of gases, the band gap and work function of insulators and semiconductors, and the work function of metals. Many natural and artificial radiation sources have much higher energy. **Table 1.1** lists some common ionizing radiation sources and their typical energies and penetration ranges.

Photons interact strongly with matter. The amount of energy required to ionize depends on the material. Radio waves, microwaves, IR etc. are completely non-ionizing radiation in single-photon processes; visible and ultraviolet light are ionizing only to some specific molecules, so they are usually not considered as ionizing radiation; X-rays and γ-rays will ionize all materials. The interactions of X-rays and γ-rays with matter can be divided into three categories, the photoelectric effect, Compton scattering and pair

Table 1.1 Energy and penetration ranges of common ionizing radiation sources [C83, MM85, VKW85]

Ionizing radiation		**Typical energy range (eV)**	**Penetration range**
Electromagnetic radiation	Soft X-rays	100 eV - 10 keV	μm
	Hard X-rays	10 keV - 1 MeV	mm
	γ-rays*	100 keV - 1 GeV	cm - m
Particulate radiation	α particle (He nucleus)	1 MeV - 200 MeV	μm
	β particle (electron)	10 keV - 15 MeV	mm
	Proton	1 MeV - 30 GeV	μm
	Deuterons	1 MeV - 200 MeV	μm
	Heavy ions (^{7}Li, ^{11}B, ^{12}C, ^{14}N, ^{16}O, ^{20}Ne, ^{40}Ar, etc.)	1 MeV - 200 MeV	μm - mm
	Fission fragments	25 MeV - 300 MeV	μm - mm
	Neutron	0.025 eV - 1 MeV	m

*Some γ-rays can be lower than 100 keV, e.g. ^{57}Fe Mössbauer γ-rays of 14.4 keV

production [BC63, C83, S92, A98, T04a]. The relative importance of these effects depends on the energy of the photons and the characteristics of the matter. Although other processes, such as elastic (coherent) interactions and photon absorption by atomic nuclei, also exist, they are usually of minor importance [T04a]. For soft X-rays, because the photon energy is low, the photoelectric absorption effect, which is called X-ray absorption in this thesis, is the dominant process. This is discussed in detail in section 1.3.1. For hard X-rays and especially γ-rays the other two effects become more important and are dominant for photon energies above 1 MeV.

Charged particles such as α particles, β particles (electrons), protons and atomic ions also strongly interact with matter. When these particles have sufficiently high kinetic energy their interactions will be ionizing through energy transfer by inelastic scattering. The interactions of these particles with matter depend on factors such as the energy, mass, charge etc. α particles, because of their relatively large mass and double positive charge,

exert a strong attractive force on the electrons of the atoms near their paths. This force will ionize some atoms and excite other atoms, as the kinetic energy of the α particle is dissipated. Due to the strong coulombic interaction the ionization track of an α particle is dense and straight, and the penetration depth is relatively small. For other positive ions, such as proton and some atomic ions, their behaviour can be figured out by comparison to the mass and charge to that of an α particle. Due to their small mass and single negative charge, electrons are easily deflected by the electrons and nuclei of atoms. Thus the path of an electron is tortuous and difficult to define. In this thesis work, low kinetic energy (<500 eV) electrons are generated in soft X-rays interactions with matter. The greatest density of ionization occurs near the end of the tracks of these electrons, when their energy has been decreased to a few tens of electron volts since the inelastic mean free path (IMFP) minimizes at this energy range [S92, TPP91, TPP93], see **Figure 1.1**.

Neutrons do not interact strongly with electrons due to the lack of electric charge. Their interactions with matter result from direct collisions with atomic nuclei. Neutrons

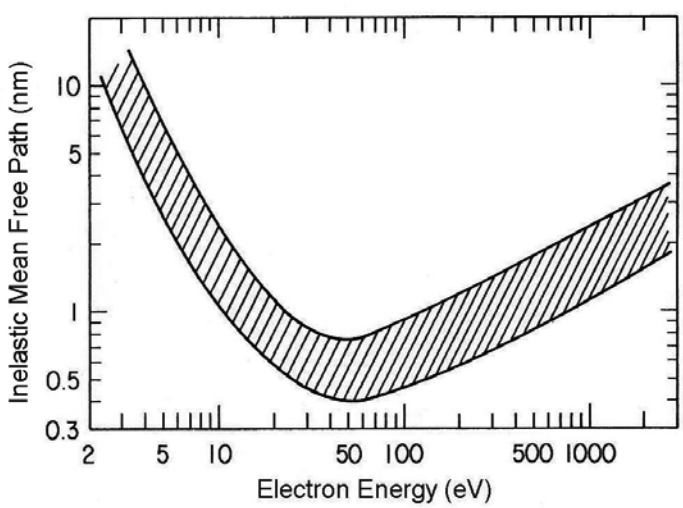

Figure 1.1 Inelastic mean free path in solids as a function of the electron kinetic energy (Adapted from [S92]).

can penetrate deep into matter. Slow or thermal neutrons (0.025 eV to 0.1 keV) interact mainly by entering the atomic nuclei and being captured there [C83]. If the resulting atomic nuclei are radioactive, ionizing radiation will be emitted when they decay. Fast neutrons (>0.02 MeV) interact mainly by elastic collisions with the nuclei. One major consequence, especially in the case of neutrons interacting with living matter, is to produce large quantities of recoil protons of energies up to that of the incident neutron [C83]. The energetic protons cause intense ionization and damage as they are slowed down. Neutrons of intermediate energy (0.1 - 20 keV) interact with matter through both capture and collision processes [C83].

1.2.2 The fields of ionizing radiation damage

The literature dealing with radiation damage is extensive. **Table 1.2** lists some selected references including books, review articles and research papers for both electromagnetic radiation damage and particulate radiation damage on different kinds of materials. For inorganic materials, references of radiation damage to metals, semiconductors and devices, and insulating materials such as oxides, ceramics, etc. are listed; for organic materials, references of damage to molecular compounds, self-assembled monolayers (SAMs), polymers, amino acids and proteins, and deoxyribonucleic acid (DNA) and its components, etc. are listed; for biological samples, references of damage to cells, organisms and tissues are listed. The radiation damage of inorganic materials is relatively simple and typically requires a larger dose than damage to organic and biological materials. The damage usually involves defect production by

Table 1.2 Selected references (books, review articles and research papers) for ionizing radiation damage to different kinds of materials.

Materials		**Ionizing radiation**				
		Electromagnetic radiation		**Particulate radiation**		
		X-rays	γ-rays	Electron beam	Ion beam	Neutron
Inorganic	Metals	---	T69, ARF&96	T69, V77, S78, ARF&96	T69, S78, K92, BO02, OB03	T69, S78, BO02, OB03
	Semiconductors and devices	MD89, CS02, P03	MD89, SBS&93, CS02, P03	MD89, SBS&93, CS02, P03	MD89, SBS&93, CS02, P03	MD89, CS02, P03
	Oxides, ceramics, etc.	T04b	T04b	DSW&98, T04b	DSW&98, T04b	T04b
Organic	Molecular compounds	BC63, C81, HN02	BC63, C81	BC63, C81	BC63, C81	BC63, C81
	Self-assembled monolayers	LGB&91, KYP&00, WVB&05	---	SFP&96, OR98, ZFH&00	AHE&95, RMB&99	---
	Polymers	BC63, M75, C81, CS91, SS91, B00a, CUA02	BC63, M75, C81, CS91, SS91, B00a	BC63, G74, M75, C81, CS91, SS91, B00a	BC63, M75, C81, CS91, SS91, B00a, LCA01	BC63, M75, C81, CS91, SS91, B00a
	Amino acids and proteins	TM00, WRK&00, SSH04, ZFW&04	K01	K01, S02	RSS&98	BPM01
	DNA and components, etc.	H94, FMG&95, YWH99, AFY04b	SNW&90, HBC&00, AFY04b	S02	ZBF94, HBC&00	BPM01, RCG&02
Biological	Cells and microorganisms	HM78, C83, CW86, FTO&96, A98, FTA&02	C83, CW86, A98, CSN&04	C83, A98	C83, A98, CSS&98	C83, A98, BPM01
	Tissues	C83, A98	C83, A98	C83, A98, SSR&98	C83, A98	C83, A98

atomic displacement, migration, desorption [ARF&96, DSW&98, BO02], and occasionally impurity production as a result of embedded incident particles and

transmutation of nuclei, etc. The macroscopic effects of the radiation damage include amorphization [T04b] and embrittlement [ARF&96] etc. of inorganic materials.

Organic materials and biological samples are typically much more sensitive to ionizing radiation. Radiation damage and accompanied effects are important in many modern technologies such as the electronics industry. Radiation damage of biological systems is crucial to the health of human beings. In the past a few decades radiation damage studies of organic materials, including biomolecules have been of particular importance [BC63, C81, C83, A98]. This thesis focuses on soft X-ray induced damage to organic materials, especially polymers. The following sections of this chapter are restricted to radiation damage of organic and biological materials.

Although ionizing radiation can be harmful if one is exposed to high doses, it is very useful in many applications. In industry, ionizing radiation is used extensively to process materials, such as polymers, crystals etc. with many outstanding advantages, such as low energy consumption, low temperature, fast times, capability to process thick materials, absence of solvents. For electronic applications ionizing radiation is used in the test and development of electronic components; in manufacturing, industrial radiography is used for non-destructive inspection; in the nuclear research and industry, ionizing radiation is used in the production of nuclides, elements, or subatomic particles, and in the study and development of structural materials. After chemical tests, diagnostic medical radiography is the second most common use of X-rays; radiation therapy with electrons, X-rays, γ-rays or atomic ions is often used to treat malignant tumors; tracer methods are frequently used in nuclear medicine; ionizing radiation is also very useful in

sterilizing medical hardware and in food preservation.

1.3 Effects of soft X-ray induced radiation damage

The soft X-ray region, defined as 100 to 1000 eV, contains the absorption edges for many low and intermediate atomic number elements [TAG&01], such as the *K*(1s) edge of B, C, N, O, F and the L_{23}(2p) edges of Si, P, S, Cl, K, Ca, Sc, Ti, V, Cr, Mn, Fe, Co, Ni and Cu. This range is of particular importance in X-ray spectromicroscopy [WAH&97, H01a, H01b, HMH&02, HMZ&05]. Soft X-ray spectromicroscopy (also known as NEXAFS microscopy) exploits the full power of the combined spatial-spectral domain by automated acquisition of image sequences, which produce a three-dimensional data set which can be analyzed to extract the maximum possible chemical information from the region studied [H01a]. However, radiation damage to samples limits the accuracy and use of soft X-ray spectromicroscopy in many cases [AUT02, KHM&02, MHC&04, KJH95, MOW&00, WJM&00, BLW&04, AHP&06, DAU03, SZH&05]. Thus it is important to understand the effects of radiation damage in terms of its physical, chemical and biological consequences etc., to characterize the damage rate and dose-damage relationship, and ultimately to find ways to minimize the impact of damage on microanalysis for specific ranges of dose relevant to microscopy.

The process of soft X-ray damage is complicated with many stages and contributing factors. **Figure 1.2** is a cartoon depiction of the timescale of soft X-ray damage to organic materials, such as polymers and biological samples. The initial interactions of soft X-rays with matter include photoabsorption followed by primary and

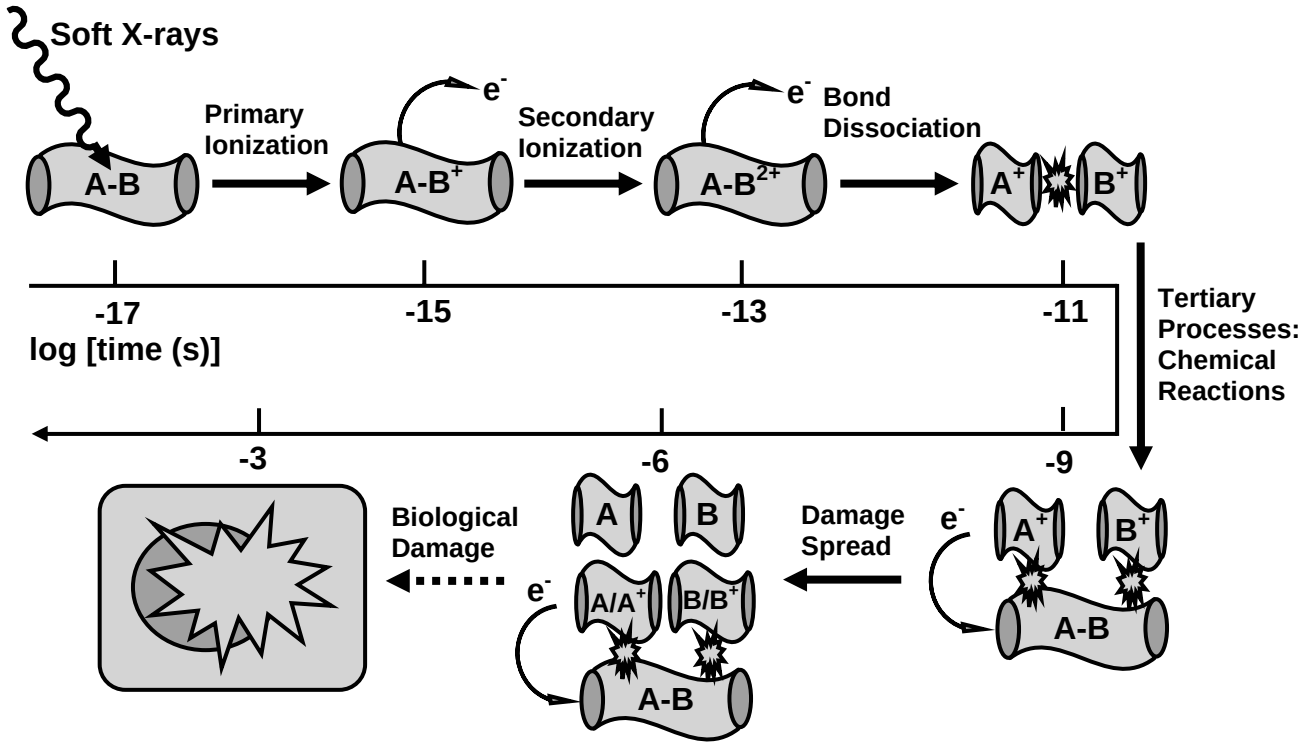

Figure 1.2 Timescale of soft X-ray damage to organic materials.

secondary ionization in the femtosecond time scale. The subsequent chemical processes include bond dissociation and tertiary processes in terms of chemical reactions initiated by ions, radicals and electrons. The radiation damage to living species starts from the damage of proteins, nucleic acids etc., which usually takes much longer time. However biological effects of radiation damage occur at very low radiation doses compared to direct chemical damage, which is the subject of this thesis.

1.3.1 Physical effects

The dominant mechanism of the interaction of soft X-rays with matter is the photoelectric effect or X-ray absorption in which an incident photon with energy *hν* is

absorbed by an atom and an electron is ejected. The kinetic energy (E_k) of the electron is given by:

$$E_k = h\nu - E_b \tag{1.1}$$

where E_b is the binding energy of the electron. This process refers to a primary photoionization process which requires the incident photon energy to be greater than the binding energy of the ejected electrons. The primary photoionization probability, i.e. the photoionization cross section, is a function of photon energy. An empirical expression for the partial photoionization cross section for *K* shell ionization of element *A* by X-rays is [C97, A91]:

$$Q(A_K) \approx 2.1\times10^{-16}\, z_K E_b^2(A_K)/h\nu^3 (cm^2) \tag{1.2}$$

where z_k is the number of electrons in *K* shell of binding energy $E_b(A_K)$ for element *A*. Replacing A_K by A_L, A_M … or B_K, B_L, B_M …, the same expression can be used for other atomic shells of the same element or another element *B*.

Apart from primary photoionization, secondary photoionization also occurs in the photoabsorption process. This is a two-step process involving first creating a core hole by primary photoionization, and second, decay of the core hole by the Auger process [S92, C95a, C95b, C97], in which an electron from a higher energy level falls into the core hole, accompanied by ejection of another electron from the same level, or from a different sublevel. The kinetic energy of the ejected Auger electron is independent of the incident photon energy, depending only on the atomic levels. For instance, the kinetic energy of the *KLL* Auger electron for element *A* is approximately:

$$E_k(A_{KLL}) = E_b(A_K) - E_b(A_L) - E_b(A_L) \tag{1.3}$$

The other major mechanism of core hole decay is X-ray fluorescence, in which an electron from an upper level falls into the core hole, causing emission of an X-ray. The emitted energy also depends only on the atomic levels. For example, the energy of the X-ray emission K_α line of element A is approximately:

$$h\nu(A_{K_\alpha}) = E_b(A_K) - E_b(A_L) \tag{1.4}$$

Typically, the probability of X-ray fluorescence is less than 5% when the binding energy is less than 2 keV and less than 1% for binding energy below 600 eV [K79, C97], so the Auger process is the dominant process for core hole decay in organic materials which are mainly comprised of low Z-value elements with core level binding energies below 2 keV.

1.3.2 Chemical effects

The chemical changes caused by ionizing radiation usually start from the secondary ionization, as shown in Fig. 1.2. Due to Coulombic interaction, the multiply charged molecules tend to undergo charge separation, directly resulting in bond dissociation. The tertiary processes after photoabsorption refer to the chemical reactions initiated by ions, radicals and electrons, which are generated either from the primary and secondary processes or produced during the tertiary processes, as shown in Fig. 1.2.

Organic molecular compounds undergo a variety of chemical changes upon X-ray and γ-ray irradiation [BC63]. For light elements, such as those of the second row, direct bond dissociation induced by Auger decay usually produces singly charged ions and radicals. For heavier elements, such as those of the third and fourth row, even quadruply charged parent molecules are possible [HN02], which are created by an Auger cascade

process and then dissociate into a multiply charged ion, or several singly charged ions. The elimination of stable small molecules, such as H_2, H_2O, CO_2 etc., is also very common for most organic materials when dissociation occurs in side chains or functional groups, or intermolecular rearrangement occurs. The chemical reactions of the tertiary processes include a number of processes, such as radical or ion induced dissociation, radical-radical recombination, radical-radical disproportionation, i.e. two identical radicals yielding two different molecules, radical-molecule abstraction, radical scavenging, isomerization etc [BC63].

For the past decade, soft X-ray induced radiation damage to small biochemical molecules such as amino acids [BZW94, SSH04, ZFW&04, ZZS&04b], DNA components such as nucleobases [AFY04a, AFY04b, YAF&04] and nucleotides [FMG&95], have been of great interest. For amino acids, decomposition is a major consequence of radiation damage, and a variety of decomposition pathways have been observed, such as deprotonation, dehydration, decarboxylation, decarbonylation, deamination and desulfurization etc., with rates depending on the specific amino acid. For nucleobases, decomposition occurs in the functional groups attached to the ring structure, and new products formed by radicals and ions are common. The existence of radicals was proved through *in situ* Electron Paramagnetic Resonance (EPR) [YAF&04]. For nucleotides, damage is characterized by fragmentation which breaks the bonds linking the nucleobase, sugar and phosphate groups.

Damage of synthetic polymers by ionizing radiation has been studied for about half a century [BC63, M75, C81, CS91, SS91, B00a]. In addition, industrial scale

radiation processing of polymers has been employed for around two decades [SS91]. However, these ionizing radiation damage studies and radiation processing mainly use electron beams from electron accelerators, or γ-rays from Cobalt-60 sources [BC63, SS91]. Over the past decade, with the growing application of soft X-rays in materials analysis, the accompanied radiation damage of polymers by soft X-rays has attracted more interest [ZJL&95, BJ02, CUA02]. Radiation-initiated chemical reactions and effects for synthetic polymers include scission, crosslinking, grafting and curing etc. [B00a]; however, the last two have not been reported for soft X-rays. The scission process includes both the outcome from primary interactions of polymer chains with soft X-rays and secondary interactions through the radiation induced radicals. If scission occurs in polymer side chains, fragmentation and desorption of small molecules as a result of mass loss may happen, as occurs for instance in polymethylmethacrylate (PMMA) [TTM&94]. The consequences of scission are a reduction of molecular weight and an increase in polymer solubility. Crosslinking which involves inter-chain bond formation increases the molecular weight, ultimately leading to a three-dimensional polymer network, which reduces polymer solubility. Grafting is a process in which monomers are introduced onto the polymer chain through radiation. Curing is a method to rapidly polymerize an oligomer-monomer mixture by forming a coating on a substrate and initiating polymerization by irradiation with electron beams or UV.

Soft X-ray radiation damage of some natural polymers, i.e. biopolymers such as proteins [B00b, RM00, TM00, WRK&00, KAF04, LTR&06, FVA&07] and DNA [H94, HHA&96, WH98, YWH99, DSA00, RDB03, CCS&05, CDG&05, MCR&07], has been

reported increasingly as synchrotron light has become widely applied in modern structural biology. In addition, because the brightness of the third-generation synchrotron sources is very high, radiation damage has become a serious problem even when cryo-techniques [GS97, MOW&00, WJM&00] are used. For protein damage as observed by protein crystallography, early studies proposed that the damage was nonspecific, being associated with a general decrease of diffraction spot intensities [BJ76, SA88, GN94]. However, recent studies have shown that X-rays also can cause highly specific damage, such as breakage of disulfide bonds, decarboxylation, loss of hydroxyl groups from specific amino acids, and conformational change through hydrogen-bond breaking of the acidic residues in proteins [B00b, RM00, WRK&00, FVA&07]. Soft X-ray damage of DNA has several major consequences, such as single strand breaks (SSB), double strand breaks (DSB) [HHA&96, YWH99, RDB03], crosslinking [CCS&05], and damage to nucleobases or the sugar moiety [CDG&05]. SSBs are usually formed by a single ionizing event, for instance *K*-shell photoabsorption on carbon, nitrogen or oxygen [YWH99], followed by Auger decay leading to multiple ionization and then bond dissociation. The damage tends to occur at the non-phosphorylated sites and is relatively indiscriminate with respect to base sequence [RDB03]. DSBs are induced by the same mechanism as SSB, but only form at much higher radiation dose [HHA&96, YWH99]. In addition to SSB, irradiation of DNA produces a large number of radical species [WH98, CDG&05], which are mainly nucleobase and sugar based radicals if DNA is dehydrated, or mainly OH· radicals if DNA is hydrated or is in cells. These radicals are responsible for further DNA damage in terms of SSB, DSB, crosslinking of intrastrand, interstrand

and interduplex, and DNA components damage.

1.3.3 Radiation effects on living species

The damage of important biological molecules, such as proteins, DNA and RNA, results in a wide range of biological effects when living organisms are irradiated. **Table 1.3** lists the major biological effects for ionizing radiation damage to different levels of biological organization. The biological damage depends on the type, dose, rate and the distribution of the radiation [C83]. For soft X-rays, there are many radiation damage studies on live biological samples [HM78, CW86, FBB&92, FTO&96, C98, CRC02, FTA&02, SBC&02]. However, most of the studies are at the cellular level. Since DNA is considered to be the primary target of radiation induced cell lethality, mutation and carcinogenesis, recent investigations are focusing on DNA damage in cells *in vivo*. The SSB of DNA damage is repairable with high speed and efficiency, while the DSB is generally not repairable [C83]. Recent studies are investigating the mechanisms resulting in DSB so as to understand cell viability upon soft X-ray radiation [FTA&02, SBC&02].

Table 1.3 Some biological effects of ionizing radiation damage (adapted from [C83]).

Level of biological organization	Biological effects of radiation damage
Subcellular	Damage to cell membranes, nucleus, chromosomes, mitochondria and lysosomes etc.
Cellular	Inhibition of cell division, transformation to a malignant state, cell inactivation, cell death etc.
Tissue, organ	Damage of tissues and organs, disruption of such systems as the central nervous system, the bone marrow and intestinal tract, induction of cancer etc.
Whole species	Death, radiation lifeshortening
Populations of species	Changes in genetic characteristics due to gene and chromosomal mutations in individual members of the species

1.4 Qualitative and quantitative characterization of soft X-ray radiation damage

A number of techniques have been used to study soft X-ray damage of organic materials. **Table 1.4** lists these techniques, their application to the characterization of soft X-ray damage of organic materials, and selected references. Most techniques can provide both qualitative and quantitative damage information.

X-ray Photoelectron Spectroscopy (XPS) and Ultraviolet Photoelectron Spectroscopy (UPS) are techniques which detect photoelectrons ejected from the core and valence levels, respectively, after photo absorption. XPS is element specific and sensitive to the chemical state of the element, while UPS is sensitive to the valence electronic structure. XPS has been used to investigate soft X-ray damage for a few organic materials, such as amino acids [BZW94, ZFW&04, ZZS&04b], SAMs [LGB&91, KYP&00, HZG&01, KCH&05, WVB&05, SZF&06], and polymers [YT02, CDS&06]. XPS is sensitive to the chemical states of the major elements in organic compounds, such as carbon, nitrogen, oxygen and sulfur etc. Different oxidation states, or chemical environments, can be resolved by XPS, such as $C_{C\text{-}C}$, $C_{C\text{-}X}$ (X = O, F etc.), $C_{C=C}$, $C_{C=O}$, $C_{N\text{-}C=O}$, $C_{O\text{-}C=O}$ for carbon, $N_{NH_3^+}$, N_{NH_2}, N_{NO_2}, N_{NO} for nitrogen, $O_{C=O}$, O_{OH} for oxygen, $S_{S\text{-}C}$, $S_{S\text{-}S}$ for sulfur etc. The development of these chemical states through radiation damage and their quantitation is reflected in XPS peak shapes and intensities. This information can be useful to determine damage mechanisms, such as decarboxylation, deprotonation for amino acids and polymers, bond scission between sulfur and substrate for SAMs. The quantitative evaluation of radiation damage with XPS has also been performed for many materials, including amino acids [BZW94, ZFW&04, ZZS&04b],

Table 1.4 Techniques to characterize soft X-ray damage of organic materials

Technique		Principle	Characterization of soft X-ray damage of organic materials		Selected references
			Qualitative	Quantitative	
Photoelectron Spectroscopy	X-ray Photoelectron Spectroscopy (XPS)	Irradiation with energy-fixed X-rays, detection of kinetic energy of emitted electrons	Spectroscopic variation	Peak intensity $I(t)$	BZW94, ZFW&04, ZZS&04b, LGB&91, KYP&00, HZG&01, KCH&05, WVB&05, SZF&06, YT02, CDS&06
	Ultraviolet Photoelectron Spectroscopy (UPS)	Irradiation with energy-fixed ultraviolet radiation, detection of kinetic energy of emitted electrons	Spectroscopic variation	Peak intensity $I(t)$	MMC&99, CMM&00, CDS&06
Near Edge X-ray Absorption Fine Structure (NEXAFS) Spectroscopy	Total Electron Yield (TEY) / Partial Electron Yield (PEY)	Irradiation with monochromatic X-rays, detection of secondary electrons	Spectroscopic variation	---	HAN&85, UKM&93, TTM&94, TUM&96, CDS&06, WVB&05, SZF&06
	X-ray Photoemission Electron Microscopy (X-PEEM)	Irradiation with monochromatic X-rays, detection of secondary electrons imaged via electron optics	Spectroscopic and image variation	Dose-spectroscopic damage relationship	---
	Total Ion Yield (TIY) / Partial Ion Yield (PIY)	Irradiation with monochromatic X-rays, detection of emitted ions	Spectroscopic variation	---	HAN&85, UKM&93, TTM&94, TUM&96
	Total Fluorescence Yield (TFY)	Irradiation with monochromatic X-rays, detection of fluorescence	Spectroscopic variation	---	ZFW&04, ZZS&04b
	Scanning Transmission X-ray Microscopy (STXM)	Irradiation with scanned focused monochromatic X-rays, detection of transmitted X-rays	Spectroscopic and image variation	Dose-spectroscopic damage relationship	Refer to Table 1.5
Mass Spectrometry (MS)		Detection of mass-to-charge ratio of ions	Evolution of new species	Peak intensity $I(t)$	ZFW&04, ZZS&04b, UKM&93, TTM&94, TUM&96, MMC&99, CMM&00
Single-crystal X-ray Diffraction (XRD) and small-angle X-ray scattering (SAXS)		Irradiation with monowavelength X-rays, detection of diffraction pattern or intensity	Decay in the overall diffraction intensity and deterioration of the diffraction pattern resolution etc.	Time/dose-diffraction parameters relationship	B00b, RM00, TM00, WRK&00, LTR&06, FVA&07, BGC&07, SHH&07, CRC02, KAF04
Vibrational Spectroscopy	Infrared Reflection Absorption Spectroscopy (IRRAS)	Irradiation with IR radiation, detection of molecular vibrations	Spectroscopic variation	---	LJK&03, CDS&06
	Raman	Irradiation with IR radiation, detection of molecular vibrations	Spectroscopic variation	Dose-peak intensity relationship	MCR&07
Electron Paramagnetic Resonance (EPR)		Under strong magnetic field and upon microwave radiation, detection of species with unpaired electrons	Spectroscopic observation and variation	Temperature-peak intensity relationship, dose-spin number relationship	SSH04, AFY04a, YAF&04, WH98

Separation techniques	High Performance Liquid Chromatography (HPLC)	Use column chromatography to separate and collect all the species	Evolution of new species	Dose-peak intensity/ concentration relationship	AFY04b, DSA00, RDB03
	Electrophoresis	Separate charged substances under an electric field	Evolution of new species	Dose-peak intensity/ concentration relationship	HHA&96, YWH99, CCS&05
Topography techniques	Atomic Force Microscopy (AFM)	Measurement of the forces between atoms in a surface and in a tip	Image of damaged areas or patterns	Numerical profile of damaged areas or patterns	ZJL&95, LJK&03
	Scanning Photoelectron Microscopy (SPEM)	Irradiation with scanned focused energy-fixed X-rays, detection and image of emitted electrons with the same kinetic energy	Image of damaged areas or patterns	Numerical profile of damaged areas or patterns	KHW&04, KCH&05
X-ray Reflectivity		Irradiation with energy-fixed monochromatic X-rays, detection of reflected X-rays	Reflectivity variation	Profile of reflectivity and fluence-change of layer thickness relationship	RGS&06
Ellipsometry		Oblique incidence of a polarized monochromatic plane wave, detection of polarization change upon reflection	Polarization change	Dose-layer thickness relationship	KYP&00
Contact Angle		Measurement of liquid wetting of surfaces	Variation of contact angle	Dose-contact angle relationship	KYP&00

*PIY usually does not represent the real NEXAFS profile for a species.

Table 1.5 STXM characterization of soft X-ray damage in polymers

Polymer	Characterization of soft X-ray radiation damage		Reference
	Qualitative	Quantitative	
Polymethylmethacrylate (PMMA)	Spectroscopic and image variation	Dose-spectroscopic damage relationship, critical doses of mass loss and C=O damage, fractional mass	ZJL&95, BJ02, CUA02
Polystyrene (PS)	Spectroscopic variation	Fractional mass	CUA02
Poly(ethylene terephthalate) (PET)	Spectroscopic variation	Dose-spectroscopic damage relationship, critical doses of mass loss and C=O damage, fractional mass	RHA&97, CUA02
Poly(bisphenol-A-carbonate) (PC)	Spectroscopic variation	Dose-spectroscopic damage relationship, critical dose of C=O damage, fractional mass	CUA02
Nylon 6	Spectroscopic variation	Dose-spectroscopic damage relationship, critical doses of mass loss and C=O damage, fractional mass	CUA02
Poly(vinyl methyl ketone) (PVMK)	Spectroscopic variation	Dose-spectroscopic damage relationship, critical doses of mass loss and C=O damage, fractional mass	CUA02
Polyurethane (PU)	Spectroscopic variation	Dose-spectroscopic damage relationship, critical dose of C=O damage, fractional mass	CUA02
Poly(ethylene succinate) (PES)	Spectroscopic variation	Dose-spectroscopic damage relationship, critical doses of mass loss and C=O damage, fractional mass	CUA02
Polyethylene (PE)	Spectroscopic variation	Fractional mass	CUA02
Poly(propylene oxide) (PPO)	Spectroscopic variation	Dose-spectroscopic damage relationship, critical dose of mass loss, fractional mass	CUA02

SAMs [HZG&01, WVB&05, SZF&06] and polymers [YT02]. The general approach is to plot the XPS peak intensity as a function of exposure time; a linear relationship is usually observed [YT02, HZG&01]. UPS has been used to characterize some polymers after irradiation with soft X-rays [MMC&99, CMM&00, CDS&06]. UPS is sensitive to changes of the valence band structure during radiation damage, such as decrease of the CH band, growth of the C=C band and broadening of the C-C band etc. Through UPS observations, two main polymer damage mechanisms were proposed [MMC&99, CMM&00, CDS&06], i.e. the dehydrogenation of alkyl chains to form C=C double bonds and crosslinking in/between the polymer chains. Quantitative evaluation of radiation damage with UPS has been reported [CMM&00] and a similar approach as that of XPS was used, i.e. exploring the relationship between peak intensity or binding energy and exposure. Once again linear behavior was often observed [CMM&00].

Near Edge X-ray Absorption Fine Structure (NEXAFS) spectroscopy is an element-specific electronic structure spectroscopy, which is widely used in surface science [S92] and recently has been extensively applied to a variety of organic materials, such as molecular compounds [SZH&05], natural and synthetic polymers [AUT02], biomolecular compounds, i.e. amino acids and peptides [KOJ&02, ZZS&04a], DNA bases [FAM&03], etc. NEXAFS spectra identify chemical modifications caused by soft X-rays, such as functional group changes, formation of new structure, mass loss etc. NEXAFS spectra can be measured by Total Electron Yield (TEY) / Partial Electron Yield (PEY) [S92], Total Fluorescence Yield (TFY) [S92], and transmission [AZC92, ASE98, AUT02]. Electron and fluorescence yields are linearly proportional to photoabsorption,

while the transmission is related to the absorption by the Beer-Lambert law (eqn. 2.10). The use of PEY can eliminate low energy secondary electrons so as to achieve a better signal-to-background ratio. TEY/PEY-NEXAFS has been used for monitoring soft X-ray photochemistry of polymers, such as polyethylene (PE) [HAN&85], polystyrene (PS) [HAN&85], polymethylmethacrylate (PMMA) [UKM&93, TTM&94, TUM&96]), poly(3-hexylthiophene) [CDS&06], and SAMs [WVB&05, SZF&06]. TEY/PEY was often combined with Total Ion Yield (TIY) / Partial Ion Yield (PIY) to elucidate more clearly the radiation damage mechanisms [HAN&85, UKM&93, TTM&94, TUM&96]. For instance PMMA was shown to undergo site specific photo fragmentation in the ester side chain [TUM&96]. A systematic characterization of damage to polymers by X-PEEM was conducted in this thesis, as presented in Chapter 5. TFY-NEXAFS has been used to characterize soft X-ray induced radiation damage of a series of amino acids at the C, N, O and S edges [ZFW&04, ZZS&04b]. There are significant spectral changes as damage occurs, which are consistent with specific damage mechanisms including dehydrogenation, dehydration, decarboxylation etc. Compared to TEY, which is very surface sensitive, TFY can provide more information about the bulk of the sample since fluorescence samples much more deeply than electrons.

Recently STXM was used to study radiation damage in a number of polymer materials, as listed in **Table 1.5**. NEXAFS spectroscopy in a STXM has shown high sensitivity to radiation damage. STXM is very useful for quantitative studies of soft X-ray damage [ZJL&95, RHA&97, BJ02, CUA02] since the Beer-Lambert law for quantitation is obeyed and it is convenient to systematically control the amount of damage and to

make damage in a short time. For quantitative dose-damage evaluation, the change in optical density (OD) of a NEXAFS peak modified due to chemical changes associated with damage is measured as a function of the absorbed radiation dose, which in turn is evaluated from the photon energy, incident photon flux, photoabsorption coefficient, exposure time and mass of the sample. The experimental data are then fit to postulated rate laws, typically first order kinetics [ZJL&95], from which a critical dose for damage of the sample material is obtained. The critical dose is a characteristic property of a material. It is the dose that attenuates a specific spectroscopic feature to 37% of its initial value (or increases to 63% of its maximum value in the cases where spectral features grow up with damage). Radiation damage studies of polymers by STXM suggested the damage for PMMA, PET, Nylon 6, PVMK, PES and PPO occurs in the form of mass loss characterized by mass loss critical dose and fractional mass, and the damage for PMMA, PET, PC, Nylon 6, PVMK, PU and PES also occurs as chemical structure change, e.g. C=O functional group damage, as shown in Table 1.5. Quantitative evaluation of radiation damage with X-PEEM has not been reported to the author's knowledge. In this thesis, a similar approach as that of STXM was used and comparable results were obtained. Details of the quantitative dose-damage evaluation methodologies for STXM and X-PEEM are described in Chapter 3.

Mass Spectrometry (MS) is an analytical technique capable of directly detecting the products of radiation damage. It is often used with other techniques such as NEXAFS, XPS and UPS. Soft X-ray irradiation of solid amino acids [ZFW&04, ZZS&04b] leads to desorbed species, such as H_2, NH_2 (or O), H_2O, CO (or H_2CN), CO_2 and H_2S (only for S

containing amino acids, e.g. cysteine) etc., as monitored by conventional MS. In addition, the time evolution of the mass spectra monitors species that desorb at different times for different amino acids. The above desorbed species show that radiation damage of amino acids involves a variety of processes including: dehydrogenation, dehydration, deamination, decarbonylation (or decarboxylation) and desulfurization etc. Time of flight MS and quadrupole MS were applied to study soft X-ray damage of two important polymers, i.e. PMMA [UKM&93, TTM&94, TUM&96] and polyvinylidene fluoride (PVDF) [MMC&99, CMM&00]. The dominant ions for PMMA damage are CH_3^+, H^+, CH_2^+, CH^+, OCH^+ and $COOCH_3^+$. In order to locate the fragmentation site of CH_3^+ in PMMA, two analogous polymers, poly(methyl acrylate) (PMA) and poly(methacrylic acid) (PMAA), were also measured, thus clarifying that the CH_3^+ fragment is generated from the PMMA ester side chain [TUM&96]. Ionic desorption following PVDF damage is dominated by H_2, HF, CH_2, suggesting processes such as dehydrogenation, C-F bond and main chain scission. Electrospray MS was used to study DNA nucleotide damage upon soft X-ray radiation [FMG&95]. The fragments detected are consistent with damage at specific sites related to phosphate and some multiple scissions inside the molecule. The method for quantitative evaluation of radiation damage with MS is to plot the intensity of individual masses as a function of exposure time [CMM&00, ZFW&04, ZZS&04b]; however the plots are difficult to define mathematically.

Single-crystal X-ray Diffraction (XRD) is an analytical technique which utilizes the diffraction pattern generated by irradiation of a single crystal with X-rays (soft or hard X-rays from laboratory or synchrotron) to solve the crystal structure. This technique is

widely used for biochemical materials, such as protein, DNA etc. In protein crystallography, radiation damage is always a major concern, so XRD has been used to characterize radiation damage [B00b, RM00, TM00, WRK&00, LTR&06, FVA&07]. The qualitative damage indicators include gradual decay in the overall diffraction intensity and deterioration of the resolution of the diffraction pattern. The quantitative damage indicators are changes in several diffraction parameters such as unit cell volume, *R*-factor (i.e. agreement between experimental and calculation) and *B*-factor (i.e. temperature-factor). Plots of diffraction intensities and some parameters as a function of exposure time or dose have shown linear or exponential behavior [TM00, BGC&07, SHH&07]. Recent studies also show that protein X-ray damage can be rather site specific, see section 1.3.2. XRD was also used for monitoring radiation damage in other organic materials, such as lipids [CRC02], in which radiation damage causes broadening of reflection patterns, loss of intensity and partial or complete phase transformation resulting in pattern change. Small-angle X-ray scattering (SAXS) involves detecting scattering intensity at very low angles (typically 0.1 - 10°) to measure patterns which are sensitive to the shape and size of macromolecules. SAXS has been used to study X-ray damage of a protein solution [KAF04], in which damage causes radiation-induced protein aggregation.

Vibrational spectroscopies, such as Infrared Reflection Absorption Spectroscopy (IRRAS) and Raman, have also been used to characterize soft X-ray damage to organic materials. Several recent examples include damage to small molecule SAMs [LJK&03] and polymers [CDS&06] characterized by IRRAS, and DNA damage monitored by online Raman [MCR&07]. In these studies, the damage is reflected in a substantially

reduced intensity for specific vibrational modes, such as C=N stretching and NO_2 asymmetric/symmetric stretching in nitro-substituted aromatic imine monolayers [LJK&03], aliphatic CH_2 and aromatic CH stretching in poly(3-hexylthiophene) [CDS&06], C-Br non-symmetric bending in 8-bromo-2'-deoxyguanosine in DNA [MCR&07]. The reduced intensity is usually a direct consequence of bond dissociation. Quantitative information can be obtained from plots of peak intensity or its alternative as a function of dose, and usually shows an exponential decay profile corresponding to first order kinetics [MCR&07].

Electron Paramagnetic Resonance (EPR) is a spectroscopic technique which detects species that have unpaired electrons. EPR responding species are free radicals. Thus EPR has been used to study and confirm the involvement of radicals in soft X-ray radiation damage for some organic materials including amino acids [SSH04], nucleobases [AFY04a, YAF&04] and DNA [WH98]. Some important conclusions can be drawn from these studies: a variety of radicals are generated by soft X-ray radiation of amino acids, nucleobases and DNA; the EPR dose-response is somewhat photon energy dependent for thymine, however, the yield of the radical species is photon energy independent; one study showed that the EPR signal intensities are linearly proportional to dose rate [YAF&04], while another study demonstrated that the intensity of EPR signals is exponentially proportional to radiation dose [AFY04a]; EPR signals disappear immediately within the signal acquisition time typically of a few seconds when the beam is off; signals in EPR spectra of damaged materials are temperature dependent and decrease significantly when temperature is increased from 77 to 300 K.

Analytical separation techniques, such as High Performance Liquid Chromatography (HPLC) and electrophoresis, have been used to quantify the yields of damage products of soft X-ray irradiated nucleobase and DNA. HPLC analysis of damaged thymine [AFY04b] shows that there are a number of decomposition products resulting from scission of the functional groups attached to the ring structure, secondary reactions induced by radicals and ions, and that the decomposition process is different at different elemental absorption edges [AFY04b]. HPLC studies of damaged DNA [DSA00, RDB03] show that DNA undergoes single strand breaks (SSBs) at radiation doses up to 1000 kGy, and the cleavage site is the non-phosphorylated termini of the oligodeoxynucleotides for all four nucleobases. Electrophoresis analysis of damaged DNA [HHA&96, YWH99, CCS&05] shows that the exposures required for detectible double strand break (DSB) are 15 - 26 times higher than those for SSB; the process of SSB is independent of photon energy; DNA interduplex crosslinking is formed. Both techniques have shown that the decomposed products of DNA, both SSB and DSB, increase linearly in the appropriate dose range.

The physical properties of the soft X-ray induced damage of organic materials have been measured by a number of techniques. For topography information of the damaged or patterned areas, Atomic Force Microscopy (AFM) and Scanning Photoelectron Microscopy (SPEM) have been used. AFM measurements of damaged PMMA polymer [ZJL&95] and damaged SAMs [LJK&03], and SPEM measurements of damaged SAMs [KHW&04, KCH&05] have neatly demonstrated the profiles of the damaged areas/patterns and the spatial resolution. The thickness of SAMs during soft X-

ray radiation damage has been measured by Ellipsometry [KYP&00], which is a sensitive optical technique for thin film metrology. The thickness and interfacial roughness changes caused by X-ray damage to polymer thin films, such as poly(*tert*-butyl acrylate) (PtBA) and PS [RGS&06], have been measured by X-ray reflectivity, showing decreased film thickness and increased surface roughness for PtBA, while the film thickness increased for PS. Contact angle measurements have been used to characterize the surface properties of methyl-, vinyl-, and trifluoroacetoxy-terminated SAMs of alkylsiloxanes on SiOx/Si after soft X-ray irradiation [KYP&00]. These species show decreased contact angle, indicating the surface is transformed from hydrophobic to hydrophilic.

1.5 Significance of this work to soft X-ray radiation damage to polymers

The previous section has shown that a number of techniques can provide both qualitative and quantitative information about soft X-ray damage to polymers. Among them the capability of NEXAFS is outstanding. Compared to NEXAFS, XPS and UPS are much less sensitive to radiation damage, have much lower spatial resolution, and are very surface sensitive; MS has limited spatial resolution, has poor quantitation results, and provides mainly surface information; XRD has limited elemental and chemical sensitivity; vibrational spectroscopy and EPR have limited spatial resolution and have poor quantitation capability; separation techniques have no on-line capability to detect radiation damage and have no physical information about the damage; topography techniques have no elemental and chemical sensitivity, and have no bulk information; the other physical property techniques have no spatial resolution, and have limited elemental

and chemical sensitivity.

Although there are a few publications dealing with soft X-ray damage to polymers using NEXAFS spectroscopy in the past decade [ZJL&95, RHA&97, BJ02, CUA02], this research area is still very limited and incomplete, with some inconsistencies. For example the PMMA critical dose reported by different studies ranges from 13 to 69 MGy; this thesis work is the only damage study by X-PEEM to my knowledge; the biochemical polymers, such as protein and DNA, are much less studied by NEXAFS; quantitative methodologies need verification and improvement regarding some effects, such as mass loss; there are no theoretical predictions of damage; there is very limited understanding regarding radiation damage mechanisms; and probably most important of all, there is no application trying to utilize soft X-ray radiation damage. This work has systematically investigated radiation damage effects in a series of polymers with qualitative and quantitative characterization by NEXAFS in STXM and X-PEEM with the overall goals of (1) providing more consistent and more complete results, (2) better understanding of the radiation damage mechanism in terms of damage spread via radical migration and other factors, such as thermal effect and surface charging etc., (3) application of the damage process to chemically selective patterning.

As a major goal, applications of soft X-ray radiation damage phenomena were to be conceived and developed. One novel and promising direction is to develop chemically selective radiation damage since some NEXAFS spectroscopic features are sharp, intense and have unique energies, so it is possible to induce damage to specific functional groups by irradiation at their individual NEXAFS features. Thus chemically selective lithography

or patterning could be developed if appropriate multi-component substrate fabrication and exposure techniques can be found. One of the major challenges is that the secondary processes dominate radiation damage, cause spatial delocalization of the damage, and are non-specific. The range of damage spread is much larger than the physical separation of functional groups in homogeneous systems such as block copolymers. The solution to this challenge was found empirically to use a layered structure for different polymers; and the polymer-polymer interface was discovered to very effectively block the damage transport between different layers.

1.6 Outline of the thesis

Chapter 2 describes the fundamental principles of synchrotron radiation, NEXAFS spectroscopy, STXM and X-PEEM.

Chapter 3 first describes STXM data acquisition modes, including image scan, point scan, line scan, stack scan and pattern generation scan, and the methodology for quantitative dose-damage analysis. This is followed by a detailed description of the simulation of chemically selective patterning in multilayer polymers. Then X-PEEM data acquisition modes and quantitative dose-damage analysis are presented. In the final part of this chapter, sample preparation methods are presented, in particular spin coating fabrication of single and multilayer polymer films, microtomy and additional characterization techniques such as Atomic Force Microscopy (AFM) and Transmission Electron Microscopy (TEM).

Chapter 4 presents the results of qualitative and quantitative evaluation of

radiation damage by STXM of a series of polymer materials, including polyacrylonitrile (PAN), poly(ethyl cyanoacrylate) (PECA), poly(propylene carbonate) (PPC), poly(ethylene carbonate) (PEC) and poly(ethylene telephthalate) (PET). Factors and effects related to soft X-ray radiation damage mechanisms and kinetics are discussed.

Chapter 5 presents the results of qualitative and quantitative evaluation of radiation damage by X-PEEM of several polymer materials, such as poly(methyl methacrylate) (PMMA), polystyrene (PS) and fibrinogen (Fg). Factors and effects that influence the quantitative results are discussed. Comparison between the results of STXM and X-PEEM of these polymers are also presented. This chapter is presented in a manuscript format since it has been accepted for publication by the Journal of Electron Spectroscopy and Related Phenomena.

Chapter 6 and 7 present results and discussion of chemically selective soft X-ray patterning of single-layer, bilayer and trilayer polymers. Simulation results of chemically selective patterning in the two trilayer films are included. Chapter 6 and 7 are presented in the published format (Chapter 6: J. Wang, H.D.H. Stöver, A.P. Hitchcock and T. Tyliszczak, *J. Synchrotron Rad.* 14 (**2007**) 181-190; Chapter 7: J. Wang, H.D.H. Stöver and A.P. Hitchcock, *J. Phys. Chem. C* 111 (**2007**) 16330-16338).

Chapter 8 summarizes the results and contributions of this thesis and proposes future work.

Chapter 2

Methods

This chapter describes fundamental principles of synchrotron radiation and near edge X-ray absorption fine structure (NEXAFS). It describes X-ray microscopy and soft X-ray spectromicroscopic techniques, in particular scanning transmission X-ray microscopy (STXM) and X-ray photoemission electron microscopy (X-PEEM). For these two synchrotron-based techniques, the beamlines and microscope instrumentation used in this work are presented.

2.1 Synchrotron radiation

Classical physics has shown that any charged particle which moves in a curved trajectory or is accelerated in a straight-line path will emit electromagnetic radiation. When an electron is constrained to move in a curved orbit by a centripetal force, then it radiates. When the electron velocity (v) is much lower than the speed of light (c), i.e. $\beta = v/c$, $\beta \ll 1$ also known as non-relativistic, the frequency of the electromagnetic radiation is comparable to the revolution frequency (ω) of the electron, and the radiation pattern is a dipolar pattern as shown in **Figure 2.1a**. However, when the electron velocity approaches the speed of light, i.e. $\beta \approx 1$ also known as relativistic, the radiation frequency will extend from ω to higher-order harmonics of revolution frequency on the order of $\gamma^3\omega$ due to relativistic effects, where γ is the Lorentz factor, and the dipolar pattern is also distorted by relativistic effects and turns into a narrow cone of radiation with angular spread $\Delta\phi$, as shown in **Figure 2.1b**. The Lorentz factor (γ) is:

$$\gamma = \frac{1}{\sqrt{1-\beta^2}} = \frac{1}{\sqrt{1-(\frac{v}{c})^2}} \tag{2.1}$$

The electron total energy (E) is given by:

$$E = \gamma m_e c^2 \tag{2.2}$$

where m_e is the electron rest mass, and

$$\Delta\phi \approx \gamma^{-1} \tag{2.3}$$

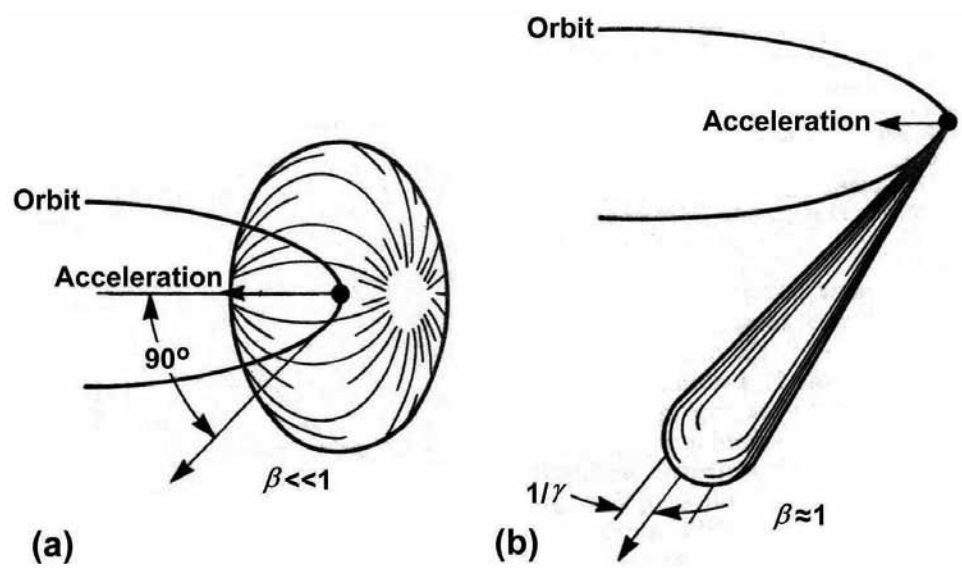

Figure 2.1 Radiation patterns of electrons in a circular orbit [R81]. (a) the pattern for non-relativistic electrons, (b) highly relativistic electrons: the radiation is concentrated in a narrow cone, the spectrum also extends to very high frequencies.

The electromagnetic radiation emitted by electrons moving at relativistic velocities along a curved orbit with a large radius of curvature from tens to hundreds of meters is known as synchrotron radiation [M88]. The higher the electron velocity, the larger γ and the larger the radiation frequency. In principle, the spectrum of synchrotron radiation is expected to be a series of sharp lines at the harmonics of the revolution

frequency up to $\gamma^3\omega$. However, in practice, the electron revolution frequency is not precisely given, because in any practical device the electron actually continuously oscillates in position and energy about its equilibrium orbit [R81]. Therefore, the spectrum for even a single electron is smeared into a continuous spectrum. This smearing is further extended for multiple electrons and for slight anharmonicites in energy and frequency. The continuous electromagnetic spectrum of synchrotron radiation ranges from microwaves to gamma-rays. The larger the γ parameter the narrower the cone of the radiation (see equation 2.3). The emitted radiation power per electron increases as the fourth power of γ [M88].

Synchrotron radiation was discovered 60 years ago [B46, EGL&47]. Since then, synchrotron radiation facilities have developed from parasitic 1st generation sources to dedicated 2nd and 3rd generation sources; from lower energy, lower brightness and longer wavelength to higher energy, higher brightness and shorter wavelength. Today synchrotron radiation has become a primary research tool in many scientific fields, including physics, chemistry, materials science, biology, medicine, geology, ecology as well as an essential tool in many technologies including micromechanics, microelectronics etc.

The first-generation of synchrotron radiation facilities were parasitic facilities since the accelerators were originally built and operated for high-energy or nuclear physics [TAG&01]. With growing interest in synchrotron radiation for solid-state research, a major advance of synchrotron radiation was to use electron storage rings, which are the basis for all of today's synchrotron facilities (synchrotrons have variable

energy while storage rings work at only one energy).

The second-generation of synchrotron radiation facilities were specifically designed as dedicated light sources [TAG&01]. These facilities typically have a large number of beamlines and experimental stations, and many users are served. In 2nd generation synchrotron radiation is primary generated from bend magnets, as shown in **Figure 2.2a**. For such sources the brightness is relatively low. Since brightness is an invariant property, X-ray optical techniques can not improve it. Instead improved source brightness is required.

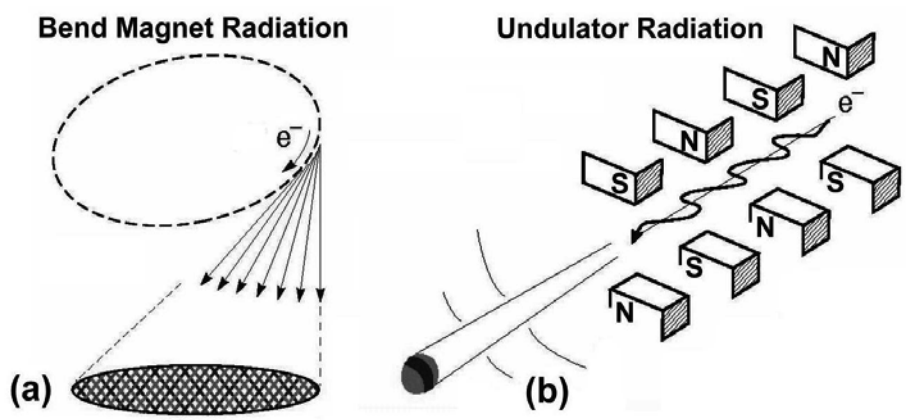

Figure 2.2 Schematic of the two main approaches used for synchrotron light generation. (a) radiation generated from one bending magnet, (b) radiation generated from undulators, which are periodic magnet structures installed in straight sections, providing much enhanced flux and brightness. (Figure adapted from ALS, LBNL).

Third-generation synchrotron radiation facilities are dedicated radiation sources which improve the beam brightness by using insertion devices, such as undulators and wigglers [WBH&81], in straight sections. In general, beam brightness helps achieve high spectral resolution since narrower slits can be used (while keeping sufficient intensity). Beam brightness also provides high coherence for new experiments and high brightness

for spatially resolved studies. Brightness of synchrotron radiation is defined as the number of photons emitted per unit time, per unit source area, per unit solid angle and 0.1% of bandwidth (i.e. in units of ph/s/mm^2/mrad^2/0.1%BW). A linear undulator is an array of closely spaced vertically oriented dipole magnets of alternating polarity, as shown in **Figure 2.2b**. As the electron beam passes through the array, its trajectory oscillates in the horizontal plane. The radiation emitted from successive bends in the trajectory interferes constructively, resulting in spectrally narrow peaks (as narrow as 20-40 eV in the soft X-ray region) at a few wavelengths. Undulators take maximum advantage of the intrinsic brightness of synchrotron radiation, and the beam is highly collimated in both horizontal and vertical directions. Wigglers are similar to undulators but basically have higher magnetic fields and fewer magnetic dipoles. Unlike undulators, wigglers produce a continuous electromagnetic spectrum. Compared to bend magnets, wigglers produce a wider spectrum extending to shorter wavelengths with a higher flux.

The development and construction of a fourth-generation of synchrotron radiation sources which are accelerator-based X-ray lasers has already started. The highest energy achieved with free-electron laser (FEL) is ~ 100 eV [OF01, RGK&03]. An FEL which aims to achieve lasing at 1 Å (12 keV) is under construction at Stanford University and other projects are underway in Hamburg, Germany and Tsukuba, Japan. These devices, which are expected to start operation in ~ 2010, are expected to produce a fully coherent pulse of 100 fs or shorter with peak brightness many orders higher than that of the third-generation sources (10^{30} versus 10^{20} in brightness units).

Synchrotron radiation is characterized by a number of advantages compared to

other laboratory electromagnetic radiation sources, such as:

- High brightness, exceeding other natural and artificial light sources (except UV-Visible lasers) by many orders of magnitude.
- High collimation, i.e. small angular divergence of the beam.
- Widely tunable photon energy by varying insertion device gaps controllably.
- High degree of linear, circular, or elliptical polarization, with control of spatial orientation of the linear E-vector in elliptically polarizing undulators (EPU).
- Pulsed light emission with pulse widths of 10 - 30 ps and typical periods of 20 (multibunch) - 1000 ns (single bunch).

2.2 NEXAFS

Near edge X-ray absorption fine structure (NEXAFS) spectroscopy is a synchrotron technique which was developed in the 1980's in order to study the electronic and geometric structures of small molecules bonded to surfaces, typically simple organic molecules containing hydrogen, carbon, nitrogen, oxygen and fluorine etc [S92]. NEXAFS selects a specific atomic species by using X-rays in the energy region of its core excitation edge(s), such as *K*-edge or *L*-edge. It probes the electronic structure associated with bonds to neighbor atoms by elevating the core electrons to unoccupied molecular orbitals. NEXAFS is a powerful technique with the ability to detect specific intra-molecular bonds, to derive the orientation of molecules or functional groups on the surface or in the solid, and sometimes to determine the bond lengths of specific bonds.

NEXAFS is X-ray photoabsorption. At the onset of inner shell excitation there is a

rapid increase in absorption cross-section and then a gradual decrease with increasing photon energy. The fine structures near the edges due to electronic structure are NEXAFS. Examples of NEXAFS spectra are presented in section 2.2.3. There is an absorption edge associated with each inner shell energy level of an element. Usually different core edges from the same element or from different elements are separated enough in energy that they can be easily identified and studied separately. NEXAFS spectroscopy is very sensitive to chemical composition and molecular structure. NEXAFS is extensively used for studies of organic molecules, either free or adsorbed on surfaces, and solids including polymers, inorganic complexes, oxides and salts etc. An alternate terminology of NEXAFS is X-ray absorption near edge structure (XANES). NEXAFS spectroscopy is discussed in detail in a comprehensive book on the theories, experimental techniques and applications [S92]. The following section about NEXAFS theories is mainly taken from that book.

2.2.1 Theory of X-ray absorption

The basic concept of X-ray absorption is the X-ray absorption cross section, $\sigma_x(E)$, which, for a given photon energy, is defined as the number of electrons excited per unit time, $P_{if}(E)$, divided by the photon flux, $F_{ph}(E)$, the number of incident photons per unit time per unit area [S92]:

$$\sigma_x(E) = \frac{P_{if}(E)}{F_{ph}(E)} \tag{2.4}$$

$P_{if}(E)$ is the probability per unit time for the transition from an initial state $|i\rangle$ to a final

state $\langle f|$. The X-ray absorption transition is caused by a resonant energy- and time-dependent perturbation $V(E,t)$, i.e. the interaction of the electric component of an electromagnetic wave with the target which causes a change in the electronic state [S92]:

$$P_{if}(E) = \frac{2\pi}{\hbar}\left|\langle f|V(E,t)|i\rangle\right|^2 \rho_f(E) \tag{2.5}$$

where $\rho_f(E)$ is the energy density of final states. $F_{ph}(E)$ can be derived from the energy flux of the electromagnetic radiation divided by the photon energy [S92]:

$$F_{ph}(E) = \frac{V_0(E)^2\omega}{8\pi\hbar c} \tag{2.6}$$

where $V_0(E)$ is the amplitude of the potential vector of the electric field, ω is the angular frequency of the electromagnetic wave, c is the speed of light. The final expression of the X-ray absorption cross section is obtained by evaluating the $V(E,t)$ perturbation and applying the electric dipole approximation [S92]:

$$\sigma_x(E) = \frac{P_{if}(E)}{F_{ph}(E)} = \frac{4\pi^2 e^2}{m^2 c\omega}\left|\langle f|\vec{e}\cdot\vec{p}|i\rangle\right|^2 \rho_f(E) \tag{2.7}$$

where e and m are the charge and mass of the electron, respectively, $\vec{e}$ is the unit potential vector and $\vec{p}$ is the sum of the linear momentum operators (i.e. dipole operator) of the electrons. For evaluation of electronic transitions, a commonly used quantity is optical oscillator strength (OS), which is related to the X-ray absorption cross section [S92] by:

$$\mathrm{OS} = \frac{2}{m\hbar\omega}\left|\langle f|\vec{e}\cdot\vec{p}|i\rangle\right|^2 \tag{2.8}$$

The absorption of linearly polarized X-rays by anisotropic solids or molecules aligned at a surface often exhibits angular dependence. That is the transition intensity (I), i.e. optical oscillator strength, depends on the angle (θ) between the X-ray electric field vector and the orientation of the electronic transition moment [S92, AUT02]:

$$I = \mathrm{OS} = \frac{2}{m\hbar\omega}\left|\left\langle f \left\| \left|\vec{e}\right| \cdot \left|\vec{p}\right| \right\| i \right\rangle\right|^2 \cos^2\theta \qquad (2.9)$$

2.2.2 Detection techniques

In NEXAFS, the X-ray photon energy is scanned and the extent of X-ray absorption is measured directly or indirectly. NEXAFS spectra can be measured in many different ways, including total electron yield (TEY) [S92], partial electron yield (PEY) [S92], partial Auger yield (PAY) [S92], total fluorescence yield (TFY) [S92], and transmission [AZC92]. Transmission is the most direct way to measure photoabsorption.

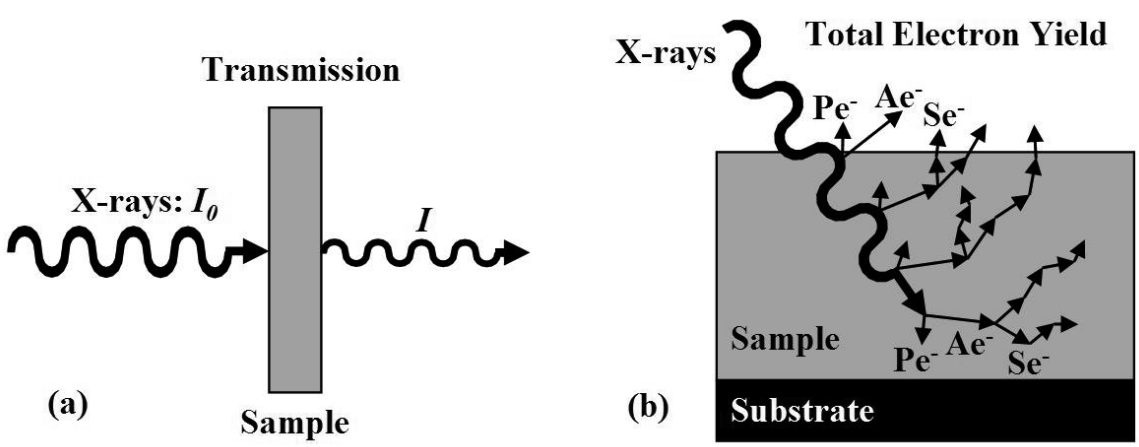

Figure 2.3 Two detection techniques of recording NEXAFS spectra, (a) transmission, (b) total electron yield, Pe^- represents photoelectron, Ae^- represents Auger electron, and Se^- represents secondary electron.

Electron and fluorescence yields are assumed to be linearly proportional to photoabsorption, but exceptions are known. The two spectromicroscopic techniques used in this work, i.e. scanning transmission X-ray microscopy (STXM) and X-ray photoemission electron microscopy (X-PEEM), utilize transmission and TEY detection respectively, and their detection methodologies are illustrated in **Figure 2.3**.

For transmission mode in STXM (**Figure 2.3a**), the photons that are not absorbed by the sample are detected by an X-ray sensitive detector. In the absence of absorption saturation the incident beam intensity and the transmitted light intensity are related by the Beer-Lambert law:

$$\mathrm{OD} = A = -\ln T = \ln\left(\frac{I_0}{I}\right) = \mu\rho l \qquad (2.10)$$

where OD is the optical density, also called absorbance (A), T is the transmittance, I_0 and I are the incident and transmitted X-ray photon flux (photons/s) respectively, μ is the energy dependent mass absorption coefficient (cm^2/g), ρ is the density (g/cm^3) of the material, and l is the sample thickness (cm or nm). For a specific compound, the elemental mass absorption coefficient, which neglects interactions such as bonding among the atoms, is obtained from the sum of the weighted atomic photoabsorption cross sections [TAG&01, HGD93] as given by

$$\mu = \frac{N_A}{M}\sum_i x_i \sigma_{ai} \qquad (2.11)$$

where N_A is the Avogadro's number, M is the molecular weight of a compound containing x_i atoms of type i, σ_{ai} is the atomic photoabsorption cross section (cm^2/atom) for type i atom. Equation 2.11 is also applicable for any pure element with simplified format.

Recommended values of the mass absorption coefficients of elements Z = 1 - 92 at photon energy E = 50 - 30000 eV derived from a combination of experiment and theoretical calculations have been published [HGD93], and are available on the website of the Center for X-Ray Optics (CXRO), http://www.cxro.msd.lbl.gov/. This makes it possible to calculate the elemental mass absorption coefficient or the elemental linear absorption coefficient (cm^{-1} or nm^{-1}, the latter is more convenient in microanalysis like this work) for any compound with known density.

For transmission detection of soft X-rays (100 - 1000 eV), samples must be very thin. For example, at the C 1s edge, the thickness should be less than 200 nm (assuming unit density) in order to avoid absorption saturation. For a higher energy edge or a lower density sample such as hydrated polymer gels or biological samples [M04], optimum sample thickness may increase to 1 - 2 microns.

Total electron yield measurements, as in X-PEEM, are complicated processes with many contributing factors, such as multiple channels of electron generation, electron propagation in the surface layer, surface work function, transport of electrons from the surface to the detector etc [M04]. Upon soft X-ray irradiation, photoelectrons from core shells may be created at different depths within the sample. The kinetic energy of these primary photoelectrons is very low because the incident photon energy is often tuned around the core edges, so only the photoelectrons with sufficient kinetic energy may overcome the surface work function to escape. When an inner shell electron is emitted or promoted to an upper unoccupied level, a core hole is created. The core hole will be filled by an electron most possibly from the next higher energy level accompanied with an

Auger electron autoionized from the same level. Although an X-ray fluorescence photon may be emitted instead of an Auger electron, the X-ray fluorescence emission probability is quite low when the binding energy is lower than 2 keV [K79, C97] for low Z-value elements, such as organic materials. The kinetic energy of Auger electrons is relatively larger than the photoelectron energy. For example, the *KLL* Auger electron energies are about 275, 389 and 510 eV for carbon, nitrogen and oxygen, respectively [CCV&95]. Both photoelectrons and Auger electrons are scattered inelastically by electron-atom interactions on their way to the surface, as shown in **Figure 2.3b**. Such interactions may occur for any given electron between the site of core ionization and the surface. If the impinging electron energy is large enough, several secondary electrons are created during those interactions. In conclusion, no matter what the origin of the free electrons are, only those having enough kinetic energy and the right trajectory may escape the surface and be detected. The effective escape depth (i.e. sampling depth) is less than 5 nm for metals and semiconductors [S92], and it is somewhat deeper for insulators and organic materials. In our studies, the sampling depth of X-PEEM has been determined experimentally to be 10 nm for polystyrene (see Chapter 5) and is assumed to be similar in natural and synthetic polymers [LHR&06].

Although a precise expression for the total electron yield as a function of the photon energy, the electron kinetic energy, the X-ray incidence angle and the electron emission angle, is not available, an approximate theory for evaluating the intensity of TEY (I_{TEY}) was proposed by Stöhr [S92], as shown below:

$$I_{TEY} = \frac{\Omega}{4\pi} I_0 \phi \frac{\mu\rho L}{\mu\rho L + \sin\theta} \qquad (2.12)$$

where Ω is the electron emission solid angle, I_0 is the incident photon flux (photons/s), ϕ is a material constant describing the conversion efficiency into low-energy electrons, μ is the energy dependent mass absorption coefficient (cm^2/g), ρ is the density (g/cm^3) of the material, L is the sampling depth (cm or nm) and θ is the X-ray incidence angle on the sample measured from the surface. At sufficiently large incidence angles ($\theta > 10^o$), since L is small, in the soft X-ray region $\mu\rho L << \sin\theta$ is generally applicable, i.e. $\mu\rho L + \sin\theta \approx \sin\theta$. In these conditions, the TEY intensity will be linearly proportional to the photoabsorption process, as indicated by the reduced equation 2.12:

$$I_{TEY} = \frac{\Omega}{4\pi} I_0 \phi \frac{\mu\rho L}{\sin\theta} \qquad (2.12a)$$

2.2.3 NEXAFS spectroscopy

2.2.3.1 NEXAFS spectroscopic features

NEXAFS spectra consist of a combination of sharp resonant peaks, some broad features and a continuum rise. The sharp peaks correspond to electronic transitions involving promotion of a core electron to virtual molecular orbitals, such as π* and σ* antibonding orbitals, where the excitation energy is lower than the ionization potential (IP) of the core electron. Features above IP are excitation to σ* orbitals (broad) or are double excitations (usually sharp). The 1s → σ* features are usually much broader due to rapid decay to the direct ionization continuum and thus a short lifetime. The relationship between the lifetime (Δt) of an excited state and the observed linewidth (ΔE) of the corresponding NEXAFS feature is given by the Heisenberg uncertainty principle [S92]:

$$\Delta E \Delta t \approx \hbar \qquad (2.13)$$

Low lying NEXAFS features, such as 1s → π* transitions, are sharper due to the longer lifetime, which is related to the stability of the excited state. The σ* features above the IP are usually described as a two step process where the core electron is first excited to a virtual σ* molecular orbital, followed quickly by the emission of a photoelectron [L06].

For quantitative analysis, a high quality NEXAFS spectrum is fit to the profile of the elemental linear absorption coefficient (nm^{-1}) to derive a reference NEXAFS spectrum per nm thickness material (called 'OD1' spectrum). This can then be used to determine the amount of that material in terms of thickness in a column (pixel) in single- or multiple-component samples in spectromicroscopic studies.

A sample NEXAFS spectrum and its spectroscopic interpretation are shown in **Figure 2.4**, which presents the C 1s NEXAFS spectrum of polystyrene (PS) and a correlated schematic energy diagram. The assignment of the spectroscopic features is based on similar features in benzene, biphenyl and their derivatives [WCT&05]. The most intense peak, also the lowest energy, is due to the C 1s → $1\pi^*_{C=C}$ transition of the phenyl ring. Following the $1\pi^*_{C=C}$ peak, two sharp but weak features can be observed which are assigned to the σ^*_{C-H} and 2π* antibonding orbitals. Above the IP that corresponds to the vacuum level of the energy diagram, several broad features are assigned to C 1s excitation to multiple σ* antibonding orbitals related to C=C and C-C bonds. The PS spectrum shown in Figure 2.4 is the linear absorption spectrum (OD per nm). Its intensity scale was determined by fitting both the pre-edge and the far continuum to the elemental linear absorption coefficient profile of C_8H_8 derived using equation 2.11 from tabulated

atomic mass absorption coefficients [HGD93], and the polymer density.

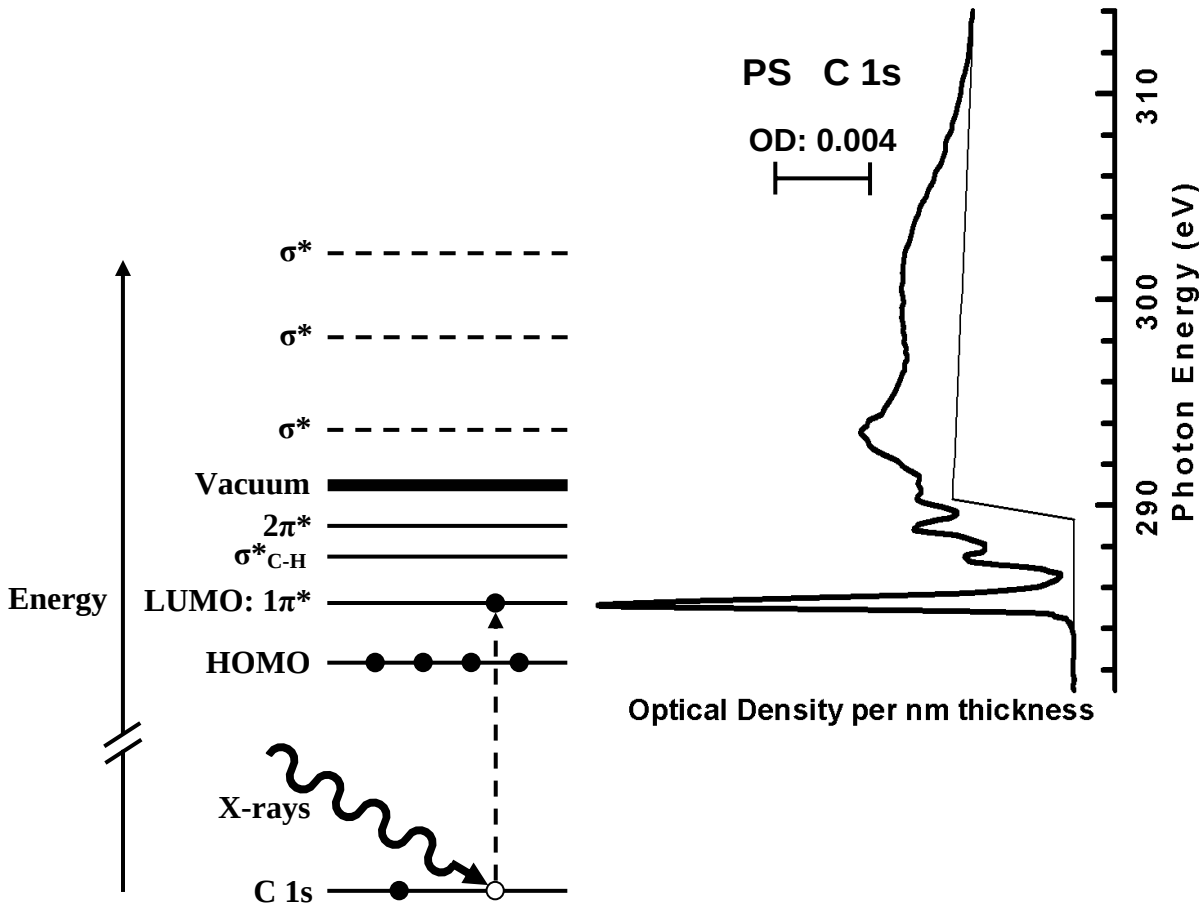

Figure 2.4 Energy diagram and the C1s NEXAFS spectrum of polystyrene (PS).

2.2.3.2 Chemical sensitivity

NEXAFS is both element specific and sensitive to the local chemical environment. In the soft X-ray region (100 - 1000 eV), *K*(1s) edges of low Z-value elements, such as carbon, nitrogen, oxygen and fluorine are located around 285, 405, 540 and 700 eV respectively, and L_{23}(2p) edges of silicon, phosphorus, sulfur and chlorine are individually located around 100, 135, 164 and 201 eV [TAG&01]. These elements are found in various organic and biological materials.

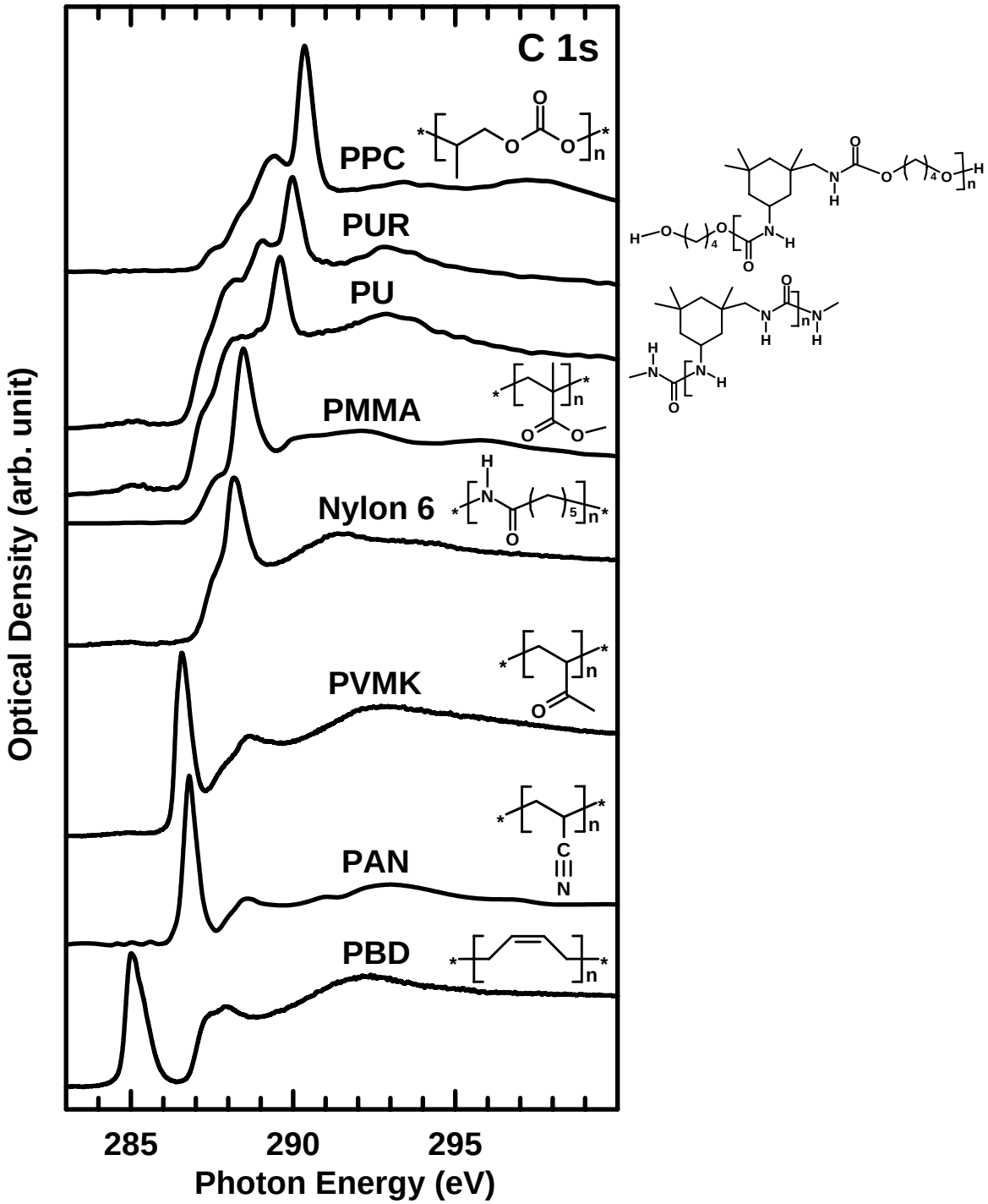

Figure 2.5 NEXAFS spectra of a series of non-aromatic polymers (PBD = polybutadiene [DAU03], PAN = polyacrylonitrile, PVMK = polyvinylmethylketone [DAU03], Nylon 6 [DAU03], PMMA = polymethylmethacrylate, PU = polyurea, PUR = polyurethane, PPC = polypropylene carbonate, the structures are shown for each polymer).

Table 2.1 Energies of C 1s → π* transitions of a series of non-aromatic polymers.

Functional group	Polymer	Energy (eV)	Reference
—C=C—	Polybutadiene (PBD)	285.1	DAU03
—C≡N	Polyacrylonitrile (PAN)	286.8	This work
—C(=O)—	Polyvinylmethylketone (PVMK)	286.6	DAU03
—C(=O)—N(H)—	Nylon 6, proteins	288.2	DAU03
—C(=O)—O—	Polymethylmethacrylate (PMMA)	288.5	This work
—N(H)—C(=O)—N(H)—	Polyurea (PU)	289.6	This work
—O—C(=O)—N(H)—	Polyurethane (PUR)	290.0	This work
—O—C(=O)—O—	Polypropylene carbonate (PPC)	290.4	This work

As an example of the sensitivity to chemical environment, **Figure 2.5** presents the C 1s NEXAFS spectra of a series of non-aromatic polymers, taken from this work and from the literature [DAU03]. All spectra are dominated by sharp C 1s → π* transitions. **Table 2.1** lists the energies of C 1s → π* transitions of the functional groups of these polymers. Two types of chemical shifts are clearly demonstrated: (a) for C=C, C≡N (C=N) and C=O, the changes in transition energy are due to changes in the electronegativity of an atom involved in the π* orbital, (b) for carbonyl (C=O) groups in different chemical environments, subtle changes in transition energy occur. C 1s → $\pi^*_{C=N}$ transitions should be located between the energies for the $\pi^*_{C=C}$ and $\pi^*_{C=O}$ transitions [KWS&98] due to the electronegativity. The energy of C 1s → $\pi^*_{C\equiv N}$ transitions should be higher than the energy of C 1s → $\pi^*_{C=N}$ transitions due to higher bond order of a triple bond than a double bond. From PVMK to PPC in **Figure 2.5** and **Table 2.1**, with the

substitution of neighbor atoms of the carbonyl group (C=O) from carbon to nitrogen and further to oxygen, the $\pi^*_{C=O}$ is shifted to much higher energy, as a result of the inductive effect which acts mainly on the core level energy. This can be interpreted as the electronegativity increases in the order of C < N < O, the electron density around the C atom of the C=O group is reduced in the sequence of C < N < O, thus the binding energy for the carbonyl C 1s is increased, which results in transitions shifting to higher energies. Similar trends can be found in molecular α,γ-dicarbonyl compounds and carbonates [LCC&07], and in the aromatic polymers containing these carbonyl related functional groups [UA02]. These carbonyl groups will shift to slightly lower energy by 0.1 to 0.3 eV when connected to a phenyl ring. This is due to the electron donating effect of the phenyl ring, or delocalization effect. Furthermore, due to direct attachment to the phenyl ring of these carbonyl groups or other electronegative atoms, such as N, O and halogens, the π* of phenyl ring will further spilt into more features [CU04]. In addition to the C 1s edge, the N 1s and O 1s are important edges for NEXAFS spectroscopy of polymers. The differences in the NEXAFS spectra of different materials form the basis of image contrast in chemically selective imaging of soft X-ray spectromicroscopy and chemically selective patterning (Chapters 6 and 7).

2.3 Introduction to X-ray microscopy

X-ray microscopy has been experiencing a fast development over the past two decades, especially accompanying the evolution of synchrotron facilities. X-ray microscopy uses both soft and hard X-rays to probe a variety of materials from soft

matter to hard materials. It can be categorized into two types, full field imaging and scanning microscopy (or microprobe).

2.3.1 Full field X-ray microscopy

Typical examples of full field X-ray microscopy include transmission X-ray microscopy (TXM) [SRN&80, KBC&03, GTG&07] and photoemission electron microscopy (PEEM). The latter will be discussed in detail in section 2.5. In TXM, synchrotron radiation, typically soft X-rays, is partially monochromated by a pre-specimen Fresnel zone plate (ZP) [A99] acting as a condenser, and focused to a ~10 μm spot at the sample. Transmitted X-rays are imaged using a second post-specimen zone plate and the image is recorded with a charge-coupled device (CCD) camera. High resolution large area images can be recorded by TXM with typical exposures from 0.1 - 10 seconds. For imaging areas larger than 10 μm in diameter, tessellation is required. The spectral capabilities of TXM are quite limited since the ZP has a resolving power of only ~100 and the line shape is far from Gaussian. Another disadvantage of TXM is larger radiation damage rates than STXM mainly due to the presence of a low efficiency ZP (10-15% or less) after the sample, which means ~ 10 times more X-ray pass through the sample to get similar statistics. It has the major advantage of high speed single image exposure times of 1 - 3 seconds versus 1 - 10 minutes for comparable STXM images.

2.3.2 Scanning X-ray microscopy

For scanning X-ray microscopy, important techniques include scanning

transmission X-ray microscopy (STXM), scanning photoelectron X-ray microscopy (SPEM) [GKG&02, K03, LBG&05] and X-ray microscopy using focusing mirror systems, such as Kirkpatrick-Baez (KB) mirrors [MYY&02, DRH&02]. STXM will be discussed in detail in section 2.4. In SPEM, high brightness soft X-rays from an undulator are shaped and monochromated using appropriate baffles, mirrors, gratings, entrance and exit slits in order to meet the requirements of the X-ray focusing device, usually a zone plate. The focused X-ray micro-probe is selected by an aperture and placed on the sample which is mounted on appropriate stages to enable positioning in x-, y and z-direction, and x-y scanning. Hemispherical sector analyzers are the most commonly used devices for energy filtering of the emitted photoelectrons. The electron lens in front of the analyzer entrance slit allow photoelectron collection using different acceptance angles in order to optimize the signal intensity and spectral resolution. The electron detectors use channeltrons or channel plates as sensor, and multichannel detection is often applied to increase efficiency. SPEM can be typically operated in two modes: the first uses fixed photon energy and energy filtering of the emitted photoelectrons or multichannel detection (XPS mode); the second is collection of emitted photoelectrons while scanning the photon energy (NEXAFS mode).

For scanning X-ray microscopy using focusing mirror systems, KB mirrors are a classical method, which were first used in ~ 1990. KB systems utilize two concave mirrors at glancing angle to collect and focus X-rays both vertically and horizontally for X-ray microfocusing. KB mirrors require an elliptical figure, which is hard to be achieved by conventional polishing. Alternative ways include benders to make elliptical figures

from flat ones [HRC&01], and application of a differential deposition technique to modify the figure of cylindrical substrates [ICT&00].

2.4 STXM principles and instrumentation

2.4.1 STXM principles

In scanning transmission X-ray microscopy (STXM), a beam of soft X-ray synchrotron radiation is focused by a Fresnel zone plate [M86, MMB93, A99, TAG&01, HJW&06] to a fine point probe of 30 - 50 nm. The sample is positioned at the focus and raster scanned with synchronized detection of transmitted X-rays to measure the energy dependent absorption as a function of position on the sample. Synchrotron radiation is necessary because the photon energy must be scanned for NEXAFS spectroscopy and a high photon flux is needed due to the low efficiency of the zone plate. The photon energy dispersion and scanning is achieved by a monochromator. The zone plate (ZP) is the key component of STXM. A ZP is a variable-line-spacing circular diffraction grating capable of 2-D focusing light waves, similar to an optical lens. It is composed of a series of concentric rings, usually made of Au or Ni and opaque to the soft X-rays, alternating with circular light transparent slots, which are the base Si_3N_4 substrate, as shown in **Figure 2.6**.

The principle of ZP focusing is based on single-slit diffraction combined with a multiple slit grating. According to the trigonometry of Figure 2.6, the interference condition of a transparent slot is described by:

$$f^2 + r_n^2 = (f + \frac{mn\lambda}{2})^2 \qquad (2.14)$$

where f is the focal length, r_n is the radii of zone edges, n is the zone number, m is m-th

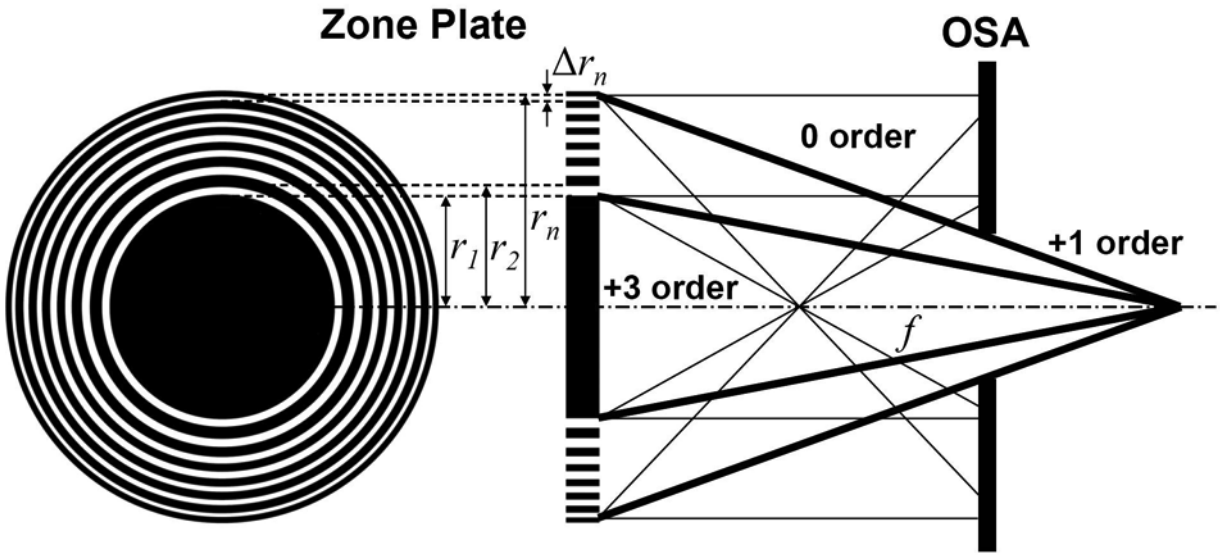

Figure 2.6 Schematic geometry of a zone plate and the focusing scheme of a STXM with a plane wave illumination of X-rays. (OSA: order sorting aperture)

diffraction order (m = 0, ±1, ±2, ±3, ±4 …, zero order is the undiffracted light, negative orders diverge and positive orders converge), and λ is the wavelength of the incident soft X-ray. When the distance between the ZP slots is about equal in width for adjacent transparent and opaque slots, the even-numbered diffraction orders will be suppressed and the remaining odd-numbered diffraction orders will interfere constructively at the focal point [BW99], as shown in Figure 2.6. The first order light is the most intense diffracted light, so most STXM work uses this light for measurements. Typically it is about 10% of the total flux [TAG&01], although efficiencies as high as 40% have been reported (http://www.xradia.com/Products/zoneplates.html). To select only the first order light, an order sorting aperture (OSA) is used in combination with a large central stop (CS) with a diameter bigger than that of the OSA. CS is fabricated in the center of ZP. Together the OSA and CS combine to block the zero order radiation, as shown in Figure 2.6. Effective

first order light filtering can only be achieved when the OSA and ZP are well aligned (within 1/3rd of the difference in diameter of OSA and central stop) and the ZP positional scale is calibrated.

For first order diffraction, m = 1, where the path difference between two adjacent transparent zones is one wavelength of the monochromatic soft X-rays, equation 2.14 reduces to:

$$r_n^2 = n\lambda f + \frac{n^2\lambda^2}{4} \tag{2.15}$$

Neglecting the second term on the right side due to $f >> n\lambda$ gives the focal length:

$$f \approx \frac{r_n^2}{n\lambda} \tag{2.16}$$

For a ZP of n zones in total, n can be calculated from the radius of the outmost zone, r_n, and its width $\Delta r_n = r_n - r_{n-1}$ on condition that equal area is set for each zone to get an evenly illuminated zone plate, i.e. $n = \pi r_n^2 / 2\pi r_n \Delta r_n = r_n / 2\Delta r_n$. Then equation 2.16 converts to:

$$f = \frac{2r_n \Delta r_n}{\lambda} \tag{2.17}$$

where $2r_n$ is the diameter of the zone plate. The focal length is reciprocally proportional to the wavelength of the light, and thus linearly proportional to the photon energy. The numerical aperture (NA) is defined as [HJW&06]:

$$NA \equiv \frac{r_n}{f} = \frac{\lambda}{2\Delta r_n} \tag{2.18}$$

The diffraction-limited spatial resolution, defined by the Rayleigh criterion [TAG&01,

HJW&06], is:

$$\text{Res.} = \frac{0.610\lambda}{NA} \tag{2.19}$$

Then the spatial resolution related to Δr_n can be obtained from Equations 2.18 and 2.19:

$$\text{Res.} = 1.22\Delta r_n \tag{2.20}$$

Thus the diffraction-limited spatial resolution is determined mainly by the outer zone width of a zone plate.

2.4.2 STXM instrumentation

2.4.2.1 STXM beamline 5.3.2

Synchrotron radiation is the ideal source to illuminate a STXM since diffraction-limited resolution is best achieved by use of coherent light. The microscope used in this work is located at the dedicated beamline 5.3.2 (polymer STXM) at the Advanced Light Source (ALS), Berkeley, CA, USA. **Figure 2.7** shows the layout of the beamline. The optical and mechanical design of this beamline, which was specifically designed for STXM, has been described elsewhere [WPA98, WAK&02].

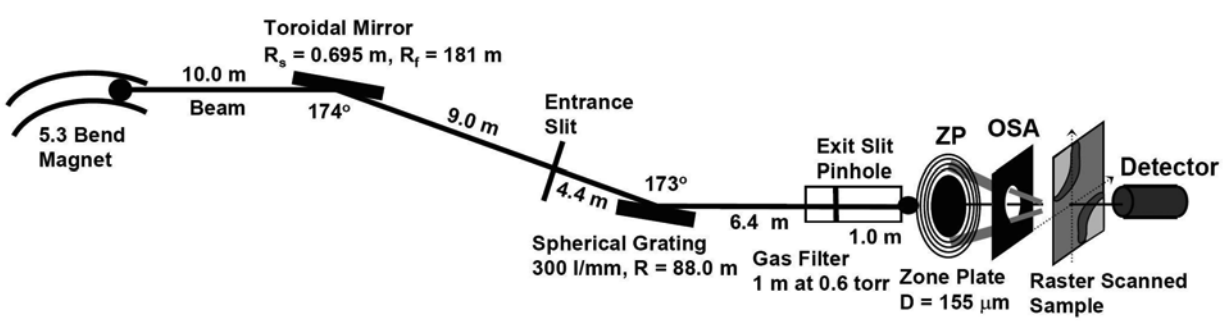

Figure 2.7 The layout of beamline 5.3.2 for polymer STXM at the ALS

The white synchrotron radiation is generated from the bend magnet 5.3, and then the beam is reflected by a toroidal mirror, which focuses the beam in the vertical direction at the entrance slit (f_V = 9 m) and in the horizontal direction at the exit slit (f_H = 19.8 m). The convolution of the entrance slit, placed between the toroidal mirror and the monochromator and the dispersive (horizontal) exit slit, controls the energy resolution. A feedback system, which measures and compares the currents induced by the edges of the beam hitting the two sides of the entrance and exit slits, is used to automatically adjust with fast response (100 Hz) the orientation of the toroidal mirror so that the beam is always centered on the entrance and exit slits. In order to monochromate the white synchrotron radiation, a spherical grating monochromator is used, which disperses the soft X-rays (150 - 1200 eV) horizontally with a nominal resolving power ($E/\Delta E$) up to 5000. The exit aperture consists of two slits in horizontal (dispersive) and vertical (non-dispersive) orientation. Varying the sizes of the entrance and exit slits allows the user to trade-off flux, energy and spatial resolution, as shown in **Table 2.2**. In the section containing exit slits, there is a differentially pumped ~1 m long gas cell (rectangle in Fig. 2.7). When it is filled with 0.7 torr nitrogen, it suppresses the second-order harmonic light (light at twice the photon energy), when operating in first order at the C 1s edge [WPA98]. The higher order harmonic light contamination is an intrinsic problem of spherical gratings. At ALS beamline 5.3.2 the 2nd order contribution is estimated 50 - 100% of the first order light at the C 1s edge with the zone plate in. In addition, harmonic purity also depends on the quality of alignment of the OSA and the central stop. Another simple and efficient solution to this issue is the use of a thin (100 - 200 nm) Ti foil as a transmission

filter [QTM&98]. Between the exit slits and the STXM chamber, there is a fast-acting (~300 µs open - close action) in-vacuum piezo shutter which is used to block the X-rays except during each line of image measurements.

Table 2.2 Trade-off of slits sizes with flux, energy and spatial resolution. (Measured in 2001 using a zone plate of 120 µm in diameter and 45 nm for the outmost zone)

Energy resolution (meV)	Spatial resolution (nm)	Slits (µm)			Flux at 320 eV (MHz)
		Entrance	Exit dispersive	Exit non-dispersive	
75	50	25	10	35	0.22
100	50	40	25	35	1.40
125	50	50	30	35	1.80
150	50	60	35	35	2.15
175	50	75	35	35	2.70
200	50	90	35	35	3.20
75	60	25	10	60	0.42
100	60	40	25	60	2.55
125	60	50	30	60	3.95
150	60	60	35	60	4.50
175	60	70	40	60	5.30
200	60	90	45	60	6.85

2.4.2.2 STXM microscope

The pioneer work of developing STXM was mainly carried out at the National Synchrotron Light Source (NSLS) NY, USA by Kirz and his co-workers [KR85, RSF&88, BRA&89]. The very early generation of STXM microscope actually used a 1 µm pinhole to define the scanning probe and exploited soft X-rays to image wet biological samples [RKK&80]. It was upgraded to the zone plate based STXM combined with undulator beamline in late 1980's [RSF&88, BRA&89]. After about a decade, the introduction of STXM to the Advanced Light Source (ALS) was accomplished in the undulator beamline 7.0.1 [WFK&98]. In 2001, a dedicated STXM for polymer analysis was built on the bend

magnet source at ALS, i.e. beamline 5.3.2 polymer STXM [WAK&02, KTS&03]. It is the second interferometer-controlled STXM in the world, but more effective than an earlier example at the NSLS [SSR&88]. Later, an interferometer was implemented on a replacement STXM on beamline 7.0.1 at ALS, which was moved to the molecular environmental science beamline 11.0.2 [BAA&06]. However, this microscope was not used for the work in this thesis. Currently there are a number of STXM microscopes operating or under construction around the world, as listed in **Table 2.3** [HDJ&07].

Table 2.3 Locations and properties of current STXM microscopes [HDJ&07].

Type	Facility	Location	Source	E-range (eV)	Status
STXM	NSLS X1A (2 STXMs)	Upton, NY, USA	undulator	250-1000	operating
STXM	Bessy	Berlin, Germany	BM	250-750	operating
STXM	ALS 5.3.2	Berkeley, CA, USA	BM	250-750	operating
STXM	ALS 11.0.2	Berkeley, CA, USA	EPU	100-2000	operating
STXM	SLS	Villigen, Switzerland	BM	250-750	operating
STXM	CLS 10ID1	Saskatoon, Canada	EPU	250-2500	operating
TXM & STXM	Elettra Twin-mic	Trieste, Italy	undulator	250 - 2000	operating
STXM	Bessy	Berlin, Germany	EPU	250 – 1500	construction
STXM	SSRL	Stanford, CA, USA	EPU	250 – 1500	construction
STXM	Soleil	Paris, France	EPU	250 – 1500	design
STXM	SSRF	Shanghai	undulator	250 - 2000	design

ALS STXM 5.3.2 was used in this work. Photos and a component scheme of the microscope are shown in **Figure 2.8**. The external appearance, i.e. the STXM chamber, is shown in Figure 2.8a. The chamber and all of the microscope components are designed to achieve a vacuum of ~ 10^{-6} torr. However, the chamber is typically filled with 1/3 atm helium gas after pumping to rough vacuum (0.1 torr) for STXM measurements. Compared with air, the helium environment provides more photon flux due to lower absorption, results in smaller interferometer drifts because of its lower index of refraction

and helps keep motors cool due to its high thermal conductivity [KTS&03]. In addition, eliminating oxygen from the sample environment significantly slows radiation damage of polymer materials [CUA02]. The chamber is mounted on a heavy base, which is further isolated from the floor by Styrofoam pads, to reduce vibrational coupling to the ALS experimental floor, which is quite noisy due to proximity of the ALS to the San Andreas Fault (~ 200 meters).

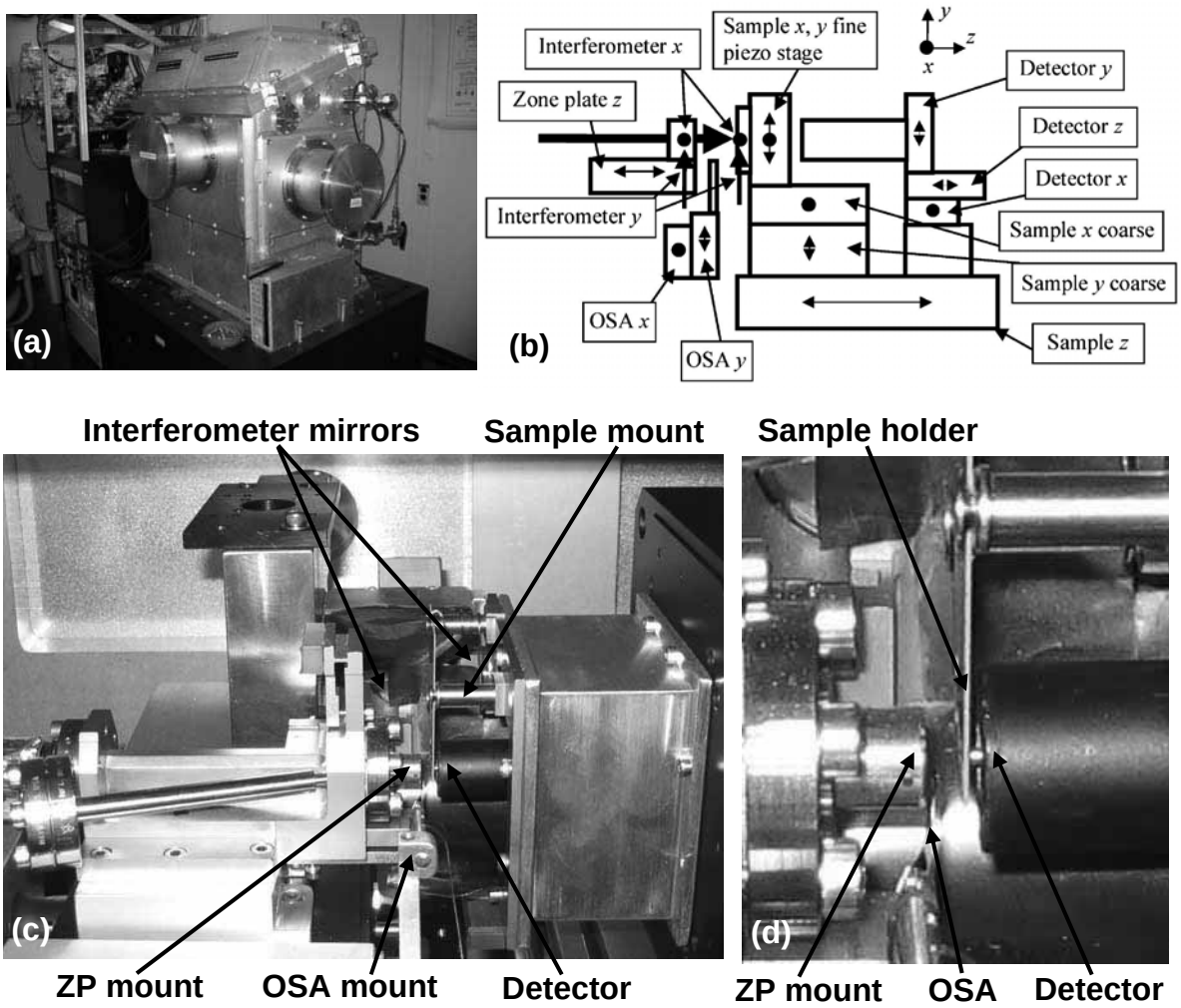

Figure 2.8 The ALS beamline 5.3.2 polymer STXM, (a) the overview of STXM, (b) the scheme of the STXM components [KTS&03], (c) the side view, and (d) the close-up side view.

Figure 2.8b shows the schematic of 5.3.2 STXM major components, including the zone plate *z* stage, OSA *x*, *y* stages, sample *x*, *y* coarse stage, sample *x*, *y* fine piezo stage, sample *z* stage, detector *x*, *y*, *z* stage and the interferometer system. The photographs of the key STXM components are shown in Figure 2.8c and d. The zone plate (ZP) used in this work was provided by the Centre for X-ray Optics, Lawrence Berkeley National Laboratory (LBNL). The ZP has a diameter of 155 μm and an outmost zone width of 35 nm, so the diffraction-limited spatial resolution is 43 nm according to equation 2.20. However the best resolution of STXM can only be achieved if the microscope is properly adjusted, such as the OSA position, ZP focus, sample-OSA distance, sample focus and the accuracy of the energy scale etc. The central stop of the ZP has a diameter of 80 μm while the order sorting aperture (OSA) is 50 μm in diameter. For this specific zone plate and OSA, the distance between any two of the ZP, the OSA and the sample as a function of photon energy can be determined, as shown in **Figure 2.9**. These distances are linear with respect to photon energy. The STXM sample holder has six round holes, designed to hold TEM grids of 3 mm in diameter. Only 5 of them can be used for samples since moving to position #1 causes collision of the sample support structure and the detector support structure, misaligning the detector. The ZP and sample must maintain a relative (*x*, *y*) positioning accuracy of 10 nm during moves over large distances (total sample scan range is 21 mm × 9 mm), which has been achieved by a laser interferometer control system [KTS&03]. Some important advantages of this interferometric system include:

- Obtaining high quality stacks of images with very limited drifting, so post-realignment is usually unnecessary.

- Providing a continuous absolute coordinate system with a field of view over 20 mm completely under computer control. The same coordinate system is adopted by a pre-indexing system based on visible-light microscopy for sample preview, so that sample navigation in STXM can be done using preview optical images.
- Compatible to zone plates with spatial resolution better than 20 nm.

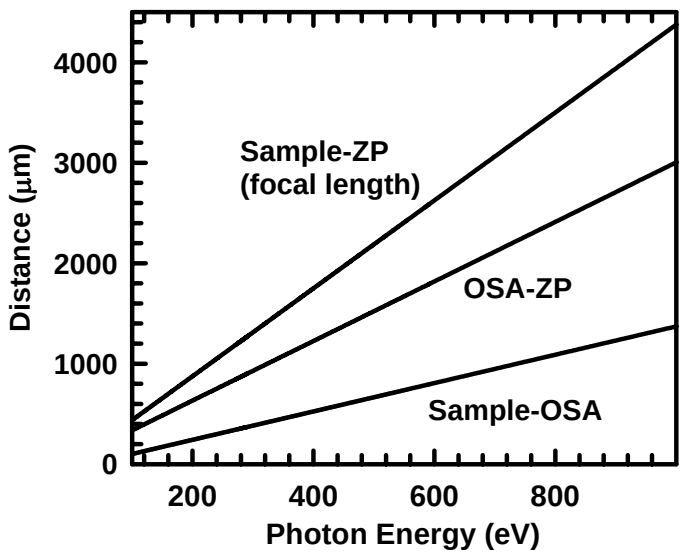

Figure 2.9 The optimal distance between any two of the zone plate, the OSA and the sample as a function of photon energy for the ALS STXM 5.3.2.

The detector used in the ALS STXM 5.3.2 consists of a phosphor to convert soft X-rays to visible light followed by a high performance photomultiplier (PMT) which can count linearly up to 20 - 30 MHz. The STXM 5.3.2 detector is shown in **Figure 2.10**. A very thin layer of a polycrystalline phosphor film (P43) is deposited on the front tip of a Lucite pipe by dusting onto the lightly greased tip. A P43 granular phosphor was used in this work. The Lucite tip is carefully shaped to increase the light collection of the granular

phosphors [KTS&03]. The absolute detection efficiency of the STXM 5.3.2 phosphor-PMT detector as determined by comparing to a quantitative silicon photodiode, was determined to be 35±5% in the C 1s regime in this work and in [KTS&03]. It is somewhat higher (50 - 60%) in the O 1s edge.

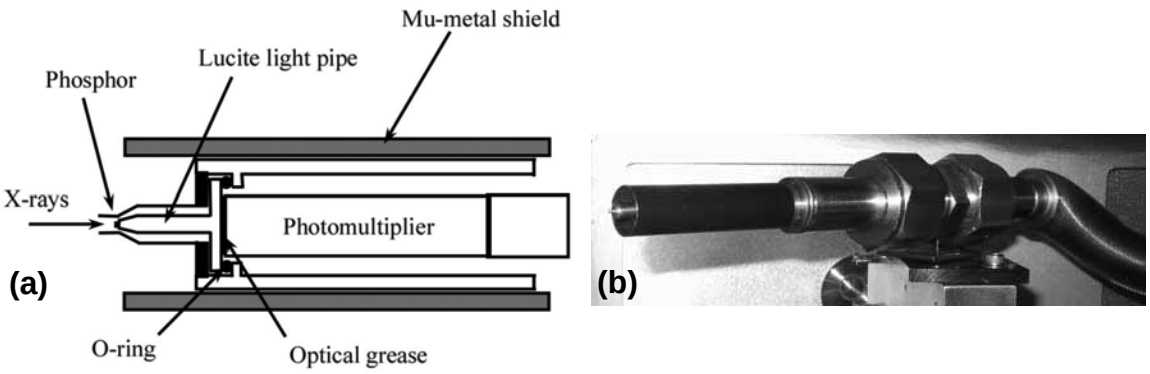

Figure 2.10 The ALS STXM 5.3.2 detector for transmitted soft X-rays, (a) schematic geometry [KTS&03], and (b) photograph.

2.5 X-PEEM principles and instrumentation

2.5.1 X-PEEM principles

In photoemission electron microscopy (PEEM), UV or soft X-ray light sources are used to illuminate the sample surface to eject photoelectrons, which are accelerated and focused by electrostatic (at ALS PEEM2) or magnetic (Elmitec PEEM) electron lenses to generate images which are recorded with a CCD camera. For UV light, the primary image contrast is due to work function changes between different local areas of the sample surface as the UV energy is comparable to the surface work function. For soft X-rays, the image contrast mainly depends on the surface chemical composition (via NEXAFS) as well as topographical features and work function effects. PEEM is an analytical technique with surface and near surface sensitivity.

Tonner *et al.* were the first to use synchrotron radiation soft X-rays in the PEEM [TH88, HHT90, THK&92]. For the X-ray photoemission electron microscopy (X-PEEM) used in this work, total electron yield (TEY) detection is used to directly generate an image of the surface. It detects all the inelastically scattered photoelectrons, Auger electrons, as well as a large number of the secondary electrons with a strong discrimination in favor of low energy secondaries. The TEY signal depends on the surface composition through the energy dependent mass absorption coefficient μ. The signal arises from the outmost 10 nm (see section 2.2.2). In X-PEEM, stacks of images as a function of photon energy are acquired for an area of tens of microns square, from which NEXAFS spectra can be extracted at any local position. With NEXAFS spectroscopy, X-PEEM can provide both elemental information through absorption edges and chemical bonding information through near edge fine structures corresponding to the electronic transitions involving the unoccupied states above the HOMO or Fermi level.

TEY imaging is relatively simple and efficient since it does not require a band-pass filter. However, because the energy distribution of the electrons is wide, usually several eV FWHM, and because the X-PEEM lenses have significant chromatic aberration, the spatial resolution is poor without a band pass filter or aberration corrector. The X-PEEM used in this work does not have a band pass filter and the spatial resolution for polymer samples is about 100 nm [M04]. The number of electrons produced per incident photon, i.e. the quantum efficiency, can be much higher than unity, so that the image intensity in X-PEEM is generally larger than that of a primary photoelectron or Auger electron microscope.

2.5.2 X-PEEM instrumentation

2.5.2.1 X-PEEM beamline 7.3.1.1

Synchrotron radiation is necessary for X-PEEM because high beam intensity and scanned photon energy are required. The microscope used in this work is located at beamline 7.3.1.1 at the Advanced Light Source (ALS). **Figure 2.11** shows the layout of the beamline. It was developed by the ALS in collaboration with the IBM Almaden Research Center (Joachim Stöhr), and it is designed for X-PEEM micro-analysis of surfaces using NEXAFS spectroscopy, X-ray magnetic circular dichroism (XMCD) and X-ray magnetic linear dichroism (XMLD) [APD&99].

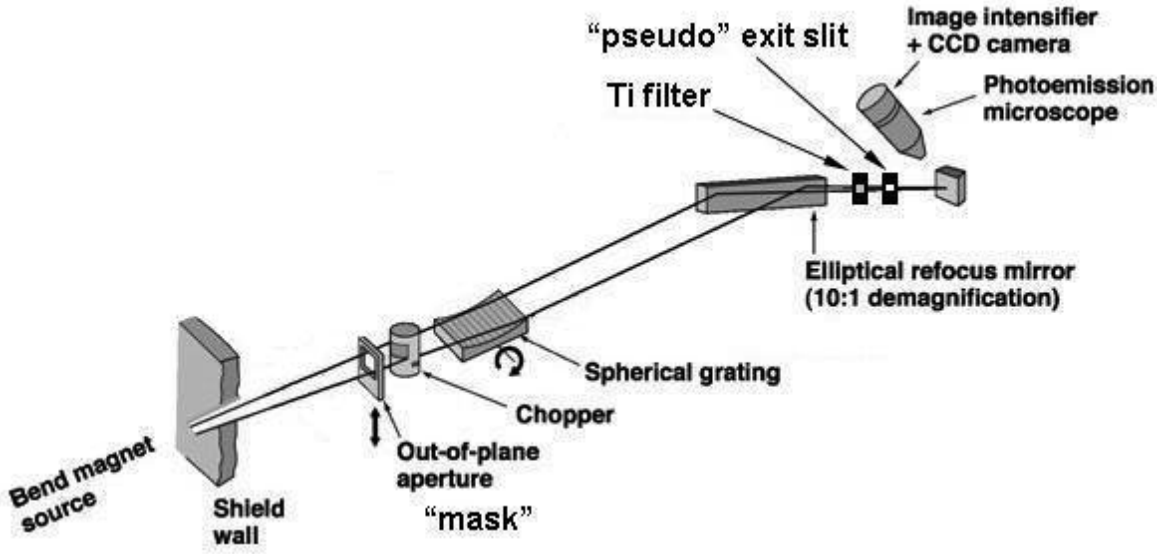

Figure 2.11 The layout of beamline 7.3.1.1 for X-PEEM at the ALS

The white synchrotron radiation is generated from bend magnet 7.3. The out-of-plane aperture, also called the "mask", and the chopper are used to control the vertical portion of the radiation from the bend magnet which is used. This can be either in the storage ring plane for linearly polarized radiation, or above or below the plane for

circularly or elliptically polarized radiation. The chopper can be quickly rotated to chop the beam so as to modulate the polarization; however this function was not used in this work. The mask and the chopper can be moved relative to each other in the vertical direction to limit the transmitted X-ray flux when studying highly radiation sensitive materials, such as polymers, proteins and some ionic compounds. A spherical grating monochromator (SGM) with no entrance slit and a low line density grating (200 lines/mm) is used to obtain high throughput and vertically disperse the X-ray spectrum of photon energy ranging from 175 to 1500 eV with a spectral resolving power between 1000 and 2000. The 1.2 m long elliptical refocusing mirror reduces the horizontal source size of ~300 μm to a spot width of 30 μm on the sample. A 100 nm Ti filter is used to suppress the second-order harmonic light at the C 1s edge. The pseudo exit slit vertically limits the size of the X-ray beam on the sample through two different slit sizes, i.e. 50 and 100 μm. The slit is also used to define the photon energy scale so that it stays fixed when changing samples as long as the pseudo exit slit is not moved. The photon flux in the beam spot on the sample is ~ 10^{11} photons/s when the storage ring is operated at 1.9 GeV with a ring current of 400 mA.

2.5.2.2 X-PEEM microscope

In the past two decades, PEEMs have been constructed by many different groups [TH88, HHT90, EKR&91, TR91, THK&92, TDD&95, MBL&97, WLL&97, DCL&98, APD&99], including the instrument that was used for this thesis, called PEEM2 [APD&99], which was the second generation of X-PEEM installed at the Advanced Light

Source. **Table 2.4** lists selected X-PEEM microscopes operating or under construction around the world. Several high resolution PEEMs are under development (SMART at BESSY [FWU&97, SGF&02] and PEEM3 at ALS [FPW&02]), which will use aberration compensation optics and are expected to achieve much higher spatial resolution and detection efficiency. Apart from these research PEEMs, commercial systems are also available, such as the PEEM3 unit of Elmitec which is in many sources, including Canadian Light Source (CLS).

Table 2.4 Locations and properties of selected PEEM microscopes.

Type	Facility	Location	Source	E-range (eV)	Status
PEEM2	ALS 7.3.1.1	Berkeley, CA, USA	BM	175-1500	operating
PEEM	APS XOR-4-ID-C	Argonne, IL, USA	EPU	500-3000	operating
PEEM	CLS 11ID1	Saskatoon, Canada	EPU	240-2000	operating
PEEM	BESSY ID-08-1	Berlin, Germany	EPU	85-1600	operating
PEEM	ANKA WERA	Eggenstein, Germany	EPU	100-1500	operating
PEEM	MAX-lab I311	Lund, Sweden	EPU	30-1500	operating
PEEM	SLS X11MA	Villigen, Switzerland	EPU	90-2000	operating
PEEM	SPring-8 25SU	Hyogo, Japan	EPU	220-2000	operating
PEEM	NSRRC 05B	Taiwan, China	EPU	60-1400	operating
PEEM	SSLS SINS	Singapore	BM	50-1200	operating
PEEM3	ALS 11.0.1	Berkeley, CA, USA	EPU	100-2000	operating
PEEM	ALBA CIRCE	Barcelona, Spain	EPU	100-2000	construction
PEEM4	Elettra	Trieste, Italy	EPU	50-1500	construction
	SOLEIL Microfocus	Paris, France			

Photographs and schematics of ALS PEEM2 are shown in **Figure 2.12**. PEEM2 is equipped with a partly automated sample-transfer system with a loadlock, three-sample parking stage and a sample preparation chamber. The preparation chamber, **Figure 2.12a** to the left, contains four evaporators, an Ar sputter gun, a sample heater, a magnet and a LEED system for sample analysis.

Figure 2.12b and **c** present the photograph and the schematics of PEEM2. The X-ray incidence angle is 30º with respect to the sample surface. The microscope optical axis

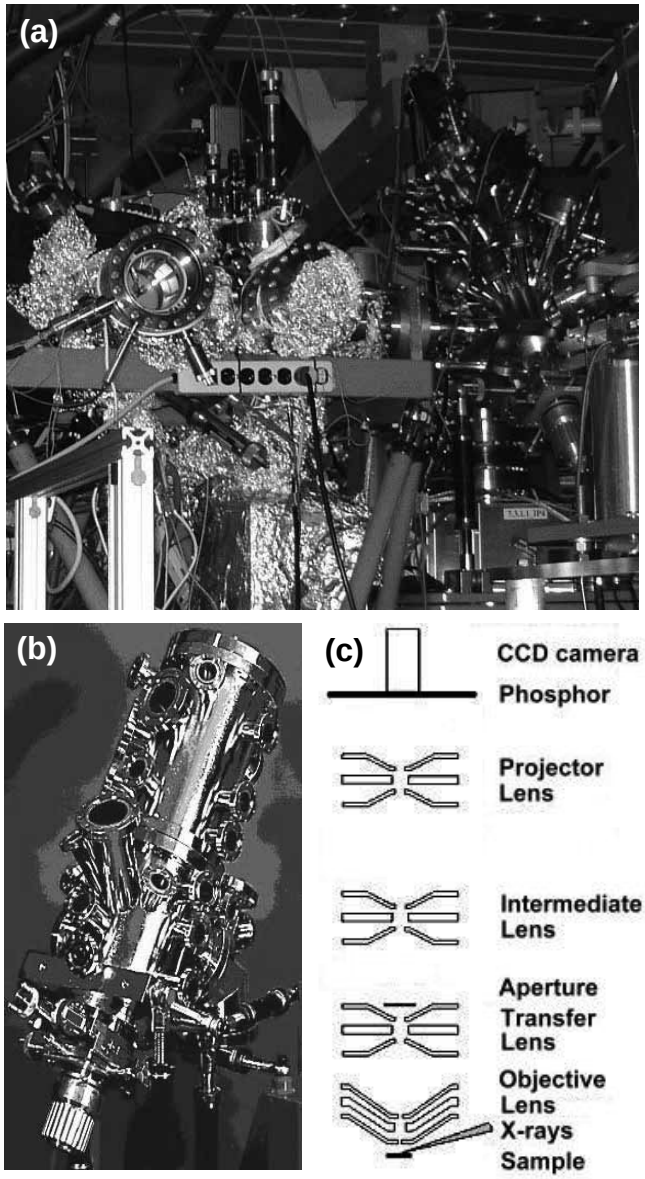

Figure 2.12 The ALS PEEM2 at beamline 7.3.1.1, (a) the overview of preparation chamber to the left and the PEEM2 microscope to the right, (b) the PEEM2 chamber, (c) the schematics of PEEM2 [M04].

is oriented at 90º with respect to the electric field vector of the linearly polarized light. The emitted electrons are extracted into an electron optical imaging system by a strong electric field that is applied between the sample and the objective lens. Typically the

sample is biased at -15 or -18 kV relative to the objective which is at ground potential. Several electron optical lenses, i.e. the objective lens, a transfer lens, an intermediate lens, and a projector lens, are used to form a full field image of the emitted electrons onto a phosphor screen which converts the electrons into visible photons detected by a charge coupled device (CCD) camera. The objective lens is an electrostatic tetrode lens with a stigmator/deflector assembly located in its back focal plane. It is adjusted to achieve focus and can be operated up to 20 kV. The transfer lens produces a 1:1 image at the second objective back focal plane outside the lens where an aperture is located. There are four different apertures (12, 20, 50 and 2000 μm diameter) mounted on a small flexure stage and the four apertures can be switched from one to another in vacuum. The transfer lens and associated aperture affect both the efficiency and the spatial resolution. The intermediate lens and the projector lens are used to control the magnification of the microscope. For large fields of view (from hundreds of μm down to 20-25 μm) only the intermediate lens is used. The projector lens is used to magnify fields of view smaller than 20 μm, and it was turned off in this work. The detector consists of an electron sensitive phosphor, a fiber bundle coupling the phosphor to the CCD camera (Princeton Instrument) and serving as the window separating vacuum and air where the CCD camera is mounted.

X-PEEM samples must be adequately conductive, reasonably flat, UHV-compatible, e.g. non-outgassing, solids. By recording a sequence of images with incrementally increasing photon energy ('stack acquisition'), a NEXAFS spectrum can be extracted for each image pixel. X-PEEM is similar to STXM in some aspects. A

comparison between these two soft X-ray spectromicroscopic techniques used in this thesis is presented in **Table 2.5**.

Table 2.5 Comparison of ALS STXM and X-PEEM ([L06] and http://www-als.lbl.gov)

	STXM	**X-PEEM**
Beamline	5.3.2	7.3.1.1
Source characteristics	Bend magnet	Bend magnet
Energy range	250-700 eV	175-1500 eV
Monochromator	Low-dispersion, spherical-grating monochromator, one grating	High efficiency spherical-grating monochromator
Flux in focused spot (1.9 GeV, 400 mA)	1 x 10^7 photons/s at sample	3 x 10^{12} photons/s/0.1%BW at 800 eV (linearly polarized)
Resolving power ($E/\Delta E$)	$\leq$ 5000	1800 at 800 eV
Characteristics	Active servo-stabilized toroidal premirror	X-ray absorption spectromicroscopy, psec laser for time-resolved studies
Spatial resolution	30 nm with current 25 nm outermost zone plate	Better than 50 nm depending on sample; 100 nm typical
Detectors	Phosphor converts to visible light, light pulses detected by high performance photomultiplier (PMT) system	Phosphor converts to visible light, detected by slow scan CCD
Spot size at sample	40 nm (for this work)	Less than or equal to 30 x 30 μm
Sample requirements	Thin sections, films, and particulates (20-100) nm thick, supported using Si_3N_4 windows or TEM grids.	UHV-compatible flat, conductive samples up to 1 cm^2 in area
Sample environment	Helium up to 1 atm, vacuum to 10^{-2} Torr	UHV
Scientific applications	Polymers, materials sciences, and biological sciences	Real-time and pump-probe study of elemental, chemical, magnetic, and topographical properties of materials
Experimental techniques	NEXAFS spectromicroscopy at the C, N, and O K edges; electrochemical STXM; tomography	NEXAFS spectromicroscopy; XMCD, XMLD

Chapter 3

Experimental

This chapter describes how STXM and PEEM measurements were performed and how the data were treated. Specifically, for STXM, the data acquisition, the quantitative dose-damage evaluation method, and the simulation of chemically selective patterning in multilayer polymer systems are presented. For X-PEEM, the data acquisition and the quantitative dose-damage evaluation method are described. In addition, the polymer sample preparation used for STXM and X-PEEM radiation damage and chemically selective patterning studies is detailed.

3.1 STXM data acquisition

Several data acquisition modes were used in this thesis, including single energy image, point scan, linescan, image sequence (or stack) and pattern generation. Except the last one, the measured transmission signal is converted to optical density using equation 2.10. This section presents the principles and examples for each of these data acquisition modes.

3.1.1 Single energy images

For the acquisition of a single energy transmission image, a few parameters need to be defined by the user. These include the photon energy, (x, y) position of the center of the image, (Δx, Δy) dimensions of the image, (δx, δy) the point spacing (or pixel size) in each dimension and the dwell time at each pixel. The image size depends on which

sample moving motor is used. For a large size image (>120 μm on STXM 5.3.2), the coarse stepper motor is used to scan the sample, while for a small size image (<120 μm), the piezo stage is used, which provides a higher scan speed, better stability and greater precision. In addition, it is possible to measure multiple spatial regions in the same scan.

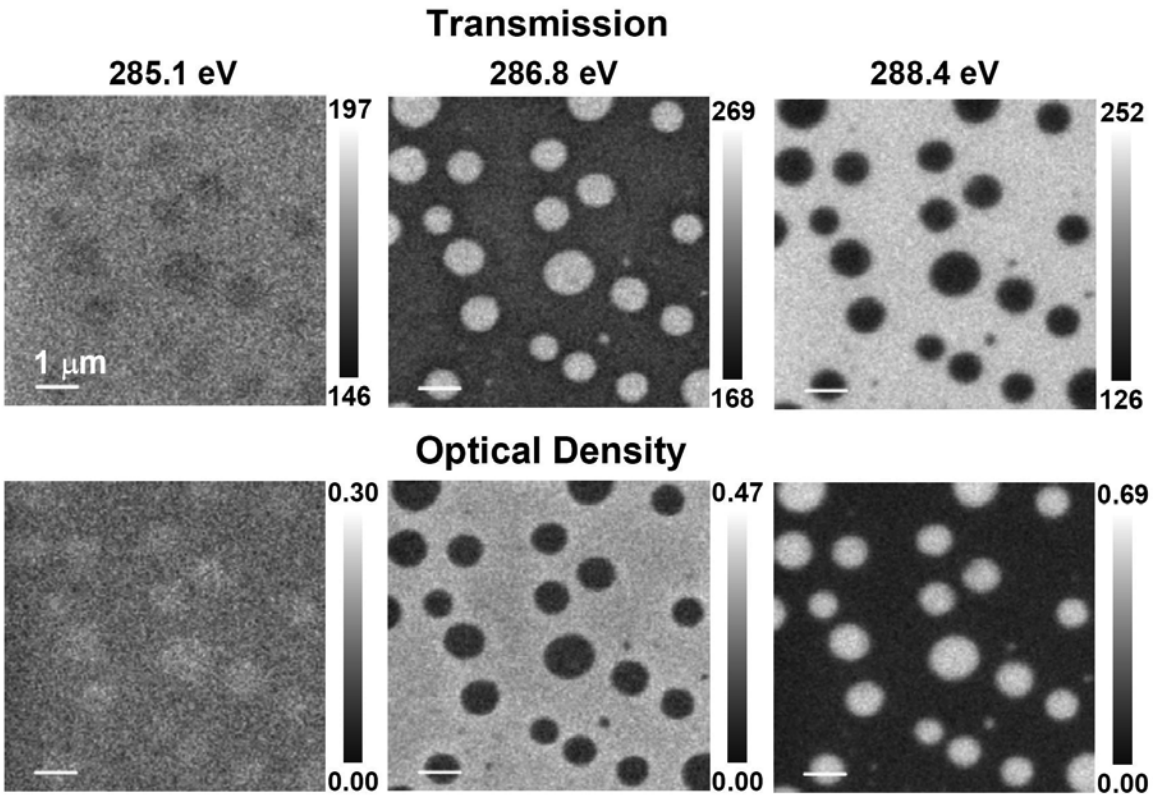

Figure 3.1 STXM images of a micro phase-separated polymer film, PMMA-*blend*-PAN, at three energies: 285.1, 286.8 and 288.4 eV in transmission mode (top row) and optical density mode (bottom row) (8 μm × 8 μm, 160 × 160 pixel, 2.4 ms dwell time).

Figure 3.1 shows fine scan single energy images of a micro phase-separated polymer film, polymethylmethacrylate (PMMA)-*blend*-polyacrylonitrile (PAN), at three photon energies: 285.1, 286.8 and 288.4 eV in transmission mode and converted to optical density. The first energy is a non-characteristic absorption energy for both polymers, so sample morphology is almost invisible. The other two photon energies are

the characteristic absorption energies of PAN (286.8 eV) and PMMA (288.4 eV). For the transmission images, the dark areas correspond to lower transmission, or larger absorbance, while the white areas refer to regions that do not absorb the specific photon energy or are empty areas. The 286.8 eV transmission image shows PAN is the continuous phase, and the 288.4 eV transmission image confirms that PMMA is the discrete domains. When transmission images are converted to optical density (OD) images, the image contrast is reversed - i.e. a larger OD or stronger absorption corresponds to lower transmission, as shown in Figure 3.1 bottom row.

3.1.2 Point scans

When an interesting feature is detected in a single energy image, the fast way to acquire the NEXAFS spectrum of this feature is to perform a point scan, i.e. acquisition of the soft X-ray transmission signal as a function of photon energy at the spot of interest. The minimum detectable feature size is approximately the size of the focused beam of ~40 nm. Usually multiple point are acquired quasi-simultaneously, i.e. the sample stage moves quickly from one point to the next with signal acquisition at each point, before the monochromator moves to the next photon energy. These multiple points include not only different positions on the sample, but also one or more empty regions for I_0 determination. It is important to have I_0 recorded under the same conditions because the incident X-ray profile has a strong spectral structure, its intensity decreases with the storage ring current decay and, although the synchrotron, beamline and microscope are generally very stable during one injection (8 hours), there can be sudden changes caused by e.g. shift of

position of the electron beam in the storage ring. In addition to multiple spatial regions (points or areas), one can select multiple spectral regions with varying increments of energy and varying dwell time per energy point. Defocus of the X-ray beam can be used in order to minimize spectral distortion due to radiation damage.

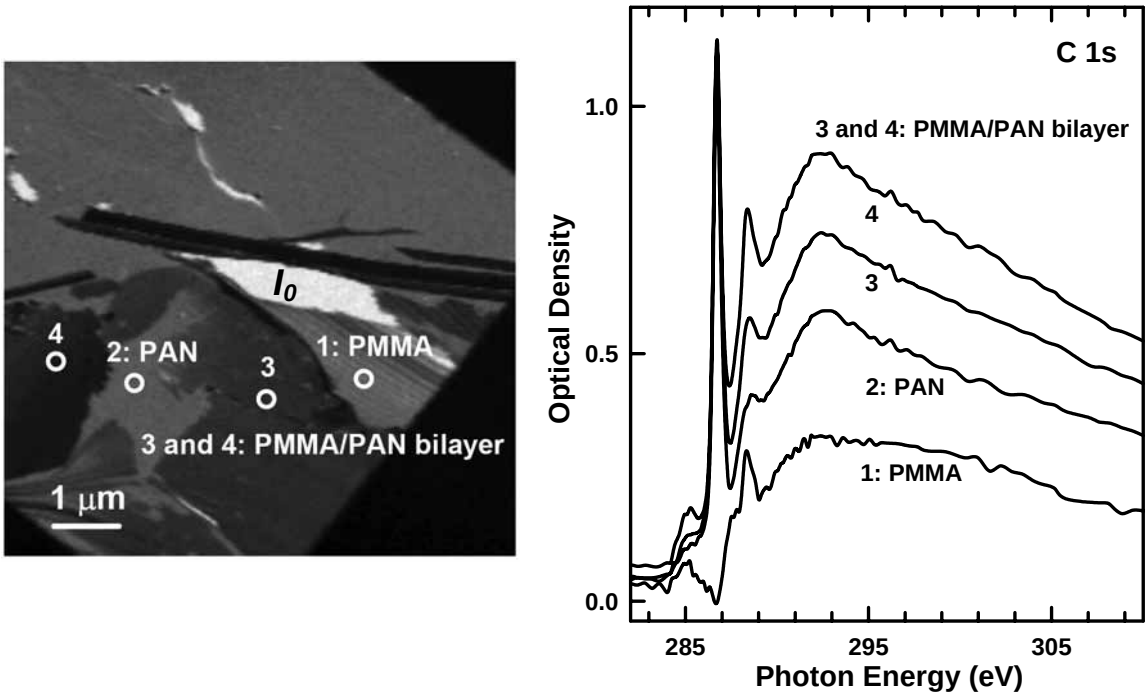

Figure 3.2 Point scan of a multilayer polymer film fabricated from microtomed PMMA and PAN single layer films, (left) location of points in the transmission image where the spectra were acquired, (right) spectra derived from point signals, which were normalized to I_0 of the empty area near the center of the image and recorded at the same time.

Figure 3.2 presents an example of point scan of a multilayer polymer film fabricated from microtomed PMMA and PAN single layer films. Spectra acquired at point 1 and 2 indicate single layers of PMMA and PAN respectively, while the spectra obtained at point 3 and 4 show a bilayer structure with varied thickness for the PMMA layer. The feature at 285 eV is due to radiation damage of the sample during the point

scan. Spectrum 1 indicates that PMMA is heavily damaged because the peak at 288.4 eV is much lower (relative to the continuum) than in an undamaged spectrum and the feature at 285 eV is relatively higher.

3.1.3 Linescan spectra

Linescan spectra refer to repeated acquisition of soft X-ray transmission signal along a line while varying the photon energy. The STXM interferometric control system ensures a positioning accuracy of ~ 10 nm [KTS&03]. The line is defined by drawing a line on a single energy image with user specified parameters, i.e. the length of the line, the number of pixels along the line, the energy ranges of interest with variable increments, and the dwell times at each pixel of the line. The result of a linescan spectrum is a "line-spectral image" where the vertical axis is the length of the line in μm, and the horizontal axis is the photon energy range. The physical width of the line is determined by the spot size and the radiation damage spread.

Figure 3.3 shows the linescan spectrum of a spun coated multilayer polymer film, PMMA/polyurethane (PUR)/PAN. **Figure 3.3a** is the optical density image of the sample taken at 286.8 eV with the arrow indicating the location of the linescan. The image contrast shows that PAN forms isolated domains. The line (defined by the arrow) traverses the sample from the black empty area onto the film across several of the discrete PAN domains. **Figure 3.3b** shows the line-spectral image in optical density format, which was derived from the original transmission linescan spectrum image by normalization to the signal in the empty region. Two boxes on Figure 3.3b corresponding

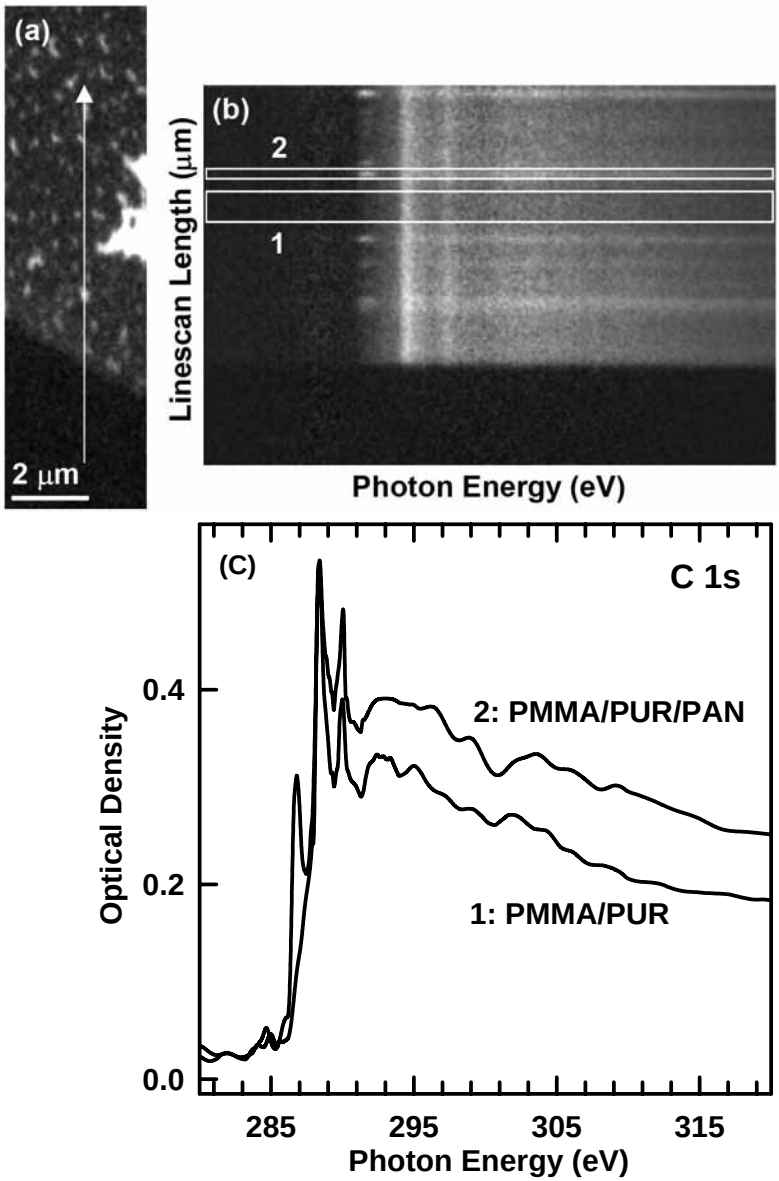

Figure 3.3 Line scan of a spun coated multilayer polymer film, PMMA/PUR/PAN, (a) optical density image of the sample at 286.8 eV with the arrow indicating the location of the linescan, (b) optical density format of the line-spectral image, (c) spectra derived from the two boxes on (b).

to different sections of the line were selected to derive NEXAFS spectra by averaging the intensity of the pixels along the line sections for each photon energy. The derived spectra are presented in **Figure 3.3c**. The spectrum of box 1 shows two characteristic peaks,

corresponding to two components, i.e. PMMA (288.4 eV) / PUR (290.0 eV) in a uniform bilayer structure. The spectrum of box 2 shows three characteristic peaks, referring to all three components, i.e. PMMA/PUR/PAN. Actually the width of box 2 corresponds to the section of the linescan across a PAN domain. Based on spin coating experience, uniform PAN layers cannot be formed without heating under vacuum to completely remove the solvent dimethylformamide (DMF).

3.1.4 Image sequences (stacks)

A STXM image sequence, i.e. a stack [JWF&00], performs acquisition of a set of X-ray transmission images for one or more spatial regions, such as sample and empty areas, over a set of photon energies. Similar to single energy imaging, the spatial regions in an image sequence scan and the spectral regions with varying increments of photon

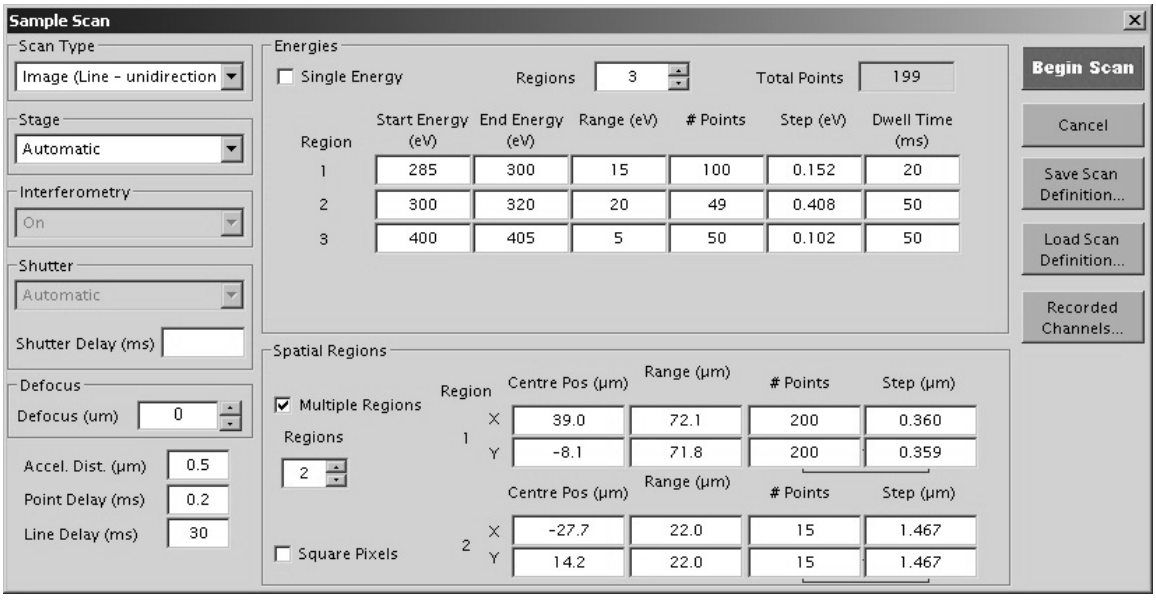

Figure 3.4 Screen shot of the STXM_control scan definition panel set up for a STXM image sequence.

energy are specified by the user. The STXM_control software allows acquisition of up to 10 spatial and 10 energy regions in one image sequence scan. A screen shot of the scan definition panel set up for a STXM image sequence is shown in **Figure 3.4**.

Although the interferometric control system ensures high accuracy in positioning, occasionally the sequence images do drift over a long period of acquisition time or for other unpredictable reasons. In this case, post alignment of the stack is carried out using automatic or manual alignment procedures available in the *aXis2000* program [AXIS].

Figure 3.5 shows selected optical density images from an image sequence recorded from a micro phase-separated polymer film, PMMA-*blend*-PAN, the same

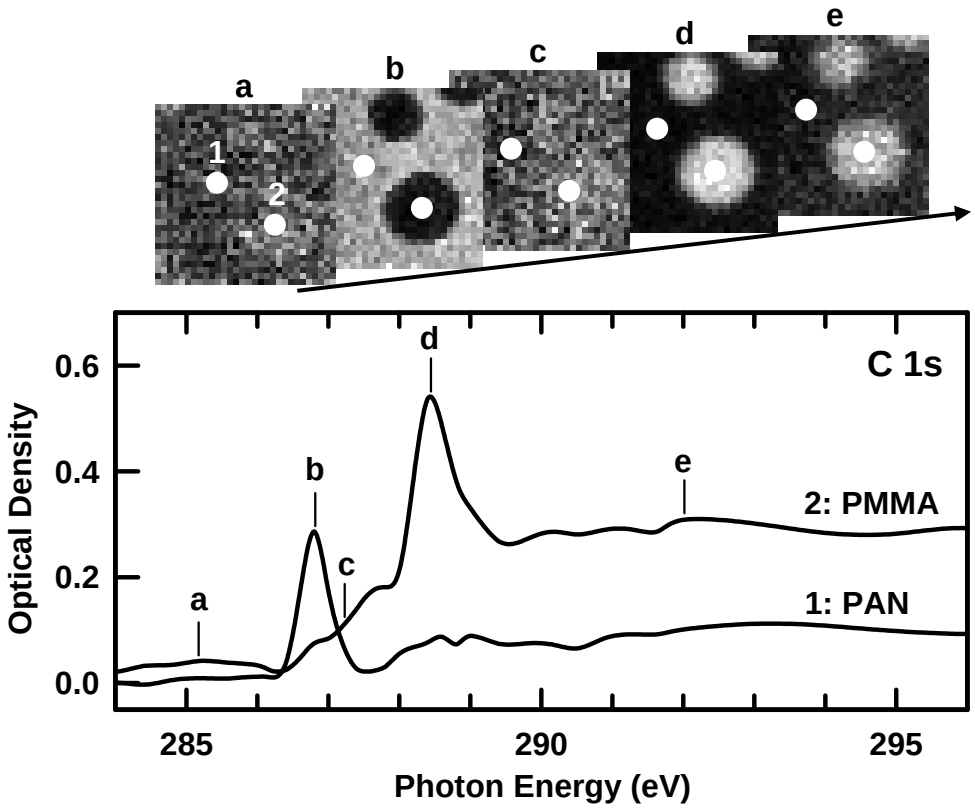

Figure 3.5 Image sequence of a micro phase-separated polymer film, PMMA-*blend*-PAN, (top) selected optical density sequence images at the photon energies as indicated by the marks on the bottom spectra, (bottom) spectra obtained from two white circles as shown in the top images.

sample as that in Figure 3.1. The spectra displayed were extracted from the two regions shown on the images as white circles. The complete image sequence consists of 49 images of dimensions 3 μm x 3 μm (30 x 30 pixels) at energies between 280 - 320 eV. The image contrast changes throughout the C 1s absorption edge as the PAN and PMMA components absorb strongly at different energies. Circle 1 is located in the continuous phase of the sample, and the spectrum confirms that the continuous phase is PAN. Circle 2 is selected on an isolated domain, and the spectrum confirms the discrete domains are PMMA.

3.1.5 Pattern generation

The focused X-ray spot of ~40 nm in STXM can be used to direct-write micro patterns in polymer films. This approach was used for convenience in my quantitative radiation damage studies and may be potentially useful for lithography. The pattern generation program was coded by Tolek Tyliszczak (ALS, LBNL), and is incorporated into STXM_control, the microscope control and data acquisition software. In the pattern generation mode, the sample is positioned to predefined (x, y) locations with ~10 nm precision under laser interferometer control; specifically a selected point on the sample is assigned to the origin of the coordinate system of an input pattern. Then a fast acting (~300 μs) in-vacuum piezo shutter is opened for a precise, predefined, position-dependent time interval (usually 50 - 2000 ms) to expose the sample to the flux of monochromated X-rays. With the slits typically used for pattern generation (80/40/40 microns), the incident fluxes are 2 - 3 MHz in the C 1s edge when using the ~1 meter long N_2 gas filter

filled at ~700 mtorr to eliminate 2nd order radiation. Note the measured detector efficiency is 35±5 % in the C 1s edge in this work, and thus the actual incident photon flux is about 3 times larger. The energy resolution is ~200 meV and the spatial resolution is ~50 nm with slit settings 80/40/40 microns. Input pattern files consist of lists of (x, y, t) values for each pixel. The exposure energy is set for each pattern in advance. For convenience, the exposure times (t) in the pattern file are scaled between 0 and 1. During patterning a time multiplier is specified by the user to determine the actual exposure time. The pattern input files can be generated from images starting from many different graphic formats using routines in *aXis2000* [AXIS]. For multi-color patterns (multi-photon energy exposures), color images are color separated and used to generate patterns for each color sequentially at the appropriate photon energies. The overall physical size, the pixel density, and thus sampling resolution of the input pattern can be adjusted by changing the image characteristics prior to generating the pattern generation input file.

Figure 3.6 shows two examples of pattern generation on polymer films with STXM 5.3.2. **Figure 3.6a** presents a 9-pad input pattern file (0.6 μm x 0.6 μm, 10 x 10 pixels for each pad) which was used to create a replica (**Figure 3.6b**) in a PMMA single layer film by exposure at 300 eV, I_0 = 2.2 MHz and the indicated exposure times which were computed from the image grey scale and the time multiplier. The pattern is best visualized at the characteristic energy for PMMA, the C 1s $\rightarrow$ $\pi^*_{C=O}$ transition at 288.4 eV. **Figure 3.6c** presents a two-color Lawrence Berkeley National Laboratory (LBNL) logo input pattern file (the roof in red, point spacing 84 nm, total 399 pixels, and the window/tower in blue, point spacing 84 nm, total 807 pixels) which was chemically

selectively transferred to a PMMA/PAN bilayer film (**Figure 3.6d**) in which PMMA damage (288.4 eV, I_0 = 2.0 MHz, exposure time = 100 ms/pixel) was used to generate the roof indicated in red, and PAN damage (286.8 eV, I_0 = 2.3 MHz, exposure time = 200 ms/pixel) was used to generate the window/tower indicated in blue. The patterning was imaged at 288.4 eV (PMMA damage) and 286.8 eV (PAN damage), respectively. The color coded composite image shown in Fig. 3.6d was made from the two original images

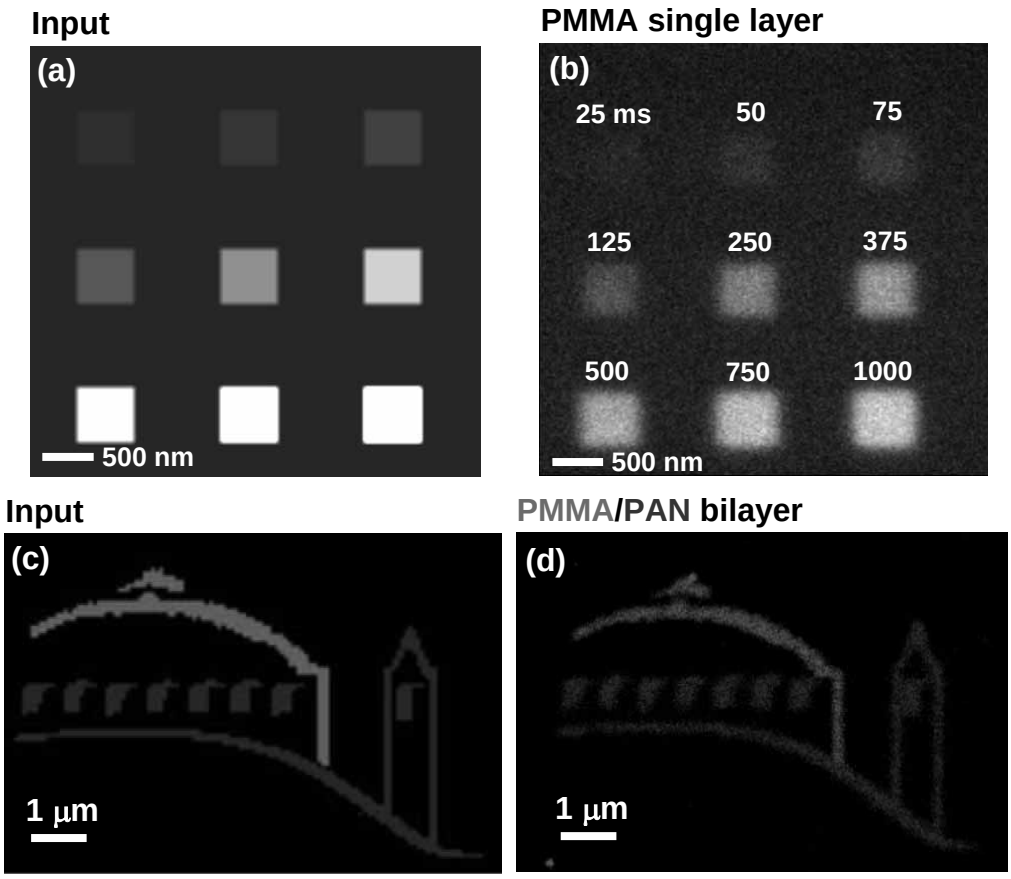

Figure 3.6 STXM pattern generation for polymer films. (a) Input file of 9 pads with different exposure times as indicated in (b), (b) pattern of (a) generated in a PMMA single layer film and imaged at 288.4 eV, (c) LBNL logo input file, (d) pattern of (c) chemically selectively transferred to a PMMA/PAN bilayer film, with PMMA damage indicated in red, and PAN damage indicated in blue, the composite image of (d) made from two images at 288.4 (PMMA damage) and 286.8 eV (PAN damage).

in *aXis2000* [AXIS]. Currently, full color chemically selective patterning has been successfully developed in trilayer polymer systems; detailed examples are presented in Chapter 7.

3.2 Quantitative dose-damage analysis in STXM

The major motivation of this thesis is to use quantitative dose-damage relations to study radiation damage to polymer materials. For STXM quantitative microanalysis of sufficiently thin samples, the Beer-Lambert law is obeyed (equation 2.10) so that the optical density (OD) of a sample is linearly proportional to the amount of material. The approach used to evaluate radiation damage in this thesis is to find the relationship between the damage in terms of OD change and the absorbed radiation dose a in units of grays (Gy) (1 Gy = 1 J/kg, 1 MGy = 1 x 10^6 Gy). The dose can be obtained from:

$$a = \frac{FEt}{\varepsilon m} = \frac{I_0(1-e^{-\mathrm{OD}})Et}{\varepsilon V \rho} \qquad (3.1)$$

where F is the absorbed flux (absorbed photons per second) of a specific volume pixel (voxel), which can be derived from the incident flux (I_0) and the dynamic OD of the exposed sample region at exposure photon energy E using equation 2.10, t is the exposure time, ε is the measured detector efficiency (35±5 % in this work), m is the mass of the voxel, V is the volume of the voxel (i.e. 60 nm x 60 nm x l_i, where 60 nm point spacing was routinely used and l_i is the sample thickness), and ρ is the polymer density.

For quantitative dose-damage studies the exposure photon energy was chosen in the C 1s continuum, e.g. 300 eV, because the OD or absorbance of the exposed sample

region will stay almost constant at these energies for many polymers having no or small mass loss during radiation damage [CUA02]. As a result, the dose rate (Gy/s) will be constant as derived from equation 3.1. However, in the case of large mass loss or at other exposure energies, e.g. the characteristic energies, the OD of the exposed sample area will dynamically decrease with exposure time. In such cases the thinning of the sample is assumed to follow a first order kinetic process [ZJL&95, RHA&97, A98, BJ02, CUA02]:

$$\mathrm{OD} = y_0 + c\exp(-bt) \tag{3.2}$$

where y_0, c and b are fitting constants. Then an integrated OD (denoted as S_{OD}), which is equivalent to the dynamic OD of the exposed area, can be obtained through integration over the entire exposure time:

$$\mathrm{S_{OD}} = \frac{\int_0^t (y_0 + ce^{-bt})dt}{t} = \frac{y_0 t + \frac{c}{b}(1 - e^{-bt})}{t} \tag{3.3}$$

Subsequently, the dose rate will keep decreasing as the integrated exposure time increases.

The quantitative radiation damage kinetics can be worked out once the STXM radiation dose is defined. Specifically, the data of dose versus remaining OD at an analysis photon energy are acquired. The analysis energy should give the best contrast between damaged and undamaged regions as a result of chemistry changes or mass loss. Then the data are fit to postulated rate laws, e.g. first order kinetics (equation 3.2):

$$\mathrm{OD_t} = \mathrm{OD}_\infty + C\exp(-\frac{a}{a_c}) \tag{3.4}$$

where $\mathrm{OD_t}$ is the remaining optical density of the exposed region at an analysis energy, OD_∞ is the extrapolated optical density after infinite dose, C is a constant, which is equal

to the infinite damage ($D_\infty = OD_0 - OD_\infty$, where OD_0 is the initial optical density), and a_c is the critical dose, i.e. the dose required to attenuate (or increase, in the case of feature growth upon radiation damage) the OD at the analysis energy by (1-1/e) or 63% of the infinite damage (D_∞). The larger the critical dose of a polymer, the slower the damage rate will be. In order to compare between different layer thicknesses and polymer materials, both sides of equation 3.4 are divided by the initial optical density (OD_0) at the corresponding analysis energy to get the normalized optical density as a function of radiation dose.

When subtracting both sides of equation 3.4 from the initial optical density (OD_0) of the sample, an alternative dose-damage equation of the damage kinetics can be obtained:

$$\mathrm{D} = \mathrm{D}_\infty - C\exp(-\frac{a}{a_c}) \qquad (3.5)$$

where D is the damage in terms of OD change after exposure, i.e. $D = OD_0 - OD_t$. If the damage process exhibits first order kinetics, a plot of $\ln(D_\infty - D)$ versus dose a is linear with a slope of $-1/a_c$. Similar to above, equation 3.5 is also conveniently divided by the infinite damage (D_∞) on both sides to get the normalized damage as a function of radiation dose. The analysis of dose-damage numerical data was performed in an Excel™ worksheet, which was developed based on all the principles outlined above. An example is shown in **Figure 3.7** for polypropylene carbonate (PPC), which suffers large mass loss during radiation damage.

For experimental dose-damage analysis in STXM, adjacent small regions (pads)

STANDARD DOSE-DAMAGE WORKBOOK

DOSE (energy/mass)
= {(energy absorption rate)*(time)*(photon energy)}/(density*volume)
= {(Io-I)*E*t/ε}/(ρ*A*d)

{Io(1-exp(-OD))*E*t/ε}/(ρ*A*d)

Sample	Edge	Data file		
PPC (60209-2)	C 1s	60210056	image at 300 eV	Damage pattern: pad

Converting exposure times to dose

symbol	property	value	Error	source	note	
OD	optical density	0.773	0.01	ls60210051od-ppc.txt		
slits	(check on intensity)	80/40/40		logbook		
Io	Io (MHz)	1.60	0.05	logbook	N2 filter	
Io-I	absorbed flux/volume (MHz)	0.86	0.028	calc		
pad size	(nm)	480	0	central 80%	64	Points of 100
d	thickness (nm)	148	10	ls60210051od-ppc.txt	ratio to ls60210051od1-ppc.txt	
V	volume (nm^3)	3.41E+07	2.30E+06		A*d	
ρ	density (g/cc)	1.26	0.01			
m	mass (kg)	4.30E-17	2.92E-18		1.00E+21	
E	energy	300	0.1			
ε	detector efficiency	0.40	0.05	STXM532 paper		
MGy/s	**dose/ms**	**154.1**	**22.5**		1.60E-19	

transfer the NEGATIVE OF THE SLOPE of the linear fit into cell H27 to derive the T-1/2 for the damage

1/T-1/2	0.049727	**T-1/2 (MGy)**	**20.1**	**2.9**	**15%**
			Critical dose	**Error**	**Error percentage**

$$Integrated\ OD = \frac{\int_0^x (y_0 + ae^{-bx})dx}{x} = \frac{y_0 x + \frac{a}{b}(1-e^{-bx})}{x}$$

Exposure time (ms)	300eV (data: 60210056) Time (ms)	OD	Integrated OD during exposure	Integrated dose rate during exposure (MGy/s)
0	0	0.7735	0.7735	**154.1**
12.5	12.5	0.7415	0.7698	**153.6**
25	25	0.7215	0.7489	**150.8**
37.5	37.5	0.6935	0.7293	**148.1**
62.5	62.5	0.6175	0.6935	**143.1**
125	125	0.4845	0.6207	**132.3**
187.5	187.5	0.4225	0.5661	**123.7**
250	250	0.3575	0.5247	**116.8**
375	375	0.3495	0.4679	**106.9**
500	500	0.3220	0.4322	**100.4**
SigmaPlot fit: y = y_0 + a*exp(-bx)				
y_0	**a**	**b**		
0.3068	0.4852	7.5602E-03		

x: exposure time, y: OD at 300 eV

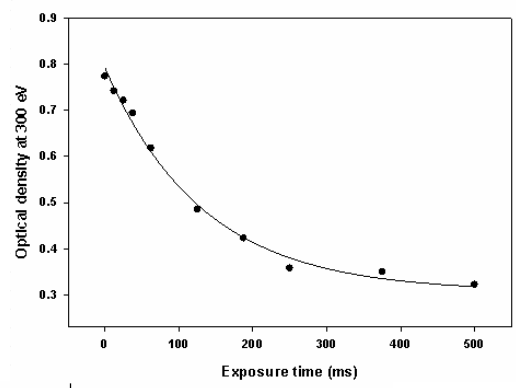

Damage at 300 eV			saturation signal level c =	0.5
Time (ms)	**Dose (MGy)**	**Dmg-del-OD**	**c-dmg**	**ln{(c-dmg)}**
12.5	1.92	0.032	0.468	-0.759
25	3.77	0.052	0.448	-0.803
37.5	5.55	0.080	0.42	-0.868
62.5	8.94	0.156	0.344	-1.067
125	16.54	0.289	0.211	-1.556
187.5	23.19	0.351	0.149	-1.904
250	29.20	0.416	0.084	-2.477
375	40.09	0.424	0.076	-2.577
500	50.20	0.452	0.0485	-3.026

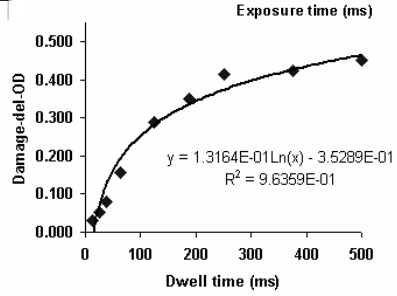

Pad #	Avg. Relative OD	S.D.	Dwell	Time Multiplier
1	0.486	0.027	0.0250	500
2	0.466	0.026	0.0500	
3	0.438	0.029	0.0750	
4	0.362	0.029	0.1250	
5	0.229	0.056	0.2500	
6	0.167	0.063	0.3750	
7	0.102	0.026	0.5000	
8	0.094	0.041	0.7500	
9	0.067	0.029	1.0000	
Undmg	0.518	0.032		

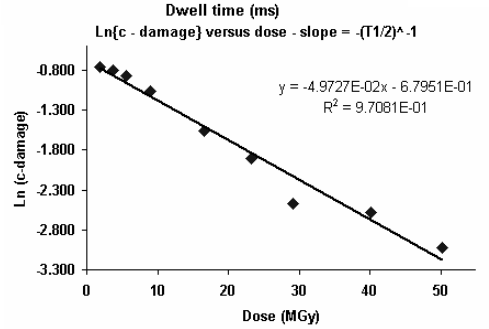

Figure 3.7 Screen shots of Excel™ worksheet for STXM dose-damage analysis.

of the polymer films (typically 0.6 μm x 0.6 μm, using 10 x 10 pixels) were exposed using systematically varied dwell times so as to span a range of doses that adequately samples the dose-damage curve. The exposure was initially carried out using single energy imaging with manual control of the sample position. After the pattern generation mode was developed, automatic exposure was achieved, as illustrated in section 3.1.5, which turned out to be much more efficient and reproducible. The entrance slit and both the dispersive and non-dispersive exit slits of the monochromator were adjusted to control the photon flux and dose rate on the sample. A typical setting was 80/40/40 μm (entrance/exit-dispersive/exit-nondispersive). A N_2 gas filter was used to ensure there was negligible higher order radiation. The incident photon flux under these conditions was between 1.5 and 2.5 MHz. After exposure, analysis images were recorded at the characteristic and other selected photon energies for each polymer. Then these images were converted to OD images by normalizing to the incident photon flux (I_0) which was measured in the absence of the sample. The OD of the damaged regions was evaluated by averaging all pixels in the uniform central portion of the damage pads (~60%). The OD of the undamaged region was determined by averaging a large area away from the damage pattern. The difference between these two OD values is the damage value corresponding to a specific damage region and thus dose. In addition, the NEXAFS spectra of the damaged and undamaged regions were acquired using image sequences scans with much lower photon flux. Reference spectra on absolute linear absorbance scales (i.e. OD per nm thickness sample) were derived by scaling the spectra of the undamaged and damaged material to the X-ray absorption response in the regions of 275-282 eV and 320-350 eV,

to match that of the linear X-ray absorption (OD for 1 nm) for the elemental composition of the sample derived from literature absorption coefficients [HGD93]. The ratio between the spectrum of the undamaged material and the reference spectrum gives the polymer film thickness.

Figure 3.8 shows an example of STXM dose-damage analysis for radiation damage in PMMA. **Figure 3.8a** is an optical density image of a uniform region of a

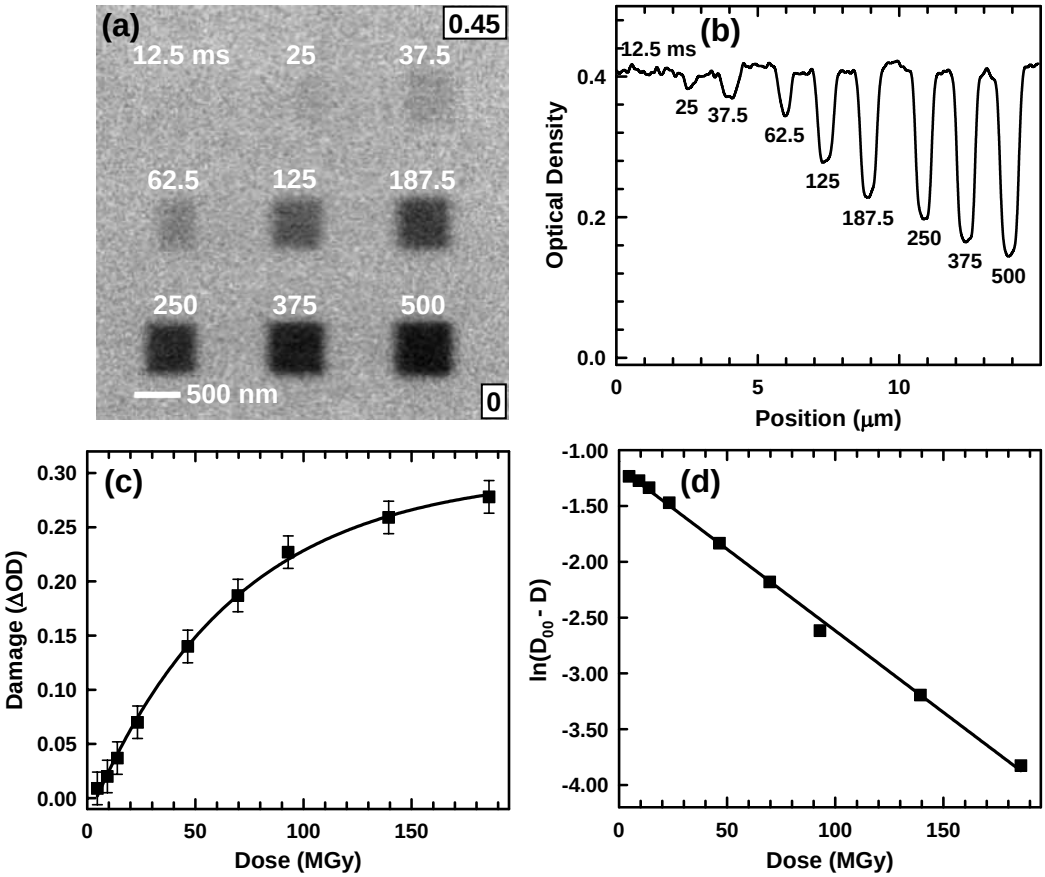

Figure 3.8 STXM dose-damage analysis of radiation damage in PMMA, (a) optical density image of 9 pads created in an initially undamaged, free standing PMMA thin film by exposure at 300 eV with indicated exposure times, and imaged at 288.45 eV, the numbers in lower and upper left are the minimum and maximum OD, (b) plot of the sum of line profiles across the set of pads, with the three successive rows concatenated, (c) plot of damage versus dose, (d) the linearized plot of the data of (c) fitted with equation 3.5.

PMMA film that was damaged in the indicated pattern of 0.6 μm x 0.6 μm (10 x 10 pixel) pads where each successive pad was subjected to a systematically increased dose by adjusting the dwell time per pixel between 12.5 and 500 ms at a dose rate 3.7 x 10^2 MGy/s. **Figure 3.8b** plots the OD profiles of the 9 pads with nearby undamaged regions shown as the baseline. **Figure 3.8c** plots the damage derived from the change in the optical density against the dose in the central 60% of the pad, and **Figure 3.8d** is the linearized version of that data fitted with equation 3.5 to determine the critical dose. After a number of repeat measurements, the critical dose for PMMA damage in terms of C=O loss (288.45 eV) was determined to be 67 ± 10 MGy. The quantitative dose-damage analysis by STXM for other polymer materials is presented in Chapter 4.

3.3 Chemically selective patterning of multilayer polymer systems by STXM

3.3.1 Experimental approach

Chemically selective radiation damage was initially explored on four different polymer systems (details in Chapter 6): a PMMA/PAN bilayer film, a PMMA-*blend*-PAN micro phase-separated film, a poly(MMA-*co*-AN) copolymer film and a poly(ethyl cyanoacrylate) (PECA) homopolymer film. A high level of chemically selective modification was only achieved for the PMMA/PAN bilayer; in particular, irradiation at 288.45 eV selectively removed the carbonyl group from PMMA while irradiation at 286.80 eV selectively reduced the nitrile group of PAN. In the last two homogenous polymer systems similar amounts of damage to the nitrile and carbonyl groups occurred during irradiation at either 286.80 or 288.45 eV. As discussed in detail in chapter 6, this

was attributed to spread of damage from the site of X-ray absorption to surrounding areas up to ~300 nm away, depending on the polymer. Although the electrons generated from photoabsorption can be damaging, their range is limited to a few nanometers due to their strong interactions in condensed media. It might be the energetic radicals and ions that are responsible for the longer range damage, possibly through radical or ion induced chain processes, such as depolymerization and fragmentation. Certainly the range of any single radical or ion will be very small, less than a nanometer.

Radiation damage spreading in a polymer should occur in three dimensions. The interface of the bilayer system very effectively blocks the transport of damage from one layer to the other. This is surprising since the range of damage spread in homogenous polymers (150 - 300 nm) far exceeds the thickness of the combined bilayer system (60 - 80 nm). There are several possibilities attributed to the interface effect: (1) there is a physical gap between the two layers; (2) there are small amounts of impurities trapped in the interface which quench the damage spread via radicals and ions; (3) there is a potential energy barrier at the interface between two incompatible polymers, which traps or blocks the reactive migrating species, etc.

Transmission electron microscopy (TEM) and STXM chemical mapping were used to exclude the possibility of a physical gap between the layers by checking the cross-section of the interface of a PMMA/PAN bilayer, as shown in **Figure 3.9**. The cross-section was prepared by embedding the bilayer polymer into non-reactive epoxy resin then microtoming to thin films. The TEM image (**Fig. 3.9a**) shows the interface is very tight (about a few nanometers) at the arrows. Other regions of the interface are a little

wider, which are probably partly altered during microtomy. Since TEM is not chemically sensitive, the bilayer films are not well resolved. STXM chemical mapping of the bilayer cross-section was generated by fitting an image stack of the cross-section with the reference spectrum of each component, i.e. PMMA, PAN, epoxy. The STXM result (**Fig. 3.9b**) indicates a compact bilayer cross-section, ~ 100 nm covering the two layers and the interface, as shown at the arrows. The left side of the interface is greener, corresponding to the PMMA layer, while the right side of the interface is bluer, referring to the PAN layer. Because the spatial resolution of STXM is about 50 nm, the layers and the interface can not be resolved. The interface of a similar bilayer film Polycarbonate/PMMA prepared by spin coating without annealing indicates that the interface is very tight (0.5 nm) [HRT&01], which suggests there should be no physical gap for a layered polymer film prepared by spin coating.

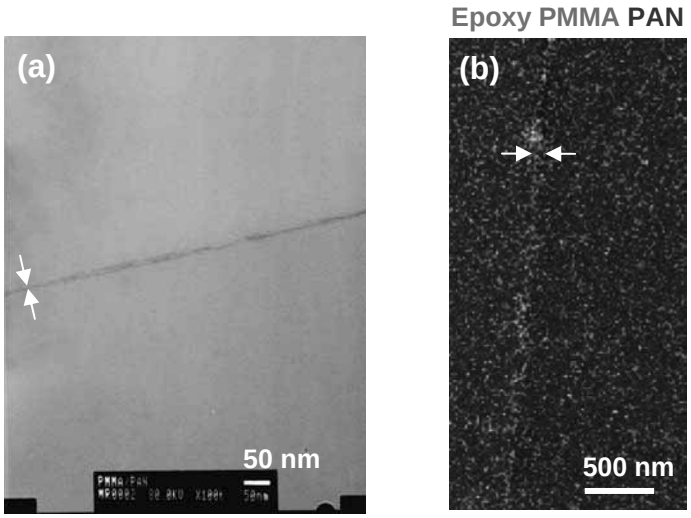

Figure 3.9 TEM image and STXM chemical mapping of the cross section of a bilayer polymer system, i.e. PMMA/PAN, which was embedded in epoxy resin and microtomed, (a) TEM image acquired with 80 kV electron beam, (b) chemical mapping by STXM, red color: epoxy, green color: PMMA, and blue color: PAN.

NEXAFS spectroscopy showed there were no detectable impurities in a PMMA/PAN bilayer as comparing its spectrum in Fig. 6.2 to the sum of the spectrum of each component in Fig. 6.1. Furthermore, pure polymers and solvents were used in sample preparation to eliminate possible impurity sources.

The potential energy barrier at the interface seems more reasonable. One possibility is the Gibbs free energy well at the interface, which may trap the migrating species; another possibility in an electric field built up in the interface due to more emission of electrons from one layer to the other as a function of photon energy during radiation damage [C97]. As a result, the side of the interface with more radiation damage could become positively charged, while the other side would be negatively charged [C97]. The electric double-layer at the interface may effectively block the migration of radicals and ions. More details regarding the interface effect are presented in Chapter 6. Even if not fully understood, the multilayer structure has become a general approach to achieve chemically selective damage and patterning in this thesis.

The development of trilayer chemically selective patterning in order to enable full color image reproduction was achieved by adding a third layer to the PMMA/PAN bilayer. The selection of polymer materials as the third layer can be difficult. It requires: (i) a chemically-distinct and intense absorption feature, shifted by at least 1 eV with respect to other layers; (ii) a proper damage rate, i.e. critical dose; (iii) low absorption at the photon energies used to damage other layers; and (iv) good film forming capability. We started to explore non-aromatic instead of aromatic polymers since the latter is much more damage resistant, especially the phenyl rings [FRH&02, ELM04]. Spin coating has

been the most successful multilayer sample preparation method to date. A high molecular weight (usually >100 kdalton) is needed for spin coating and also helps to sustain the vacuum annealing needed to produce uniform films for some of the polymers. Non-aromatic polycarbonates, specifically polypropylene carbonate (PPC) and polyethylene carbonate (PEC), turned out to provide the best match with the above criteria. Two trilayer systems, i.e. PMMA/PPC/PAN and PMMA/PEC/PAN, were successfully fabricated by successive spin coating steps and chemically selectively patterned. The experimental details and results of chemically selective patterning for multilayer polymer systems are presented in Chapter 6 and 7.

3.3.2 Simulations: ChemLith

If quantitative NEXAFS spectra and critical doses for each polymer are known, it is possible to simulate the chemically selective patterning (or damage) that will result from a defined exposure protocol. The theories dealing with the simulations of chemically selective patterning are presented in Chapter 7. These include the computation of optical density as a function of exposure time (derived from equation 3.1 and 3.4), the concept of pattern contrast, the definition of patterning selectivity and the approach of patterning optimization.

ChemLith is an Excel™ worksheet developed to simulate chemically selective patterning for multilayer polymer systems using the principles presented in Chapter 7. **Figure 3.10** displays screen shots of **ChemLith** for the patterning of a PMMA/PPC/PAN trilayer. For a given set of input parameters and exposure time, **ChemLith** computes the

(a) ChemLith input and computing worksheet

Trilayer	Linear absorbance at exposure energy		Layer thickness (nm)	Pixel (nm)	Input parameters						D_∞ at exposure energy	Absorbed flux (Io-I) (MHz)	Detector ε	Dose (MGy)	Damage (ΔOD)	Contrast of each pattern in each layer ($OD_{undamage}/OD_{remaining}$)
				60		Exposure							0.4			
	Energy (eV)	OD1 (nm^{-1})		Mass per pixel (kg)	Polymer density (g/cm^3)	Energy (eV)	Io (MHz)	Time (ms)	Critical dose (MGy)	Estimated $OD1_\infty$ at exposure			Dose rate (MGy/s)			
PMMA	286.8	5.494E-04	27.4	1.164E-19	1.18	288.45	2.00	100	60	5.50E-03	0.217	0.03	33	7	0.023	1.07
	288.45	1.342E-02										0.62	610	61	0.138	1.60
	290.4	6.886E-03										0.31	305	31	0.086	1.31
PPC	286.8	5.771E-04	26.5	1.201E-19	1.26	290.4	1.78	100	25	5.50E-03	0.262	0.03	32	6	0.060	1.17
	288.45	4.450E-03										0.15	148	15	0.118	1.41
	290.4	1.540E-02										0.49	477	48	0.224	2.22
PAN	286.8	1.640E-02	35.7	1.505E-19	1.17	286.8	2.25	200	150	5.00E-03	0.407	0.97	738	148	0.255	1.77
	288.45	4.429E-03										0.18	138	14	0.036	1.07
	290.4	4.162E-03										0.14	105	10	0.027	1.05

Input NEXAFS

pmma-c-od1-sm.txt		ls60210051od1-ppc.txt		pan-od1.txt		Trilayer 60212052.txt	
Energy (eV)	OD1	Energy (eV)	OD1	Energy (eV)	OD1	Energy (eV)	OD
277.92	4.315E-04	278.00	5.058E-04	280.00	2.783E-04	280.00	4.045E-02
278.22	4.123E-04	278.40	5.009E-04	280.60	5.081E-04	280.53	4.843E-02
278.52	3.698E-04	278.80	4.598E-04	281.20	9.081E-05	281.07	4.273E-02
278.82	3.493E-04	279.20	4.557E-04	281.80	2.991E-04	281.60	4.739E-02
279.12	3.352E-04	279.60	4.324E-04	282.40	3.818E-04	282.13	4.637E-02
279.42	3.519E-04	280.00	4.474E-04	282.80	2.312E-04	282.67	3.691E-02
279.72	3.590E-04	280.40	4.493E-04	283.20	3.173E-04	283.20	4.136E-02
280.02	3.518E-04	280.80	4.424E-04	283.60	3.750E-04	283.50	4.528E-02
280.32	3.430E-04	281.20	4.583E-04	284.00	3.050E-04	283.60	3.754E-02
280.62	3.397E-04	281.60	4.677E-04	284.40	1.965E-04	283.70	4.802E-02
280.92	3.400E-04	282.00	4.600E-04	284.58	3.565E-04	283.80	4.508E-02
281.22	3.346E-04	282.40	3.962E-04	284.80	2.378E-04	283.90	4.840E-02
281.52	3.375E-04	282.80	4.820E-04	285.00	4.539E-04	284.00	4.389E-02
281.82	3.415E-04	283.20	4.381E-04	285.20	3.356E-04	284.10	5.172E-02
282.12	3.451E-04	283.60	4.611E-04	285.40	2.939E-04	284.20	4.869E-02
282.42	3.423E-04	284.00	4.566E-04	285.60	5.196E-04	284.30	4.934E-02
282.72	3.386E-04	284.20	3.973E-04	285.80	3.198E-04	284.40	4.573E-02
283.02	3.359E-04	284.35	4.623E-04	286.00	3.533E-04	284.50	5.705E-02
283.32	3.356E-04	284.50	5.204E-04	286.10	4.676E-04	284.60	5.209E-02
283.62	3.369E-04	284.65	4.656E-04	286.20	7.922E-04	284.70	5.669E-02
283.92	3.362E-04	284.80	5.352E-04	286.30	1.463E-03	284.80	6.136E-02
284.02	3.375E-04	284.95	4.644E-04	286.40	2.342E-03	284.90	5.392E-02
284.14	3.363E-04	285.10	5.143E-04	286.50	4.286E-03	285.00	5.780E-02
284.26	3.366E-04	285.25	5.094E-04	286.60	8.508E-03	285.10	6.058E-02
284.50	3.429E-04	285.40	5.352E-04	286.70	1.365E-02	285.20	6.377E-02
284.62	3.565E-04	285.55	5.166E-04	286.80	1.640E-02	285.30	5.938E-02

Matrix solution for each layer thickness

Linear absorption NEXAFS				Trilayer thickness (nm)	Trilayer NEXAFS	
Peak energy	OD1 (nm^{-1}) PMMA	PPC	PAN		Peak energy	OD
288.45	1.342E-02	4.450E-03	4.429E-03	27.4	288.45	0.6436
290.4	6.886E-03	1.540E-02	4.162E-03	26.5	290.3	0.7451
286.8	5.494E-04	5.771E-04	1.640E-02	35.7	286.7	0.6163

Model: $OD = OD_\infty + A^*\exp(-a/a_0)$
$D = D_\infty - A^*\exp(-a/a_0)$
$A = D_\infty = OD_0 - OD_\infty$

Black shading: input parameters

Ctrl-Shift-Enter for lookup values and matrix operation

Input pattern

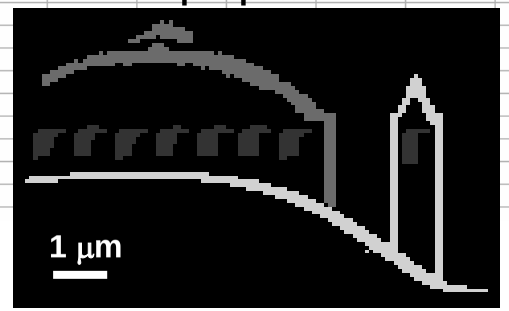

(b) Output

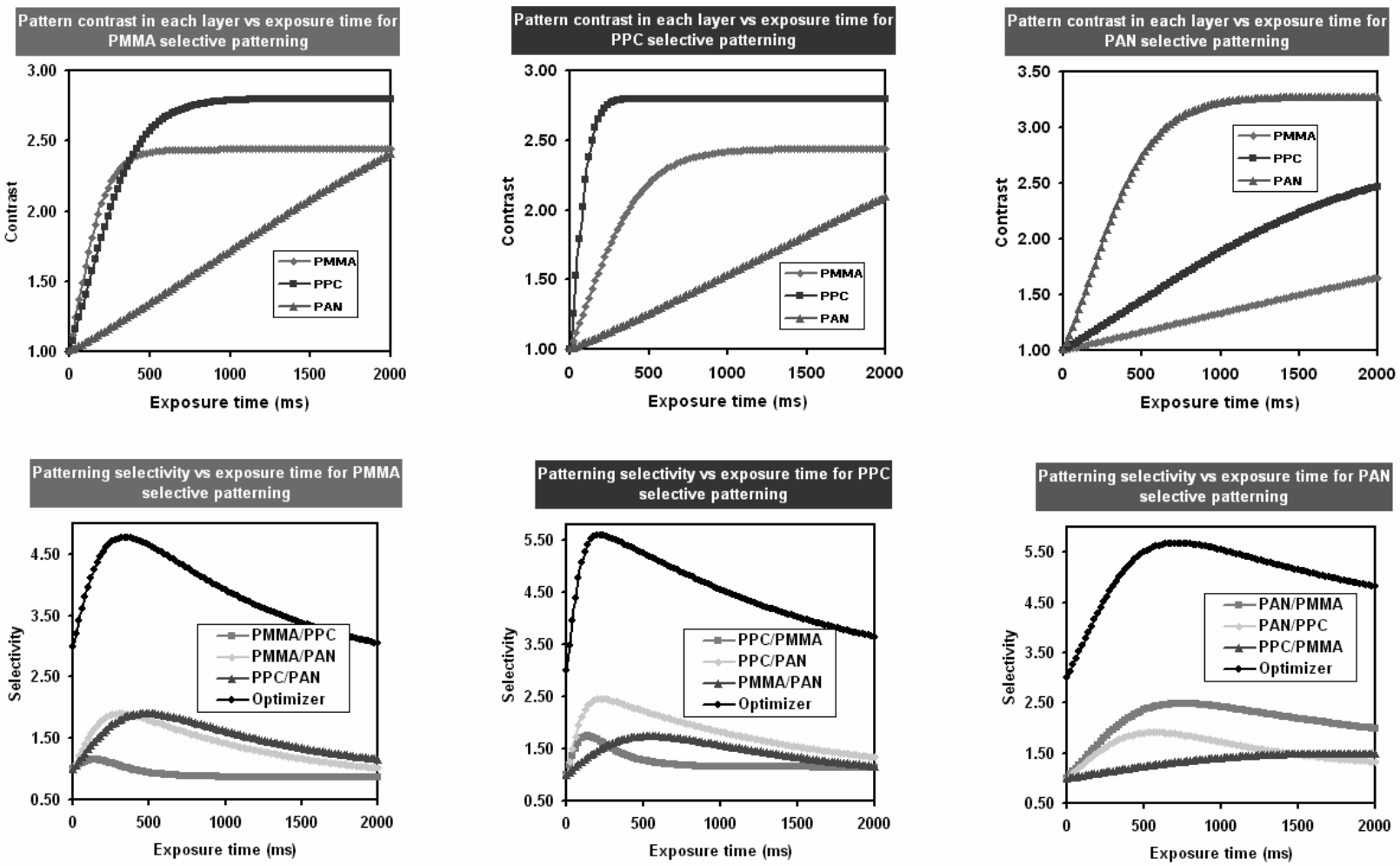

Figure 3.10 Screen shots of **ChemLith** for the patterning of a PMMA/PPC/PAN trilayer using exposure at the three photon energies indicated, (a) input and computing worksheet, (b) output of the contrast, selectivity and optimizer plots.

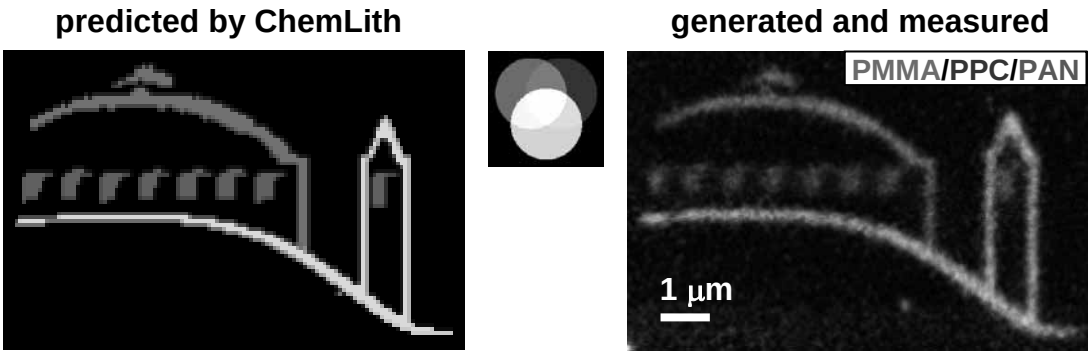

Figure 3.11 Visual display using *aXis2000* of the predicted patterns for the best exposure protocol in terms of optimizer for a PMMA/PPC/PAN trilayer, compared with experimental results.

absorbed dose, the spectral change caused by the radiation damage, and the pattern contrast for each layer, as shown in **Figure 3.10a**. After computing for a range of exposure times at specified photon energies for each layer, the computed contrast in each layer, the selectivity factors for all pairs, and the optimizer are plotted as shown in **Figure 3.10b**. The optimum exposure times correspond to the maximum of the optimizer profile, or in some cases refer to the maximum of the selectivity profile for a critical pair of polymer layers. Furthermore, one can simulate the output of a 3-color pattern generated from the best exposure protocol predicted by **ChemLith**, in the form of a color-coded image using *aXis2000* in order to compare the predicted output to that generated experimentally, as shown in **Figure 3.11**.

The procedures to use **ChemLith** and a listing of the input required are outlined in **Table 3.1**. The selection of the polymer materials is based on their NEXAFS spectra and measured critical doses. Although an optimum ordering of the three polymers within the trilayer structure usually exists, if spin coating is used to fabricate the trilayer, there can be further constraints due to preferential solubilities in the solvents used. Thus some

predicted layer structures may not be readily achieved experimentally. The input for each polymer layer includes the polymer properties (i.e. density, NEXAFS spectrum, damage saturation level (OD_∞) and critical dose), the layer thickness, and the exposure conditions (i.e. exposure energy, incident flux, and exposure time). Polymer properties are constants for a selected polymer. The layer thickness is determined by the spin coating conditions, such as the concentration, the spin speed and the time. For a prepared trilayer, the thickness of each layer can be obtained by fitting the overall NEXAFS spectrum of the trilayer with a weighted sum of the component reference spectra, placed on absolute linear absorbance scales. The NEXAFS spectra and the patterning templates are those appropriate for regions of the sample which have uniform thickness (i.e. the methodology assumes a uniform layer thickness). As for the exposure conditions, first the exposure

Table 3.1 ChemLith simulation procedure and input parameters for trilayer systems
a. ChemLith simulation procedure

Step	Procedure of ChemLith simulation
1	Input trilayer components, layer order and quantitative NEXAFS spectrum (in optical density per nm) for each component. ChemLith finds the linear absorption coefficient for the exposure energy selected for each component
2	Input the NEXAFS spectrum of the trilayer in OD. ChemLith computes each layer thickness by fitting the overall spectrum with each component spectrum at the characteristic energies
3	Input each polymer density. ChemLith computes the mass of the exposure pixel volume for each component
4	Input selected exposure energy for each component
5	Input the critical dose for each component and the $A_\infty(E)$ at the exposure energy for each component. ChemLith computes the infinite damage ($D_\infty = OD_0 - OD_\infty$) for each component
6	Input incident fluxes at the exposure energies and the detector efficiency. ChemLith computes the absorbed flux and the dose rate for each layer.
7	Input the exposure time at each exposure energy
8	ChemLith computes dose, damage (OD change) and contrast in each component for each exposure time at each exposure energy
9	Repeat 7 and 8 until a broad range of exposure time is explored, then ChemLith generates a number of plots, such as contrast, selectivity and optimizer as a function of exposure time at each exposure energy.
10	Input images of each color component. ChemLith generates a visual display of the predicted output from the computed layer absorptions.

b. Overall input

Parameter		Units	Source	Comments
Composition		n.a.	Library of polymer radiation damage studies	Polymers with sharp distinct spectral features
Layer order		n.a.	Arbitrarily assigned or pre-determined by spin coating	More robust polymer as upstream
Trilayer	NEXAFS spectrum	n.a.	Measured by STXM	No radiation damage
	E1	eV	peak energy of polymer 1	
	E2	eV	peak energy of polymer 2	
	E3	eV	peak energy of polymer 3	

c. Input specific to each layer (for example polymer 1)

Parameter		Units	Source	Comments
Polymer density		g/cm^3	supplier	
Linear absorption NEXAFS spectrum	NEXAFS	n.a.	NEXAFS spectrum of pure polymer	Rescaled to linear X-ray absorption for the elemental composition of 1 nm thickness
	OD1(E1)	nm^{-1}	Automatically look up the peak energy	For sharp peaks, imaging at the top of the peak is important for high quality patterns
	OD1(E2)	nm^{-1}	Automatically look up	
	OD1(E3)	nm^{-1}	Automatically look up	
	$OD1_{\infty}(E1)$	nm^{-1}	Estimated linear absorbance for completely damaged spectral feature based on extrapolation of experimental data	
Thickness		nm	Fit trilayer NEXAFS spectrum with three linear absorption spectra; or vary to optimize for a virtual trilayer	Total multilayer thickness should be below 150 nm to avoid absorption saturation
Exposure	Energy	eV	Spectral peak; or vary to optimize based on NEXAFS spectrum	
	Io	Hz	Typical beamline conditions; or vary to optimize	Tradeoff with exposure time
	Time	ms	Vary to optimize	Sample longer enough time
Critical dose		MGy	Measured	
Image of pattern		n.a.	Color separation in aXis2000	Physical size, pixel density and color intensity can all be adjusted

energy is chosen at the characteristic absorption energy for each polymer component. This gives the best patterning selectivity, as is evident from the ratio of any two NEXAFS

spectra of these polymers. Second the incident flux or the exposure time is systematically modified to optimize the chemically selective patterning for a specific trilayer system. If one is using **ChemLith** to compare predicted and actual patterns, the exposure dose rate and time are those used experimentally.

Initially **ChemLith** was used to simulate the patterns of an actual system in order to develop the program and evaluate its accuracy. The next step was to use **ChemLith** to vary layer thickness, layer ordering and polymer species to guide preparation of optimal samples. For a multilayer system with known polymer materials, one needs to optimize the layer order and layer thickness first. All six possible layer orders can be evaluated, though not all may be easily accessible due to solubility interference. A good starting point for optimizing layer thickness is to set equal layer thickness, for example, 40 nm per layer, then systematically explore the effects of layer thickness and thickness ratio in subsequent optimization steps. **ChemLith** is also used to compare different sets of polymer species; in particular, it predicted *a priori* that the PMMA/PEC/PAN system would be a significant improvement over the PMMA/PPC/PAN system (see details in Chapter 7).

3.4 X-PEEM data acquisition

Similar to STXM, there are three modes of data acquisition in X-PEEM, i.e. single energy images, spectra and image sequences (or stacks). The latter two modes both record a sequence of images over a range of photon energies, with the only difference being that the averaged intensity of each image versus photon energy is saved in the case of spectra,

whereas the complete image is saved in the case of image sequences. This section presents the principles and examples for these data acquisition modes.

3.4.1 Single energy images

Initially the X-PEEM (ALS PEEM2 on beamline 7.3.1) microscope should be tuned properly, which involves optimizing mask and chopper settings, aperture size, radiation polarization and flux, Ti filter, lens voltages, and distance and tilting of the microscope with respect to the sample. The tuning is crucial to achieve high quality images. Then for the acquisition of a single energy image, more parameters need to be defined by the user, such as the photon energy, the dwell time (usually 1 - 10 seconds), flat field and dark current corrections, data binning operations (from original 1024 x 1024 pixels of a full image or part of this image to reduced pixel numbers by integer scaling factors (2 x 2, 4 x 4 binning)), and the size of the image, which is determined by drawing a box, or area-of-interest (AOI), onto a larger field-of-view (FOV) image. **Figure 3.12**

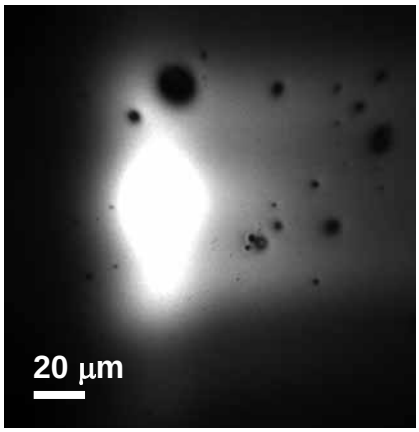

Figure 3.12 X-PEEM image at 288.5 eV of sample PMMA/Si (the defects are shown on the film areas where the film charges thus preventing photoemission).

shows a large scale image recorded at 288.5 eV of a thin PMMA film spin coated on a Si substrate, denoted as PMMA/Si. The image was acquired at the PMMA characteristic energy, so that the best image contrast could be achieved. Because the FOV of Fig. 3.12 is large, the beam spot, i.e. the illumination area, can be completely viewed. Uniform images can be obtained by working at larger magnification in one of the evenly illuminated areas. The magnification is set by the sample and intermediate lens voltages. There are two ways to identify the physical size, i.e. FOV, of an image. One is to measure the FOV using a micrometer to measure the displacement as one feature of the sample is moved from one side of the screen to the other. The other way is to obtain the FOV from the graphs in **Figure 3.13**, using the voltages of the microscope [MHI&02]. The *y* axis of the graph is the FOV in microns for the whole area of the CCD. The *x* axis represents the voltage of the magnification (intermediate) lens as a fraction of the sample voltage. The two plots on the graphs represent the high and low magnification operational modes of the microscope. The higher curve is used when the projector lens is turned off, while the lower curve is used when the intermediate lens is set at a fixed value (0.9 of the sample voltage), and in this case the *x* axis represents the value of the projector lens voltage as a function of the sample voltage. The lower graph is a magnification of the lower portion of the upper graph. For Figure 3.12, the sample and microscope lens voltages settings are 15.0/11.46/10.38/10.58 kV (sample/objective/transfer/intermediate), thus the ratio of intermediate/sample equals to 10.58/15 = 0.71, which corresponds to a FOV of ~180 μm, as shown in Figure 3.13 upper graph. The FOV derived using Figure 3.13 typically has an estimated uncertainty of 10%.

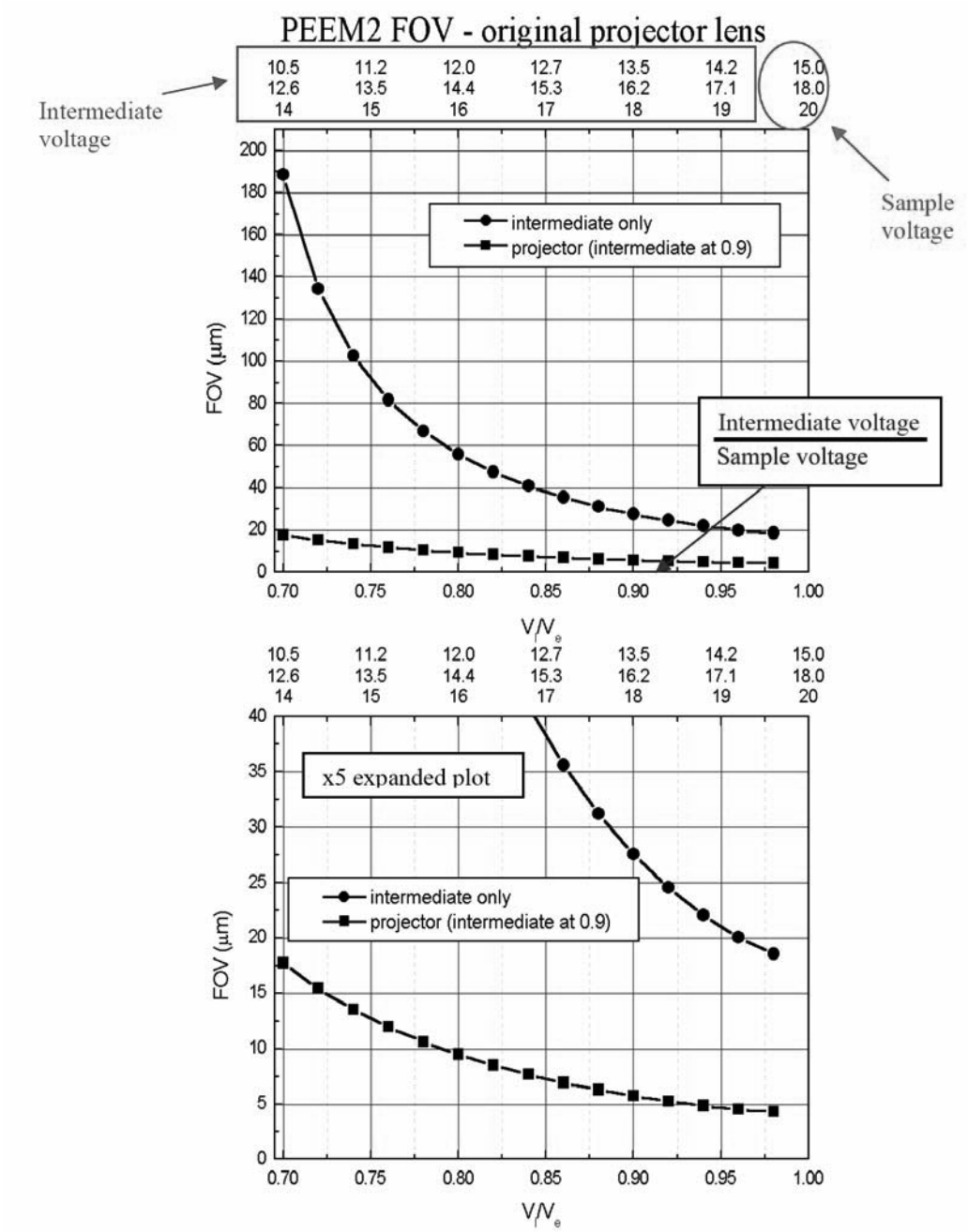

Figure 3.13 PEEM2 FOV as a function of voltages [MHI&02].

3.4.2 Spectra

X-PEEM spectra are the averaged intensity of photoemitted electrons in a user defined area of the sample as a function of incident photon energy. Although the total

electron yield (TEY) signal in X-PEEM is linearly proportional to the photoabsorption, the raw spectra are distorted by the incident photon (I_0) profile, and energy dependent detector response (bolometry). Thus the raw spectra need to be divided by the I_0 spectrum to get the correct shape and spectral details. A convenient way to obtain the I_0 spectrum is to use the X-PEEM spectrum of clean Si. The I_0 spectrum can also be recorded from a scratch on the sample which exposes the Si substrate, or it can be acquired externally using an HF-etched Si wafer as a separate sample. It is important to mount the Si I_0 wafer at the same height and tilt so that the energy scale is identical.

Figure 3.14 shows the raw X-PEEM spectrum of PMMA/Si and the spectrum after normalization to the I_0 spectrum of HF-etched Si. After normalization, the shape of the PMMA spectrum is closer to the true spectrum; however the shape of the low energy

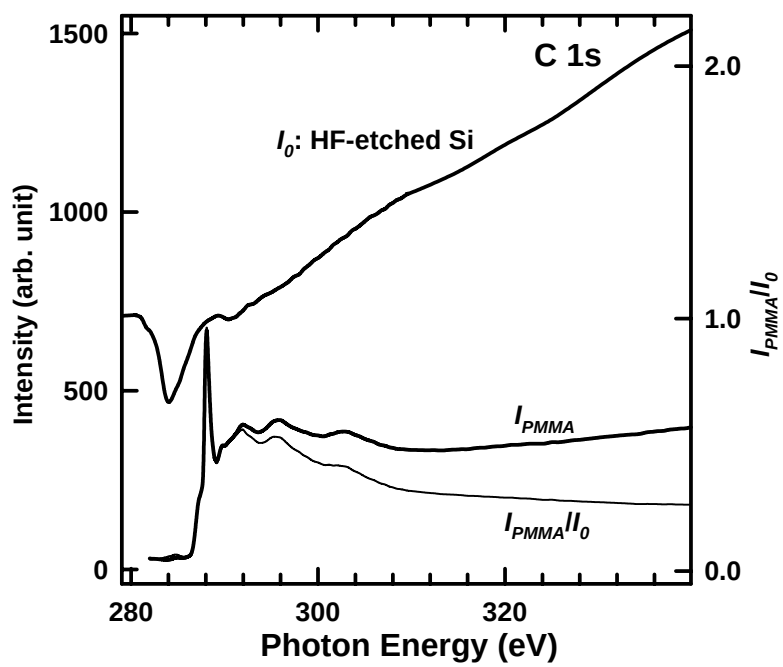

Figure 3.14 Raw X-PEEM spectrum of PMMA/Si and the spectrum after normalization to the I_0 spectrum of an HF-etched Si wafer with Ti filter in.

region is almost not influenced. The X-PEEM spectra are actually acquired on the fly without saving images, as is done in image sequence mode.

3.4.3 Image sequences (stacks)

X-PEEM image sequences (stacks) consist of a series of images recorded over a set of photon energies. They can be the full image (1024 x 1024 pixel or ~2 Mb/image) or only a user defined sample area, i.e. the area of interest (AOI). All images of the image sequence are acquired with the same dwell time (~0.5-5 seconds/image). The spectral

Table 3.2 Comparison of radiation dose in STXM and X-PEEM for an image sequence

Mode	Typical dose rate (MGy/s)	Typical time to record an image sequence of 100 images (s)	Total dose (MGy)
STXM	200	0.1	20
X-PEEM	5	100	500

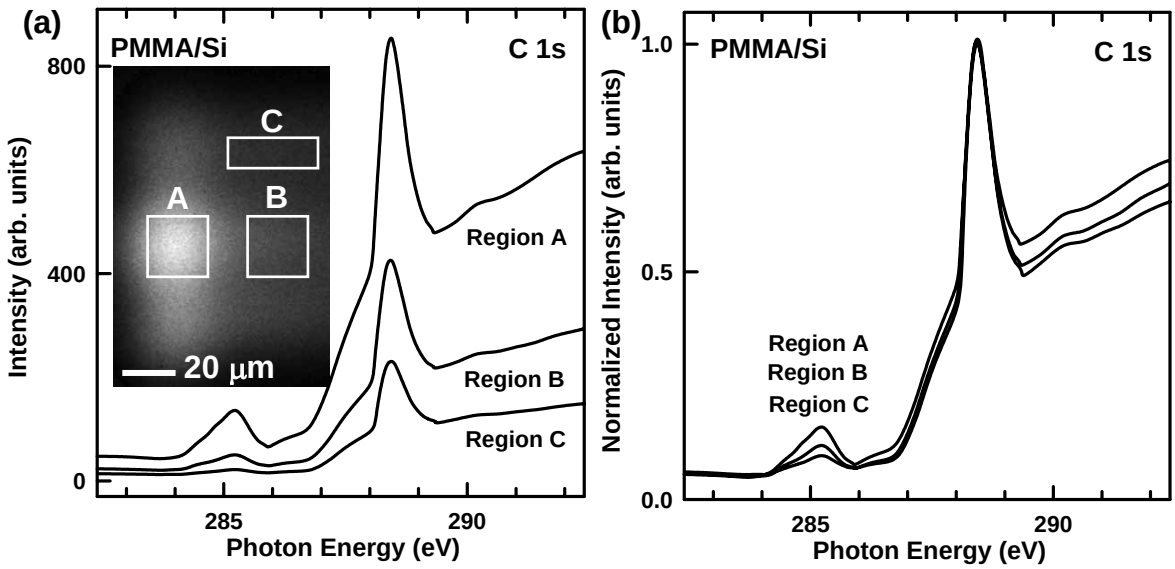

Figure 3.15 X-PEEM image sequence of sample PMMA/Si, the inset is a selected sequence image at 288.5 eV, in which three different illumination regions are selected to derive spectra, (a) NEXAFS spectra derived in the three regions, (b) spectra of (a) normalized to the maximum peak intensity.

regions with varying increments of photon energy are defined by the user. Compared to STXM, radiation damage is much more of a challenge in X-PEEM due to higher integrated doses associated with the much longer dwell times even although the dose rate is relatively lower in X-PEEM than STXM, as shown in **Table 3.2**. For radiation sensitive polymer samples, the dwell time should be as short as possible, and the minimum number of energy points should be used. Typically only the fine spectral features of interest are acquired with small energy steps (0.1 eV is the minimum due to the limited energy resolution of the beamline), and other regions are recorded with coarse steps (0.5 or 1.0 eV). **Figure 3.15** presents the spectra derived from an image sequence scan of a PMMA/Si sample. The inset is a selected sequence image at 288.5 eV, in which three illumination regions are selected from which spectra were extracted. The brighter the selected region, the higher the spectral intensity, and the more the radiation damage.

3.5 Quantitative dose-damage analysis in X-PEEM

For quantitative dose-damage evaluation in X-PEEM, it is necessary to know the spot size and shape of the beam on the sample, the incident flux, and the sampling depth. Together these parameters let one determine the absorbed dose, and the fraction of that absorbed dose contributing to the detected signal. With the pseudo exit slit installed, the sample is not illuminated uniformly. To circumvent this problem, we only measure the regions over which illumination is relatively uniform. The key to accurate dose evaluation is to determine the correct flux corresponding to the measured region. For PEEM imaging of heterogeneous samples, the X-PEEM images are typically divided by a heavily

smoothed (55 point Savitsky-Golay) version of the image to correct for uneven illumination.

3.5.1 Determination of the absolute I_0 profile

In X-PEEM spectroscopy and qualitative applications, the I_0 spectrum is obtained from an HF-etched Si wafer, which produces strong signals due to low work function, good conductance and large quantum efficiency. In addition, the TEY signal of HF cleaned Si is more accurate compared to the native Si oxide surface because there is no oxygen absorption and other contamination. Although this approach gives the correct shape of the I_0 spectrum, it is not sufficient to derive the absolute photon flux because the relationship between the absolute photon flux and TEY is not known. For quantitative dose-damage analysis in X-PEEM, the absolute photon flux for the full beam was calibrated using a Si photodiode (IRD AXUV-100) [KPC&03] as the sample. When the photodiode is exposed to photons of energy greater than 1.12 eV, electron-hole pairs are created with each pair generated by 3.6 eV photon energy. The quantum efficiency is almost 100% in the soft X-ray regime (100 - 1000 eV) as reported in the technical information of the product [KPC&03]. The signal recorded under identical beamline conditions as the polymer sample and the HF-etched Si wafer was measured to determine the total intensity of the beam as a function of photon energy over the whole monochromator. In order to remove higher order light, a Ti filter (200 nm, Lebow) was used for the C 1s and N 1s measurements, but it was removed for the O 1s measurements.

Figure 3.16a shows the I_0 spectra normalized to 400 mA ring current from a HF-

etched Si wafer and a Si photodiode both with and without Ti filter. The I_0 spectral shape is generally similar between HF-etched Si and Si photodiode except different at higher photon energy for the former, which can be further corrected by dividing by the Si photo absorption profile [HGD93]. The Ti filter effectively removes the higher order light at the C 1s edge and reduces the overall intensity by about two before 450 eV (Ti 2p absorption edge). The photo current generated by the photodiode was measured by Keithley 428 current amplifier; then it was converted to electrons per second; and multiplied by 3.6 eV to get the total energy equivalent of the photon beam. Finally the calculated value was divided by a bolometry correction. This accounts for the linear increase in yield as the

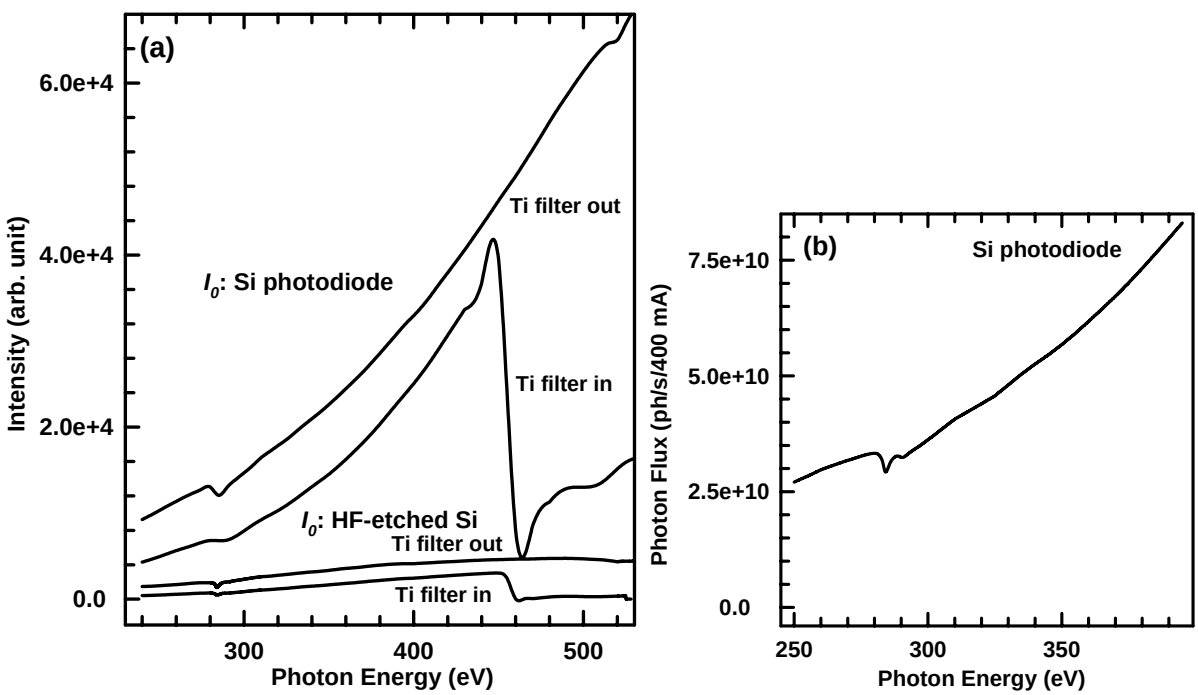

Figure 3.16 X-PEEM I_0 spectra and determined absolute photon flux, (a) I_0 spectra obtained from a HF-etched Si wafer and a Si photodiode both with and without Ti filter, (b) absolute total photon flux determined by a Si photodiode with Ti filter in. (X-PEEM conditions: aperture: 20 µm; mask: -10.7; chopper: 13.5; polarization: linear; flux scale: -0.5; voltage (kV) for the sample and the lenses: 15.0/11.4/10.38/9.9)

photon energy increases (*E*/3.6 is the number of electrons generated). **Figure 3.16b** presents the absolute total photon flux determined by a Si photodiode with Ti filter applied under the same X-PEEM conditions as those of the radiation damage studies in this work. Compared to HF-etched Si, the Si photodiode has excellent stability and spatial homogeneity of quantum efficiency, large dynamic range (over eight orders of magnitude), UHV compatibility and it is robust even in the presence of gases [KPC&03]. When Si photodiode is used to determine the absolute photon flux, the photo current was measured directly from the photodiode with X-PEEM microscope and ion gage off. Thus X-PEEM images were not recorded.

3.5.2 Photon flux in the measured region

The beam spot shape and intensity distribution were also measured on a clean HF-etched Si under the same beamline and X-PEEM lens conditions as used for the damage quantitation studies, and with low magnification of the X-PEEM, such that all the photons that passed through the 'exit slit' were imaged, as shown in **Figure 3.17a**. When dose-damage measurements were made on specimens, the system was carefully adjusted so that the image from the sample was similar to that measured for clean Si **Figure 3.17b**. Then the intensity in the region contributing to the damage signal was measured and the incident flux corresponding to that region was evaluated from the ratio of the signal in that similar area, to the total signal in Fig. 3.17b (i.e. ratio of signal in the highlighted square to all the signal in Fig. 3.17a, using the ratio of intensities of Fig. 3.17b and Fig. 3.17a as an intermediate). Image corrections (flat field and dark current) were applied

during data acquisition.

The beam spot shape is reproducible at the C 1s edge, as can be seen by comparing the images in Figure 3.12, 3.15, 3.17 and 3.18a at different photon energies in the C 1s edge for different samples. However, when the photon energy was increased to

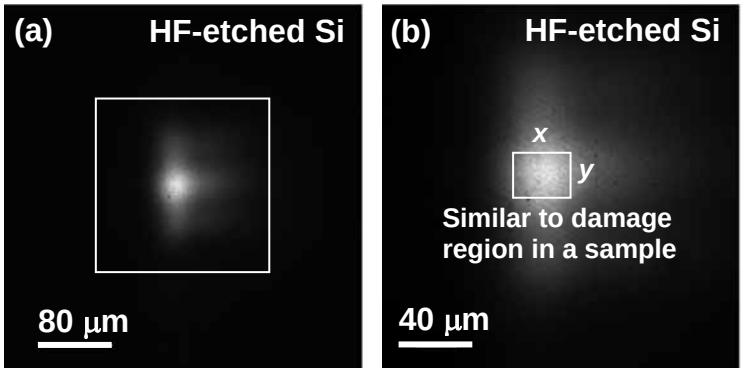

Figure 3.17 X-PEEM images used to determine the photon flux in a measured sample region, (a) Si I_0 image recorded at 230 eV with sample and lens voltages (kV): 15.0/11.4/10.38/9.9, total image signal = 3.3 x 10^8, signal fraction of (b) in (a) = 0.92, (b) Si I_0 image recorded at 230 eV with sample and lens voltages (kV): 15.0/11.4/10.38/10.5, signal fraction of highlighted square in (b) = *s*. (Other same X-PEEM settings: Ti filter: in; aperture: 20 μm; mask: -10.7; chopper: 13.5; polarization: linear; flux scale: -0.5)

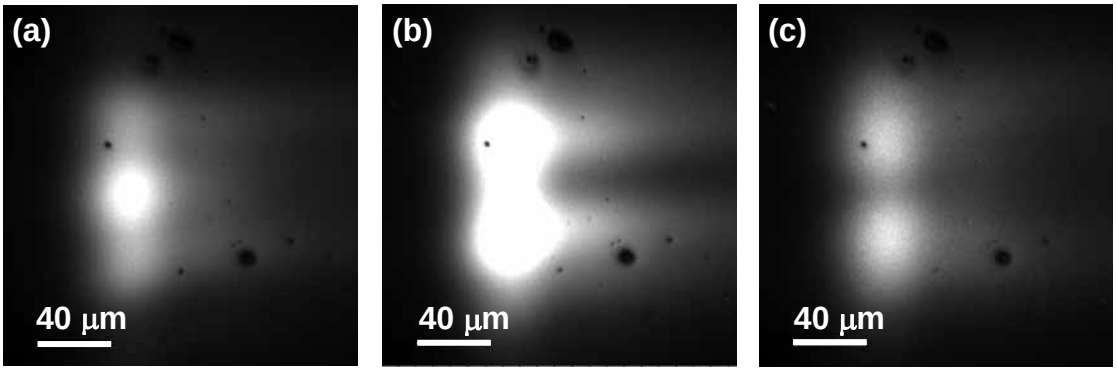

Figure 3.18 X-PEEM beam spot shape as a function of photon energy on a PMMA/Si sample, (a) image recorded at 300 eV, (b) at 401 eV, and (c) at 532 eV. (X-PEEM conditions: Ti filter: in; aperture: 20 μm; mask: -10.7; chopper: 13.5; polarization: linear; flux scale: -0.5; sample and lens voltages (kV): 15.0/11.46/10.38/10.58)

that for the N 1s (401 eV) and O 1s (532 eV) regions, the beam spot became a two maximum shape, as shown in **Figure 3.18b** and **c**, due to diffraction of the X-rays by the exit slit. In these cases, new Si reference images at the corresponding photon energies need to be acquired in order to quantify the photon flux in the measured sample regions at these energies. Since the quantitative critical doses were mainly derived from C 1s studies, this does not affect the results of this thesis.

3.5.3 Critical dose

All X-PEEM data acquired were scaled to 400 mA ring current to compensate for the actual ring current (200 - 400 mA in multi-bunch, 10 - 30 mA in 2-bunch mode) during any given measurement. The data used in determining the critical dose was obtained by repetitively acquiring X-PEEM spectra on the same region. After a specific exposure time on the sample at a fixed photon energy or a range of photon energies, the NEXAFS spectrum of the damaged region was acquired using a very short image stack so that the stack acquisition time was negligible compared to the exposure time. The spectra were averaged from all pixels of the damaged region or from specific sub-regions if the damage region was not uniform. Then the quantitative damage was evaluated in terms of peak area change. Flat field and dark current corrections were directly applied during data acquisition.

The absolute dose or dose rate in X-PEEM was derived from the incident photon flux, the damage region, and the sampling depth. Although soft X-rays penetrate many hundreds of nanometers, the X-PEEM sampling depth is only ~10 nm for polymer

materials as measured for PS/Si (see Chapter 5) and confirmed in a recent X-PEEM study of adsorption of albumin on PS/PMMA [LHR&06]. The dose absorbed by the sample in X-PEEM is based on equation 3.1 with the photon flux in the measured region determined as above. A complete expression of the dose for sample PMMA/Si damage is:

$$a = \frac{I_0 \frac{\text{Actual ring current}}{400} \times 0.92 s(1 - e^{-\text{OD1}\cdot d})Et}{xyd\rho} \qquad (3.6)$$

where I_0 is the absolute total photon flux of 400 mA ring current at the exposure energy E, i.e. value read in Fig. 3.16b, 0.92 is the signal fraction of Fig. 3.17b in Fig. 3.17a, s is the signal fraction of the highlighted square in Fig. 3.17b, which is similar to the damage region in the PMMA/Si sample, OD1 is the linear absorption coefficient (i.e. OD per nm) of PMMA from STXM, d is the sampling depth (10 nm), t is the exposure time, x and y are dimensions of the damage region box, and ρ is the polymer density.

As for evaluation of dose-damage data recorded by STXM, the critical dose was derived from X-PEEM dose-damage data by analysis with the postulated first order kinetics of section 3.2. Specifically, the critical dose for damage in X-PEEM was determined by plotting the peak area (or the change of peak area) of the selected features as a function of radiation dose a. Then the critical dose for the sample material was derived from fitting the data points to Equation 3.4 (or Equation 3.5). The alternative linear format of the data can also be used to find the critical dose. In order to compare among different experimental conditions and samples, it is more convenient to plot the normalized peak area as a function of radiation dose. In some cases, when the dose-peak area profile was far from the damage saturation, the saturation level was estimated based

on extrapolation using this functional form. The X-PEEM data analysis was also carried out in an Excel™ worksheet, slightly modified from the STXM worksheet in Fig. 3.7.

Figure 3.19 presents an example of X-PEEM dose-damage analysis for radiation damage of PMMA at 300 eV. The inset image indicates the selected illumination area for radiation damage quantitation. **Figure 3.19a** plots a sequence of C 1s spectra of PMMA in the damage region, and **Figure 3.19b** plots the normalized peak area at 288.4 and 285.1 eV as a function of radiation dose. The plots were fit with equation 3.4, from which the critical doses were determined. The critical dose evaluated from C=O functional group damage was 98(15) MGy, while the critical dose evaluated from C=C functional group generation during radiation damage was 76(11) MGy, comparable with that of 67 (10) MGy determined in STXM in section 3.2.

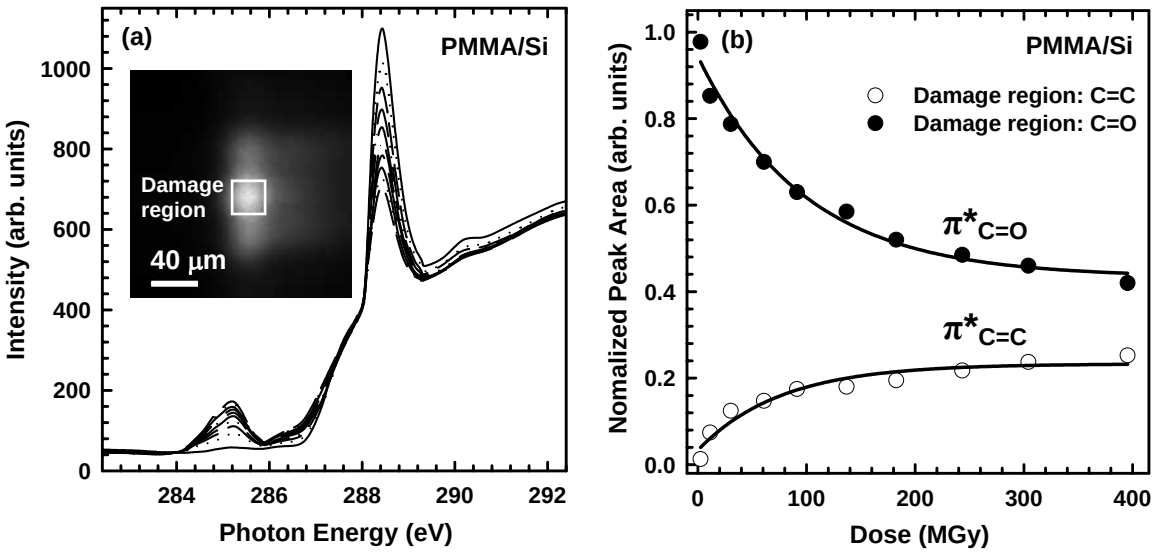

Figure 3.19 X-PEEM dose-damage analysis of radiation damage in PMMA/Si, (a) sequence of C 1s spectra of PMMA in the damage region, the inset X-PEEM image indicates the illumination region monitored for radiation damage, (b) plots of the normalized peak area of the C 1s $\rightarrow \pi^*_{C=O}$ (288.4 eV) and the C 1s $\rightarrow \pi^*_{C=O}$ (285.1 eV) transitions as a function of radiation dose for the damage region.

3.6 Sample preparation

3.6.1 STXM sample preparation

3.6.1.1 Spin coating

(1) Samples for NEXAFS spectroscopy and radiation damage

Table 3.3 lists all the polymers studied in this work. For the author and collaborator synthesized polymers, routine characterization with NMR, IR and Mass spectrometry (MALDI-TOF) and purification was performed. Other purchased polymers were used without further purification. In order to carry out NEXAFS spectroscopy and critical dose measurements, free standing single layer films or films on Si_3N_4 windows (750 μm × 750 μm window back-etched into a 7.5 mm × 7.5 mm × 200 μm silicon wafer chip coated with 75 nm of Si_3N_4, Silson Ltd.) were prepared for most polymers by a spin coater (Speedline Technologies P6204) according to the procedure outlined below. First, 1% (w/w) solution of each polymer was prepared in suitable solvents, as shown in Table 3.3. Then ~ 50 μl of each solution was spun cast (3000 or 4000 rpm, 30 s) onto a clean substrate, i.e. mica, slide cover glass or Si_3N_4 window, of about 2.5 cm × 2.5 cm surface. Most polymer films could be used directly after spin coating. However, several polymers needed vacuum heating at 70°C for 0.5 hr to remove all solvents and form more uniform films. These include PAN, PPC and PEC. The vacuum oven is shown in **Figure 3.20**. It consists of a heater, a support heat plate and a vacuum desiccator pumped by a cryo-trapped turbo pump backed by an oil mechanical pump. Subsequently, all formed films were cut into 3 mm × 3 mm pieces on the substrate surfaces except the Si_3N_4 windows, and then floated onto milli-Q or distilled deionized (DDI) water. A piece of the polymer

Table 3.3 Polymer film samples with selected preparation conditions for STXM and X-PEEM measurements

Polymer film samples	Molecular weight (polymer source)	Fabrication method	Coating application conditions					Coating drying conditions		
			Solvent	Conc.	Substrate	Speed (rpm)	Time (s)	Pressure (torr)	Temp. (^oC)	Time (hr.)
PMMA	312K (Polymer Source Inc.)	Spin coating + water floating	Toluene	1%	Mica	3000	30	atm.	r.t.	> 1
PMMA*	,,	Spin coating	,,	,,	Si wafer	4000	,,	,,	,,	,,
PMMA+Inhibitor	,,	Spin coating + water floating	,,	1%+0.05%	Mica	3000	,,	,,	,,	,,
Au/PMMA/Au	,,	Spin coating + water floating + Au sputtering coating	,,	1%	Mica	,,	,,	,,	,,	,,
PAN	150K (Aldrich)	Spin coating + water floating	DMF	,,	,,	,,	,,	< 0.01	70	0.5
P(MMA-co-AN)	--- (Synthesized)	Solvent casting	Toluene	~ 1%	Si_3N_4 window	---	---	atm.	r.t.	> 1
PECA	--- (Commercial)	,,	,,	,,	,,	,,	,,	,,	,,	,,
		Microtomy of a chunk	---							
PUR	~1500 (Synthesized)	Spin coating + water floating	DME	1%	Mica	3000	30	atm.	r.t.	> 1
PU	--- (Synthesized)	Hydraulic press + microtomy	---							
PPC	250K (Empower Materials)	Spin coating + water floating	1,4-dioxane	1%	Glass	3000	30	atm.	r.t.	> 1
PEC	150K (Empower Materials)	,,	,,	,,	,,	,,	,,	,,	,,	,,
		Solvent casting	TCE	~ 1%	Si_3N_4 window	---	---	atm.	r.t.	> 1
PET	--- (Commercial)	Spin coating + water floating	HFIP	1%	Mica	3000	30	,,	,,	,,
		Microtomy of a chunk	---							
PS	1.07M (Polymer Source Inc.)	Spin coating	Toluene	1%	Si_3N_4 window	4000	30	atm.	r.t.	> 1
PS*	,,	,,	,,	,,	Si wafer	,,	,,	< 0.01	140	4
Fg	--- (Calbiochem)	Solvent casting	DDI water	0.1%	Si_3N_4 window	---	---	atm.	r.t.	> 1
Fg*	,,	Spin coating	,,	,,	Si wafer	4000	30	,,	,,	,,
PAN-embed-PMMA	Same as single layers	PAN particles embedded in PMMA toluene solution, dry, + microtomy	---							
PMMA-blend-PAN	,,	Spin coating, first PMMA, then PAN, + water floating	Same as single layers							
PMMA/PAN	,,	Spin coating, first PAN, then PMMA, + water floating	,,							
PMMA+Inhibitor/ PAN+Inhibitor										
PMMA/PUR/PAN	,,	Spin coating, first PAN, then PUR, last PMMA, + water floating	,,							
		Hydraulic press, microtomy, + manual overlapping each layer	---							
PMMA/PPC/PAN	,,	Spin coating, first PAN, then PPC (PEC), last PMMA, + water floating	Same as single layers except PPC (PEC) coating drying under vacuum at 70 ^oC							
PMMA/PEC/PAN	,,									

*: X-PEEM samples; ,,: ditto; ---: no data or not applicable.

PMMA: polymethylmethacrylate; Inhibitor: 4-methoxyphenol or Irganox 1076; PAN: polyacrylonitrile; DMF: N,N-dimethylformamide; PUR: polyurethane, DME: 1,2-dimethoxyethane, PU: polyurea; PPC: polypropylene carbonate; PEC: polyethylene carbonate; TCE: trichloroethylene; PET: polyethylene terephthalate; HFIP: Hexafluoro-2-propanol; PS: polystyrene; Fg: fibrinogen; DDI: distilled deionized.

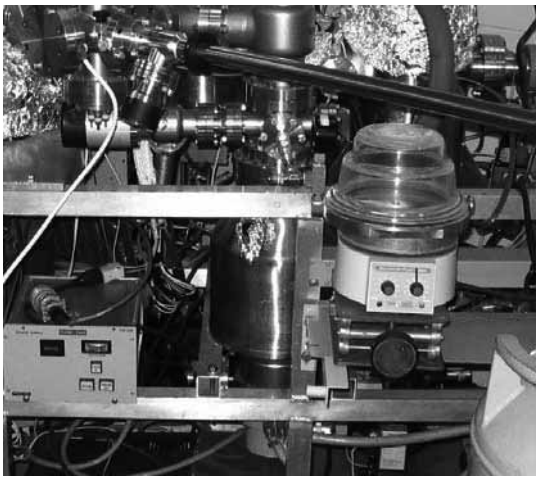

Figure 3.20 Setup of the vacuum oven.

film was transferred to a degreased hexacomb grid or a TEM grid, and used for STXM measurements. The samples on Si_3N_4 windows were used in STXM directly. The single layer films formed under the above conditions were 30 - 40 nm thick, according to STXM measurements.

(2) Samples for chemically selective patterning

Free standing multilayer polymer films for chemically selective patterning were fabricated by successive spin coating using almost the same procedure as above, including drying conditions, of the single layer. The solvents and order of the layers were carefully selected so that the solutions applied on top of an already deposited layer would not dissolve the previously fabricated polymer film. Reversing the spin coating sequence can result in a non-uniform micro phase-separated film due to re-dissolution of the already deposited layer as was found in the preparation of the PMMA/PAN bilayer system in Chapter 6.

For trilayer systems, the PMMA/PAN bilayer was augmented with a third polymer. Three generic polymer materials were examined as the third layer: non-aromatic polyurethane, polyurea, and polycarbonate. Non-aromatic polyurethanes are less commercially available than aromatic polyurethanes. In addition, the molecular weights of commercial polyurethanes and polyurethanes synthesized by the author are too low to form spin coated films. For non-aromatic polyureas, including those the author synthesized, no suitable organic solvents could be found, so spin coating was not possible. Non-aromatic polycarbonates, specifically PPC and PEC, were finally demonstrated as the best candidates to form the third layer.

3.6.1.2 Solvent casting

For polymers not suitable for spin coating, or for NEXAFS reference spectra, the solvent casting method was used. A few milligrams of each sample were dissolved in a solvent to make ~ 1% solution, then a drop of this solution was placed on a Si_3N_4 window and allowed to dry. When the solvent was evaporated, polymer particles and film pieces were deposited on the Si_3N_4 surface. Then the window with sample was used in STXM directly. Thin, uniform thickness regions sufficiently large (up to 10 μm) for quantitative radiation damage studies could be found on these otherwise heterogeneous samples.

3.6.1.3 Microtomy

For polymers not suitable for spin coating or solvent casting, such as PECA, PU and PET, microtomy was used to cut polymer chunks or hydraulically pressed pellets to

form films of 60 nm thickness or as thin as possible at the Electron Microscopy Facility of the Faculty of Health Sciences, McMaster University. The cut films were placed onto TEM grids for STXM measurements. This method was also used to fabricate multilayer films, such as PMMA/PUR/PAN, by manual overlapping each microtomed layer; however, the prepared multilayer films were not uniform and were easily broken during fabrication. In addition, microtomy was a very useful technique to prepare cross sections of multilayer films in order to investigate the morphology and chemistry of the interface, as illustrated in Fig. 3.9.

3.6.2 X-PEEM sample preparation

3.6.2.1 Spin coating

Similar spin coating procedures as that used for STXM samples were used to prepare X-PEEM samples (see details in Table 3.3), except that the substrate was native oxide Si (111) wafer (Wafer World, Inc.), which had previously been degreased with trichloroethylene (Aldrich, +99.5% pure), acetone (Burdick & Jackson, HPLC grade), and methanol (Caledon), then rinsed under running milli-Q water. Another spin coater (Specialty Coating Systems, P-6708) was also used for sample preparation. In order to make uniform films to determine the X-PEEM sampling depth, PS thin films on Si wafers were annealed at 140°C for 4 hours under pressure < 10^{-2} torr using the vacuum oven.

3.6.2.2 HF-etched Si wafer

The substrates used to measure the incident flux (I_0) in X-PEEM were the same Si

wafers cleaned as described above. Just prior to use they were exposed for 30 s to 10% HF (Aldrich, 48 wt.% in water, 99.99+%)[1], then rinsed under running deionized water. The HF-etched Si was mounted on the same sample puck, next to the sample of interest and brought under vacuum within 10 minutes of preparation.

3.6.3 Characterization of samples

3.6.3.1 Optical microscope

Two optical microscopes, a Leica DMR visible light microscope (VLM) and an Olympus BX51 microscope, were used to preview STXM samples on grids and Si_3N_4 windows. The VLM microscope at the ALS 5.3.2 beamline has an encoded stage with the same coordinate system as STXM. This can greatly decrease the time needed to find regions of interest, as well as providing complementary information. **Figure 3.21**

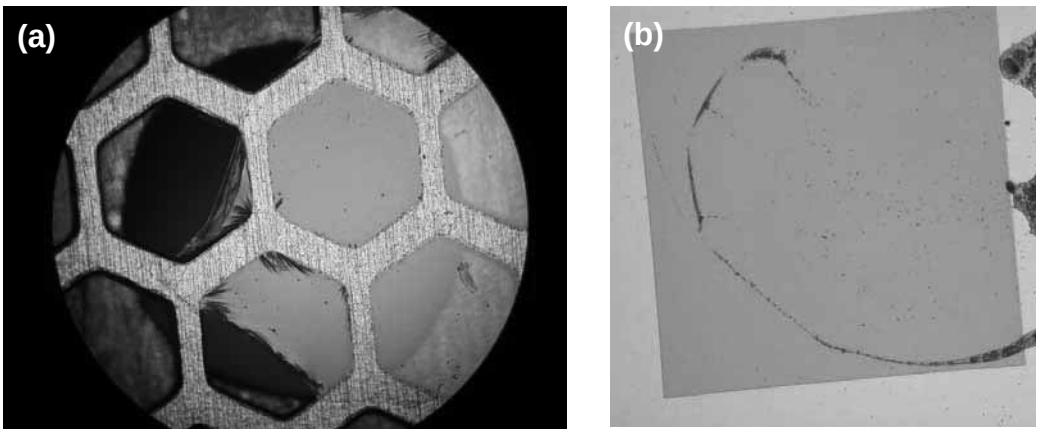

Figure 3.21 VLM images of STXM samples, (a) a free standing PMMA/PAN bilayer polymer film on a hexacomb grid placed on the sample holder, (b) a solvent cast biphenyl sample on a Si_3N_4 window.

[1]HF etching was done in ALS chemical lab 2233 while wearing protective clothing. A glutothinate safety pad was at hand.

illustrates two VLM images of STXM samples, the left image showing a free standing PMMA/PAN bilayer polymer film on a hexacomb grid placed on the sample holder, and the right image showing a solvent cast biphenyl sample on a Si_3N_4 window.

3.6.3.2 Atomic Force Microscopy

Atomic force microscopy (AFM) (Quesant Q-scope 350 or Veeco Digitial Instruments Nanoscope III) was used to determine the layer thickness of the spun coated polymer films on hard substrates, such as Si wafer or cover glass slide. A sharp tweezer tip was used to scratch through the polymer film and the profile across the scratch was checked by AFM. **Figure 3.22** shows an AFM image of a PMMA/PAN bilayer film on a cover glass slide scratched by a tweezer. The Z direction (height) profile indicated ~ 80 nm thick for the bilayer film, which was consistent with the thickness derived by STXM for a similar sample. For a series of PS films prepared to determine the X-PEEM sampling depth, non-contact mode AFM was used to measure the film thickness in the region of a scratch. The results showed that the PS films made by spin coating (4000 rpm) of toluene solutions of concentrations of 0.05%, 0.1%, 0.5%, 1% and 2% had thicknesses of 2(0.2), 5(0.5), 16(2), 32(3), and 95(9) nm respectively.

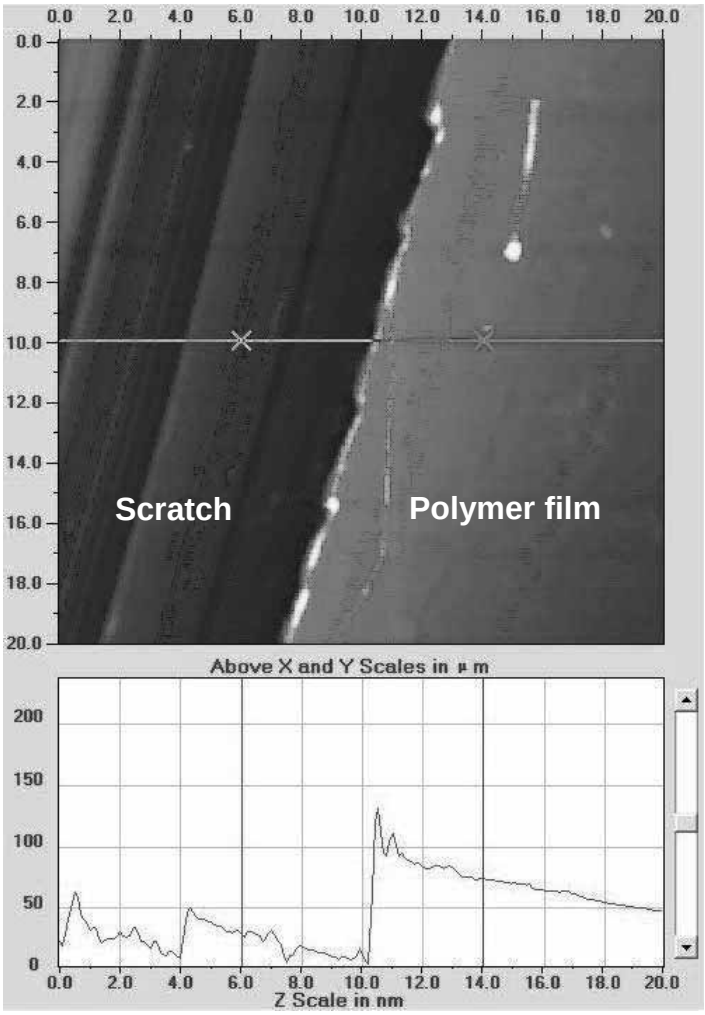

Figure 3.22 AFM image of a PMMA/PAN bilayer film on a cover glass slide scratched by a sharp tweezer tip. The top panel shows the topography of the polymer film and the scratch. The bottom panel shows the Z direction (height) profile corresponding to the line drawn in the center of the top image.

3.6.3.3 Transmission Electron Microscopy

TEM (JEOL-1200EX) was used in this work for two purposes. The first was as a complementary imaging method to STXM to obtain higher spatial resolution, as shown in Fig. 3.9a. The second was as an alternate radiation source to compare the radiation damage effect of electron and soft X-rays. **Figure 3.23** shows two series of spots created

on a PET film by a TEM electron beam of 80 kV at 4 and 88 pA/cm^2 beam current density with the indicated exposure times. The sample was then imaged by STXM at 288.2 eV, i.e. the C 1s $\rightarrow \pi^*_{C=O}$ transitions of PET.

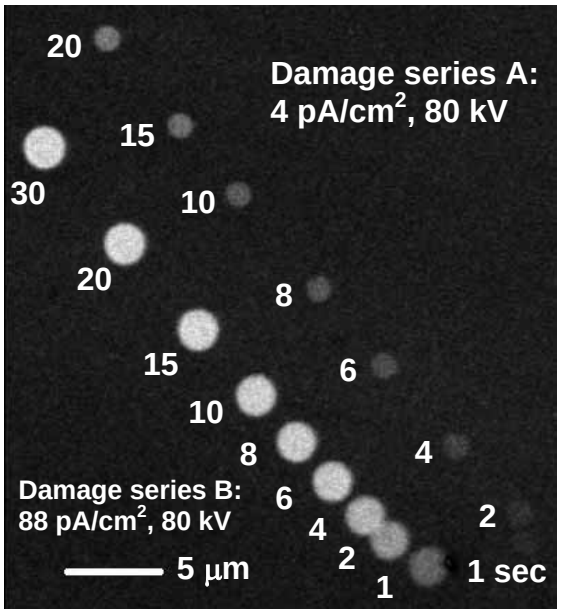

Figure 3.23 STXM image at 288.2 eV of a PET film, which was damaged by TEM at two series of spots with designated exposure times and beam current density.

Chapter 4

Characterization of polymer radiation damage

This chapter presents experimental results of soft X-ray radiation damage to polymers created and characterized by STXM. Selected polymer materials, such as PAN, PECA, PPC, PEC, PET etc. were investigated in detail in terms of radiation induced changes to their NEXAFS spectra and damage rates. A comparison of these polymers and a discussion about the radiation damage are presented at the end of this chapter.

4.1 Introduction

In the past decade, with the growing applications of synchrotron soft X-rays in organic materials analysis [KJH95, KT96, AUT02, KOJ&02, ZZS&04a, FAM&03], the accompanied radiation damage effects on synthetic and natural polymers have been studied increasingly [TTM&94, TUM&96, YWH99, TM00]. Damage to some synthetic polymers by soft X-rays has been studied qualitatively and quantitatively through near edge X-ray absorption spectroscopy [RHA&97] and spectromicroscopy [ZJL&95, BJ02, CUA02]. In our group, soft X-ray damage to a variety of organic materials, including polymers and molecular compounds, has been studied in the past several years. The results show that phenyl groups are much more radiation resistant than any other functional groups. In order to investigate damage for a more complete collection of organic materials with different damage rates, selected non-aromatic and aromatic organic materials are studied in this thesis. Specifically, in Chapter 4 selected polymers, including polyacrylonitrile (PAN), poly(ethyl cyanoacrylate) (PECA), poly(propylene

carbonate) (PPC), poly(ethylene carbonate) (PEC), and polyethylene terephthalate (PET), were investigated by measuring damage rates and associated changes in NEXAFS spectra to show diverse damage rates of different functional groups in different chemical environments. More examples are presented in Chapter 5 in comparison to X-PEEM studies of radiation damage effects, including polymethylmethacrylate (PMMA), polystyrene (PS), and protein (fibrinogen (Fg)). Chapter 5 also includes a detailed comparison between radiation damage in STXM and X-PEEM, evaluated for PMMA. Damage of protein is illustrated in fibrinogen. In addition, studies of some extremely damage-resistant organic materials, such as polyphenyls (e.g. hexaphenylbenzene) and fused ring aromatic systems (e.g. coronene), are included in appendix A of this thesis. Radiation damage to these compounds requires very high radiation doses and thus long exposure times. As a result, in the current STXM microscopes, a side effect is dissociation deposition of carbon contaminants on the surface of these samples, which often prevents accurate measurements. Methods to overcome this problem are proposed in the last chapter as future work.

The radiation damage effects observed can be mainly classified into three categories: (i) chemistry change without mass loss, such as PAN, (ii) chemistry change with small mass loss, such as PECA, and (iii) chemistry change with large mass loss, such as PPC and PEC. These behaviors have been characterized by comparing the C 1s, N 1s and O 1s NEXAFS spectra of the damaged and undamaged polymers, and determining the critical doses of each polymer at the C 1s edge. The experimental details have been presented in Chapter 3.

4.2 NEXAFS of radiation damaged non-aromatic polymers and kinetics

4.2.1 Chemistry change without mass loss

The C 1s NEXAFS spectra of undamaged and heavily radiation damaged PAN is discussed in more detail in Chapter 6 [WSH&07]. Here the C 1s spectra are plotted in **Figure 4.1a** and compared with N 1s edge spectra. The major NEXAFS features of the undamaged PAN and new features created in the damaged PAN at both C 1s and N 1s edges are listed in **Table 4.1**. The main spectroscopic changes in the C 1s edge due to

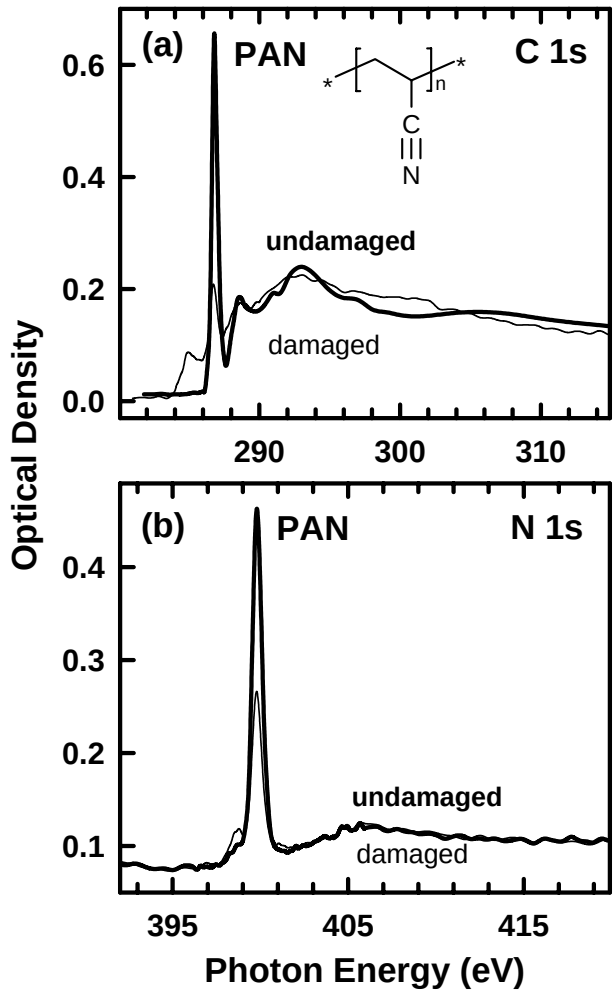

Figure 4.1 Near edge X-ray absorption fine structure (NEXAFS) spectra of undamaged and damaged PAN, (a) C 1s edge, the PAN structure is shown, and (b) N 1s edge.

Table 4.1 The major NEXAFS features of undamaged PAN, PECA, PPC, PEC and PET polymers and new features created in the damaged polymers.

PAN		PECA		PPC (PEC)		PET		Assignment
Udmg	**Dmg**	**Udmg**	**Dmg**	**Udmg**	**Dmg**	**Udmg**	**Dmg**	
C 1s								
	285.1		285.1		285.0 (285.0)	284.8		$\pi^*_{C=C}$
						285.4		$\pi^*_{C=C}$
					286.6 (286.6)		286.5	$\pi^*_{C=O}$
286.8		286.7						$\pi^*_{C\equiv N}$
		288.6			288.5 (288.5)	288.2		$\pi^*_{C=O}$
288.7								$2\pi^*_{C\equiv N}$
						289.1		$\pi^*_{C=C/C=O}$
				289.4 (289.4)				$(CH_2\text{-}O) \rightarrow \pi^*_{C=O}$
						290.2		$\pi^*_{C=C/C=O}$
				290.4 (290.4)				$\pi^*_{C=O}$
293.0		293.0		293.5 (293.4)		293.1		σ^*_{C-C}
				297.4 (297.5)		296.4		σ^*_{C-C}
	301.0							$\sigma^*_{C=N}$
				304.5 (304.4)		303.5		$\sigma^*_{C=O}$
306.0								$\sigma^*_{C\equiv N}$
N 1s								
	398.7		398.7					$\pi^*_{C=N}$
			399.0					$\pi^*_{C=C}$
399.8		399.8						$\pi^*_{C\equiv N}$
405.7		405.8						$\sigma^*_{C\equiv N}$
O 1s								
					531.2 (531.2)		531.2	$\pi^*_{C=O}$
		532.1			532.0 (532.0)	531.6		$\pi^*_{C=O}$
				532.9 (532.8)				$\pi^*_{C=O}$
		534.8			534.7 (534.7)	534.1		$(O\text{-}CH_2) \rightarrow \pi^*_{C=O}$
				536.4 (535.9)				$(O\text{-}CH_2) \rightarrow \pi^*_{C=O}$
						537.1		$\pi^*_{C=C/C=O}$
		541.3		540.3 (539.5)		540.5	539.7	σ^*_{C-O}
		547.2		548.4 (548.4)		546.5		$\sigma^*_{C=O}$

Udmg = undamaged; Dmg = damaged.

radiation damage are: a significant decrease of the strong C 1s $\rightarrow \pi^*_{C\equiv N}$ transition at 286.8 eV; development and increase of the C 1s $\rightarrow \pi^*_{C=C}$ transition at 285.1 eV arising

from C=C bonds formed in the damaged polymer backbone; development of a rather broad feature between 284 and 286 eV which may contain the C 1s $\rightarrow \pi^*_{C=N}$ transitions of C=N double bonds from transformed nitrile groups; and almost no decrease of the intensity in the C 1s continuum. These observations suggest when PAN is radiation damaged it primarily undergoes structural changes without mass loss since the intensity of the continuum must decrease if there is mass loss upon radiation damage [CUA02].

Figure 4.1b compares the N 1s NEXAFS spectra of undamaged and substantially damaged PAN. The spectroscopic signatures of damaged PAN at the N 1s edge are: a decrease of the N 1s $\rightarrow \pi^*_{C\equiv N}$ transition at 399.8 eV; and a rise of a pre-edge feature at 398.7 eV, which is attributed to the formation of C=N double bonds, similar to the N 1s $\rightarrow \pi^*_{C=N}$ transitions in polyaniline [MGB&99] and in quinoid molecules [BFB&00]. This is consistent with expectations that the position of $\pi^*_{C=N}$ is at lower energy than that of $\pi^*_{C\equiv N}$. Note in the associated C 1s spectrum of damaged PAN, a weak broad peak appears at 301 eV which is likely associated with C 1s $\rightarrow \sigma^*_{C=N}$ transitions in the transformed material. Similar N 1s spectroscopic changes were also observed in soft X-ray radiation damage to amide functional groups in amino acids [ZFW&04] and proteins (results presented in Chapter 5). In those systems the new pre-edge features were attributed to the formation of C-N multiple bonds or C=N bonds with different local environments. Note that a high resolution Auger yield study has assigned a feature at 398.9 eV to N 1s $\rightarrow \pi^*_{C=C}$ transitions in solid acrylonitrile [GBK&02]. However, this has a different origin from the pre-edge feature created in damaged PAN as discussed in detail in section 4.2.2. As at the C 1s edge, the N 1s continuum of PAN doesn't change at all upon radiation

damage, which confirms the damage is not accompanied by loss of nitrogen, at least in the dose regime explored.

Based on C 1s and N 1s NEXAFS spectroscopy, mechanisms of soft X-ray damage to PAN are proposed in **Figure 4.2**. The initial process involves hydrogen transfer from the polymer backbone to the C≡N group after C-H cleavage so that C=C double bond is formed in the main chain and C≡N group is reduced to C=N group. The next step involves cyclization of the reduced C=N group with a neighbor C≡N (or C=N) group through nucleophilic reaction, which is more energetically favorable than other possible pathways, such as cleavage of the C=N group from the main chain, bond dissociation within the C=N group, further hydrogenation of C=N etc; in the mean time, aromatization is achieved by more C-H cleavages and loss of hydrogen in the main chain. Finally heavily damaged PAN may develop a fused-pyridine structure. A similar mechanism of cyclization and aromatization was proposed and accepted for thermal degradation of PAN [XMW97, KWS&98]. These mechanisms are consistent with the NEXAFS observations of soft X-ray damage to PAN: a somewhat broad feature at 285.1 eV in the C 1s spectrum actually due to C 1s $\rightarrow$ π^*(pyridine ring) with feature broadening due to a nitrogen atom present in the pyridine ring and delocalization of the fused rings; a broad feature at 301 eV due to C 1s $\rightarrow$ $\sigma^*_{C=N}$(pyridine ring); a pre-edge feature at 398.7 eV in the N 1s spectrum essentially attributed to N 1s $\rightarrow$ π^*(pyridine ring) localized on nitrogen; almost no mass loss with respect to carbon and nitrogen. The C 1s and N 1s inner shell excitation spectra of gas phase pyridine have the same π^* and σ^* features [HSH&85] as those of the heavily damaged PAN, as shown in **Figure 4.3**.

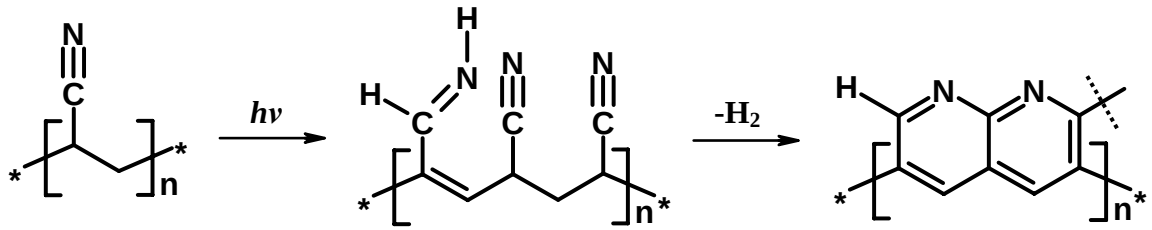

Figure 4.2 Proposed mechanisms of soft X-ray damage to PAN.

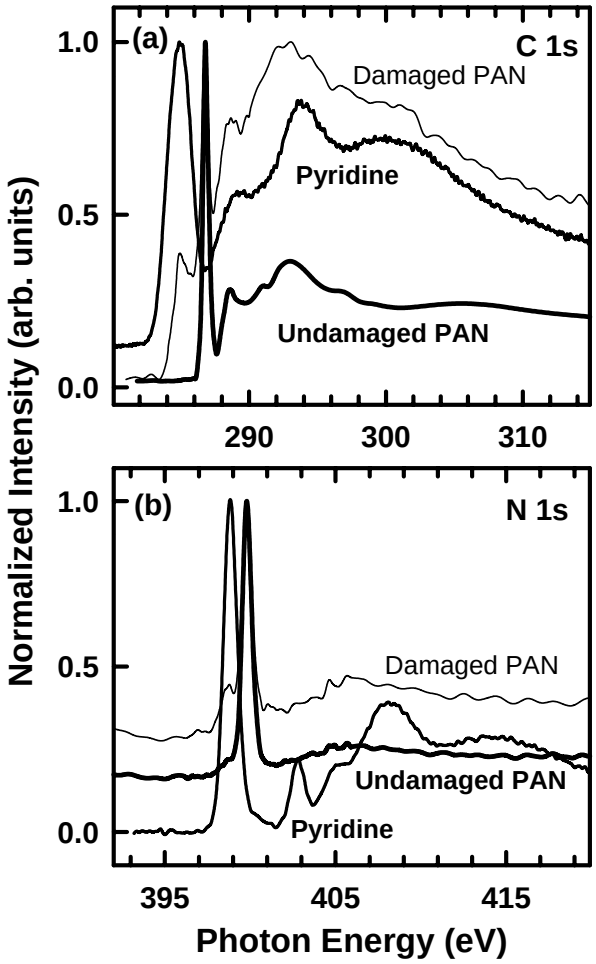

Figure 4.3 NEXAFS spectra of undamaged and damaged PAN compared to inner shell electron energy loss spectra (ISEELS) of gas phase pyridine [HSH&85], (a) C 1s edge, and (b) N 1s edge. For clarity each spectrum was normalized to the maximum intensity of each spectrum.

Figure 4.4 plots the normalized optical density at 286.8 and 285.1 eV as a function of radiation dose for PAN after exposure at 300 eV in the C 1s continuum. The

300 eV photon energy was chosen to ensure low absorbance variation during irradiation and thus a near constant dose rate. The analysis energy at 286.8 eV monitors the damage of C≡N functional groups, while the energy at 285.1 eV tracks the growth of the C=C groups. The extrapolated OD after infinite dose (i.e. OD_∞) was estimated for both energies. In order to compare between samples with different layer thicknesses, the normalized OD was derived by dividing the signal at 286.8 eV by the initial OD (i.e. OD_0), and by dividing the signal at 285.1 eV by the extrapolated OD_∞ with the background level at 285.1 eV of zero dose subtracted from both values in advance because of feature growth during radiation damage. The normalized OD_∞ values at 285.1, 286.8 and 300 eV for PAN are listed in **Table 4.2**, with uncertainties estimated from reproducibility of 5 different measurements. The data points of normalized OD versus

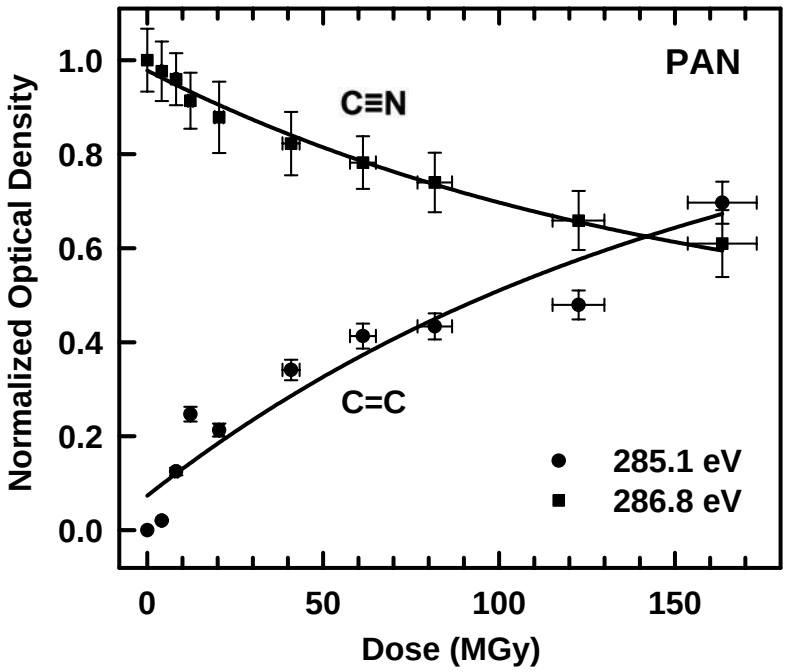

Figure 4.4 Plots of the normalized optical density at 286.8 and 285.1 eV as a function of radiation dose for PAN by exposure at 300 eV with dose rate 409 MGy/s.

Table 4.2 Photon energies and normalized infinite optical densities used to monitor and quantify chemistry changes and mass loss for PAN, PECA, PPC, PEC and PET polymers.

Polymer	C=C growth		C≡N damage		C=O damage		Mass loss	
	Energy (eV)	OD_∞*	Energy (eV)	OD_∞*	Energy (eV)	OD_∞*	Energy (eV)	OD_∞*
PAN	285.1	1.00(5)	286.8	0.40(5)	---	---	300	1.00(5)
PECA	285.1	1.00(5)	286.7	0.55(5)	288.6	0.60(5)	300	0.85(5)
PPC (PEC)	285.0	1.00(5)	---	---	290.4	0.15(5)	300	0.35(5)
PET	---	---	---	---	288.2	0.45(5)	---	---

OD_∞*: the normalized optical density after infinite dose.

radiation dose (Figure 4.4) were fit to equation 3.4. From the fitting equations critical doses were obtained. The errors of the dose evaluation and the measured OD are both around 6%. However, other factors, such as differences of the detector efficiency, the uncertainty in the estimated OD_∞ (or the normalized OD_∞) also contribute systematic errors. The total uncertainty in the critical dose is estimated to be about 15% in these STXM radiation damage studies. The final derived critical dose is 150 ± 23 MGy at 286.8 eV for C≡N functional group damage and it is 157 ± 24 MGy at 285.1 eV for C=C group growth. Since the difference between these two critical doses is much smaller than the uncertainties of the data, this indicates that the kinetics for C≡N functional group damage and C=C functional group growth are comparable. The proposed damage mechanisms in Figure 4.2 also imply the rate of decrease of the C≡N group and the rate of growth of the C=C group should be comparable. In addition, during soft X-ray radiation damage, a large number of electrons, radicals or ions are generated, which may dominate the damage process and mask any subtle intrinsic differences of damage rates of different functional groups.

4.2.2 Chemistry change with small mass loss

The C 1s NEXAFS spectra of undamaged and heavily radiation damaged PECA are shown in **Figure 4.5a**. The damage was made by exposure at 300 eV for a series of radiation doses (exposure times). The main NEXAFS features of undamaged PECA and new features created in damaged PECA in C 1s, N 1s and O 1s edges are summarized in Table 4.1. As shown in Chapter 6 [WSH&07], both functional groups, i.e. C≡N and C=O, were non-selectively damaged in terms of a similar intensity decrease of the C 1s $\rightarrow$ $\pi^*_{C\equiv N}$ transition at 286.7 eV and the C 1s $\rightarrow$ $\pi^*_{C=O}$ transition at 288.6 eV. Other spectroscopic changes caused by radiation damage are: an increase of the C 1s $\rightarrow$ $\pi^*_{C=C}$ transition at 285.1 eV due to formation of C=C bonds in the main chain; and a decrease of the intensity in the C 1s continuum regime. These changes indicate that PECA undergoes both structural changes and a small amount of mass loss upon radiation damage.

Figure 4.5b presents the corresponding N 1s NEXAFS spectra of undamaged and heavily damaged PECA. The spectroscopic signatures of damaged PECA at the N 1s edge are: the decrease of the N 1s $\rightarrow$ $\pi^*_{C\equiv N}$ transition at 399.8 eV; the creation of two pre-edge features at 398.7 and 399.0 eV respectively (see Fig. 4.5b inset for details); and decrease in the intensity of both the pre-edge and the N 1s continuum. The pre-edge feature at 398.7 eV is attributed to the formation of C=N double bonds. The other pre-edge feature at 399.0 eV may be attributed to N 1s $\rightarrow$ $\pi^*_{C=C}$ transitions, an analogy to the transition at 398.9 eV in solid acrylonitrile [GBK&02]. This suggests damaged units with structures C=C-C=N or C=C-C≡N are produced during radiation damage of PECA. If the C=C group is adjacent to a C=N or C≡N group, N 1s $\rightarrow$ $\pi^*_{C=C}$ transitions may occur due to

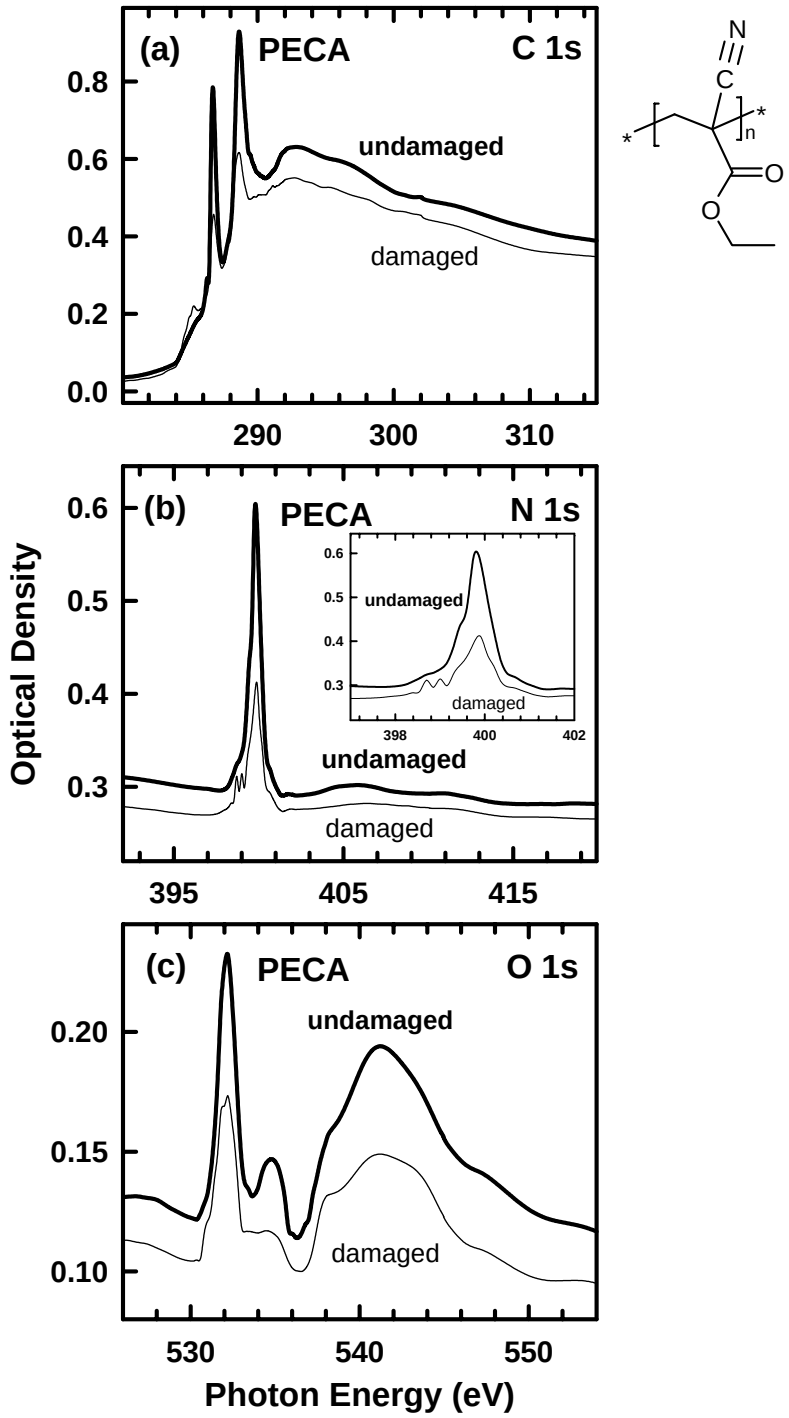

Figure 4.5 NEXAFS spectra of undamaged and radiation damaged PECA, (a) C 1s edge, the PECA structure is shown beside (a) to the right, (b) N 1s edge (the inset shows the details of the undamaged and the damaged spectra), and (c) O 1s edge.

interaction of the $\pi^*_{C=C}$ and $\pi^*_{C=N}$ or $\pi^*_{C\equiv N}$ moieties through partial delocalization of $\pi^*_{C=C}$ on to the nitrogen atom. The formation of these two structures is due to reduction of polymer main chain and C≡N groups through C-H cleavage and elimination of the ester side groups. However, a depolymerization mechanism plus further radiation damage may also account for these structures. Actually industrial purification of alkyl cyanoacrylate monomers is achieved by depolymerization of poly(alkyl cyanoacrylate) at elevated temperatures of 150-190 ^{o}C [A01]. In this case, the depolymerization is believed to be introduced by radiation damage instead of thermally since the temperature-rise can be neglected during irradiation by soft X-rays in STXM (see Chapter 6 for details), and this was confirmed by measuring the temperature using a thermal couple upon irradiation. Although PAN damage also involves the creation of C=C double bonds in the damaged polymer, it is cyclization and aromatization that create a fused-pyridine ring structure, and as a result the N 1s $\rightarrow \pi^*_{C=N}$ and N 1s $\rightarrow \pi^*_{C=C}$ are merged into one π^* feature. Also in contrast to PAN, the N 1s continuum of PECA does decrease significantly, so there is appreciable mass loss of N-containing fragments during radiation damage. In conclusion, since the intensity of the created N 1s $\rightarrow \pi^*_{C=C}$ transition is small, the depolymerization process should be a small fraction of the total radiation damage.

The corresponding O 1s NEXAFS spectra of undamaged and heavily damaged PECA are presented in **Figure 4.5c**. The spectroscopic variations of damaged PECA at the O 1s edge are dominated by: a decrease of O 1s $\rightarrow \pi^*_{C=O}$ transition at 532.1 eV; an even larger decrease of O 1s (OEt) $\rightarrow \pi^*_{C=O}$ transition at 534.8 eV; and relatively large intensity decreases in both the pre-edge and the O 1s continuum compared to that at the C

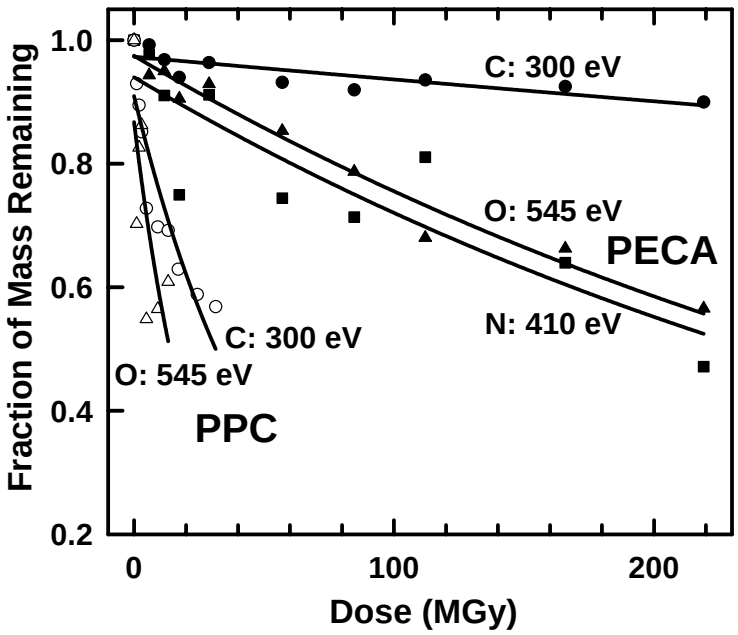

Figure 4.6 Plots of the fraction of elemental mass remaining as a function of radiation dose for PECA and PPC. The fraction of elemental mass remaining was evaluated from NEXAFS spectra of undamaged and a series of radiation damaged polymers at 300 eV for carbon, 410 eV for nitrogen and 545 eV for oxygen.

1s edge. The fraction of elemental mass remaining as a function of radiation dose for PECA is presented in **Figure 4.6**. The fraction of elemental mass remaining was evaluated at 300 eV for carbon, at 410 eV for nitrogen and at 545 eV for oxygen. The difference of the optical density at each of these energies and its corresponding pre-edge as a function of radiation dose was used as a scale of elemental mass remaining. From the plots of PECA in Figure 4.6, the fraction of mass loss of oxygen and nitrogen are comparable in heavily damaged samples, up to 50%, much greater than that of carbon about 15%. This indicates there is selective mass loss of the pendant functional groups in PECA. Mass loss in the damaged PECA is probably due to loss of the degraded side chains in the form of small fragments and molecules, such as $HCOOC_2H_5$, HOC_2H_5, CO_2,

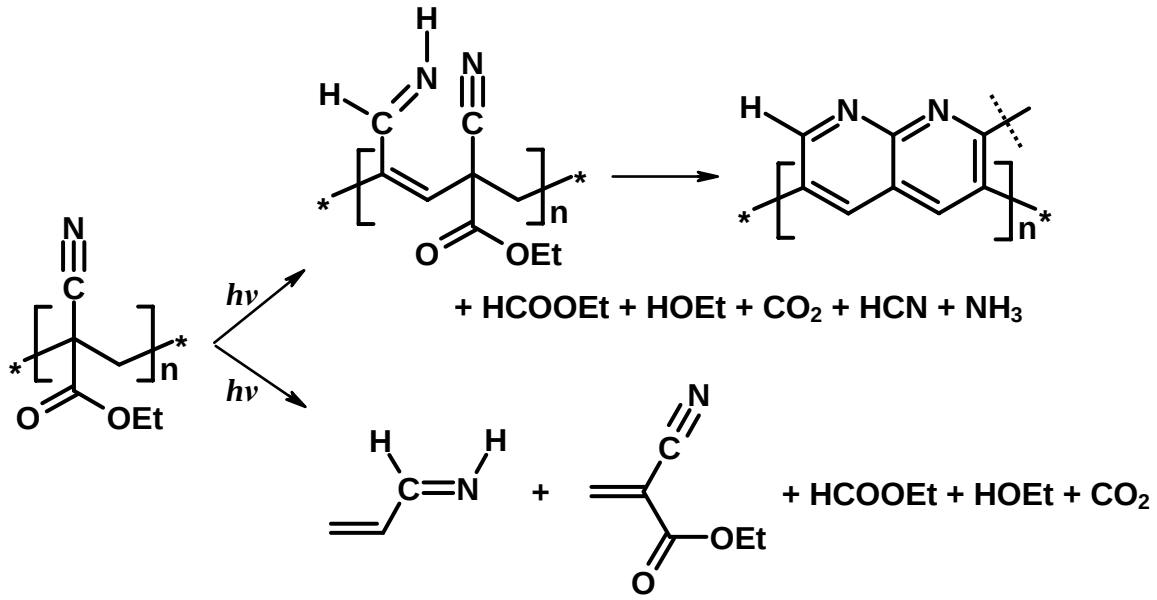

Figure 4.7 Proposed mechanisms of soft X-ray damage to PECA.

HCN, NH_3, as well as de-polymerized monomers. Note NH_3 (or $-NH_2$) is favorably transformed from a terminal imine group after the formation of a pyridine or a fused-pyridine. Much larger mass loss in the O 1s and N 1s edges than that of C 1s edge implies that species containing higher percentages of oxygen or nitrogen, such as CO_2, NH_3, HCN, may be generated more than other species. The mechanisms of soft X-ray damage to PECA are summarized in **Figure 4.7**. The damage of the ester group and the polymer main chain is similar to soft X-ray damage of PMMA [TTM&94, TUM&96, WSH&07].

Figure 4.8 illustrates quantitative determination by STXM of the critical doses in PECA at different analysis energies in the C 1s edge. **Figure 4.8a** includes four optical density images at 285.1, 286.7, 288.6 and 300 eV, respectively, of a uniform region of a PECA film that was damaged in the indicated pattern of nine 0.6 μm x 0.6 μm (10 x 10 pixel) pads where each successive pad was subjected to a systematically increased dose

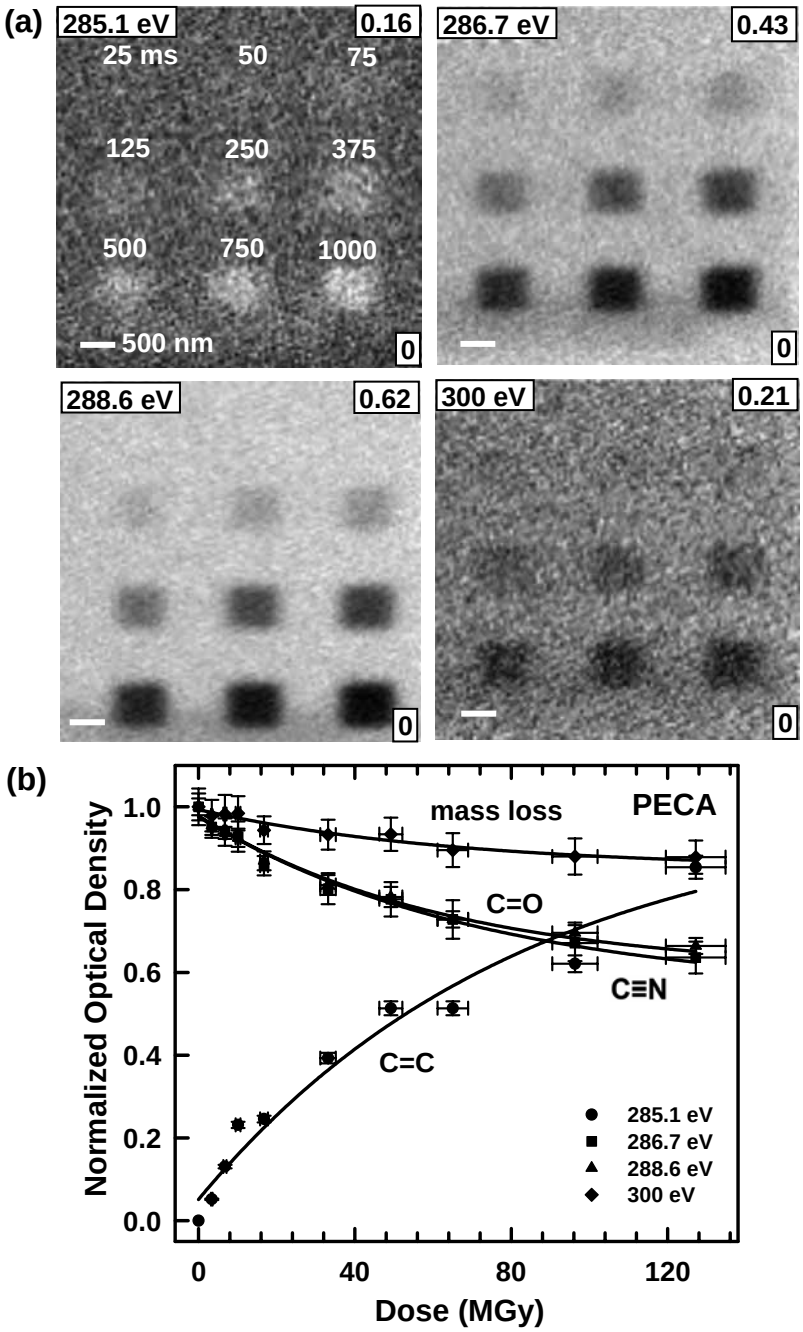

Figure 4.8 STXM damage of PECA. (a) Patterns created in an initially undamaged, free standing PECA thin film by exposure at 300 eV using a 10x10 pixel, 0.6 μm x 0.6 μm raster scan with the indicated per-pixel dwell times and the dynamic dose rate exponential decaying from 137 to 127 MGy/s, and imaged at 285.1, 286.7, 288.6 and 300 eV. The numbers in the lower and upper right boxes are the optical density scale. Note that these images are actually relative optical density images, which were converted from their transmission images by normalized to the maximum intensity of each individual transmission image. (b) Plots of the normalized optical density at 285.1, 286.7, 288.6 and 300 eV as a function of radiation dose for PECA after exposure at 300 eV.

by adjusting the dwell time per pixel between 25 and 1000 ms. At these four energies the chemical changes of damaged PECA, such as growth of C=C groups, damage of C≡N groups, damage of C=O groups and mass loss, were clearly visualized. **Figure 4.8b** plots the normalized optical density at each of these four energies as a function of radiation dose for PECA after exposure at 300 eV in the C 1s continuum. Since mass loss occurs when irradiating PECA at 300 eV, there is a concomitant decrease of the absorbance. The absorbed dose was calculated according to the dynamic OD at 300 eV using equation 3.3. The data points of each series of normalized OD versus radiation dose were fit to equation 3.4 with extrapolated OD_∞, as shown in Table 4.2 as normalized OD_∞. The final derived critical dose is 83 ± 12 MGy at 285.1 eV for the C=C group growth, 73 ± 11 MGy at 286.7 eV for the C≡N group damage, 63 ± 9 MGy at 288.6 eV for C=O group damage, and 66 ± 10 MGy at 300 eV for mass loss. Since the difference between some of these critical doses is comparable or larger than the uncertainties of the data, the difference in critical dose may be related to the difference in chemistry changes in PECA upon radiation damage. However, the magnitude of difference is still small. The derived critical doses of PECA are comparable to those of PMMA [ZJL&95, CUA02, WSH&07], and the spectroscopic changes are also similar, especially the C 1s continuum decrease due to mass loss. However the C≡N group damage of PECA is much faster than that of PAN, indicating that the same functional group can have different damage rates in different chemical environments. This indicates that there are damage mechanisms involving synergy in changes at the C≡N and C=O groups in PECA.

4.2.3 Chemistry change with large mass loss

The C 1s and O 1s NEXAFS spectra of undamaged and heavily radiation damaged PPC are shown in **Figure 4.9**. The damage was made by systematic exposure at 300 eV. The main NEXAFS features of undamaged PPC and new features created in damaged PPC in C 1s and O 1s edges are listed in Table 4.1. For the C 1s spectra in **Figure 4.9a**, the damaged PPC was characterized by a number of spectroscopic changes.

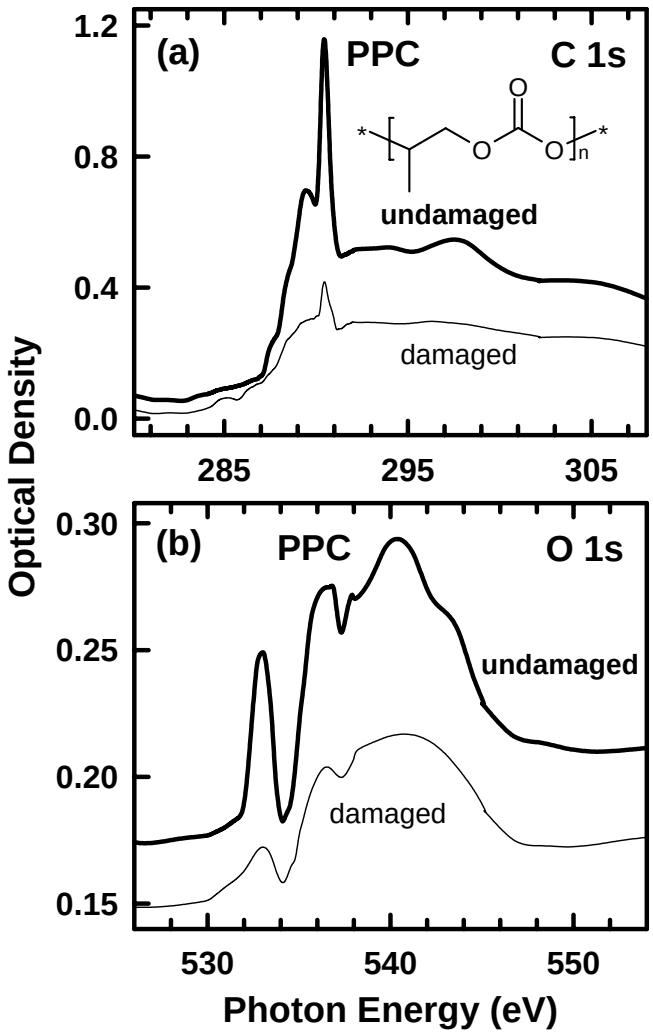

Figure 4.9 NEXAFS spectra of undamaged and radiation damaged PPC, (a) C 1s edge, the PPC structure is shown, and (b) O 1s edge. The dose for the damaged spectra is about 30 MGy (1.5 a_c).

Some features decrease during radiation damage, including: a large decrease of the C 1s $\rightarrow \pi^*_{C=O}$ transition of the carbonate group at 290.4 eV; decrease of the shoulder peak at 289.4 eV, which is probably due to C 1s (CH_2-O) $\rightarrow \pi^*_{C=O}$ transitions; a large decrease of the continuum and some associated broad σ* features at 293.5, 297.4 and 304.5 eV; and a decrease of the pre-edge. Some new and weak features are created during radiation damage, including: a peak growth at 285.1 eV, due to C 1s $\rightarrow \pi^*_{C=C}$ transitions of the C=C bonds created in the main chain; a feature rise at 286.6 eV, due to C 1s $\rightarrow \pi^*_{C=O}$ transitions of isolated carbonyl groups generated by scission of the two C-O bonds of the initial carbonate groups; and a feature increase at 288.5 eV, due to C 1s $\rightarrow \pi^*_{C=O}$ transitions of the ester groups generated by one C-O bond scission of the carbonate groups. The large decrease in continuum intensity shows that PPC damage not only involves extensive chemical structural changes, but also significant mass loss, probably due to lots of polymer backbone scissions which lead to emission of small molecules and fragments.

The O 1s NEXAFS spectra of undamaged and heavily radiation damaged PPC are presented in **Figure 4.9b**. Similar to the C 1s edge, the O 1s edge was also characterized by several spectroscopic changes. Some features decrease during radiation damage, including: a large decrease of the resonant features (O 1s $\rightarrow \pi^*_{C=O}$ transitions at 532.9 eV and O 1s (CH_2-O) $\rightarrow \pi^*_{C=O}$ transitions at 536 eV); a large decrease of the O 1s continuum and associated broad σ* features at 540.3 and 548.4 eV; and a decrease of the pre-edge. Some new and weak features are created upon radiation damage, including: broadening of the low energy side of the π* feature at 532.9 eV, due to two new features, one at 531.2

eV attributed to O 1s → $\pi^*_{C=O}$ transitions of isolated carbonyl groups, and the other at 532.0 eV assigned to O 1s → $\pi^*_{C=O}$ transitions of created ester groups; and a small feature rise at 534.7 eV, due to O 1s (CH_2-O) → $\pi^*_{C=O}$ transitions of created ester groups. The O 1s spectroscopic changes are consistent with those at the C 1s edge. The elemental mass loss of PPC was also evaluated. The fraction of elemental mass remaining as a

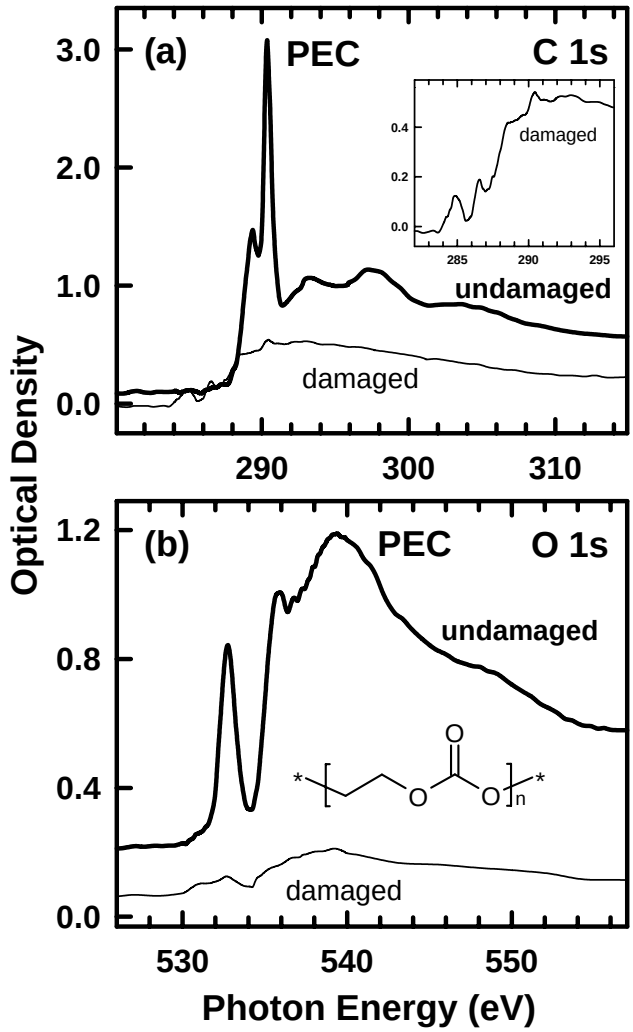

Figure 4.10 NEXAFS spectra of undamaged and completely radiation damaged PEC at, (a) C 1s edge, the inset shows an expanded view of the lowlying region of damaged PEC, and (b) O 1s edge. The PEC structure is shown. The dose for the damaged spectra is about 80 MGy (4.0 a_c).

function of radiation dose for PPC is plotted in **Figure 4.6**. The plots show that PPC undergoes large mass loss of both carbon and oxygen although a little more mass loss of oxygen is observed under the same radiation dose. This is different to PECA, which has much less carbon mass loss during radiation damage. This is consistent with PECA having an all carbon backbone whereas PPC has both C and O in the polymer backbone.

The C 1s and O 1s NEXAFS spectra of undamaged and completely damaged PEC are shown in **Figure 4.10**. The main NEXAFS features of undamaged PEC and new features created in damaged PEC in C 1s and O 1s edges are listed in Table 4.1. Due to the same generic chemical structure and composition of PEC and PPC, similar NEXAFS spectroscopic changes were observed in damaged PEC. The inset to Fig. 4.10a more clearly shows the lowlying C 1s features created by radiation damage.

As for the O 1s edge of PPC, the same NEXAFS spectroscopic changes were observed in the O 1s spectrum of damaged PEC (see Table 4.1 for feature assignments).

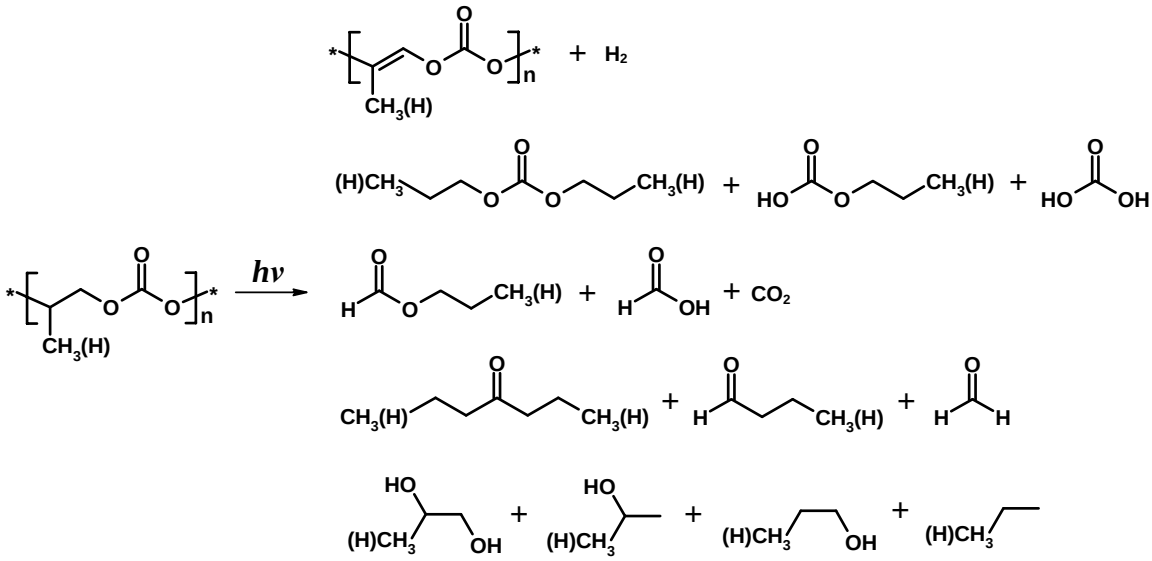

Figure 4.11 Possible created species of soft X-ray damage to PPC and PEC.

These changes at the O 1s edge of PPC and PEC confirm there is major structural collapse of the carbonate group and simultaneous large loss of O-containing fragments upon radiation damage. **Figure 4.11** depicts possible structures created in soft X-ray damage to PPC and PEC.

Figure 4.12 plots the normalized optical density at 290.4 and 300 eV as a function of radiation dose for PPC after exposure at 300 eV. Since mass loss was huge during exposure, the actual absorbed dose was corrected according to the dynamic OD at 300 eV during irradiation using equation 3.3. Then the two series of dose versus normalized OD data points were fit to equation 3.4 with extrapolated normalized OD_{∞}, as shown in Table 4.2. The final derived critical dose is 20 ± 3 MGy at 290.4 eV for C=O group damage, and 19 ± 3 MGy at 300 eV for mass loss. These two critical doses agree with each other

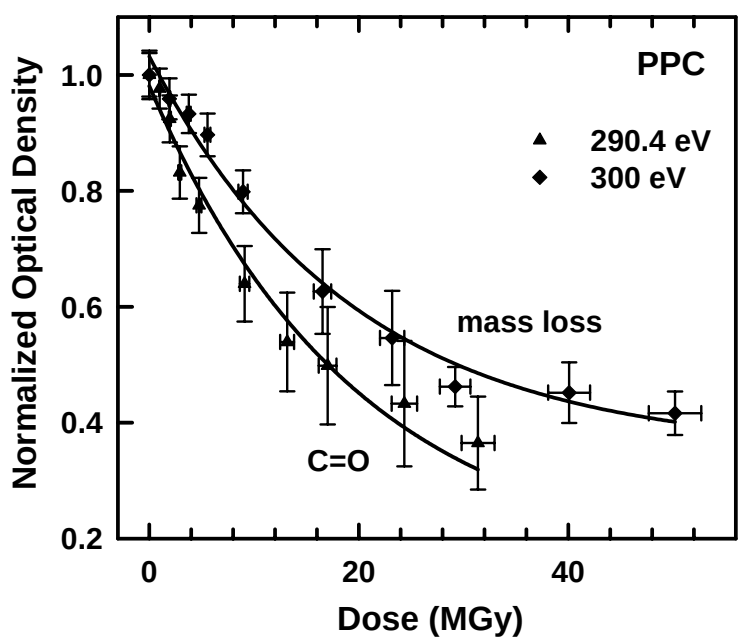

Figure 4.12 Plots of the normalized optical density at 290.4 and 300 eV as a function of radiation dose for PPC by exposure at 300 eV with dynamic dose rate exponential decaying from 201 to 157 MGy/s for C=O group damage, and from 154 to 100 MGy/s for mass loss.

within the uncertainties of the measurements. The quantitative determination of damage kinetics of PEC was carried out under similar conditions of incident photon flux, dose rate, and comparable sample thickness etc. The derived critical dose is the same as that of PPC at 290.4 eV for C=O group damage. The carbon mass loss for both PPC and PEC is about 65% when the C=O NEXAFS feature is completely damaged.

4.3 NEXAFS of radiation damaged aromatic polymers and kinetics

Aromatic polymers are generally much more radiation robust than non-aromatic polymers. Polyethylene terephthalate (PET), an aromatic polymer with in-chain C-O bonds, was selected to explore the effect of phenyl ring during radiation damage to the ester functional groups. The C 1s and O 1s NEXAFS spectra of undamaged and two series of radiation damaged PET are shown in **Figure 4.13**. The damage was made by exposure at 300 eV for a series of exposure times. For the C 1s edge, the main NEXAFS features of undamaged PET are shown in **Fig. 4.13a** and are listed in Table 4.1, including: C 1s $\rightarrow$ $\pi^*_{C=C}$ transitions at 284.8 (phenyl ring C-H) and 285.4 eV (phenyl ring C-COOR); the C 1s $\rightarrow$ $\pi^*_{C=O}$ transitions of the ester group at 288.2 eV; the mixed $\pi^*_{C=C/C=O}$ at 289.1 and 290.2 eV; and σ^* features at 293.1 and 296.4 eV. The damaged PET was characterized by a number of spectroscopic changes: a decrease, loss and merging of C-R fine structure features at 284.8 and 285.4 eV associated with the phenyl ring (as shown more clearly in Fig. 4.13a inset), mainly caused by bond cleavage between the ester group and the phenyl ring; the creation of the $\pi^*_{C=O}$ feature at 286.5 eV due to C-O bond dissociation in the ester groups; the decrease of the $\pi^*_{C=O}$ feature at 288.2 eV of the ester

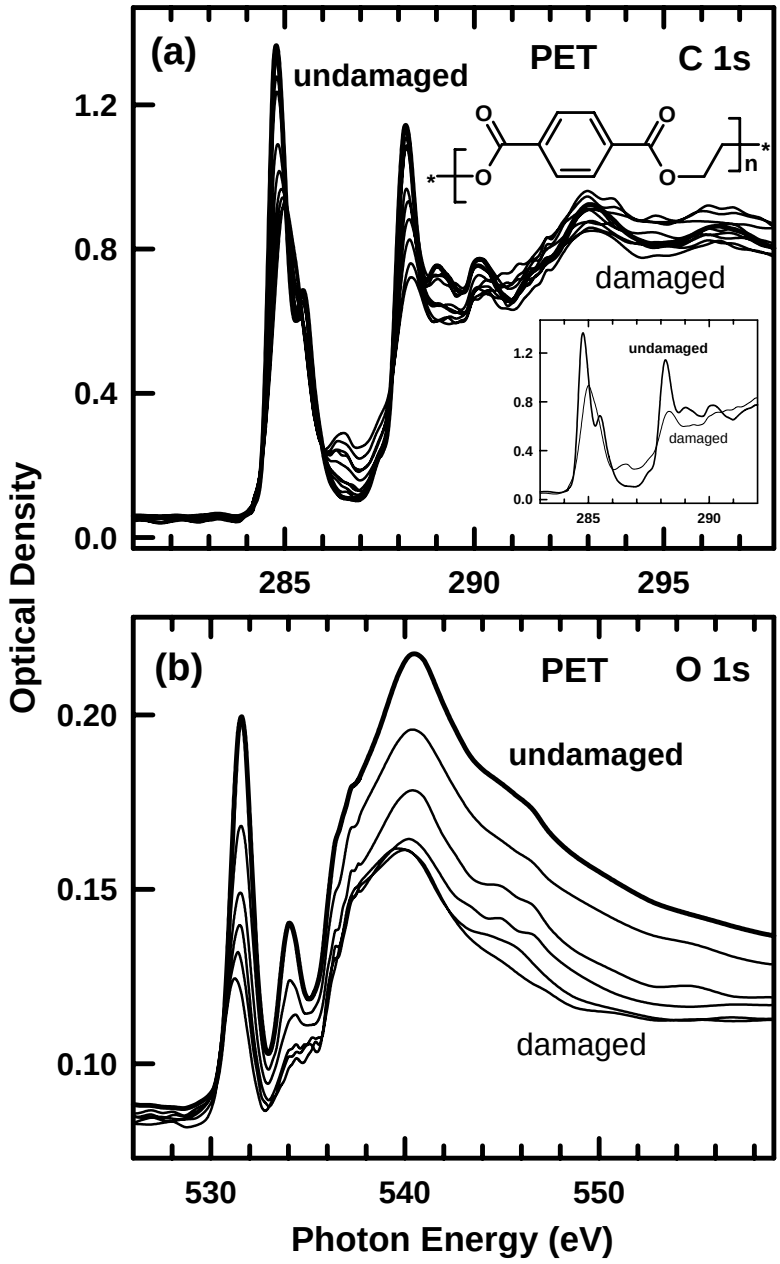

Figure 4.13 NEXAFS spectra of undamaged and two series of radiation damaged PET at, (a) C 1s edge (thick line: undamaged PET, thin lines: damaged PET). The inset shows the details of the undamaged and damaged spectra. The exposure condition is the same as that in the caption of Figure 15. The PET structure is shown. (b) O 1s edge. The dose rate is 784 MGy/s for this series of damage.

group; and decrease or deformation of the features between 289 and 298 eV. Similar spectroscopic changes have been reported in an earlier study of PET radiation damage by

X-rays and electron beams [RHA&97]. In Fig. 4.13a the variation of the intensity of the C 1s continuum above 290 eV is a little complicated, with a slight decrease below the level recorded after relatively lower radiation doses, and then an increase to values above the undamaged PET after relatively larger doses. This is probably caused by carbon contaminant photo-deposition over a long exposure time which was in the range of a few seconds/pixel. The C 1s pre-edge of damaged PET almost does not change.

The O1s NEXAFS spectra of undamaged and a series of radiation damaged PET are shown in **Figure 4.13b**. The feature assignments are listed in Table 4.1. The O 1s edge was characterized by several spectroscopic changes: a large decrease of the resonant features (O 1s $\rightarrow \pi^*_{C=O}$ transitions at 531.6 eV and O 1s (CH_2-O) $\rightarrow \pi^*_{C=O}$ transitions at 534.1 eV); a large decrease of the O 1s continuum and associated π^* and σ^* features at 537.1, 540.5 and 546.5 eV; and a decrease of the pre-edge. The decrease of the feature at 531.6 eV is due to damage or loss of the C=O functional group, while decrease of the feature at 534.1 eV is specifically due to cleavage of the C-O bond in the ester group. When all the ester groups were cleaved and damaged as suggested by the disappearance of the 534.1 eV feature, the $\pi^*_{C=O}$ feature at 531.6 eV and the σ^*_{C-O} feature at 540.5 eV shifted down to 531.2 and 539.7 eV respectively, indicating formation of isolated carbonyl groups as ketones (or aldehydes) in the damaged polymer. Although the carbon mass loss is small as reflected by the change of the C 1s continuum in Fig. 4.13a and in other similar measurements with wider energy range, there is considerable mass loss of oxygen as shown by a large intensity decrease in the O 1s continuum in Fig. 4.13b. This is due to loss of species containing higher percentages of oxygen, such as CO and CO_2.

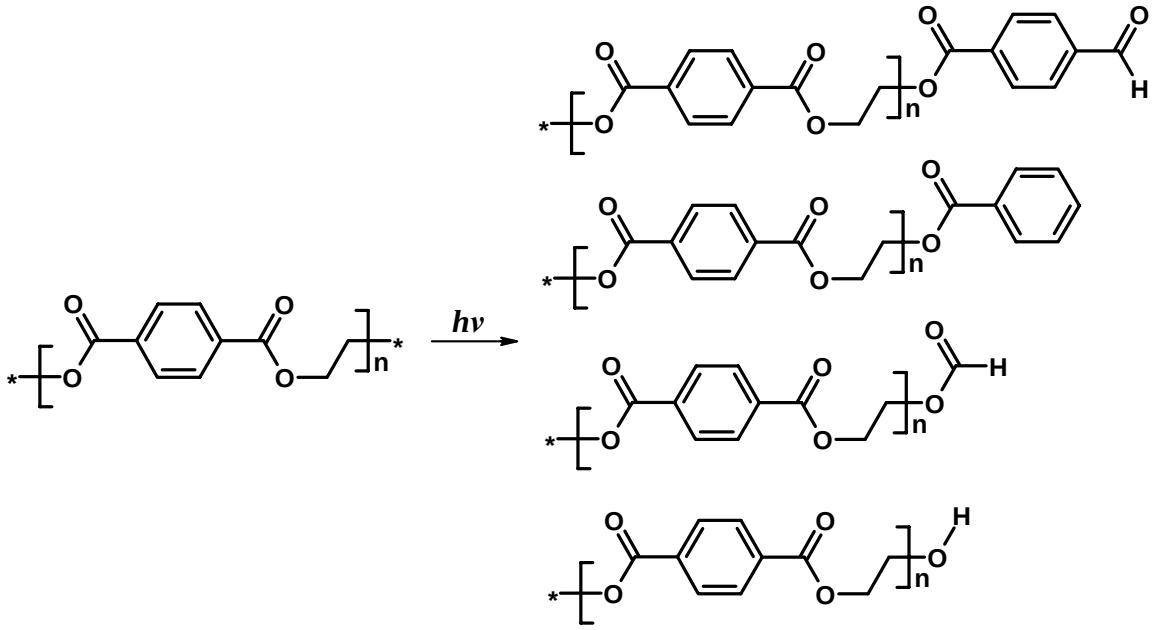

Figure 4.14 Possible structures due to main chain scission in soft X-ray damaged PET.

These spectroscopic variations suggest PET radiation damage primarily undergoes chemical structural changes, and overall mass loss is small. The structural changes mainly occur by bond dissociation in the ester group for C-O bond and between the phenyl ring and the ester group, as illustrated in **Figure 4.14**.

Figure 4.15 illustrates the quantitative determination of critical dose for damage of PET monitored at 284.8, 286.5 and 288.2 eV in the C 1s edge. **Figure 4.15a** includes an optical density image at 288.2 eV of a uniform region of a PET film that was damaged in the indicated pattern of nine pads where each successive pad was subjected to a systematically increased dwell time per pixel between 125 and 5000 ms. **Figure 4.15b** plots the normalized optical density at 284.8, 286.5 and 288.2 eV as a function of radiation dose for PET after exposure at 300 eV. The damage of the ester group was monitored at 288.2 eV, and was simultaneously tracked at 286.5 eV, the development and

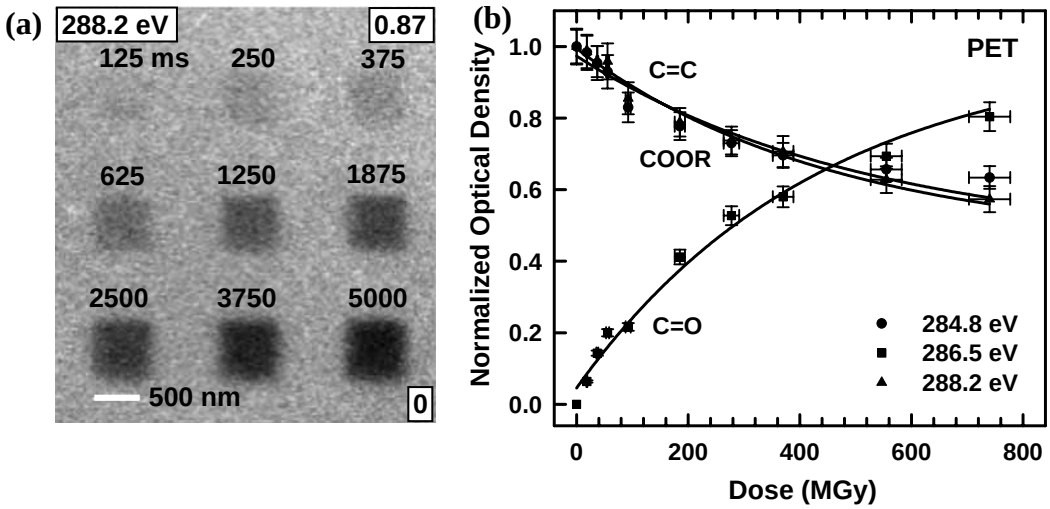

Figure 4.15 STXM damage of PET. (a) Patterns created in an initially undamaged, free standing uniform PET thin film by exposure at 300 eV using a 10x10 pixel, 0.6 μm x 0.6 μm raster scan with the indicated per-pixel dwell times and the dose rate 148 MGy/s, and imaged at 288.2 eV. The numbers in the lower and upper right boxes are the relative optical density scale. (b) Plots of the normalized optical density at 284.8, 286.5 and 288.2 eV as a function of radiation dose for PET after exposure at 300 eV.

growth of the carbonyl group generated due to C-O bond dissociation in the ester groups. The cleavage between the ester group and the phenyl ring was represented by the optical density decrease at 284.8 and 285.4 eV (data not shown due to this shoulder feature is too small and the change is hard to define accurately). Further damage of the phenyl ring should be tracked at the peak 285.0 eV in the damaged PET (see Fig. 4.13 inset) when the cleavage between the two ester groups and the phenyl ring is complete. The damage to phenyl rings requires much higher radiation dose. The data points of radiation dose versus normalized OD were fit to equation 3.4 with extrapolated normalized OD_∞ of 0.45(5) at 288.2 eV (listed in Table 4.2), 1.00(5) at 286.5 eV and 0.45(5) at 284.8 eV. The final derived critical dose is 462 ± 70 MGy at 288.2 eV for the ester group damage, 437 ± 65 MGy at 286.5 eV for the carbonyl group growth, and 523 ± 80 MGy at 284.8 eV for the

cleavage between the ester group and the phenyl ring. The critical doses derived at 288.2 and 286.5 eV are consistent as expected since they essentially characterize the same damage pathway. The critical dose obtained at 284.8 eV is slightly larger yet comparable to those at 288.2 and 286.5 eV, suggesting the two damage pathways of PET are comparable.

The critical dose of the ester group in PET is about seven times larger than that of PECA and PMMA, and also much greater than other carbonyl groups in non-aromatic polymers, such as PPC and PEC, by up to 23 fold. This clearly shows the effect of phenyl ring in stabilizing the ester group upon soft X-ray irradiation. This demonstrates again that the same functional group may have rather different damage rates in different chemical environments.

A substantial damage to the phenyl ring was achieved with even higher radiation doses, as demonstrated in soft X-ray damage to polystyrene (PS) in Chapter 5. The results show that the phenyl ring damage in PS is about three times more difficult than the damage to the ester group directly attached to a phenyl ring in PET.

4.4 Discussion

Soft X-ray radiation damage to polymers and other materials involves two successive stages, i.e. the primary process(es) and the secondary processes. The primary process(es) include(s) photoabsorption (photo ionization and photo excitation), and immediate ($< 10^{-14}$ s) decay of the core ionized or core excided states by Auger process [C95a, C97]. Although these processes occur similarly at the same functional group in

different polymers, the overall radiation damage behavior of these polymers can be rather different, as in PAN and PECA. This must be due to differences in the secondary processes of radiation damage and their consequences in different chemical environments. The secondary processes involve the generation of secondary electrons, free radicals and ions directly from Auger process, the transportation of photo electrons in bulk materials, or further generation of electrons, radicals and ions by energetic secondary electrons. The chemical consequences of the secondary processes include electron, radical or ion induced chemical reactions, such as fragmentation, polymer backbone scission and crosslinking, depolymerization, polymerization, reduction, etc. The involvement of radicals in soft X-ray damage to some organic materials, including amino acids [SSH04], nucleobases [AFY04a, YAF&04] and DNA [WH98], was confirmed by Electron

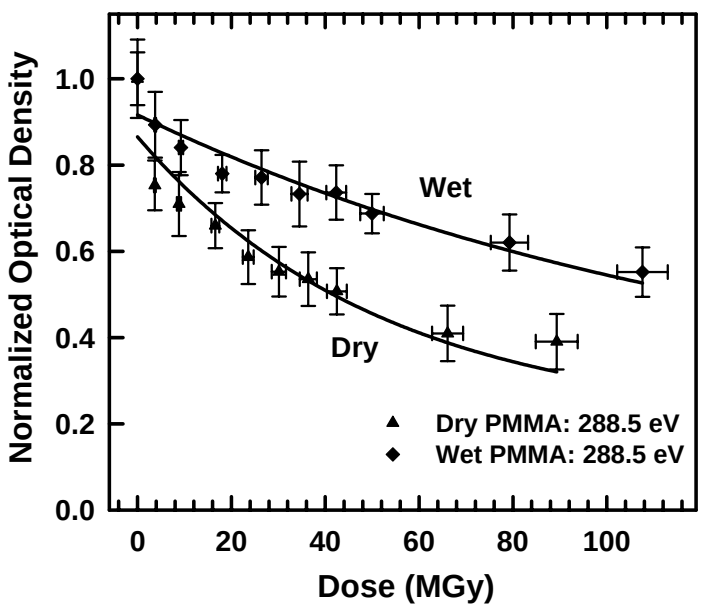

Figure 4.16 Plots of the normalized optical density at 288.5 eV of $\pi^*_{C=O}$ as a function of radiation dose for dry and wet PMMA by exposure at 288.5 eV with dynamic dose rate exponential decaying from 1907 to 1276 MGy/s for the dry sample, and from 1907 to 1537 MGy/s for the wet sample.

Paramagnetic Resonance (EPR). In our group, an earlier study of dry PMMA polymer versus wet PMMA upon soft X-ray irradiation shows the damage rate of the wet polymer was decreased, as shown in **Figure 4.16**. The critical dose of the ester group of dry PMMA was determined to be 62(10) MGy, whereas the critical dose of wet PMMA was 144(22) MGy, about two fold larger than the dry polymer. Similar phenomena were also observed in soft X-ray damage to dry and wet porous Nafion in our group (unpublished results). The decreased damage rate in wet polymers is probably due to wicking away of radicals and ions into fluids during radiation damage.

The chemical consequences of the secondary processes can be rather diverse. Specifically in this chapter, the nitrile groups in PAN mainly undergo reduction or transformation instead of being eliminated. This is probably due to fact that breaking the strong C≡N bond and cleavage of the nitrile group from the polymer backbone are not as energetically favorable as the cyclization reaction which is initiated by excited and reduced C≡N groups, or other radicals and ions. The perturbation from secondary electrons, and some hydrogen atoms or ions, resulting from C=C bond formation in the damaged polymer backbone, is also not favored to cleave C-CN bonds.

When an ester side chain is present in the repeating unit of PAN to form PECA, the damage to nitrile groups changes substantially. Since ester groups are sensitive to soft X-rays (e.g. PMMA in ref. [TTM&94, TUM&96, ZJL&95, BJ02, CUA02] and Chapter 5 and 6), multiple bond cleavages within the ester group may occur to produce C_2H_5, OC_2H_5 and $COOC_2H_5$ fragments in PECA, as reflected by carbon and oxygen mass loss in Fig. 4.5a and 4.5c, respectively. These energetic fragments appear to make a strong

impact on the nitrile group which is in spatial proximity in PECA, i.e. induction of bond cleavage between nitrile groups and the polymer backbone, as reflected by nitrogen mass loss in Fig. 4.5b, although the depolymerization process may also contribute a small fraction of nitrogen mass loss. So the fragmentation of nitrile groups changes dramatically in different chemical environments.

Oxygen containing functional groups in non-aromatic polymers are generally very sensitive to damage by soft X-rays, such as the carbonyl group in poly(vinyl methyl ketone) (PVMK) [CUA02], the ester group in side chain in PMMA [TTM&94, TUM&96, ZJL&95, BJ02, CUA02] and in the polymer backbone in poly(ethylene succinate) (PES) [CUA02], the amide group in nylon 6 [CUA02], the urea and urethane groups in non-aromatic polymers (unpublished data), and the ether group in poly(propylene oxide) (PPO) [CUA02]. In this work, we also demonstrate that non-aromatic carbonate groups are very sensitive to soft X-ray damage. Furthermore, when the functional groups are located in the polymer backbone instead of the side chain, they are much more susceptible to mass loss through backbone scissions. These modes are important in radiation damage of PES [CUA02] and polylactide (PLA) (unpublished results) compared to PMMA. Since carbonate groups are also present in polymer backbones, PPC and PEC suffer as much as ~ 65% mass loss during radiation damage, similar to the mass loss in PES (~ 68%) [CUA02].

Our results have shown that aromatic polymers, such as PET and PS (results presented in chapter 5) are generally much more robust upon irradiation than non-aromatic polymers (i.e. larger critical dose), and exhibit much less mass loss. This is also

consistent with other radiation studies, such as electron beam radiation damage in polymers [FRH&02, ELM04]. Damage of a phenyl ring is more difficult than other functional groups. This is interpreted as due to cross-linking between aromatic groups initiated by the radiation-induced scission of C-H bonds in the aromatic rings, and delocalization of the primary excitation over an extended π-σ system [FRH&02]. The damage resistance is significantly increased for the ester group directly attached to a phenyl ring in PET, compared to that in PECA, PMMA, PES and PLA. The stabilization due to the presence of a phenyl ring is probably due to a conjugation (or delocalization) of the ester group to the phenyl ring, so that the primary electronic excitation is delocalized over a much larger extended π-σ system.

The soft X-ray damage kinetics generally fit first order kinetics [ZJL&95, RHA&97, A98, BJ02, CUA02] if there is no or small mass loss. How about the fits in cases when the mass loss is large, such as PPC and PEC? From equations 3.1 and 3.3, an equation can be obtained to compute the radiation dose *a* for polymer damage with mass loss, as shown in **equation 4.1**, which is also applicable for damage without mass loss.

$$a = \frac{I_0\{1-\exp[-\frac{y_0 t + \frac{c}{b}(1-e^{-bt})}{t}]\}Et}{\varepsilon V \rho} \qquad (4.1)$$

Then the dose-damage relationship can be obtained by fitting the data with equation 3.5. It is more convenient to convert equation 3.5 to a linearized version to find the critical dose and to a normalized version to compare samples of different thickness. The linearized and normalized version of equation 3.5 is:

$$\ln(1-\frac{D}{D_\infty}) = -\frac{a}{a_c} + \ln(\frac{C}{D_\infty}) \quad (4.2)$$

For ideal first order kinetics, constant C equals to D_∞, and then the linear plot passes through the origin (0, 0) of the coordinate system.

Figure 4.17 plots a linearized version of the dose-damage data fit to equation 4.2 to determine the critical dose for PPC. The dose was evaluated using two approaches: (1) using only the initial optical density at 300 eV (i.e. ignoring mass loss), and (2) using the dynamic optical density at 300 eV during exposure using equation 4.1. For both C=O group damage and the mass loss of PPC, if the OD at 300 eV is always considered as

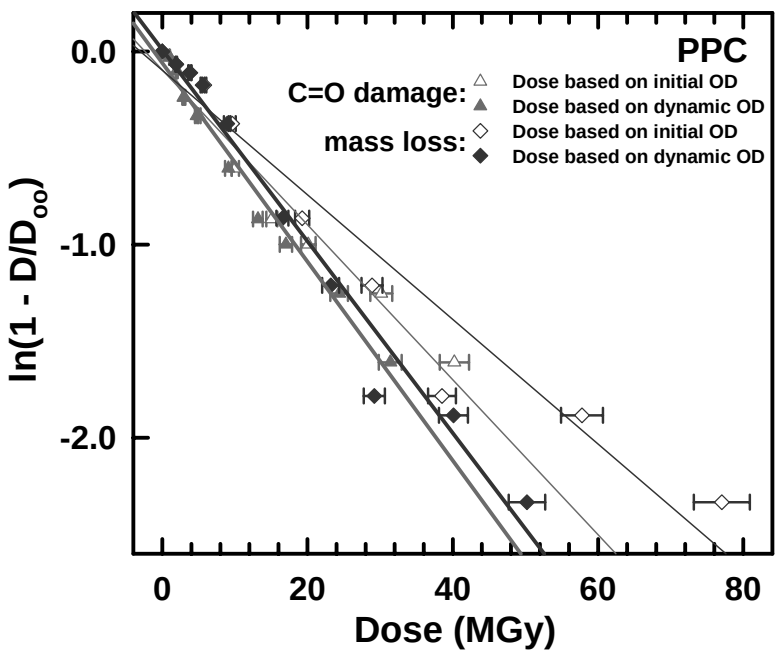

Figure 4.17 Plots of the linearized version of the dose-damage data fit to equation 4.2 to determine the critical dose for PPC. The fits are shown as the straight lines. The dose was evaluated according to only the initial optical density at 300 eV (dose rate is 201 and 154 MGy/s for C=O group damage and mass loss, respectively) and according to the dynamic optical density at 300 eV during exposure (the dynamic dose rate exponentially decays from 201 to 157 MGy/s for C=O group damage, and from 154 to 100 MGy/s for mass loss).

constant, the dose is significantly over estimated at relatively longer exposure time and the quality of the linear fit is poor. When the dose is corrected to the dynamic OD at 300 eV during exposure, the dose evaluation is more accurate, and the quality of the linear fit becomes much better. In addition, the linear plots pass through the origin (0, 0), demonstrating ideal first order kinetics. So not only pure spectroscopic changes but also mass loss follows first order kinetics if appropriate compensation for the mass loss is made. First order kinetics seem to be generally applicable to soft X-ray damage of polymers.

The soft X-ray damage studies in this chapter complement a previous study [CUA02]. **Table 4.3** lists critical dose values for all polymers discussed in this thesis. More results from unpublished work not explicitly discussed in this thesis, as well as

Table 4.3 Photon energies used to quantify soft X-ray damage rate and determined critical doses for PMMA, PAN, PECA, PPC, PEC, PET, Fg and PS polymers.

Polymer	C=C growth		C≡N damage		C=O damage		Mass loss	
	Energy (eV)	Critical dose (MGy)	Energy (eV)	Critical dose (MGy)	Energy (eV)	Critical dose (MGy)	Energy (eV)	Critical dose (MGy)
PMMA	285.1	?	---	---	288.45	67(10)	300	?
PMMA*	285.1	71(11)	---	---	288.45	92(14)	300	?
PAN	285.1	157(24)	286.8	150(23)	---	---	---	---
PECA	285.1	83(12)	286.7	73(11)	288.6	63(9)	300	66(10)
PPC	285.0	---	---	---	290.4	20(3)	300	19(3)
PEC	285.0	---	---	---	290.4	20(3)	300	20(3)
PET	---	---	---	---	288.2	462(70)	---	---
Fg	285.1	?	---	---	288.2	298(45)	?	?
Fg*	285.1	540(80)	---	---	288.2	270(40)	?	?
	Phenyl ring damage							
PS	285.1	1260(190)	---	---	---	---	---	---
PS*	285.1	1200(180)	---	---	---	---	---	---

*: determined by X-PEEM.

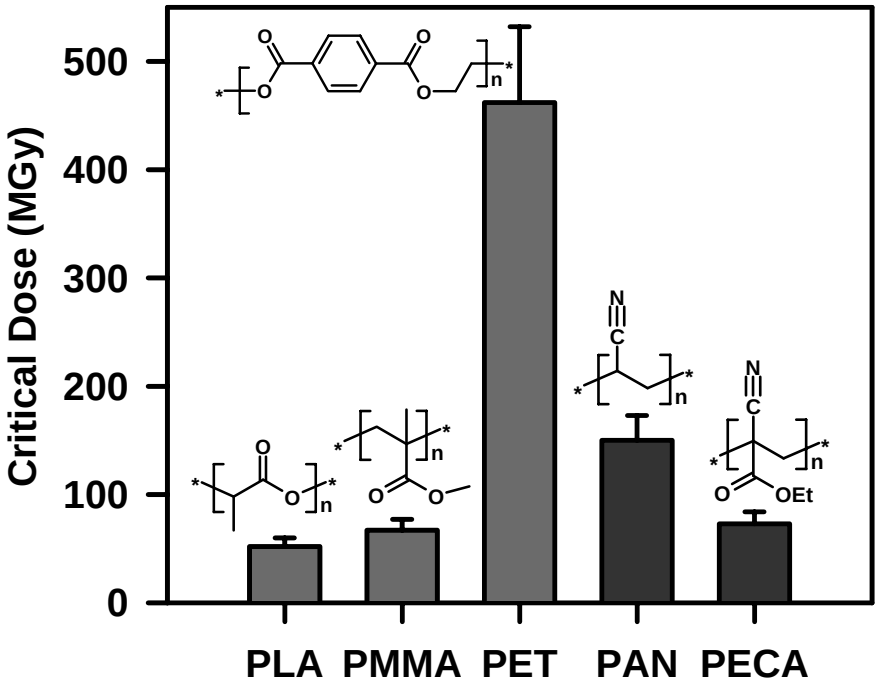

Figure 4.18 Comparison of critical doses of the ester group in PLA, PMMA and PET (red bars), and critical doses of the nitrile group in PAN and PECA (blue bars). Structures of these polymers are shown.

literature values are presented in appendix A of this thesis. From the critical dose values, one important observation is that the same functional group may have rather different critical doses, i.e. damage rates, in different chemical environments. **Figure 4.18** red bars compare critical doses of the ester group in PLA, PMMA and PET, showing how the ester group is better protected; blue bars compare the nitrile group in PAN and PECA, demonstrating sensitization of the damage in different chemical environments.

These radiation damage results are not only essential to X-ray spectromicroscopy analysis for radiation sensitive materials such as polymers and biological samples, but also are fundamental results needed to develop applications of soft X-ray damage in X-ray lithography and other types of nanofabrication involving surface or bulk chemistry

modification using soft X-rays, such as lithography or patterned damage to self-assembled monolayers (SAMs) [KYP&00, HZG&01, LJK&03, KHW&04, KCH&05, WVB&05]. Recently we have successfully demonstrated a novel approach, i.e. chemically selective soft X-ray direct-write patterning of multilayer polymer films with STXM, see Chapter 6 and 7, based on these systematic radiation damage studies. With more understanding of the radiation damage kinetics and mechanisms through the qualitative and quantitative evaluation methods presented in this work, more applications of soft X-ray radiation damage will be possibly designed and developed in the future. One predicable application is to design improved photoresist polymers by optimizing the types of oxygen containing functional groups and their locations in polymer materials, so as to control the mass loss during exposure, or to convert a positive photoresist to a negative one, and vice versa.

Chapter 5

Characterization of polymer radiation damage in X-PEEM and comparison with STXM

This chapter presents experimental results of soft X-ray radiation damage of polymers characterized by X-PEEM. Selected synthetic and natural polymers, such as PS, PMMA and Fg were investigated to determine radiation damage kinetics and radiation chemistry as revealed through NEXAFS spectroscopic changes. The radiation damage effects of these polymers were also characterized by STXM in order to compare damage rates with X-PEEM results. Damage mechanisms are proposed and described. This work has been submitted to the Journal of Electron Spectroscopy and Related Phenomena and is presented here in manuscript form since it has been accepted for publication. Since the essential part of the supplemental material for this manuscript has been integrated into the experimental section (Chapter 3), the supplemental material is not presented in this Chapter.

The author of this thesis prepared PMMA samples for this publication, performed part of the X-PEEM and STXM experiments, such as PMMA measurements by X-PEEM, PMMA and PS measurements by STXM, analyzed most of the X-PEEM and STXM data (in collaboration with Prof. A. P. Hitchcock and Dr. Cynthia Morin) and re-wrote the publication, which was initially drafted by Dr. Cynthia Morin, with assistance in later stages by Prof. A. P. Hitchcock. PS and Fg samples were prepared and partly measured by Dr. Cynthia Morin.

Radiation Damage in Soft X-ray Microscopy

J. Wang, C. Morin, L. Li, A.P. Hitchcock(*),
Department of Chemistry and Brockhouse Institute for Materials Research,
McMaster University, Hamilton, ON, Canada L8S 4M1
A. Scholl and A. Doran
Advanced Light Source, Berkeley Lab, Berkeley, CA 94720

Abstract

The rates of chemical transformation by radiation damage of polystyrene (PS), poly(methyl methacrylate) (PMMA), and fibrinogen (Fg) in a X-ray photoemission electron microscope (X-PEEM) and in a scanning transmission X-ray microscope (STXM) have been measured quantitatively using synchrotron radiation. As part of the method of dose evaluation in X-PEEM, the characteristic (1/e) sampling depth of X-PEEM for polystyrene in the C 1s region was measured to be 4 ± 1 nm. Critical doses for chemical change as monitored by changes in the X-ray absorption spectra are 80(12), 280(40) and 1230(180) MGy (1 MGy = 6.242*ρ eV/nm^3, where ρ is the polymer density in g/cm^3) at 300 eV photon energy for PMMA, Fg and PS respectively. The critical dose for each material is comparable in X-PEEM and STXM and the values cited are thus the mean of the values determined by XPEEM and STXM. C 1s, N 1s and O 1s spectroscopy of the damaged materials is used to gain insight into the chemical changes that soft X-rays induce in these materials.

Keywords: radiation damage; soft X-rays; photoemission electron microscopy; scanning transmission X-ray microscopy; polystyrene; poly(methyl methacrylate); fibrinogen; polymer thin films.

J . Electron Spectrosc. Special issue on radiation damage in microscopy
(submitted 24-Oct-06, revised submitted 20-Nov-07)
File: Radiation-dmg.doc Last changed: 20-nov-07

+ Corresponding author: Dr. A.P. Hitchcock, Brockhouse Institute for Materials Research, McMaster University, 1280 Main St. W, Hamilton, ON L8S 4M1 Canada. Tel: (+1) 905 525-9140 x24749, Fax: (+) 905 521-2773, E: aph@mcmaster.ca

1. Introduction

Radiation damage occurs whenever ionizing radiation is absorbed by a material. In biological materials - proteins, nucleic acids, cells and multi-cell organisms - very low doses (a few Gray) are sufficient to modify and inactivate biomacromolecules, and thus incapacitate or kill organisms [1,2], while somewhat higher doses impede structural studies by crystallography, unless the crystal is cooled [3]. In inanimate materials changes caused by radiation include formation of defects in ionic and semiconductor materials [4], and changes in covalent bonding, and ultimately mass loss via elimination of low molecular weight fragments in organic materials [5]. In this work we are concerned with characterizing the nature and rate of chemical changes caused by soft X-rays in modern synchrotron soft X-ray microscopes, specifically in the techniques of X-ray photoemission electron microscopy (X-PEEM) [6-9] and scanning transmission X-ray microscopy (STXM) [10-15]. Both techniques are mostly carried out using high brilliance third generation synchrotron facilities which provide high dose rates which can lead to damage, particularly in soft materials such as polymers and biological samples. These microscopies are being used successfully to study a wide range of scientific problems, ranging from environmental biofilms [16], water filtration membranes [17], polymer microspheres and capsules for chemical [18] and pharmaceutical delivery [19], fundamental polymer physics [20], biomaterials [21-23], among many other areas. In both X-ray microscopies, radiation damage limits the precision in some cases [14,17,22,24-30], even when cryo-techniques [25-26, 31] are used. Cryo techniques are effective in minimizing mass loss; however damage to chemical bonds has been found to occur at the same rate as at room temperature [32]. This work deals with soft X-ray damage at room temperature, where most materials studies are carried out. In our previous studies of fibrinogen adsorption on a phase segregated surface of a polystyrene / polymethyl-methacrylate blend, radiation damage to polymethylmethacrylate leads to a signal that could be mistaken for either polystyrene [20] or fibrinogen [22]. Brandes et al. [27] used STXM to analyze carbohydrates in the marine sinking particulate organic matter (POM). Radiation damage occurred as a decrease in the dominant 289.5 eV feature, and an increase in a new peak at 286.5 eV. Although a number of ways were tried to minimize this problem, the radiation damage effect still couldn't be eliminated. For biological samples, they are rather radiation damage susceptible. For example, Anderson et al. [28] used air-dried melanosomes for X-ray microscopic analysis, which experienced significant damage during spectral scans, often abruptly rupturing. This problem was fortunately solved by utilizing a freeze-drying protocol. Thus it is essential to characterize both the rate and the nature of the spectroscopic changes that accompany radiation damage, in order to identify damage when it occurs and to be able to select acquisition strategies that give maximum amount of meaningful information for a given level of damage. An aspect of this issue is cross-comparison of the X-PEEM and STXM with regard to their relative sensitivity for a given analytical problem.

Soft X-ray damage rates in polymers and biological materials have been measured previously, both through near edge X-ray absorption spectroscopy [33,34] and spectromicroscopy [32, 35, 36]. More generally there is an extensive literature on the chemical effects of high energy electrons, hard X-rays and gamma rays [2,37,38],

especially in microscopes [39, 40] where radiation doses are typically high. With regard to the relative impact of radiation damage on chemical analysis, Rightor et al. [33] compared the damage rates of poly(ethylene terephthalate) by soft X-rays and 100 keV electrons as measured by X-ray absorption and electron energy loss spectroscopy. As deduced from the changes in the near edge spectra, the damage products were the same in the two cases. This is as expected since much of the damage in each technique arises from secondary electrons rather than the primary absorption or inelastic scattering events. Interestingly, when the photon and electron damage rates were compared in terms of equivalent information, that study found a ~500-fold advantage in terms of analytical information per unit damage for X-ray absorption relative to electron energy loss in a TEM [33]. Jacobsen's group has made several quantitative studies of radiation damage in the Stony Brook STXM at NSLS, including quantitative studies of the damage rate for PMMA at room and liquid nitrogen temperatures and at both the C 1s and O 1s edges [35,32]. Coffey et al. [36] used C 1s near edge X-ray absorption spectroscopy (NEXAFS) spectroscopy also recorded in the Stony Brook STXM to study radiation chemistry of a series of common polymers that contain the carbonyl functional group. Both groups used a first-order kinetics model to characterize radiation damage in terms of a critical dose parameter, which is the dose required to attenuate the intensity of a specific spectroscopic feature by ($1-e^{-1}$) or 63%. Coffey et al. [36], emphasized the need to control the local environment in quantitative dose-damage studies as the damage rates and damage chemistry differ significantly between a He and an air environment.

This work is an investigation of the quantitative dose-damage relationship for polystyrene (PS), polymethylmethacrylate (PMMA), and protein (fibrinogen (Fg)), using two different X-ray microscopies, X-PEEM and STXM. Characteristic critical doses for each material are derived following irradiation at several different photon energies (specifically, PMMA and Fg at 300 eV in STXM, PS at 285.1 eV in STXM and PMMA, PS and Fg at each core edge in X-PEEM). The relative damage rates in X-PEEM and STXM are compared. The damage chemistry has been studied by comparing the C 1s, N 1s and O1s NEXAFS spectra of the damaged and undamaged materials. Based on these quantitative dose-damage measurements, procedures in X-PEEM and STXM are recommended which allow analysis of these materials with damage restricted to a level that has minimum impact on chemical analysis. We also suggest general procedures for deriving dose limits for X-ray microscopy studies of other materials.

To our knowledge, NEXAFS studies of the dose/damage relationship of protein have not been reported, although the effect of X-ray damage on the structure of protein crystals has been investigated [2,41]. A study investigating the effects of radiation damage on fluorescent yield NEXAFS and XPS spectra of amino acids was reported recently [34], but critical doses were not determined. There is an extensive literature on damage rates of organic materials by X-ray photoelectron spectroscopy [42].

This paper is organized as follows. Section 2 outlines materials, experimental methods, and the approaches used to interpret the results. Section 3 presents the dose-damage results from X-PEEM and STXM for all 3 materials. Critical doses are derived and compared to literature values. Section 4 presents the spectroscopy of the radiation damage and discusses the likely chemical transformations that are occurring. Section 5

recommends procedures for minimizing the impact of radiation damage in soft X-ray microscopy.

2. Experimental

2.1. Sample preparation

2.1.1. PMMA and PS

PMMA (MW =312 K, polydispersity index δ = 1.01) and PS (MW = 1.07 M, δ = 1.06) were obtained from Polymer Source Inc. and used without further purification. A 1 weight-% toluene solution was prepared using anhydrous toluene (Aldrich, 99.8%). For X-PEEM sample preparation, a 50 μl drop was spun cast (4000 rpm, 30 s) onto clean, 1 cm^2, native oxide Si wafers (111) (Wafer World, Inc.), which had previously been degreased with trichloroethylene (Aldrich, +99.5% pure), acetone (Burdick & Jackson, HPLC grade), and methanol (Caledon), then rinsed under running milli-Q water. In order to make uniform films to determine the X-PEEM sampling depth, the PS thin films on Si substrates were further annealed at 140°C for 4 hours in a vacuum oven with pressure < 10^{-2} torr achieved by a liquid nitrogen trapped rotary pump or a turbo pump. Then the X-PEEM sampling depth was measured by recording the signal from PS films of varying thickness which were prepared on clean, native oxide silicon using the same spin coating procedure. Non-contact mode atomic force microscopy (AFM) (Veeco Digitial Instruments Nanoscope III or Quesant Q-scope 350) instruments was used to characterize the polymer films. A sharp tweezer tip was used to scratch through the polymer film and the profile across the scratch was measured by AFM to determine the film thickness. PS films made by spin coating (4000 rpm) of toluene solutions of concentrations of 0.05, 0.1, 0.5, 1 and 2 wt% had thicknesses of 2, 5, 16, 32, and 95 nm respectively.

The STXM sample was prepared from the same solution and spun cast onto silicon nitride (Si_3N_4) windows (750 μm x 750 μm window back etched into a 7.5 mm x 7.5 mm x 200 μm silicon wafer chip coated with 75 nm of Si_3N_4), which were obtained from Silson Ltd. [43] and were rigorously cleaned to semiconductor industry standards by the manufacturer. They were stored in gelatin capsules and used without further surface preparation. The thickness of the polymer films was non uniform due to sagging of the Si3N4 membrane while spinning. However it was possible to find uniform regions larger than 10 μm x 10 μm which were suitable for quantitative radiation damage studies with STXM. For PMMA, large uniform free standing films were also prepared from spin coating (3000 rpm, 30 s) onto a freshly peeled mica surface of 2.5 cm × 2.5 cm. The film was dried in ambient at room temperature, then was cut into 3 mm × 3 mm pieces on the mica surface, and was subsequently floated onto milli-Q water. 2 or 3 film pieces were transferred to a degreased hexacomb grid or a TEM grid for STXM experiments. The single layer film thickness is ~ 40 nm according to STXM measurements under the above preparation conditions.

2.1.2. Protein samples for X-PEEM and STXM

Plasminogen-free human plasma fibrinogen (Calbiochem) was used as received. It is reported to be > 95% clottable by thrombin, and pure as judged by sodium dodecyl sulphate polyacrylamide gel electrophoresis. The X-PEEM sample was prepared by spin

casting 50 µl of a 1.0 mg/ml Fg solution in deionized water (4000 rpm, 30 s) onto clean, 1 cm^2, Si wafers (same origin and cleaning protocol as above). The STXM sample was prepared by solvent casting, i.e. depositing a 50 µl drop of the same solution onto a clean Si_3N_4 window, without spin coating.

2.1.3. HF-etched Si - X-PEEM Io substrate

The substrates used to measure the incident flux (Io) in X-PEEM were Si wafer chips cleaned as described in 2.1.1. Just prior to use they were exposed for 30 s to 10% HF (Aldrich, 48 wt.% in water, 99.99+%), then rinsed under running deionized water. The HF-etched Si was mounted on the same sample holder, next to the sample of interest and brought under vacuum within 10 minutes of preparation. No O 1s signal was detected.

2.2. X-PEEM

The PEEM2 instrument at beamline 7.3.1 of the Advanced Light Source (ALS) was used. Details of the instrument [8] and the operating principles [20] have been presented elsewhere. In order to quantify the dose received by the sample, it is necessary to know the spot size on the sample, the incident flux, the sampling depth and thus the absorbed dose, and the fraction of that absorbed dose contributing to the detected signal. A pseudo exit slit vertically limits the size of the X-ray beam on the sample through two different slit sizes, i.e. 50 and 100 µm. With the pseudo exit slit installed, the sample is not illuminated uniformly due to edge diffraction effects. To circumvent this problem, we only measure the regions over which illumination is relatively uniform. In order to remove higher order light, a Ti filter (200 nm, Lebow) was used for the C 1s and N 1s measurements, but it was removed for the O 1s measurements. The duty cycle of X-PEEM acquisition was also optimized in order to limit un-necessary damage: first a shutter is used so that X-rays impinge on the sample only during measurements; second data binning operations can be directly applied during data acquisition to reduce data transfer times. All X-PEEM data acquired were scaled to 400 mA ring current to compensate for the actual ring current during any given measurement. The data used in determining the critical dose were recorded by repetitively acquiring X-PEEM spectra on the same damage region. After a specific exposure time on the sample at a fixed photon energy or a range of photon energies, the NEXAFS spectrum of the damage region was acquired using a short image sequence (stack) to evaluate the damage in terms of peak area change. The spectra were derived by averaging the signal at all pixels in the damaged region or from specific sub-regions, if the damage region was not uniform. Flat-field and dark current corrections were directly applied during data acquisition. After measuring the sample, the sample puck was translated to place the Io substrate, an HF-etched Si wafer, under the objective lens of the X-PEEM without changing the height of the sample so as to maintain the same energy scale and illumination. The incident flux (Io spectrum) was recorded and calibrated with a silicon photodiode [44] according to the details presented in the **Supplemental Material**. The absolute dose and dose rate in the X-PEEM was derived from incident flux measurements and the sampling depth. The absorbed dose (in units of mega grays, where 1 MGy = 10^6 J/kg, (1 MGy = 6.242*ρ eV/nm^3, where ρ is the polymer density in g/cm^3) was obtained as:

$$a = F*E*t/m \quad \text{(eqn. 1)}$$

where F is the absorbed flux (photons per second absorbed into the volume contributing to the measured signal), E is the photon energy, t is the exposure time, and m is the mass of the volume. Since the Beer-Lambert law is obeyed for soft X-ray spectromicroscopy applied to thin samples, the absorbed flux can be derived from the incident flux (I_0) and the optical density (absorbance) of the material at the energy of exposure. The optical density (OD) of the sample can be further considered as a product of the linear absorption coefficient (A, optical density per nm, in nm^{-1}) of the material and the sampling depth (d, in nm).

$$F = I_0 - I = I_0*(1 - e^{-OD}) = I_0*(1 - e^{-A*d}) \quad \text{(eqn. 2)}$$

In order to determine the critical dose for damage of a specific material from the measured damage-exposure data, the damage versus dose data was fit to postulated rate laws, such as a first order kinetic process [32, 33, 35, 36] which appears to be suitable in these cases where mass loss is relatively small and the damage is mainly chemical change. Specifically, the critical dose for damage in X-PEEM was determined by plotting the area of the C 1s $\rightarrow \pi^*_{C=O}$ and C 1s $\rightarrow \pi^*_{C=C}$ peaks (or the change of peak area) as a function of radiation dose a. Then the critical dose for the sample material was derived from the dose-damage data by mathematical fitting it with [32, 33, 35, 36]:

$$D = D_\infty + A \cdot \exp(-\frac{a}{a_c}) \quad \text{(eqn. 3)}$$

where D is a relative measure of damage, D_∞ is the saturation damage in the same scale, A is a constant, which has similar magnitude as D_∞ if mass loss is small or negligible in most of our cases, otherwise a large difference between A and D_∞ indicates that significant mass loss occurs, a is radiation dose, and a_c is the critical dose, which is the dose that attenuates (or increments) a specific spectroscopic feature by 63%. Thus, if the damage process follows first order kinetics, a plot of $\ln(D - D_\infty)$ versus dose a (in MGy) should be linear with a slope of $-1/a_c$. In some cases, when the dose-peak area profile was far from the damage saturation, the saturation level (D_∞) was estimated based on extrapolation using this functional form.

2.3. STXM

Scanning Transmission X-ray Microscopy (STXM) was performed using the polymer STXM [15] at beamline 5.3.2 [45] at the Advanced Light Source. STXM uses a Fresnel zone plate to focus monochromated X-rays to a small probe. With the zone plates used in this work (diameter of 155 μm, 35 nm outer zone size [46]), the diameter of the beam at focus is ~40 nm, as judged by evaluation of the diffraction limited spatial resolution. The sample is raster scanned with synchronized detection of transmitted X-rays to measure the energy dependent absorption by a column of material. In order to investigate radiation damage rates, adjacent small regions of the sample (typically 0.6 μm x 0.6 μm, using 10 x 10 pixels) were exposed using systematically varied dwell times so as to span a range of doses that adequately sample the dose-damage curve. The entrance and exit slits were adjusted to control the photon flux and dose rate on the sample. Since the point size changes slightly with changes in the slit sizes, the dose was evaluated by

considering the flux passing through the uniform central portion of the damage pads (~60%), from which signals at single energies or spectra were extracted. The damaged region was analyzed by imaging it at the photon energy giving the best contrast of the damaged relative to the undamaged material, which was at the strong C 1s $\rightarrow$ π^* transitions (285.15(5) eV for PS, 288.45(5) eV for PMMA and 288.20(5) eV for Fg). The NEXAFS spectra of the damaged and undamaged regions were acquired using an image sequence (stack [47]) with much lower photon flux achieved by reduced slit settings. Reference spectra on absolute linear absorbance scales (i.e. OD per nm thickness sample) were derived by scaling the spectra of the undamaged material to the X-ray absorption response in the regions of 275-282 eV and 320-350 eV, to match that of the linear X-ray absorption for the elemental composition of the sample derived from literature absorption coefficients [48].

The dose in STXM was also obtained using equations 1 and 2 with the known optical density of the sample, the incident flux, the irradiated sample area (central 60% of the pad), the sample thickness (*d*, also the sampling depth in STXM), which is easily derived from the measured optical density and the linear absorption coefficient, and the sample density ρ (see the example for PMMA in the **Supplemental Material**). The incident flux was measured in a region without the sample (through a hole, or bare part of the silicon nitride window, as appropriate). The measured flux was corrected for the detector efficiency (ε), which was further calibrated to be 35 ± 5% in the C 1s region by silicon photodiode. A N_2 gas filter (1 meter path length at ~1 torr) was used to ensure that the incident photon beam contained negligible higher order radiation. This can be quite important in quantitative dose-damage studies for polymers containing nitrogen or oxygen since the second order photon flux is quite large in beamline 5.3.2 (without the N_2 gas filter), and these second order photons deposit twice the amount of energy per absorbed photon. Similar to X-PEEM, the critical dose for damage in STXM was determined from the damage, expressed in terms of change in signal, usually optical density, at a damage sensitive energy, as a function of radiation dose by fitting with equation 3.

3. Quantitative dose-damage results

3.1. X-PEEM sampling depth

In order to determine the sampling depth, C 1s spectra were measured for a series of thin films of polystyrene with thicknesses of 2, 5, 16 and 32 nm, as measured using AFM to profile a scratch (uncertainty in film thickness from the AFM is < 1 nm). **Fig. 1** plots the signal at 285.1 eV (C 1s $\rightarrow$ π^* transition of PS) and at 282 eV (where the signal from the underlying silicon substrate is intrinsically stronger) as a function of the film thickness. The inset to Fig. 1 shows the measured spectra, which have been normalized to the signal in the adjacent scratch (that from Si). These measurements indicate that almost all of the signal arises from the outer 10 nm, although there are still small contributions from layers as deep as 20 nm. We have used 10 nm as the total sampling depth in evaluating the absorbed dose, and in deriving quantitative amounts in studies of protein adsorption on PS/PMMA blends [23]. However, since both the absorbed energy and the amount of material vary linearly with sampling depth (since very little of the incident X-

ray flux is absorbed in the sampling depth), this factor cancels in determining the critical dose (the thickness enters linearly in determining both the amount of energy absorbed and the mass of material).

The variation of signal with the PS film thickness has been fit to an exponential which yields a characteristic sampling depth (1/e decrease from the maximum detected C 1s signal or increase in the detected Si signal) of 4 ±1 nm for X-PEEM of polystyrene in the C 1s region. This measured value of 4 nm for PS is in good agreement with a value of 3.5 nm for the escape depth of carbon KLL Auger electrons in multilayers of n-alkanes reported by Zharnikov et al. [49]. It is also similar to values of 3 nm (for 120 eV photon energy) and 5 nm (for 460 eV photon energy) reported by Frazer et al [50] for the X-PEEM sampling depth in Cr metal. For the latter situation, this level of agreement is rather surprising since metals have much greater density of states for low energy electrons and Cr is about seven times denser than polymers, thus Cr would be expected to scatter the slow electrons that dominate X-PEEM signals to a much greater extent. At the same time metals have much lower work functions, which will enhance yield. There could be a fortuitous cancellation of effects at work, since the sampling depth is a complex function of near surface electron transport, and work function, which differ considerably between polystyrene and chromium.

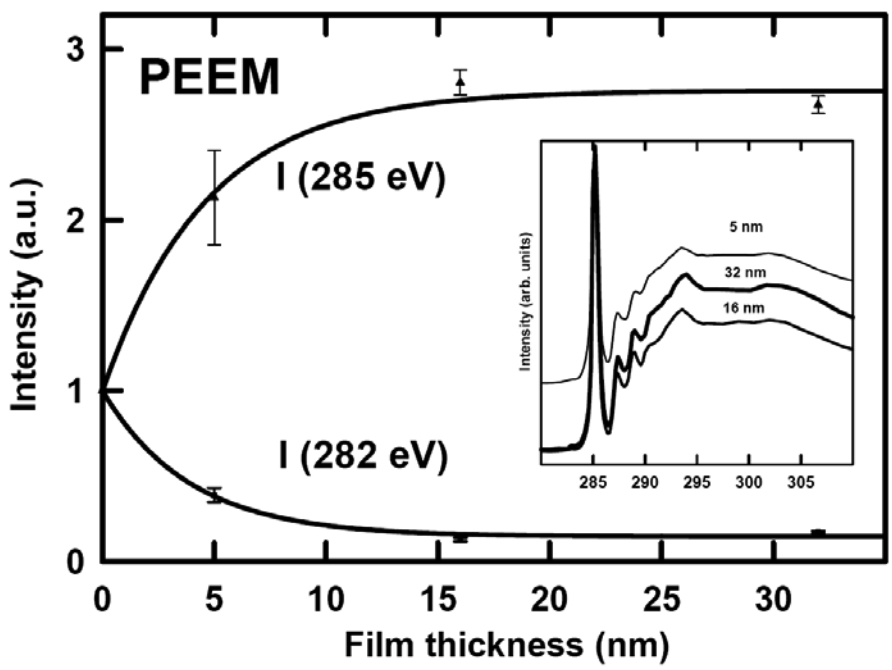

Fig. 1 X-PEEM signal intensity at 285 eV and 282 eV as a function of the thickness of a spun cast polystyrene (PS) film on a native oxide silicon substrate. The film thickness was determined from the height profile across a scratch in an AFM image. The exponential fits to the increase in the C 1s $\rightarrow \pi^*$ signal and the decrease in the Si 2p continuum signal correspond to a sampling depth (1/e) of 4 nm. The inset plots the measured C 1s spectra. The large pre-edge signal seen for the 5 nm thin film is caused by electrons from the underlying Si substrate.

3.2. PMMA - radiation damage in X-PEEM

Figure 2 presents a series of time- and thus dose-dependent spectra, acquired by successive X-PEEM measurements from the same area of a ~60 nm thick PMMA film on a Si substrate. Each spectrum was normalized to the ring current and the shape of the Io signal (which in turn was corrected for the photoabsorption cross section for Si and the bolometry effect for electron yield) [23]. The absolute dose was derived as outlined above. As the accumulated dose increases, the intensity of the C 1s(C=O) $\rightarrow \pi^*_{C=O}$ transition at 288.4 eV decreases. Simultaneously a peak grows in at 285.1 eV, corresponding to the C 1s(C=C) $\rightarrow \pi^*_{C=C}$ transition of re-arranged and reduced parts of the polymer backbone.

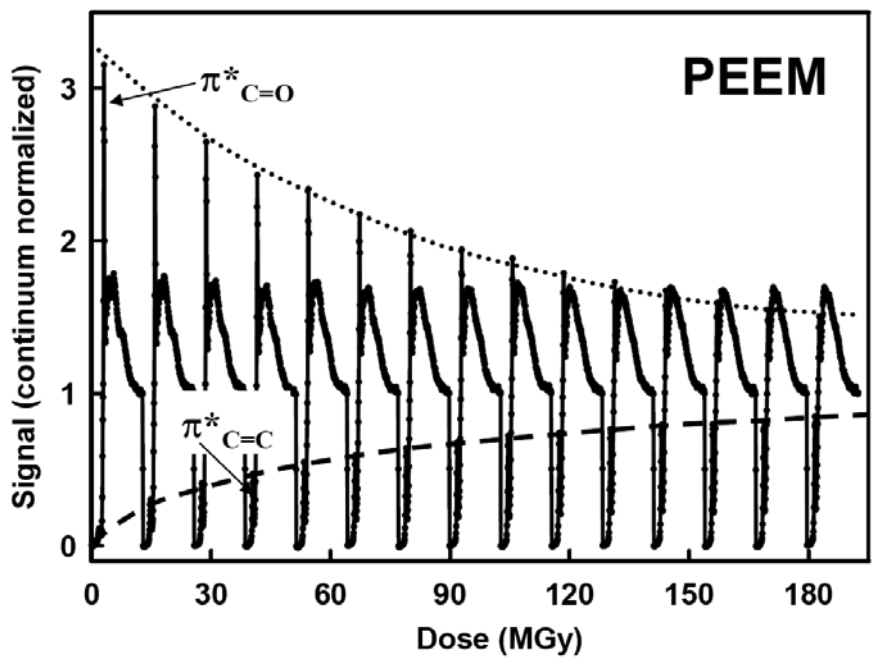

Fig. 2 Sequence of C 1s spectra of PMMA recorded by X-PEEM with a reduced flux on the same area. The integrated dose accrued during the 150 seconds it took to record each spectrum was 13 (± 1.3) MGy.

Figure 3 presents spectra and dose-damage curves for radiation damage by irradiating PMMA at 300 eV in the X-PEEM. The inset to 3a is an image of PMMA under the low-magnification conditions used for the damage study, along with boxes identifying the different regions of PMMA that were measured in order to have a range of radiation doses. Figure **3a** plots the sequence of spectra of region A, the highest dose area. Figure **3b** plots the normalized peak areas at 288.4 and 285.1 eV as a function of radiation dose for all three damage regions. The curves are fit to equation 3 from which a critical dose was determined. The damage saturation level from the data of region A was also used for analysis of the data of regions B and C. Due to mass loss and thus additional signal contributions from deeper layers (> 10 nm) of the sample in X-PEEM, the damage saturated PMMA spectrum may still show some $\pi^*_{C=O}$ intensity. The saturation level for X-PEEM damage to PMMA is thus defined as that dose where there is no longer further

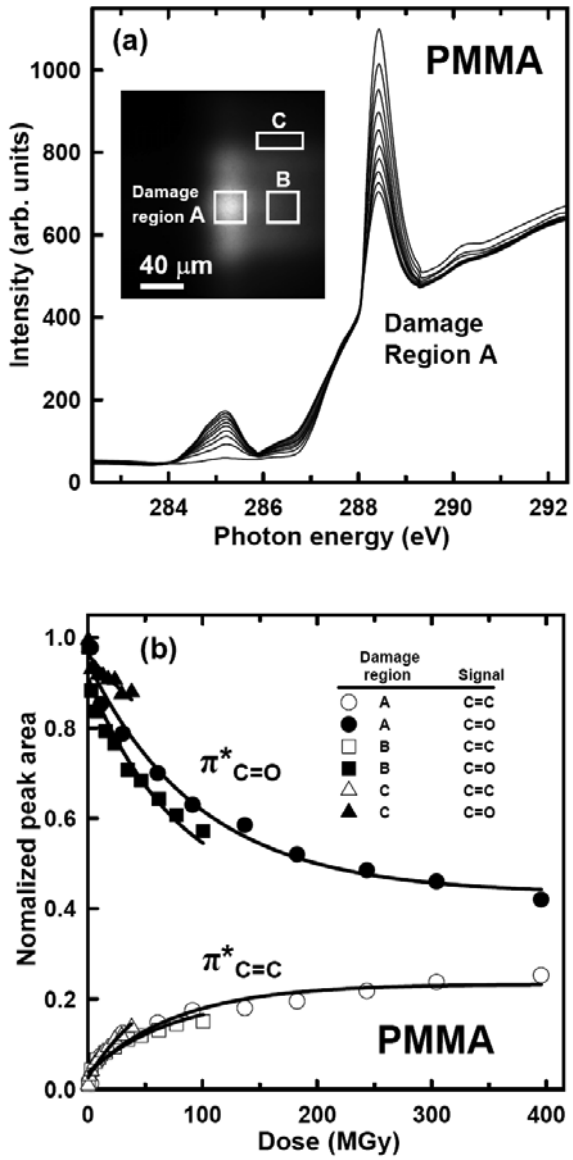

Fig. 3 (a) Sequence of C 1s spectra of PMMA recorded by X-PEEM in region A. The inset X-PEEM image indicates the three different illumination regions monitored for radiation damage. **(b)** Plots of the peak area of the C 1s $\rightarrow \pi^*_{C=O}$(288.4 eV) and the C 1s $\rightarrow \pi^*_{C=O}$(285.1 eV) transitions as a function of radiation dose for regions A, B and C.

change of the $\pi^*_{C=O}$ peak intensity. The critical dose from the data shown in Fig. 3, as well as from a repeat measurement at a different area of the sample conducted on a different date are summarized in **table 1**. The critical dose for C=O loss or destruction was found to be 92(14) MGy, while the critical dose for C=C generation was 71(11) MGy. While the dose rate varies considerably in the different regions of the illumination, there is no obvious trend of critical dose with dose rate. The critical dose for C=O loss was always found to be higher than that for C=C growth, although the difference is within the

uncertainties of the measurements as determined from the replicates. If there is a real difference, it could be due to the existence of different reaction pathways with different reaction rate for the two types of chemical change (see further discussion in section 4).

Table 1: Reproducibility of dose - damage data from X-PEEM measurements on PMMA with various dose rates

Sample	Exposure energy (eV)	Dose rate (MGy/s)	Critical dose (MGy)	
			C=C growth	C=O damage
60208-7- Region A	300	0.51	76 (11)	98 (15)
60208-7- Region B	300	0.13	74 (11)	79 (12)
60208-7 - Region C	300	0.049	60 (9)	99 (15)
60211-3	300	0.098	74 (11)	91 (14)
Average	---	---	71 (11)	92 (14)

Table 2: Critical doses for radiation damage of PMMA, PS and Fg at C 1s, N 1s and O 1s edges as determined by X-PEEM

Material	Exposure energy (eV)	Dose rate (MGy/s)	Analysis energy (eV)	Critical dose (MGy)	
				X-PEEM	Literature (STXM)
PMMA	280 - 320	0.18	285.1	96 (14)	10.8^{35}; [$12.3^{35(+)}$]
			288.4	101 (15)	50^{35}, $69^{36(\$)}$; [$13.1^{35(+)}$*]
	525 - 565	0.42	531	133 (20)	[$18^{32(+)}$*]
			534	143 (20)	---
PS	280 - 330	0.56	285.1	1200 (180)	---
Fg	280 - 320	0.20	285.1	540 (80)	---
			288.2	270 (40)	---
	390 - 450	0.28	397	300 (45)	---
			401	345 (52)	---
	525 - 565	0.46	531	300 (45)	---

$^{(+)}$ The PMMA film was annealed at 150 ^{o}C for 2 h.
$^{(\$)}$ Converted from the reported value of 520 eV/nm^3 using 1 MGy = 6.242ρ eV/nm^3, where ρ is the polymer density in g/cm^3.
* Note that the critical dose for PMMA films was found to be quite sensitive to annealing, with values measured at 288.4 eV changing from 50 for unannealed films to 13 - 15 MGy for films annealed at 150 - 200 ^{o}C [35]. Since we did not anneal our films for these studies, the relevant value to compare from ref. 35 is 50 MGy.

Table 2 lists the critical doses for radiation damage of PMMA in X-PEEM, determined at the C 1s and O 1s edges through exposure at 280 - 320 and 525 - 565 eV, respectively. The radiation dose was obtained by integrating the incident flux spectrum through the entire exposure energy region, taking into account the optical density spectrum of PMMA for a 10 nm sampling depth and the exposure time at each energy

point. The damage was monitored by measuring the spectral intensity change at four different photon energies (285.1, 288.4, 531.2 (O 1s(CO) $\rightarrow \pi^*_{C=O}$) and 534 eV (O 1s($OCH_3 \rightarrow \pi^*_{C=O}$)). Plots of the signal change against dose were fit to equation 3 to find the critical doses. The results obtained from this method are summarized in table 2. They are comparable to those reported in table 1, even though the exposure protocol for the latter is rather different. Table 2 also compares our results to those measured by STXM from the literature [32, 35, 36]. The average value for the critical dose for decrease in the $\pi^*_{C=O}$ peak is similar to but larger than that reported elsewhere [35,36]. Zhang et al. [35] reported critical doses for soft X-ray damage of PMMA ranging from 11 to 69 MGy and suggested that the critical dose at 288.4 eV is much larger than that at 285.1 eV [35]. Our quantitative critical dose values (tables 1,2) and the qualitative spectroscopic data (Fig. 2) strongly suggest that the rate of change of the signals at these two energies are quite similar, in disagreement with their observations.

3.3. PMMA - radiation damage in STXM

Figure 4 presents results of a STXM measurement of radiation damage in PMMA. Fig. 4a is an optical density image of a uniform region of a PMMA film that was damaged in a 3 x 3 pattern of nine 600 x 600 nm (10 x10 pixel) pads where each successive pad was subjected to a systematically increased dose rate by adjusting the dwell time per pixel between 12.5 and 500 ms. Fig. 4b plots the damage derived from the change in the optical density in the central 60% of each pad against the dose. Fig. 4c is the linearized version of that data fit to equation 3 to determine the critical dose. The critical dose for damage to PMMA with 300 eV incident photons, as measured by the decrease in the C 1s $\rightarrow \pi^*_{C=O}$ peak intensity is summarized in **table 3,** in comparison to literature values. The uncertainties cited are obtained from replicates. The derived critical dose of 67 ± 10 MGy for damage to PMMA measured at 288.45 eV is in good agreement with the values in the literature [35,36]. We note that the critical dose of 69 MGy reported in ref. 36 (converted from 520 eV/nm^3) was cited as 14 MGy in ref. 32; probably the latter is the normalized carbonyl critical dose, which is computed from the critical dose by multiplying by the number of carbonyl groups, then dividing by the total number of carbon atoms in the monomer [36].

Zhang et al. [35] have shown that the critical dose for PMMA is sensitive to annealing, with values measured at 288.4 eV changing from 50 MGy for unannealed films to 13 - 15 MGy for films annealed at 150 - 200 ^oC [35]. Our results are consistent with the critical dose reported by Zhang et al. [35] for the as-prepared PMMA films, without high temperature annealing. Further studies may be needed to clarify the effect of annealing on critical dose for radiation damage to PMMA. Apart from differences in sample preparation, critical doses may be significantly influenced by a number of other factors, including measurement environment [36], second order light, detector efficiency, damage data extraction errors, change of photon flux during damage, variation of sample thickness and defining of the saturation level, etc. Systematic errors associated with the first three factors can be minimized through use of a helium environment, use of a second order filter, and careful calibration of the detector efficiency, respectively. The remaining factors contribute much less to the total uncertainty although defining the damage

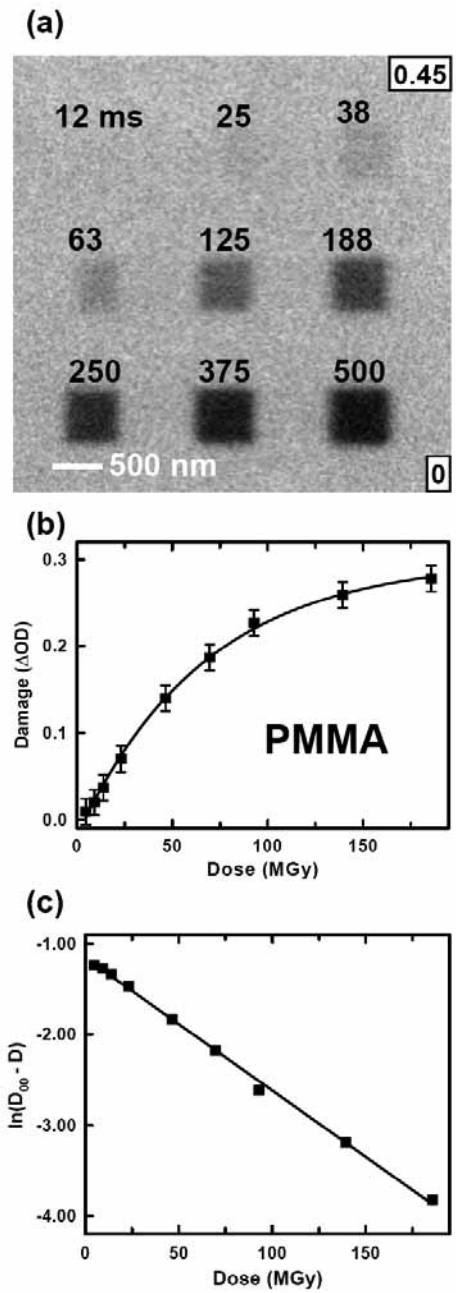

Fig. 4 STXM damage of PMMA. **(a)** Patterns created in an initially undamaged, free standing PMMA thin film by exposure at 300 eV (dose rate = 3.7 x 10^2 MGy/s) using a 10x10 pixel, 0.6x0.6 μm raster scan with the indicated per-pixel dwell times The image was recorded after the exposure at 288.45 eV using ~1/3rd the dose rate used to create the radiation damage.. The numbers in the lower and upper left boxes are the optical density limits to the image gray scale. **(b)** Plot of damage (determined from the central 60% of each pad) versus dose. **(c)** Linearized plot of the data of (b) corresponding to the analysis (equation 3) used to derive the critical dose.

saturation level is somewhat arbitrary, especially for cases where the extent of damage is low. We estimate the total uncertainty to be about 15% for our STXM damage studies. A similar magnitude of uncertainty was also estimated for the results of the X-PEEM damage studies although the contributing factors are different in the two techniques. For example, in X-PEEM the determination of irradiation area and volume gives rise to the largest uncertainties.

Table 3: Critical doses for radiation damage of PMMA, PS and Fg as determined by STXM

Material	Exposure energy (eV)	Dose rate (MGy/s)	Analysis energy (eV)	Critical dose (MGy)	
				STXM	Literature (STXM)
PMMA	300	3.7×10^2	288.4	67 (10)	50[35], 69[36($)]; [13.1[35(+)]*]
PS	285.1	$5.3 \times 10^{2(\#)}$	285.1	1260 (190)	---
Fg	300	5.9×10^2	288.2	298 (45)	---

(+) The PMMA film was annealed at 150 ^oC for 2 h.
($) Converted from the reported value of 520 eV/nm^3 using 1 MGy = 6.242ρ eV/nm^3, where ρ is the polymer density in g/cm^3.
* Note that the critical dose for PMMA films was found to be quite sensitive to annealing, with values measured at 288.4 eV changing from 50 for unannealed films to 13 - 15 MGy for films annealed at 150 - 200 C [35]. Since we did not anneal our films for these studies, the relevant value to compare from ref. 35 is 50 MGy.
(#) Average from the dose rate range of 5.7×10^2 to 4.9×10^2 MGy/s.

3.4. Dose-damage relationships for PMMA, PS and Fg in X-PEEM and STXM

Methods similar to those described for PMMA in the preceding sections were also applied to measurements of dose-damage relationships for polystyrene (PS) and fibrinogen (Fg), in both X-PEEM and STXM. **Figure 5** plots the normalized radiation damage as a function of dose for PMMA, PS and Fg as measured in X-PEEM. The derived critical doses for these species at different edges as monitored at a number of photon energies are summarized in **table 2**. Figure 5a plots PMMA dose-damage results measured at both C 1s and O 1s edges. The variation in the incident flux over the spectral region (C 1s: from 282-320 eV; O 1s: from 525 - 565 eV) was taken into account in deriving these results. The damage as a function of dose is similar for both edges. The critical doses for damage at the O 1s edge derived from these measurements are slightly larger than those at the C 1s edge. Beetz and Jacobsen [32] also found a somewhat higher critical dose for an annealed PMMA sample at the O 1s edge compared to the C 1s edge (18 versus 13 MGy). However, this difference is probably not outside the uncertainties in the measurement since there are large differences in the dose parameters at the two edges. Systematic errors in the absorption coefficient, the incident flux (I_0) and the detection efficiency (ε) may exist when two different edges are compared.

Figure 5b presents the damage versus dose curve for polystyrene measured with X-PEEM at the C 1s edge. There is a lot of mobile hydrocarbon contaminant present in the STXM (mostly from stage and motor lubricants). If the radiation dose is large enough,

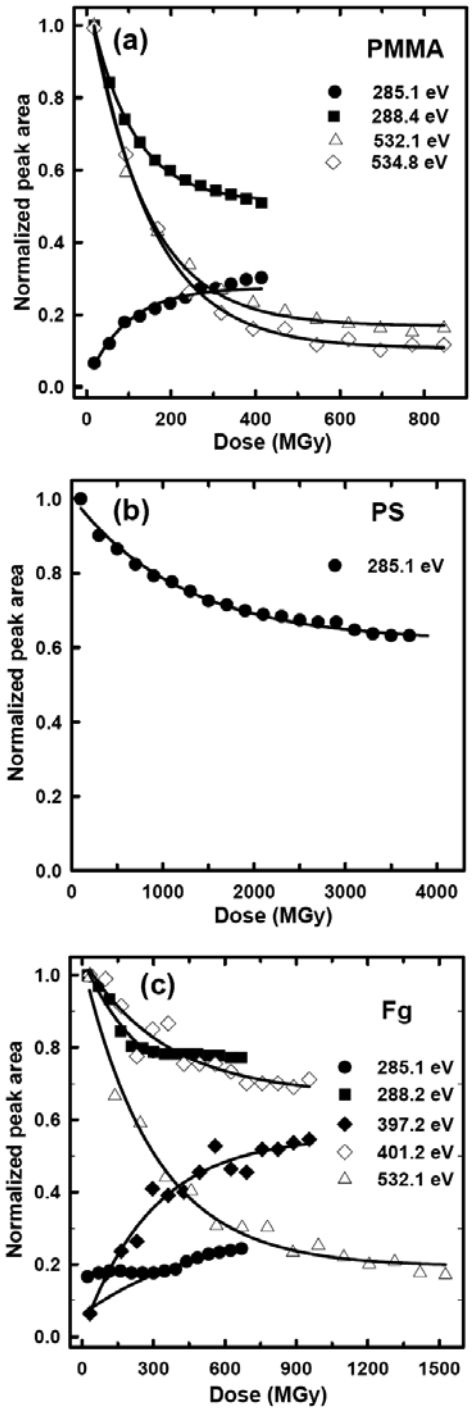

Fig. 5 Damage versus dose curves for (top) PMMA, (middle) PS and (lower) Fg derived from X-PEEM spectral measurements at the C 1s, N 1s (Fg) and O 1s edges. See table 2 for details of the exposure energies and average dose rates used. The damage signal corresponds to the peak area as monitored at the photon energies listed in table 2. The solid curves are fits to exponentials from which the critical doses were derived.

the hydrocarbon contaminants are cracked and deposited on the sample surface, leading to an increase in the C 1s continuum signal. Initial dose – damage measurements on PS were negatively influenced by this effect. In order to avoid this problem in measuring the critical dose for PS, the exposure was performed at 285.1 eV where the absorbance of the hydrocarbon contaminants is low, the absorbance by PS is maximum, and thus the photo deposition rate is much less than the damage rate. When the exposure energy is 285.1 eV, carbon build-up did not occur, even at the highest radiation dose used. However, when irradiation was performed at 320, 300 and 390 eV there were large increases in the C 1s continuum signal at the doses needed to visibly damage PS. When PS is damaged at 285.1 eV in STXM, there is a significant decrease of the absorbance since breaking the phenyl rings is the main consequence of the radiation damage (see section 4). In order to account for the changing absorbance, the dose was evaluated by integrating the optical density over the exposure time using the following equation:

$$S_{OD} = \frac{\int_0^t (y_0 + ce^{-bt})dt}{t} = \frac{y_0 t + \frac{c}{b}(1 - e^{-bt})}{t} \qquad \text{(eqn. 4)}$$

where S_{OD} is the integrated optical density up to time, t and y_0, c and b are fitting constants. The critical dose for chemical damage to PS is much larger than that for PMMA. This is as expected since it is much more difficult to break the stable phenyl group than to remove CO_2 from PMMA. The critical dose for PS derived from this measurement is 1200(180) MGy.

Figure 5c presents the damage versus dose curves for fibrinogen (Fg) as monitored at five energies around the C 1s, N 1s and O 1s edges. The signals at 288.2 eV (C 1s $\rightarrow \pi^*_{C=O}$) and 285.1 eV (C1s $\rightarrow \pi^*_{C=C}$) show complicated non-exponential signals. This could be due to the interplay of a number of different damage processes, such as damage and rearrangement of amide groups, damage of radiation sensitive R-groups etc. which could have quite different characteristic doses such that multiple exponential are required to fit the dose-damage curve. In these cases, the curve fitting was performed on that sub-set of the data points which best represents a single exponential change in the intensities of the C 1s $\rightarrow \pi^*_{C=O}$ and C 1s $\rightarrow \pi^*_{C=C}$ peaks. As with PMMA, the critical doses for damage of Fg at different edges are comparable except for the change in the C 1s $\rightarrow \pi^*_{C=C}$ signal. The derived critical doses are intermediate between those for PS and PMMA.

Figure 6 shows the damage versus dose curves for PMMA, PS and Fg derived from STXM measurements at the C 1s edge. The samples were irradiated at 300, 285.1 and 300 eV respectively, while the damage was evaluated from changes in image contrast at 288.45 (C 1s $\rightarrow \pi^*_{C=O}$ transition) for PMMA, 285.1 (C 1s $\rightarrow \pi^*_{C=C}$ transition) for PS, and 288.2 eV (C 1s $\rightarrow \pi^*_{C=O}$ amide transition) for fibrinogen. In Fig. 6 the damage signals for the three molecules are presented after normalization to the saturation level for ease of comparison. The critical doses derived from fitting these curves are listed in table 3, i.e. the critical doses for PMMA, PS and Fg in STXM are 67(10), 1260(190) and 298(45) MGy, respectively. The relative ordering of the critical doses is the same as found in X-PEEM. PMMA is by far the most sensitive of the 3 materials, with Fg more

sensitive (lower critical dose) than PS.

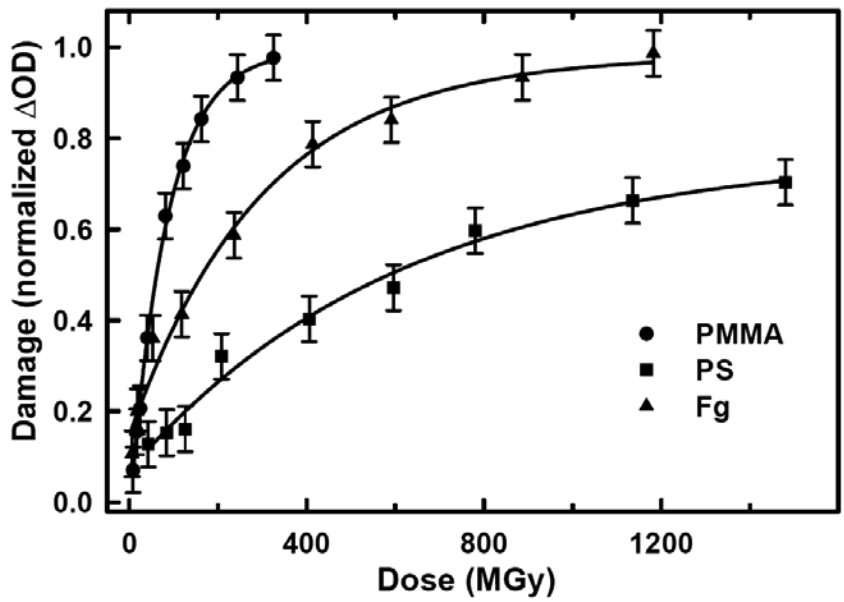

Fig. 6 Damage versus dose curves for PMMA, PS and Fg derived from STXM damage pattern spectral measurements at the C 1s edge. The exposure energy and dose rates are listed in table 3. The damage signal, which is the change in optical density monitored at the photon energies listed in table 3, tracks the amount of damaged product and thus integrates over possible different damage rates for different reactions. To allow comparison the damage signals are normalized to a value of 1 at the signals for infinite dose (see text).

While the trends in relative damage rates are similar for the two different microscopies, there are still some differences between the critical doses derived from the two techniques. This could be related to the different sample environments, combined with the very different doses needed to damage each polymer. The sample is in a very clean UHV environment in X-PEEM whereas the sample is in He at 1/3rd of atmospheric pressure in the STXM. This environmental change could also affect aspects of the secondary damage process such as electron transport. It is also possible there are an undetected systematic errors, such as detection efficiency (ε) or calibration of the incident flux (I_0). Finally there are large differences in the dose rate - X-PEEM dose rates (100-500 kGy/s) are three orders of magnitude smaller than those of STXM (300 - 600 MGy/s) and it is possible that the critical dose changes as a function of dose rate.

The relative damage rates for these three materials are PMMA > Fg > PS, or conversely, the critical dose is the smallest for PMMA and the largest for PS. These measurements monitor the fast chemical change and ignore slower processes such as mass loss. Zhang et al. [35] and Coffey and Ade [36] considered both processes, and showed that mass loss occurs at a much slower rate. Since the motivation for this study is to determine critical doses to guide chemical analysis (i.e. doses below that which

significantly modifies the NEXAFS spectrum), we consider our operational definition of the critical dose as the appropriate one to use. Note that mass loss has little effect in these X-PEEM measurements since the sample is ~40 nm thick, whereas the sampling depth is less than 10 nm and thus there is always material (albeit damaged) from deeper in the sample even when mass loss is occurring. The mass loss is readily detected in STXM since it samples the full thickness of the film.

4. Chemical changes from radiation damage as probed by NEXAFS

Figure 7 compares the C 1s spectra of undamaged and heavily damaged PMMA, PS and Fg from STXM. The radiation damage induced changes in the NEXAFS spectra are the same in STXM and X-PEEM and thus the same structural changes are occurring. In PMMA the most prominent change is the decrease in the 288.45 eV peak corresponding to loss of C 1s $\rightarrow \pi^*_{C=O}$ transitions as $COOCH_3$ or CO_2 is removed. At the same time, signal grows at 285.1 eV peak, the C 1s(C=C) $\rightarrow \pi^*_{C=C}$ transition, associated with re-organization and introduction of an unsaturated C=C bond. A third aspect is the disappearance of a weak peak at 290 eV and the C 1s $\rightarrow \sigma^*_{C=O}$ signal at 296 eV.

Radiation damage in PS takes the form of loss of intensity at the 285.1 eV C 1s(C=C) $\rightarrow \pi^*_{C=C}$ transition associated with damage to the phenyl ring, and a simultaneous increase in signal at 284.5 eV, attributed to dehydrogenation of the saturated backbone chain. The destruction of the aromatic rings is also indicated by loss of the C 1s $\rightarrow 2\pi^*$ transition (289 eV) and the double peaked C 1s $\rightarrow \sigma^*_{C=C}$ continuum signals (293, 303 eV), both of which are characteristic of phenyl rings [51]. The C 1s continuum intensity stays constant with dose indicating that there is negligible mass loss during radiation damage of PS, a result also reported by Coffey et al. [36]. A very weak signal grows at 286.5 eV. It is assigned to C 1s(C=O) $\rightarrow \pi^*_{C=O}$ transitions in carbonyls probably formed from oxidation of PS, since residual oxygen and oxygen-containing contaminants may be present during STXM measurements.

Radiation damage of Fg is dominated by loss of the C1s $\rightarrow \pi^*_{C=O}$ transition at 288.2 eV. In this case, CO_2 is not likely to be a dominant radiation product since there is no oxygen atom adjacent to the carbonyl. C=N double bond formation and elimination of water are more likely. The formation of C=N bonds is consistent with the growth of signals at 398 - 399 eV (N 1s $\rightarrow \pi^*_{C=N}$ transitions, see below) and at 287 eV (C 1s $\rightarrow \pi^*_{C=N}$ transitions) [52]. There is relatively little, if any, increase in signal at 285 eV consistent with the presence of relatively few saturated CH-CH linkages in proteins which are the structures that are susceptible to radiation induced dehydrogenation.

Figure 8 compares the N 1s spectra of damaged and undamaged Fg and the O 1s spectra of damaged and undamaged Fg and PMMA. The signature of radiation damaged proteins at the N 1s edge is a decrease in intensity at 401.2 eV, the N 1s $\rightarrow \pi^*_{C=O}$ amide transition [53], and the creation of two sharp signals at 398 and 399 eV. The latter peaks are attributed to formation of C=N bonds with different local environments. Mass loss during radiation damage of Fg is also evident since the N 1s $\rightarrow \sigma^*$ transition at 403 eV and the N 1s continuum intensities decrease significantly. This probably involves evolution of NH_3. At the O 1s edge the O 1s $\rightarrow \pi^*_{C=O}$ transition at 532.1 eV is selectively

lost, and there is large loss of oxygen atoms, as indicated by the decrease in the O 1s continuum signal. The damage observed at the O 1s edge for PMMA parallels that seen in the C 1s edge. In particular, the O 1s (C=O) $\rightarrow \pi^*_{C=O}$ transition decreases in intensity, as does the O 1s (OCH_3) $\rightarrow \pi^*_{C=O}$ transition at 534.8 eV. Mass loss in PMMA is much more visible in the O 1s than the C 1s edge since all of the oxygen atoms in a given repeat unit are lost when CO_2 is evolved.

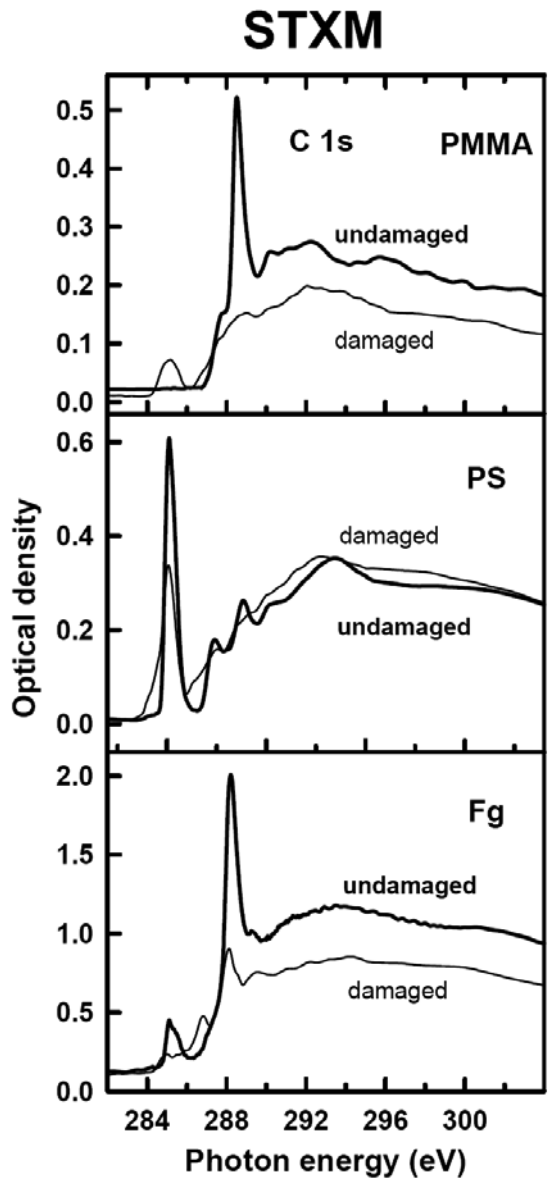

Fig. 7 Changes with radiation damage in the C 1s spectra recorded by STXM for PMMA, PS and Fg. The thicker line corresponds to the undamaged material, while the thinner line corresponds to a heavily radiation damaged sample. Mass loss is indicated by changes in the continuum intensity above 296 eV.

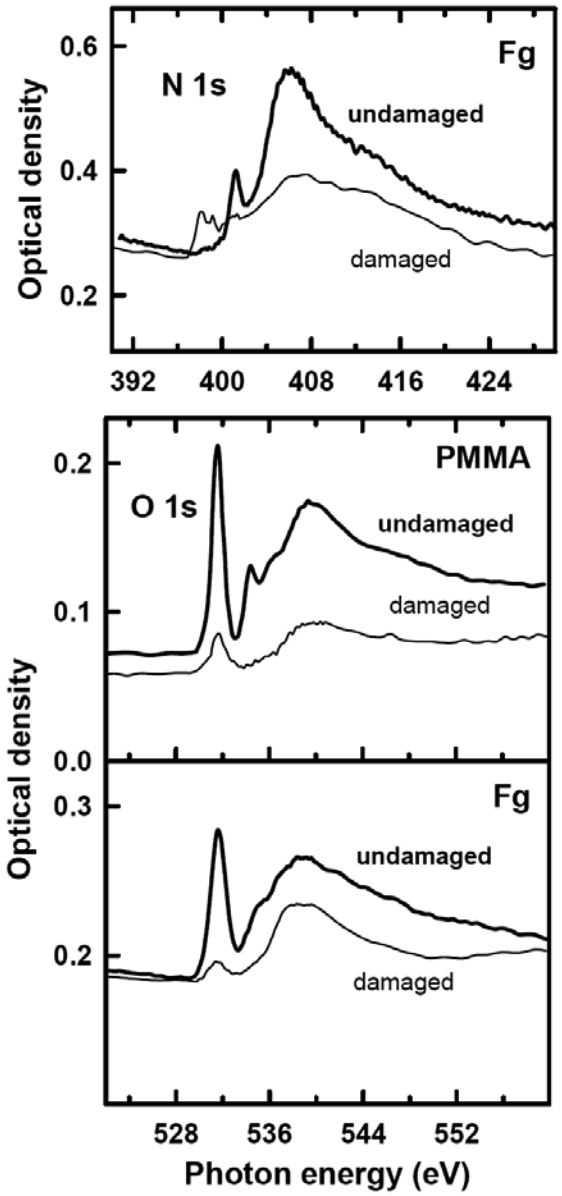

Fig. 8 Changes with radiation damage in the N 1s spectra of Fg recorded by STXM, and in the O1s spectra of PMMA and Fg by STXM. The thicker line corresponds to the undamaged material, while the thinner line corresponds to a heavily radiation damaged sample. Mass loss is indicated by changes in the continuum intensities.

Figure 9 presents some possible reactions involved in the radiation damage of these three materials. These suggestions are based on the spectral changes observed. **9a** presents some possible pathways for radiation damage of PMMA. The first damage pathway involves the loss of the ester side group and 1,2 H-migration, leading to formation of C=C bonds in the main chain of the polymer. The second pathway also involves the loss of ester group and then the main chain is cleaved to form an end group

with a C=C bond. This main-chain scission was proposed by David et al. [54]. These two possible pathways would result in a decrease in the intensity of the 288.4, 532.1 and 534.8 eV peaks, and the creation of signal at 285.1 eV. The third possible pathway involves decarboxylation, which would cause decreased intensity of the 288.4, 532.1 and 534.8 eV peaks, the major spectral changes. Since there are different pathways contributing to two different spectral changes in the C 1s spectrum, it is possible that the dose-damage rate derived from spectral change at 288.4 eV and 285.1 eV will differ. The critical dose for C=O loss is somewhat higher than that for C=C growth as derived by X-PEEM measurements.

Figure 9b presents three possible damage pathways for PS. The first one involves dehydrogenation of the C-C backbone. Typically the C 1s $\rightarrow$ $\pi^*_{C=C}$ transition for backbone unsaturation comes at lower energy than the $\pi^*_{C=C}$ in aromatic rings. Thus the appearance of the low energy shoulder at 284.5 eV may be explained this way. The second pathway represents damage to the rings where one or more of the double bonds are saturated by hydrogen generated from the first pathway, or, more likely, by abstraction of H from the backbone of adjacent PS chains or phenyl rings. Breakage of the aromatic ring structure is a surprisingly important reaction, which leads to the observed decrease in the main $1\pi^*$ peak and creation of lower energy $\pi^*_{C=C}$ signals. Mass loss could occur by elimination of hydrocarbon fragments, as represented by the third pathway. However, this is a low probability process since there is negligible change in the C 1s continuum intensity.

Figure 9c shows proposed reactions for radiation damage to the fibrinogen protein. While some loss of the 288.2 eV $\pi^*_{C=O}$ feature is undoubtedly associated with loss of CO_2 from the acid terminal end, this is a very small portion of the total protein. Thus a damage reaction, such as that shown in Fig 9c, which leads to loss of the C=O bond and formation of a C=N bond is required, and would be consistent with the formation of C 1s $\rightarrow\pi^*_{C=N}$ and N 1s $\rightarrow$ $\pi^*_{C=N}$ excitation signals. More than one structure containing C=N bonds can be envisaged, and this is suggested by the presence of fine structure in the 399-400 eV region of the spectrum of damaged fibrinogen. Note that both the N 1s and O 1s continuum intensities change significantly, indicating large mass loss. This suggests contributions from a reaction that involves degradation of the protein and generation of small molecules, such as CO_2, NH_3 and amino acids. The full set of radiation damage reactions in proteins is very complicated and probably impossible to figure out in detail using only NEXAFS spectroscopy. For example, a number of studies of the radiation damage chemistry of individual amino acids [34, 55-57] have shown that the decomposition induced by soft X-rays follows a number of pathways, including dehydration, decarboxylation, decarbonylation, deamination and desulfurization, accompanied by desorption of H_2, H_2O, CO_2, CO, NH_3 and H_2S with rates depending on the specific amino acid. In general, while these various reactions are consistent with the observed spectral changes, there are many other possible structures that could also give rise to the changes. Given the probably very reactive character of the radicals and ions produced in X-ray ionization and subsequent secondary events, a wide variety of reaction products may be formed.

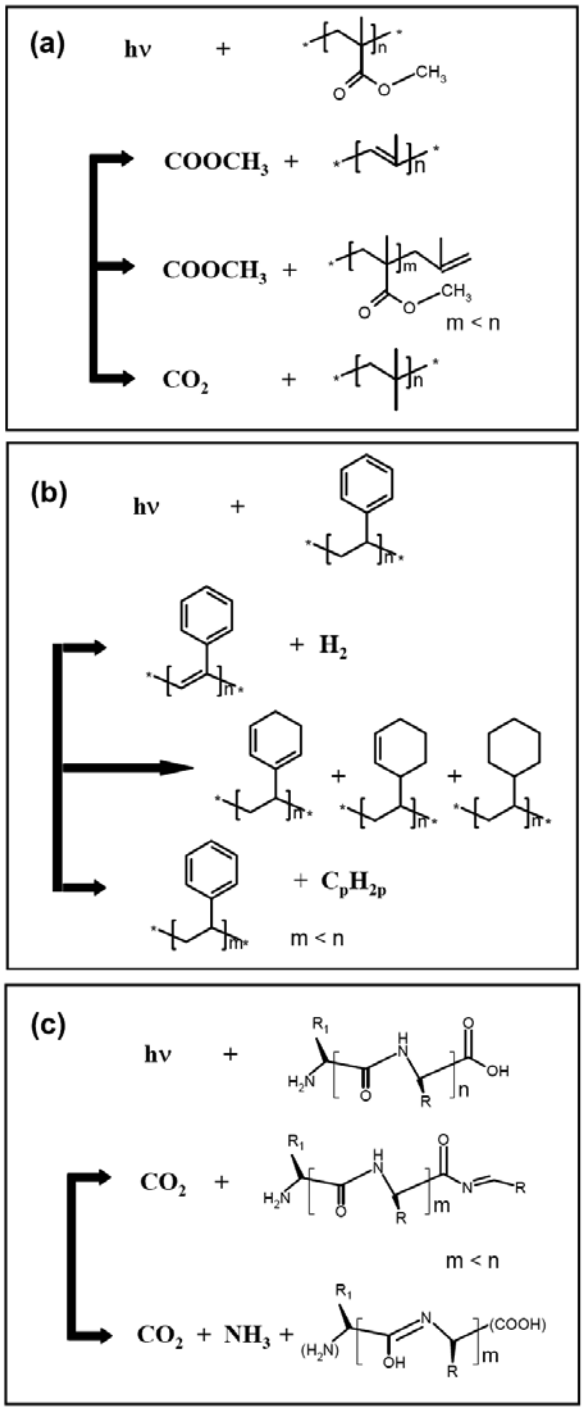

Fig. 9 Proposed reactions for radiation damage of **(a)** PMMA, **(b)** PS and **(c)** Fg.

Although radiation damage to polymers and other materials initiated by soft X-rays is a complicated process with many contributing factors, it can be generally characterized by two phases, i.e. the initial photoabsorption and femtosecond scale

electronic decay at the site of the X-ray absorption (a single atom), and subsequent secondary processes [58] on a longer time scale (ps to seconds) which produce secondary electrons, free radicals and ions. These particles extend the range of the damage [59] and are responsible for creating a cascade of damage to the irradiated material. The transport range of electrons is limited to a few tens of nanometers at most due to their strong interactions in condensed media. It is probably energetic radicals or ions that are responsible for the longer range effects since they are much more damaging and there is the possibility of chain processes. Reaction of these radicals and ions with nearby molecules can create new radicals/ions thereby setting up a chain reaction which can transfer the damage to regions far (~100 nm) from the initial absorption site. This process can be viewed as radical or ion initiated chain depolymerization or fragmentation. Another factor that might contribute is localized heating and associated thermal damage. However this has been shown to be a minor effect [59].

The soft X-ray radiation damage studies of this work are not only essential to X-ray spectromicroscopy analysis of radiation sensitive materials such as polymers and biological samples, but also may have potential applications in X-ray lithography and other types of nanofabrication involving surface or bulk chemical modification by soft X-rays. We have demonstrated a novel method with STXM that adds chemical selectivity to lithography. Specifically e X-ray absorption in a bilayer [59] or trilayer [60] polymer system is used to pattern wirg chemically selectivity through radiation damage to each polymer layer without affecting other layers. The other feature of this method is the direct-write capability, which is controlled by a pattern generation program, incorporated into the microscope control and data acquisition software. Input files for pattern generation consist of lists of (x, y, t, E) values for each pixel. This approach was used to make the 3x3 patterns of pads covering a range of doses which were used for quantitative dose-damage analysis in this work. This has made radiation damage studies more efficient with STXM.

5. Recommended procedures for X-ray microscopy studies of radiation sensitive samples

1. Identify the more damage-sensitive chemical components in the system under study. Usually inorganic materials are more robust under radiation than organic materials. Among the latter, saturated compounds tend to be more radiation sensitive than unsaturated compounds. Species with C-O single and double bonds are also quite sensitive.
2. Use the least damaging sample environment possible (in the STXM, this is either a low vacuum (P~ 0.1 torr), or 1/3 atm pressure of He).
3. When it is clear radiation damage will be critical, measure the critical dose using procedures similar to this work, and use that as a guideline for measurement protocols. Typically we find 20% of the critical dose as a practical limit to acceptable levels damage.
4. Use the lowest dose possible to survey the sample for interesting sample regions.
5. Adjust the dose on the sample through slits or dwell time to keep the dose below acceptable limits. Within that limit, adjust the experimental conditions to provide best

possible statistics, spatial and spectral resolution

6. In STXM, image sequences [49] give the best results, with line scan spectra often adequate but point spectra in fully focused mode rarely being appropriate. If the full spatial resolution is not needed, a slight defocus of the STXM beam can be very helpful at avoiding radiation damage.
7. After each analytically critical measurement, check if radiation damage occurs by recording an image at a damage sensitive energy.

6. Summary

Quantitative radiation damage rates of poly(methylmethacrylate), polystyrene and fibrinogen have been measured in an X-ray photoemission electron microscope (X-PEEM) and in a scanning transmission x-ray microscope (STXM). Similar critical dose values were obtained for both microscopes. The critical doses for PMMA damage (the only species for which literature data is available) are in good agreement with literature measurements of unannealed PMMA [35,36]. The order of sensitivity to X-ray radiation is PMMA > Fg > PS. The spectral changes in the C 1s, N 1s and O 1s regions have been used to deduce possible reactions involved in the damage chemistry.

Acknowledgements: This research is supported by NSERC (Canada) and the Canada Research Chair Program. Cynthia Morin acknowledges the support of an ALS graduate fellowship during which time much of this work was performed. We thank X. Zhang and T. Araki for assistance with the measurements. Construction and operation of the STXM 5.3.2 microscope is supported by NSF DMR-9975694, DOE DE-FG02-98ER45737, Dow Chemical, NSERC and the Canadian Foundation for Innovation. We thank David Kilcoyne, the 5.3.2 beamline scientist for his contributions to developing and maintaining the instrument. The Advanced Light Source is supported by the Director, Office of Energy Research, Office of Basic Energy Sciences, Materials Sciences Division of the U.S. Department of Energy, under Contract No. DE-AC03-76SF00098.

Supplementary material: On-line supporting information and figures describe in detail the methodology used to determine the absorbed dose for X-PEEM and for STXM, and an example is provided.

References

1. C.L. Greenstock, Med. Hypoth. 41 (1993) 473.
2. E.S. Kempner, J. Pharm. Sci. 90 (2001) 1637.
3. A. Gonzalez, A.W. Thompson, C. Nave, Rev. Sci. Instrum. 63 (1992) 1177.
4. J.R. Srour, C.J. Marshall, P.W. Marshall, IEEE Trans. Nucl. Sci. 50 (2003) 653.
5. R.L. Clough, S.W. Shalaby (Eds.), Radiation Effects on Polymers, ACS Symposium Series 475 (1991); *ibid*, Irradiation of Polymers: Fundamentals and Technological Applications, ACS Symposium Series 620 (1996).
6. B.P. Tonner, G.R. Harp, S.F. Koranda, J. Zhang, Rev. Sci. Instrum. 63 (1992) 564.
7. G. De Stasio, M. Capozi, G.F. Lorusso, P.A. Baudat, T.C. Droubay, P. Perfetti, G. Margaritondo, B.P. Tonner, Rev. Sci. Instrum. 69 (1998) 2062.

8. S. Anders, H.A. Padmore, R.M. Duarte, T. Renner, T. Stammler, A. Scholl, M.R. Scheinfein, J. Stöhr, L. Séve, B. Sinkovic, Rev. Sci. Instrum. 70 (1999) 3973.
9. E. Bauer, J. Electron Spectrosc. Relat. Phenom. 114-116 (2001) 975.
10. J. Kirz, H. Rarback, Rev. Sci. Instrum. 56 (1985) 1.
11. H. Rarback, D. Shu, S.C. Feng, H. Ade, J. Kirz, I. McNulty, D.P. Kern, T.H.P. Chang, Y. Vladimirsky, N. Iskander, D. Attwood, K. McQuaid, S. Rothman, Rev. Sci. Instrum. 59 (1988) 52.
12. T. Warwick, K. Franck, J.B. Kortright, G. Meigs, M. Moronne, S. Myneni, E. Rotenberg, S. Seal, W. F. Steele, H. Ade, A. Garcia, S. Cerasari, J. Denlinger, S. Hayakawa, A.P. Hitchcock, T. Tyliszczak, J. Kikuma, E.G. Rightor, H.-J. Shin, B.P. Tonner, Rev. Sci. Instrum. 69 (1998) 2964.
13. H. Ade, in: J.A.R. Samson, D.L. Ederer (Eds.), Experimental Methods in the Physical Sciences, Vol. 32, Academic Press, New York, 1998, p. 225.
14. H. Ade, S.G. Urquhart, in: T.K. Sham (Ed.), Chemical Applications of Synchrotron Radiation, World Scientific Publishing, Singapore, 2002, p. 285.
15. A.L.D. Kilcoyne, T. Tyliszczak, W.F. Steele, S. Fakra, P. Hitchcock, K. Franck, E. Anderson, B. Harteneck, E.G. Rightor, G.E. Mitchell, A.P. Hitchcock, L. Yang, T. Warwick and H. Ade, J. Synchrotron Rad. 10 (2003) 125.
16. J.R. Lawrence, G.D.W. Swerhone, G.G. Leppard, T. Araki, X. Zhang, M.M. West, A.P. Hitchcock, Appl. Envir. Microbiol. 69 (2003) 5543.
17. I.N. Koprinarov, A.P. Hitchcock, C.T. McCrory, R.F. Childs, J. Phys. Chem. B 106 (2002) 5358.
18. I.N. Koprinarov, A.P. Hitchcock, W.H. Li, Y.M. Heng, H.D.H. Stöver, Macromolec. 34 (2001) 4424.
19. T. Araki, A.P. Hitchcock, F. Shen, P. Chang, M. Wang, R.F. Childs, J. Biomater. Sci. Polymer Edn. 16 (2005) 611.
20. C. Morin, H. Ikeura-Sekiguchi, T. Tyliszczak, R. Cornelius, J.L. Brash, A.P. Hitchcock, A. Scholl, F. Nolting, G. Appel, A. D. Winesett, K. Kaznacheyev, H. Ade, J. Electron Spectrosc. Relat. Phenom. 121 (2001) 203.
21. A.P. Hitchcock, C. Morin, Y.M. Heng, R.M. Cornelius, J.L. Brash, J. Biomater. Sci. Polymer Edn. 13 (2002) 919.
22. C. Morin, A.P. Hitchcock, R.M. Cornelius, J.L. Brash, S.G. Urquhart, A. Scholl, A. Doran, J. Electron Spectrosc. Relat. Phenom. 137-140 (2004) 785.
23. L. Li, A.P. Hitchcock, N. Robar, R. Cornelius, J.L. Brash, A. Scholl, A. Doran, J. Phys. Chem. B 110 (2006) 16763.
24. J. Kirz, C. Jacobsen, M. Howells, Q. Rev. Biophys. 28 (1995) 33.
25. J. Maser, A. Osanna, Y. Wang, C. Jacobsen, J. Kirz, S. Spector, B. Winn, D. Tennant, J. Micros. 197 (2000) 68.
26. Y. Wang, C. Jacobsen, J. Maser, A. Osanna, J. Micros. 197 (2000) 80.
27. J.A. Brandes, C. Lee, S. Wakeham, M. Peterson, C. Jacobsen, S. Wirick, G. Cody, Marine Chem. 92 (2004) 107.
28. M.G. Anderson, T. Haraszti, G.E. Petersen, S. Wirick, C. Jacobsen, S.W.M. John, M. Grunze, Micron 37 (2006) 689.
29. O. Dhez, H. Ade, S.G. Urquhart, J. Electron Spectrosc. Relat. Phenom. 128 (2003)

85.
30. A. Schoell, Y. Zou, D. Huebner, S.G. Urquhart, T. Schmidt, R. Fink, E. Umbach, J. Chem. Phys. 123 (2005) 044509.
31. G. Schneider, Ultramicroscopy 75 (1998) 85.
32. T. Beetz, C. Jacobsen, J. Synchrotron Rad. 10 (2002) 280.
33. E.G. Rightor, A.P.Hitchcock, H.Ade, R.D. Leapman, S.G. Urquhart, A.P.Smith, G. Mitchell, D. Fischer, H.J. Shin, T. Warwick, J. Phys. Chem. B 101 (1997) 1950.
34. Y. Zubavichus, O. Fuchs, L. Weinhardt, C. Heske, E. Umbach, J.D. Denlinger, M. Grunze, Radiat. Res. 161 (2004) 346.
35. X. Zhang, C. Jacobsen, S. Lindaas, S. Williams, J. Vac. Sci. Technol. B 13 (1995) 1477.
36. T. Coffey, S.G. Urquhart, H. Ade, J. Electron Spectrosc. Relat. Phenom. 122 (2002) 65.
37. D. Veseley, D. Finch, in: G. J. Tatlock (Ed.), Electron Microscopy and Analysis 1985, Hilger, Bristol, 1985, p. 7.
38. K. Dawes, L.C. Glover, in: J.E. Mark (Ed.), Effects of electron beam and γ-radiation on polymeric materials, Physical properties of polymers handbook, AIP Press, Woodbury, NY, 1996.
39. L.W. Hobbs, in: J.J. Hren, J.I. Goldstein, D.C. Joy (Eds.), Introduction to Analytical Electron Microscopy, Plenum Press, New York, 1987, p. 399.
40. L.C. Sawyer, D.T. Grubb, Polymer Microscopy, Chapman and Hill, New York, 1987.
41. T-Y. Teng, K. Moffat, J. Synchrotron Rad. 7 (2000) 313.
42. G. Beamson, D. Briggs, High Resolution XPS of Organic Polymers, Wiley, New York, 1992.
43. Silson Ltd. JBJ Business Park, Northampton Road, Blisworth, Northampton, UK, NN7 3DW.
44. R. Korde, C. Prince, D. Cunningham, R.E. Vest, E. Gullikson, Metrologia, 40 (2003) S145. Calibrated silicon photodiodes were obtained from International Radiation Detectors, 2527 West 237th Street Unit A, Torrance, CA 90505-5243.
45. T. Warwick, H. Ade, D. Kilcoyne, M. Kritscher, T. Tyliszczak, S. Fakra, A. Hitchcock, P. Hitchcock, H. Padmore, J. Synchrotron Rad. 9 (2002) 254.
46. Zone plate provided by the Centre for X-ray Optics, LBNL.
47. C. Jacobsen, S. Wirick, G. Flynn, C. Zimba, J. Micros. 197 (2000) 173.
48. B.L. Henke, E.M. Gullikson, J.C. Davis, At. Data Nucl. Data Tables 54 (1993) 181.
49. M. Zharnikov, S. Frey, K. Heister, M. Grunze, J. Electron Spectrosc. Relat. Phenom. 124 (2002) 15.
50. B.H. Frazer, B. Gilbert, B.R. Sonderegger, G. De Stasio, Surf. Sci. 537 (2003) 161.
51. J.A. Horsley, J. Stöhr, A.P. Hitchcock, D.C. Newbury, A.L. Johnson, F. Sette, J. Chem. Phys. 83 (1985) 6099.
52. E. Apen, A.P. Hitchcock, J.L. Gland, J. Phys. Chem. 97 (1993) 6859.
53. G. Cooper, M. Gordon, D.Tulumello, C.C. Turci, K. Kaznatcheev, A.P. Hitchcock, J. Electron Spectrosc. Relat. Phenom. 137-140 (2004) 795.
54. C. David, D. Fuld, G. Geuskens, Makromol. Chem. 139 (1970) 269; *ibid*,

Makromol. Chem. 160 (1972) 135; *ibid*, Makromol. Chem. 160 (1972) 347.
55. M.J. Boack, Y. Zhou, S.D. Worley, J. Chem. Phys. 100 (1994) 8392.
56. Y. Zubavichus, M. Zharnikov, A. Shaporenko, O. Fuchs, L. Weinhardt, C. Heske, E. Umbach, J.D. Denlinger, M. Grunze, J. Phys. Chem. A 108 (2004) 4557.
57. E. Sagstuen, A. Sanderud, E.O. Hole, Radiat. Res. 162 (2004) 112.
58. J. Cazaux, J. Microsc. 188 (1997) 106.
59. J. Wang, H.D.H. Stöver, A.P. Hitchcock, T. Tyliszczak, J. Synchrotron Rad. 14 (2007) 181.
60. J. Wang, H.D.H. Stöver, A.P. Hitchcock, J. Phys. Chem. C 111 (2007) 16330.

Chapter 6

Chemically selective soft X-ray patterning of single-layer and bilayer polymer films

This chapter presents experimental results of chemically selective soft X-ray damage and patterning of single-layer and bilayer polymer films, including a PMMA/PAN bilayer film, a PMMA-blend-PAN micro phase-separated film, a poly(MMA-co-AN) copolymer film and a PECA homopolymer film.

*Reprinted with permission from the Journal of Synchrotron Radiation 14 (**2007**) 181-190, Jian Wang, Harald D. H. Stöver, Adam P. Hitchcock, and Tolek Tyliszczak, "Chemically Selective Soft X-ray Patterning of Polymers", Copyright 2007, International Union of Crystallography.*

The author of this thesis prepared PMMA/PAN bilayer and PECA samples for this publication, performed part of the STXM experiments (in collaboration with Prof. A. P. Hitchcock and Prof. H. D. H. Stöver), analyzed all the STXM data and wrote the publication with assistance in later stages by Prof. A. P. Hitchcock and Prof. H. D. H. Stöver. PMMA-blend-PAN film and poly(MMA-co-AN) copolymer film were prepared by Prof. H. D. H. Stöver.

research papers

Journal of
Synchrotron Radiation

ISSN 0909-0495

Received 25 August 2006
Accepted 12 December 2006

Chemically selective soft X-ray patterning of polymers

Jian Wang,[a] Harald D. H. Stöver,[a] Adam P. Hitchcock[a]* and Tolek Tyliszczak[b]

[a]Department of Chemistry and Brockhouse Institute for Materials Research, McMaster University, Hamilton, ON, Canada L8S 4M1, and [b]Advanced Light Source, Lawrence Berkeley National Laboratory, Berkeley, CA 94720, USA. E-mail: aph@mcmaster.ca

The chemically selective modification of polymer mixtures by monochromated soft X-rays has been explored using the high-brightness fine-focused 50 nm beam of a scanning transmission X-ray microscope. Four different polymer systems were examined: a polymethylmethacrylate (PMMA) polyacrylonitrile (PAN) bilayer film; a PMMA-*blend*-PAN microphase-separated film; a poly(MMA-*co*-AN) copolymer film; and a poly(ethyl cyanoacrylate) homopolymer film. A high level of chemically selective modification was achieved for the PMMA/PAN bilayer; in particular, irradiation at 288.45 eV selectively removed the carbonyl group from PMMA while irradiation at 286.80 eV selectively reduced the nitrile group of PAN, even when these irradiations were carried out at the same (x,y) position of the sample. In the last two homogenous polymer systems, similar amounts of damage to the nitrile and carbonyl groups occurred during irradiation at either 286.80 or 288.45 eV. This is attributed to damage transfer between the C≡N and C=O groups mediated by primary electrons, secondary electrons or radical/ionic processes, aided by their close spatial proximity. Although the overall thickness of the bilayer sample at 70 nm is smaller than the lateral line spreading of 100 nm, the interface between the layers appears to effectively block the transport of energy, and hence damage, between the two layers. The origins of the line spreading in homogeneous phases and possible origins of the damage blocking effect of the interface are discussed. To demonstrate chemically selective patterning, high-resolution multi-wavelength patterns were created in the PMMA/PAN bilayer system.

© 2007 International Union of Crystallography
Printed in Singapore – all rights reserved

Keywords: soft X-ray; lithography; chemically selective; radiation damage; C 1*s* NEXAFS; PMMA; PAN; PECA.

1. Introduction

Current sub-micrometer and nanolithography techniques, such as X-ray or extreme ultraviolet projection lithography (Cerrina, 2000; Stulen & Sweeney, 1999), electron or ion beam lithography (Tseng *et al.*, 2003; Melngailis *et al.*, 1998), nanoimprint lithography (Guo, 2004) and scanning probe microscope-based lithography (Tseng *et al.*, 2005), do not explicitly use chemically selective interactions with multiple resist materials during pattern writing. Patterning processes can be classified into two categories: negative photoresists, which involve cross-linking, and positive photoresists, which involve main-chain scission and mass loss. All of these phenomena are a direct consequence of radiation damage to the polymers, the details of which depend on the kind of radiation used in the pattern-forming step of the lithography. However, in all methods developed to date the radiation damage is non-specific with respect to the chemical nature of the resist materials, and thus the patterning process is not chemically specific. Here we introduce a novel method that has the potential to add chemical selectivity to lithography, specifically the use of chemically selective X-ray absorption coupled with a specific substrate structure to confine the pattern (radiation damage) to specific chemical species. Many conventional resist polymers contain functional groups that have very strong resonant absorption at specific X-ray energies in the soft X-ray region (100–1000 eV). These may thus serve as a basis for chemically selective lithography, if appropriate multi-component substrate fabrication and exposure techniques can be developed. The nano-patterning technique demonstrated in this work may have potential applications in the manufacture of custom electronic circuits, micro-reactors and other types of nanofabrication.

Rates and mechanisms of radiation damage are important in many areas of science and technology and have been studied extensively (Weik *et al.*, 2000; Cherezov *et al.*, 2002; Sanche, 2002; Pease, 2003; Osetsky & Bacon, 2003; Trachenko, 2004; Sagstuen *et al.*, 2004; Cadet *et al.*, 2005; Joers *et al.*, 2006).

There are many aspects to radiation damage, such as the electronic and structural changes associated with the primary energy deposition; subsequent secondary processes associated with free electrons, inelastically scattered electrons, and radical or ionic fragments; transport processes of the products of the primary and secondary events; and ultimately thermal or chemical reactions such as oxidation and depolymerization. The aspect of radiation damage that is critical in any situation depends on the reason for carrying out a potentially damaging radiation exposure, and the sensitivity of subsequent measurements to the consequences of the damage. A hierarchy of effects ordered by increasing dose might be: biological viability, long-range structural change, short-range chemical change, mass loss. The focus of this work is chemical change since this is the basis for chemically selective lithography.

Radiation damage is a common and critical phenomenon in high-spatial-resolution X-ray microscopy (Rightor *et al.*, 1997; Zhang *et al.*, 1995; Beetz & Jacobsen, 2003; Coffey *et al.*, 2002). As soft X-ray microscopy techniques such as scanning transmission X-ray microscopy (STXM) (Ade, 1998; Ade & Urquhart, 2002) and X-ray photoelectron emission microscopy (X-PEEM) (Bauer, 2001) are applied increasingly frequently to radiation-sensitive polymer and biological samples (Koprinarov *et al.*, 2001; Hitchcock *et al.*, 2002; Morin *et al.*, 2004), it is important to understand both the nature and the rate of radiation damage by soft X-rays in order to achieve chemically meaningful microanalysis. Optimal strategies for acquisition of detailed spectroscopy, quantitative determination of radiation damage kinetics, and a better understanding of damage mechanisms by soft X-rays are not only significant for soft X-ray spectromicroscopy analysis, but are also the foundations for the development of chemically selective patterning or lithography. Jacobsen and co-workers have made several quantitative studies of radiation damage in the Stony Brook STXM at NSLS, including quantitative studies of the damage rate for polymethylmethacrylate (PMMA) at room and liquid-nitrogen temperatures and at both the C 1*s* and O 1*s* edges (Zhang *et al.*, 1995; Beetz & Jacobsen, 2003). Coffey *et al.* (2002) also used C 1*s* near-edge X-ray absorption spectroscopy (NEXAFS) recorded in STXM to study radiation chemistry of a series of common polymers that contain the carbonyl functional group. They all used a first-order kinetics model to characterize radiation damage in terms of a critical radiation dose parameter, which is the dose required to attenuate the intensity of a specific spectroscopic feature to (1/e) or 37% of its initial value.

Here we present the results of a study aimed at optimizing the sample composition, structure and procedures for chemically selective patterning of polymers by monochromatic soft X-rays. The desired polymer materials should have strong, sharp, distinct characteristic absorption peaks such as $1s \rightarrow \pi^*$ transitions, which are shifted by at least 1 eV with respect to each other. There should also be a suitable damage rate in terms of a relatively low critical dose and a high molecular weight (>100 kDa) for better film-forming capability. Both the irradiation and the subsequent chemical analysis are performed using a ~50 nm focused beam in an interferometrically controlled scanning transmission X-ray microscope (Kilcoyne *et al.*, 2003). In this study, two polymer species, PMMA and polyacrylonitrile (PAN), were first independently measured with monochromated soft X-rays to acquire NEXAFS spectra and radiation damage information. The absorption spectra are characterized by a strong C $1s \rightarrow \pi^*_{C=O}$ absorption peak at 288.4 eV for PMMA and a strong C $1s \rightarrow \pi^*_{C\equiv N}$ absorption peak at 286.8 eV for PAN. Subsequently, chemically selective X-ray patterning was explored by using specific X-ray photon energies and radiation doses to confine the radiation damage at 288.4 eV to the C═O groups of PMMA and that at 286.8 eV to the C≡N groups of PAN. Four different mixed polymer film systems were then evaluated, with different spatial scales separating the carbonyl and nitrile groups: a PMMA-*on*-PAN bilayer film, a PMMA-*blend*-PAN microphase-separated film, a poly(MMA-*co*-AN) copolymer film and a poly(ethyl cyanoacrylate) (PECA) homopolymer film. The chemical structures of PMMA, PAN and PECA are illustrated in the scheme below. Energy-specific damage of C═O in PMMA at 288.4 eV and C≡N in PAN at 286.8 eV at the same (x,y) position of the sample was achieved only for the PMMA/PAN bilayer. The reasons for the failure in the other three cases, and the success in the bilayer are discussed. To demonstrate chemically selective patterning, several chemically selective patterns were created in the PMMA/PAN bilayer system.

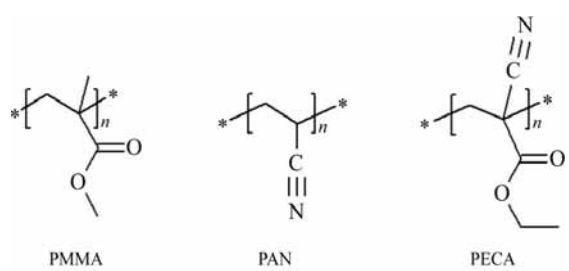

This paper is organized as follows. After describing experimental methods, the NEXAFS spectra for pure PMMA, pure PAN and four polymer film systems are presented. Then the chemical selectivity in radiation damage of the four different polymer film systems is presented. This is followed by demonstrations of chemically selective patterning in the PMMA/PAN bilayer system and a discussion of the physicochemical basis for the observations.

2. Experimental

2.1. Sample preparation

PMMA (M_w = 312 K, polydispersity index PDI = M_w/M_n = 1.01) was obtained from Polymer Source Inc. and PAN (M_w = 150 K) was obtained from Aldrich. Both were used without further purification. Free-standing films of the single polymers were made according to the following procedure. A 1 wt.% toluene solution of PMMA was prepared using anhydrous

toluene (Aldrich, 99.8%). Then a 50 µl drop was spun-cast (3000 r.p.m., 30 s) onto a freshly peeled mica surface of 2.5 cm × 2.5 cm. The film was dried in ambient atmosphere for 5 min and cut into 3 mm × 3 mm pieces on the mica surface, and then floated onto milli-Q water. A piece of the polymer was then transferred from the water surface to a degreased hexacomb grid, then was dried again in ambient atmosphere before being used for STXM measurements. For the single or multilayer films involving PAN, the solvent was dimethyl formamide (DMF) and the spun-cast PAN on mica was dried under vacuum at 343 K for 0.5 h to remove all of the DMF. The single-layer film thickness was 30–40 nm according to STXM measurements under the above conditions. Free-standing bilayer films of PMMA (upper) and PAN (lower) were fabricated by spin-coating PMMA from toluene onto a dried PAN film prepared as described above. Reversing the spin-coating sequence of the two polymers produced a microphase-separated film, PMMA-*blend*-PAN, owing to re-dissolution of the first-cast PMMA layer in the DMF solvent.

Poly(MMA-*co*-AN) was synthesized by free-radical co-polymerization (Ekpenyong & Okonkwo, 1983). Ethyl cyano-acrylate was obtained commercially (Instant Krazy Glue, Elmer's Products Inc. and Toagosei Co. Ltd) and polymerized on a glass slide by exposure to air to form PECA. A few milligrams of each sample were dissolved in toluene, then a 50 µl drop was placed on a Si_3N_4 window [750 µm × 750 µm window back-etched into a 7.5 mm × 7.5 mm × 200 µm silicon wafer chip coated with 75 nm of Si_3N_4 (Silson Ltd)]. When the solvent evaporated, polymer particles and film pieces were deposited on the Si_3N_4 surface. Thin uniform-thickness regions sufficiently large (1–2 µm) for the semi-quantitative radiation damage studies were found on these highly heterogeneous samples. A PECA film, uniform over a 10 µm × 10 µm area, was prepared by ultramicrotoming a solid block to form 60 nm-thick uniform films.

2.2. STXM

Experiments were performed using STXM at beamline 5.3.2 at the Advanced Light Source (Kilcoyne *et al.*, 2003; Warwick *et al.*, 2002). STXM uses a Fresnel zone plate to focus X-rays to a ∼50 nm point probe. The sample is raster scanned through the focused X-ray spot with synchronized detection of transmitted X-rays to measure the energy-dependent absorption by a volume pixel of material. The contrast in STXM images depends strongly on the nature of the chemical constituents and the X-ray energy; the dominant image-contrast mechanism is the variation of the inner-shell excitation or NEXAFS spectra of the constituents, although density and thickness distributions are also important. Radiation damage of the PMMA and PAN polymer samples was clearly observed when the accumulated exposure of the beam on a given spot of the sample (either in a single dwell or multiple shorter exposures) was larger than ∼100 ms with typical photon fluxes of 2–3 MHz in the focused spot. The dispersive entrance slit and both the dispersive and non-dispersive exit slits of the monochromator were adjusted to control the photon flux and dose rate on the sample. In STXM532 the entrance and dispersive exit slit control the energy resolution, while the combination of the two exit slits controls the spatial resolution. Since we form patterns using X-ray energies corresponding to strong relatively narrow absorption lines of the components, there is potentially some interplay between the energy resolution and the quantitative rates of pattern formation. However, in this case the energy resolution under even the least monochromated conditions (∼0.4 eV) is smaller than the resonance width (0.8–1.2 eV). Similarly, as discussed in detail later, the spatial resolution of our patterns (150–200 nm) is much worse than the spatial resolution of the microscope [40 nm with standard slits settings (60/30/30 µm) and 60 nm with the enlarged slits used for pattern writing (80/40/40) (Kilcoyne *et al.*, 2003)]. The line broadening is controlled by factors other than the exit slit settings. The damaged region was analyzed by imaging it at the photon energy giving the best contrast of the damaged material relative to the undamaged material, which was at the strong C 1*s* → π^* transitions (286.8 eV for PAN and 288.4 eV for PMMA). The NEXAFS spectra of the damaged and undamaged regions were acquired using an image sequence [stack (Jacobsen *et al.*, 2000)] with much lower photon flux. Reference spectra on absolute linear absorbance scales [*i.e.* optical density (OD) per nm thickness sample] were derived by scaling the spectra of the undamaged material to the X-ray absorption response in the regions of 275–282 eV and 320–350 eV, to match that of the linear X-ray absorption for the elemental composition of the sample derived from literature absorption coefficients (Henke *et al.*, 1993).

For STXM quantitative microanalysis, the Beer–Lambert law is obeyed, so the OD of a sample at any photon energy can be expressed as

$$\mathrm{OD} = -\ln(I/I_0) = \mu\rho l, \qquad (1)$$

where I and I_0 are the transmitted and incident X-ray photon flux, respectively, μ is the energy-dependent mass absorption coefficient, ρ is the polymer density, and l is the sample thickness. For radiation damage evaluation, the approach is to find the relationship between the damage in terms of OD change and the absorbed radiation dose a [in units of grays (Gy), where 1 Gy = 1 J kg^{-1}]. The dose (a) was obtained from

$$a = FEt/m = (I_0 - I)Et/m = I_0[1 - \exp(-\mathrm{OD})]Et/m, \qquad (2)$$

where F is the absorbed flux (absorbed photons per second) of a specific volume pixel (voxel), which is derived from the incident flux (I_0) and the OD at the exposure photon energy using equation (1), E is the photon energy, t is the exposure time and m is the mass of the voxel. The incident flux is measured in the absence of the sample and is corrected for the measured detector efficiency [30 ± 10% in the C 1*s* region (Kilcoyne *et al.*, 2003)]. A N_2 gas filter was used to ensure that the incident photon beam contained negligible higher-order components. This can be quite important in quantitative dose-damage studies for polymers containing N or O since the second-order photons impart a larger amount of energy per

absorbed photon and since there is a significant absorbance at the second-order energy.

In order to determine the critical dose for damage of a specific material from the measured damage-exposure data, the damage *versus* dose data were fit to postulated rate laws, such as a first-order kinetic process (Zhang *et al.*, 1995; Beetz & Jacobsen, 2003; Coffey *et al.*, 2002) which appears to be suitable in these cases where mass loss is relatively small and the damage is mainly chemical change,

$$D = D_\infty + A\exp(-a/a_c), \qquad (3)$$

where D is a relative measure of damage (*e.g.* the OD change at a damage sensitive energy), D_∞ is the absorbance that remains after the damage process saturates, A is a constant, a is the dose, and a_c is the first-order constant or the critical dose, which is the dose that attenuates a specific spectroscopic feature to 37% of its initial value. The detailed quantitative dose-damage evaluation for PMMA and other materials has been presented elsewhere (Wang *et al.*, 2007). Here we focus on radiation damage selectivity for different two-component polymer samples, and how to achieve chemically selective patterning.

The chemically selective patterning experiments were performed using a pattern generation program, incorporated into *STXM_control*, the microscope control and data-acquisition software. In this mode the sample is positioned with ~10 nm precision under laser interferometer control, to predefined (x,y) locations and then a fast-acting (~300 µs) in-vacuum piezo shutter is opened for a precise predefined position-dependent time interval to expose the sample to the flux of monochromated X-rays. With the slits typically used for pattern generation (80/40/40 µm), the energy resolution is ~400 meV and the spatial resolution is ~60 nm (Kilcoyne *et al.*, 2003). Input files for pattern generation consist of lists of (x,y,t,E) values for each pixel which are generated using routines in *aXis2000* (http://unicorn.mcmaster.ca/aXis2000.html). For multi-color patterns (exposures at multiple photon energies), color images are color separated and the individual components are used to generate pattern files for each color.

3. Results

3.1. Radiation damage for PMMA and PAN

The C 1*s* NEXAFS spectra for undamaged and heavily radiation damaged PMMA and PAN are presented in Fig. 1. For undamaged PMMA, the spectrum is characterized by the sharp strong C 1*s* $\rightarrow \pi^*_{C=O}$ transition at 288.45 eV; there are additional features at 292, 296 and 302 eV, arising from various C 1*s* $\rightarrow \sigma^*$ transitions, with that at 302 eV corresponding to C 1*s* $\rightarrow \sigma^*_{C=O}$ excitations. For heavily damaged PMMA, the 288.45 eV and 302 eV features disappear, and a new feature appears at 285 eV. (Note, for simplicity, when referring to the damage energy of PMMA we state 288.4 eV in the following, but this should be understood to be the $\pi^*_{C=O}$ peak maximum of 288.45 eV.) The 288.4 eV and 302 eV features disappear since the carbonyl and associated ester oxygen are removed by decarboxylation (ejection of CO_2). The 285 eV signal, which is associated with C 1*s* $\rightarrow \pi^*_{C=C}$ transitions, arises from C═C bonds formed in damaged parts of the polymer backbone. There is also considerable mass loss as indicated by the ~30% reduction of the C 1*s* continuum intensity. The significantly reduced absorption at energies below 284 eV in the damaged sample is consistent with a large loss of oxygen since the pre-C1*s* absorption is stronger for higher-Z elements.

The major spectral feature in the spectrum of undamaged PAN is the strong C 1*s* $\rightarrow \pi^*_{C\equiv N}$ absorption peak at 286.80 eV. This signal decreases as PAN is radiation damaged, in part owing to loss of CN (although there is much less mass loss in PAN than in PMMA) and in part owing to transformation of the C≡N triple bond to a C═N double bond or C—N single bond. Note that the associated $\sigma^*_{C\equiv N}$ transition at 306 eV is lost and there is the appearance of a broad peak at 301 eV which is likely associated with C 1*s* $\rightarrow \sigma^*_{C=N}$ transitions in the transformed material. With damage to PAN there is growth of a new feature at 285 eV, which is also associated with unsaturation in the polymer backbone, as in damaged PMMA. The intensity decrease in the continuum, *i.e.* the spectroscopic region above the inner-shell ionization potential, usually reflects mass loss upon radiation damage (Coffey *et al.*, 2002). Fig. 1 shows that PMMA undergoes apparent mass loss for completely radiation damaged as the continuum regime intensity decreases. For PAN the situation is different; there is

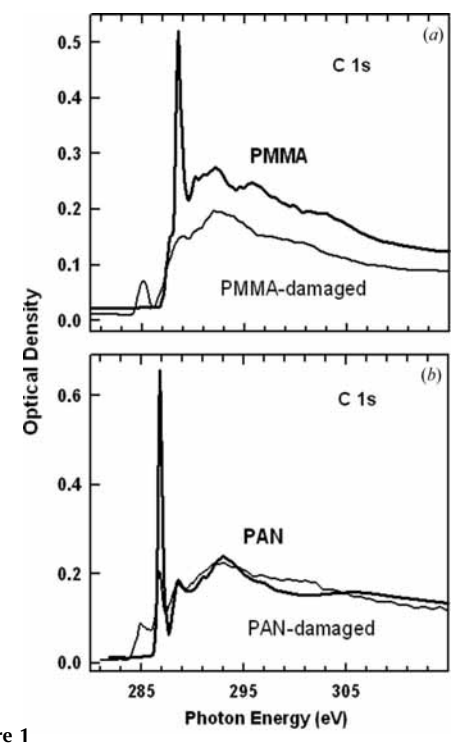

Figure 1
C 1*s* near-edge X-ray absorption fine structure (NEXAFS) spectra of undamaged and damaged PMMA (*a*) and PAN (*b*).

relatively little change in the C 1*s* continuum in the dose regime examined. This suggests that PAN does not suffer much mass loss during radiation damage.

Under similar irradiation conditions (incident photon flux, dose rate and comparable sample thickness *etc.*) the critical dose in terms of the change of the PMMA $\pi^*_{C=O}$ feature (destruction and loss of C═O groups) was determined to be $(\sim 60 \pm 8) \times 10^6$ Gy, while that of PAN associated with the change of the PAN $\pi^*_{C\equiv N}$ feature (destruction and loss of C≡N groups) was $(150 \pm 20) \times 10^6$ Gy. The critical dose of PMMA we have determined is comparable with the literature values (Zhang *et al.*, 1995; Coffey *et al.*, 2002), so the relative rate and sensitivity of the radiation damage for PMMA *versus* PAN are reliably estimated by these critical doses. The critical dose ratio was the factor used to determine the optimum exposure protocol for chemically selective damage or patterning of the samples containing the two functional groups. Detailed quantitative evaluation of the critical dose, comparison with literature values, and a discussion of the radiation chemistry of PMMA has been presented elsewhere (Wang *et al.*, 2007).

3.2. Chemically selective radiation damage

Given the large X-ray absorption coefficients of PAN and PMMA at their respective π^* resonance energies, one might naively expect that it would be possible to confine the damage to one or the other species by using monochromatic X-rays of corresponding energies. However, it is not only the initial deposition of energy that is important, but also the cascade of secondary processes (Cazaux, 1997). In fact, as shown below, it is a real challenge to retain the selectivity of the initial energy deposition process, and thereby achieve chemically selective X-ray radiation damage. We have explored this issue by examining four different polymer film systems which have different spatial scales separating carbonyl and nitrile groups: a PMMA-*on*-PAN bilayer film, a PMMA-*blend*-PAN micro-phase-separated film, a poly(MMA-*co*-AN) copolymer film and a PECA homopolymer film. Fig. 2 shows the C 1*s* NEXAFS spectra of three of these samples. The spectrum of the PMMA-*blend*-PAN sample is not included in Fig. 2 since that sample phase separated and thus contains distinct domains of essentially pure PMMA and PAN, which have C 1*s* spectra as given in Fig. 1. The PMMA/PAN bilayer film has the same π^* peak positions as single-layer PMMA (288.45 eV) and PAN (286.80 eV), but the ratio of the intensity of the $\pi^*_{C=O}$ to the $\pi^*_{C\equiv N}$ peak is higher, since the PMMA layer is thicker than the PAN layer. The π^* peak positions of poly(MMA-*co*-AN) are also the same as pure PMMA and pure PAN. Although this statistical copolymer may be nm-scale heterogeneous, at the scale of the STXM spatial resolution (50 nm) it is effectively homogeneous. The energies of the π^* peaks in the PECA sample are slightly different from those in PMMA and PAN. In particular, the C 1*s* $\rightarrow \pi^*_{C=O}$ feature (288.58 eV) is 0.13 (3) eV higher in energy than its counterpart in PMMA and the $\pi^*_{C\equiv N}$ feature (286.68 eV) is 0.12 (3) eV lower than its counterpart in PAN. These small but real chemical shifts are due to the electronic interaction between the carbonyl and nitrile groups since the two unsaturated functional groups are connected to the same carbon atom and thus their molecular orbitals interact (Stöhr, 1992).

The procedure initially used to explore chemically selective radiation damage consisted of writing lines at selected photon energies into a thin film of each system with the same slit settings and same dwell time per pixel. The four photon energies were 285.15 eV (neither species absorbs), 286.80 eV (only PAN absorbs), 288.45 eV (mainly PMMA absorbs, with a small PAN contribution) and 290.0 eV (both absorb) (note that the STXM532 energy scale is defined meaningfully to within 0.02 eV, and the PAN and PMMA peak energies are accurate to within 0.05 eV). Following this exposure sequence the region of the four lines was imaged at the same four photon energies to evaluate the radiation damage. Fig. 3 presents optical density images at the four photon energies, for the PMMA-*on*-PAN bilayer, the poly(MMA-*co*-AN) copolymer film and the PECA homopolymer film. The dark lines in the images at 286.8, 288.4 and 290 eV correspond to a decrease of optical density as radiation damage occurs, while the bright lines in the 285.1 eV image indicate increased optical density, associated with formation of C═C bonds in the polymer backbone upon radiation damage. Energy-specific damage of C≡N in PAN and C═O in PMMA was clearly achieved for the PMMA/PAN bilayer for irradiation at the respective absorption peaks. In that case, in the image recorded at 286.8 eV the line drawn at 286.8 eV is very dark, corresponding to the exposure at that energy. However, there is very little damage (only a faint line) at the same location in

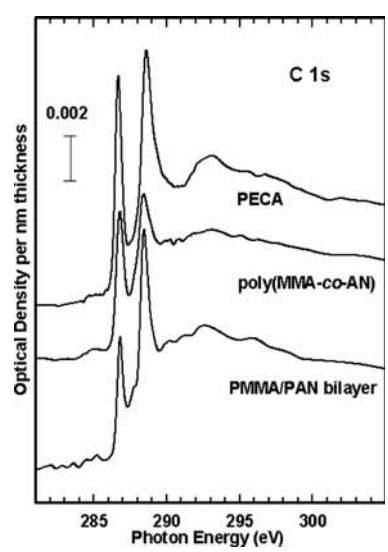

Figure 2
C 1*s* absolute linear absorption NEXAFS spectra (*i.e.* optical density per nm thickness sample) of PMMA-*on*-PAN bilayer, poly(MMA-*co*-AN) and PECA. These spectra were derived by scaling the originally recorded spectra to match that of the linear X-ray absorption for the elemental composition of the sample derived from literature absorption coefficients (Henke *et al.*, 1993).

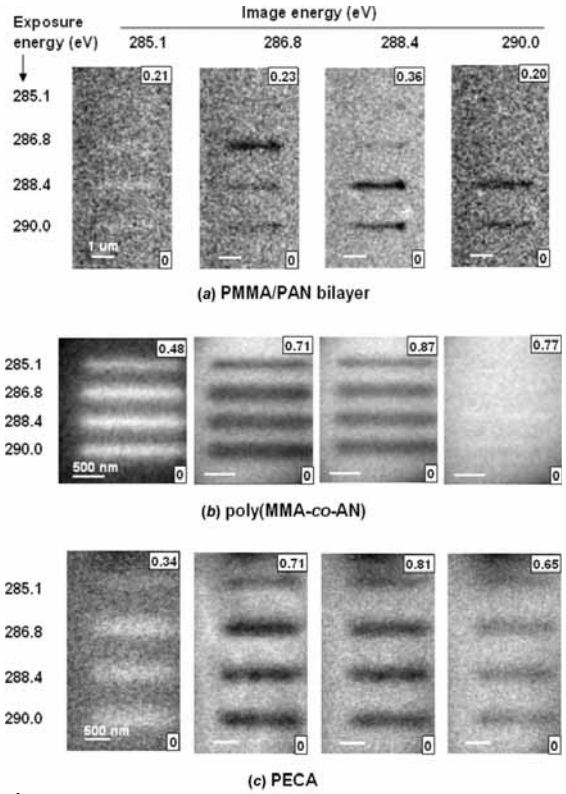

Figure 3
Optical density images of radiation damage of (*a*) PMMA/PAN bilayer, (*b*) poly(MMA-*co*-AN) and (*c*) PECA. These images are actually relative optical density images, which were converted from their transmission images by normalization to the maximum intensity of each individual transmission image. Four lines were exposed with the same slit settings, dwell time per pixel and pixel spacing, at four photon energies, respectively: 285.1 eV (neither species absorbs), 286.8 eV (only PAN absorbs), 288.4 eV (mainly PMMA absorbs, with a small PAN contribution) and 290.0 eV (both species absorb). The region of the sample exposed in this way was that imaged at the same four photon energies to evaluate the selectivity of radiation damage.

the image recorded at 288.4 eV. Similarly, in the image at 288.4 eV the line drawn at 288.4 eV is very dark corresponding to the exposure at that energy, while there is only a very faint damage line at the same location in the image at 286.8 eV. Thus we have demonstrated chemically selective damage for PAN and PMMA based on their differential absorption. Note that for this bilayer sample there is very little damage at the line exposed at 285.1 eV, while the line exposed at 290.0 eV results in damage that was imaged at both 286.8 and 288.4 eV indicating non-selective damage of the sample at 290 eV where both chemical species absorb relatively strongly. In the other two systems, similar amounts of damage to the nitrile and carbonyl groups occurred at 286.8 and 288.4 eV as indicated by the presence of two dark lines in each of the images at 286.8 and 288.4 eV. Exposure at 285.1 and 290.0 eV did not show any selective damage in these two samples. The failure to achieve chemically selective damage in the poly(MMA-*co*-AN) and PECA films is attributed to the close spatial proximity of the C≡N and C=O functional groups such that there is facile transfer of the initially absorbed energy between species *via* electrons and/or radicals and ions.

The range of damage spreading in PAN and PMMA was explored in the PMMA-*blend*-PAN microphase-separated film sample. Figs. 4(*a*) and 4(*b*) presents OD images at 286.8 and 288.4 eV for the same area of the sample. The contrast reversal indicates that, in this region of the sample, the continuous phase is PAN, while the isolated domains are PMMA. Note that other regions of the spun-cast film had the reverse phase segregation morphology, which was dictated by the local composition of the fluid as the DMF solvent evaporated. The full width at half-maximum (FWHM) of each line was derived by averaging orthogonal line profiles over a range of the line in each material. These FWHM values are then used as a measure of the range of damage migration under each condition in each material. The line width as a function of radiation dose for PMMA and PAN is plotted in Fig. 4(*c*). The width and thus the damage migration range increases in a non-linear fashion with increased radiation dose from ~100 nm to ~250 nm in PMMA and to a value above 300 nm in PAN. For the same dose the damage lines in PAN are noticeably wider than those of PMMA. The differences between line broadening in PAN and PMMA are more apparent when the line width is plotted as a function of ratio-to-critical dose (Fig. 4*d*) (the critical dose values used were 60×10^6 Gy for PMMA and 150×10^6 Gy for PAN). The increase in line width with increasing absorbed dose is roughly exponential, with an offset, suggesting that a pseudo-first-order kinetics model might be applicable. The offset value of 100–120 nm is rather larger than that expected from the spatial resolution of the STXM (50 nm). We interpret this in terms of a short-range low-dose damage process (perhaps the damage induced by photoelectron and high-energy secondary electrons) which occurs in addition to a slower longer-range damage spreading mechanism which may be radical/ion diffusion and depolymerization or some other effect (see §4). From Fig. 4(*c*) and especially Fig. 4(*d*), it would appear that the fit lines for the PAN and PMMA data are converging at the lowest dose to a value of ~120 nm. This suggests the short-range damage mechanism might be relatively similar in the two materials but that the long-range damage transport mechanisms differ appreciably (or there may be a similar mechanism but with very different rates for the two materials).

3.3. Chemically selective patterning

The selectivity of damage to PAN and PMMA in the PMMA-*on*-PAN bilayer forms the basis for chemically selective soft X-ray patterning. The results described above were used to identify the X-ray photon energies and exposures that produce good contrast in each chemical component with least damage to the other component. Exposure can be controlled by adjusting either (or both) incident flux (by changing slits) or dwell time. The exposure times used were chosen such that the radiation dose for PAN (at 286.8 eV) was 2.5 times that for PMMA (at 288.4 eV) in order to use the same fraction of the

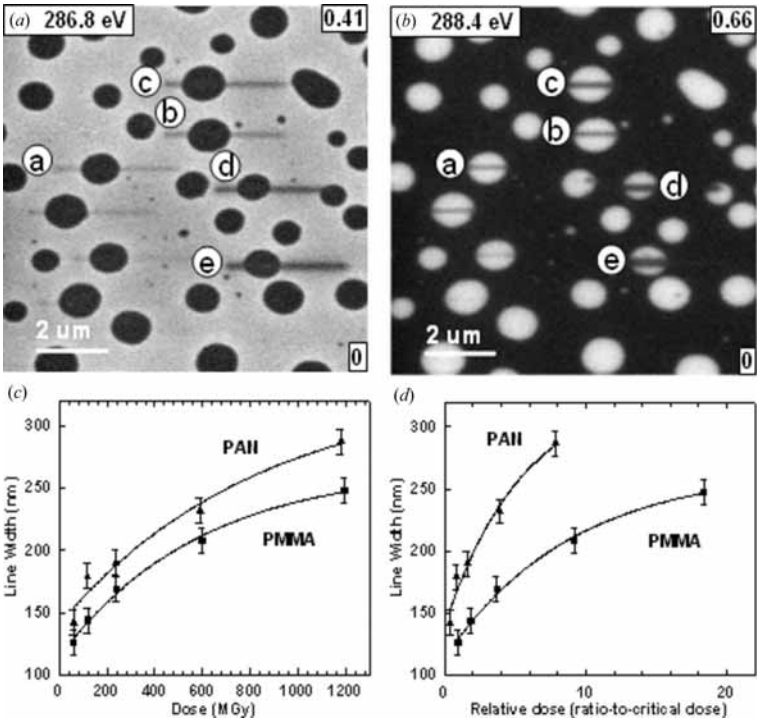

Figure 4
Evaluation of radical migration in a PMMA-*blend*-PAN microphase-separated film. (*a*) Optical density image at 286.8 eV (PAN is white). (*b*) Optical density image of the same region at 288.4 eV (PMMA is white). The lines labeled *a*, *b*, *c*, *d*, *e* were exposed to various doses at 320 eV prior to recording these images. (*c*) Plot of the average width of the damage lines in the PAN and PMMA material as a function of the dose. The data points are the measured line width (FWHM) at the indicated radiation doses for PMMA and PAN, respectively. The lines are fits of those data points to $w = w_o + a\exp(d/d_c)$. (*d*) Plot of the average width of the damage lines in the PAN and PMMA material as a function of ratio-to-critical dose (60×10^6 Gy for PMMA, 150×10^6 Gy for PAN).

critical dose of each species. Patterns at each energy were written by sequentially positioning the sample at the focused X-ray beam at a set of pre-defined points and exposing for a pre-defined dwell time which is proportional to the intensity of the 'color' at that location. In this fashion an input pattern is reproduced on the polymer film. Fig. 5(*a*) shows the input image used to reproduce a two-color version of the logo of the Lawrence Berkeley National Laboratory (LBNL). It is composed of a roof pattern in one color (red) and a window/tower pattern in a second color (blue). The red pattern was written into the PMMA layer by selectively damaging the C═O group at 288.4 eV. The blue pattern was written into the PAN layer by selectively damaging the C≡N functional group at 286.8 eV. These patterns were written in the PMMA/PAN bilayer and in the microtomed PECA film. Exposures were 100 ms pixel^{-1} at 288.4 eV with a measured incident flux (I_o) of 2.0 MHz and 200 ms pixel^{-1} at 286.8 eV with $I_o = 2.25$ MHz (note the detector efficiency is ~30% at these energies, and thus the actual incident photon flux is about three times larger). Under these conditions the estimated dose per pixel at 288.4 eV is 58×10^6 Gy into the PMMA layer and 14×10^6 Gy into the PAN layer, while the estimated dose per pixel at 286.8 eV is 7×10^6 Gy into the PMMA layer and 172×10^6 Gy into the PAN layer. Similar doses would be given to the respective ester and nitrile functional groups of PECA. As shown in Figs. 5(*b*) and 5(*c*), the input patterns were transferred in a chemically selective manner into the PMMA/PAN bilayer film, but not into the PECA film. In the latter case the initial absorption by the C═O groups generates electrons, ions and radicals which transfer the damage to the C≡N groups at the same (x,y) position, and *vice versa*. For PECA, the final generated composite image is a uniform purple color rather than the cleanly color-separated images for the PMMA/PAN bilayer film (Figs. 5*b* and 5*c*).

Several other patterns were further selectively patterned on the PMMA/PAN bilayer as shown in Figs. 5(*d*) and 5(*e*). These patterns are more complicated in that a gray scale within each color is generated by varying the dwell time for each pixel between 0 and 500 ms for PMMA and between 0 and 1000 ms for PAN with ~1 MHz incident flux to achieve a color gradient of the patterning. High gradient, good chemical contrast and precise overlay of the two separate images were created in the bilayer system. Currently the observed line widths are about 200 nm, even though the STXM beam spot is 45 nm in diameter at the focal spot (Kilcoyne *et al.*, 2003). The increased line width is not due to spatial jitter of the X-ray beam since the position of the beam relative to the sample is controlled interferometrically and is stable to better than 10 nm (Kilcoyne *et al.*, 2003). The possible factors that lead to the broadening of the line width are explored in the following section.

4. Discussion

4.1. What causes the spread of damage beyond the size of the X-ray beam?

Radiation damage to polymers and other materials initiated by soft X-rays is a complicated process with many contributing factors. The initial absorption of a soft X-ray photon excites a core electron at a specific atom in the sample to form a very short-lived (few fs) neutral high-energy excited state. The core hole rapidly relaxes by the Auger process to create a high-energy electron (~250 eV kinetic energy) and a singly or doubly ionized valence excited state (in principle the core hole can also decay by X-ray fluorescence, but that has negligible probability in the soft X-ray regime). The electronic disturbance in the valence ionized state extends over many bonds,

and has a high probability of breaking one or more bonds to form energetic and very reactive radical/ion fragments. In addition, the Auger electron has a range of ~1 nm and suffers inelastic collisions which ionize other nearby sites. In the picosecond time frame the initially absorbed energy has broken a number of bonds within a few nm of the absorption site, and released a number of energetic electrons and radicals or ions which are capable of further propagating the damage. Although the electrons are damaging, their range is limited to at most a few tens of nanometers owing to their strong interactions in condensed media. It is probably energetic radicals or (less likely) ions that are responsible for the longer-range effects since they are much more damaging and there is the possibility of chain processes. Reaction of these radicals and ions with nearby molecules can create new radicals/ions thereby setting up a chain process which may transfer the damage to regions far (~100 nm) from the initial absorption site. This process can be viewed as radical- or ion-initiated chain depolymerization or fragmentation. If so, it should be susceptible to containment by use of radical scavengers or inhibitors of radical chain reactions. We are presently exploring methods to reduce the line width by addition of radical scavengers (inhibitors) and the use of indirect methods such as chemical amplification.

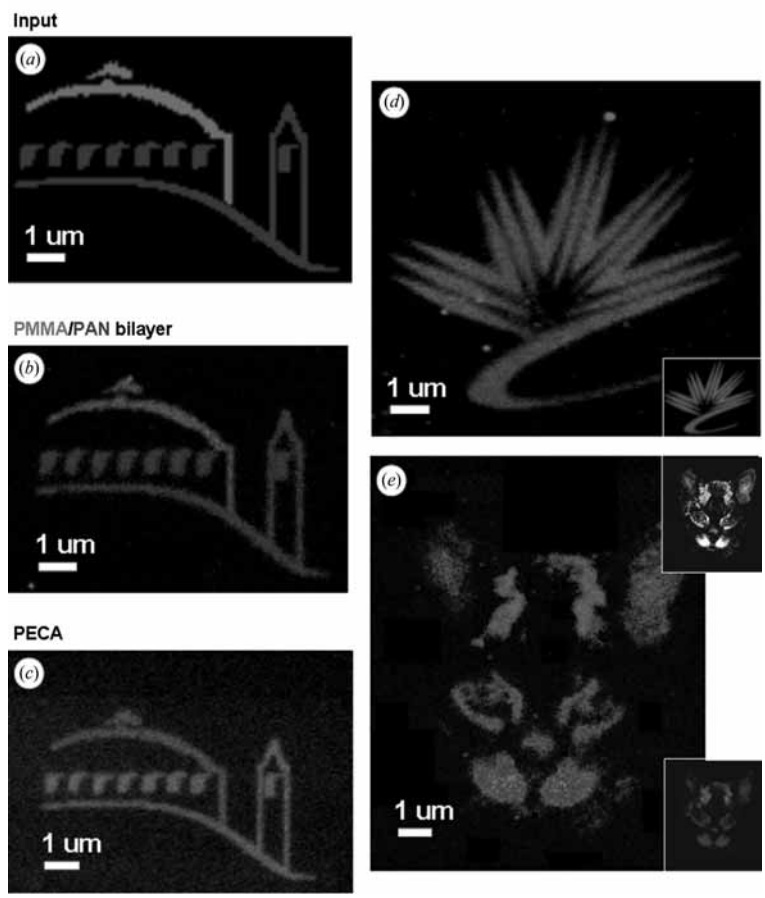

Figure 5
Demonstration of chemically selective patterning for PMMA/PAN bilayer and PECA. (*a*) LBNL logo input file, with the roof in red (PMMA) and the window/tower in blue (PAN). The lower images are color-coded composites derived from STXM images recorded at 286.8 eV (PAN damage, indicated in blue) and 288.4 eV (PMMA damage, indicated in red) of regions of (*b*) the PAN/PMMA bilayer and (*c*) PECA, into which the patterns indicated in (*a*) were written. Gradient patterns selectively generated in the PMMA/PAN bilayer system. (*d*) Logo for the Canadian Light Source (CLS). (*e*) 'Smokie' the cat (photograph courtesy of S. G. Urquhart). A different scheme to colorize the damage was used in this case. The input to make each image is shown as an inset.

Another factor that might contribute is localized heating and associated thermal damage. We have compared widths of the damage line written with the sample under vacuum, where there is very limited thermal dissipation at the sample, with that of lines written using the same dose but with the sample in helium, which provides good thermal dissipation at the sample. The results (Fig. 6) indicate that the line width in a vacuum is the same as that in helium within the measurement uncertainties. This indicates experimentally that the localized heating is low and the thermal damage is negligible. In addition, the temperature rise associated with localized heating was estimated using equation (4) which is an approach developed to describe local heating in TEM in terms of a steady-state model (Egerton *et al.*, 2004),

$$\begin{aligned}\text{Heat} &= \text{Heat}_{\text{conduction}} + \text{Heat}_{\text{radiation}} \\ &= \frac{4\pi\kappa l(T - T_0)}{0.58 + 2\ln(2R_0/d)} + \pi\left(d^2/2\right)\varepsilon\sigma\left(T^4 - T_0^4\right), \quad (4)\end{aligned}$$

where T and T_0 are the temperatures of the local spot and surroundings under steady state, respectively, κ is the thermal conductivity of the polymer, l is the sample thickness, d is the diameter of the assumed circular X-ray spot, R_0 is the distance for thermal conduction, ϵ is the radiation emissivity of the polymer, and σ is the Stefan–Boltzmann constant for radiation. Samples in a TEM are in a high or ultrahigh vacuum, so there is only conduction through the solid to dissipate thermal energy. In contrast, the sample in STXM is normally immersed in a one-third atmosphere of helium, and thus heat dissipation occurs through both the solid and the gas. Thus applying the TEM model for estimating the local heating in STXM will overestimate the possible temperature rise. An estimation of the local temperature rise was made for PMMA under typical conditions used for STXM patterning and assuming 80% of the energy deposited by photoabsorption turns into thermal

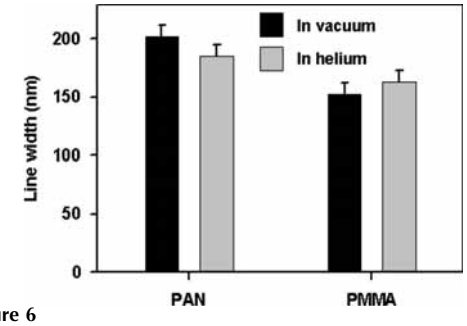

Figure 6
Effect of environment (vacuum *versus* one-third atmosphere of helium) on the line width with adjusted same dose for vacuum and helium for both PMMA and PAN.

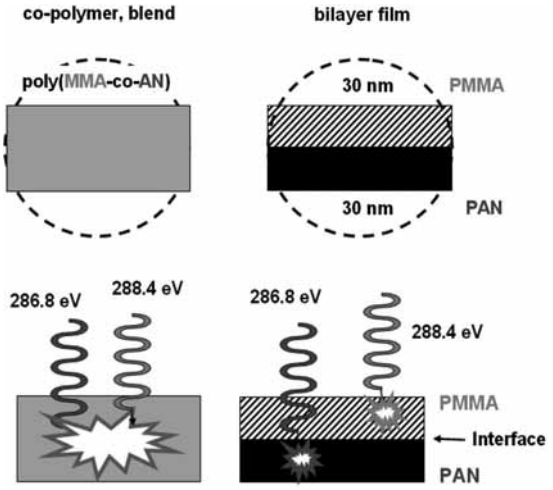

Figure 7
Diagram emphasizing the critical role of the interface in achieving chemically selective patterning by minimizing radical migration between layers.

energy. The calculation shows that the thermal radiation factor is a few orders of magnitude smaller than thermal conduction and that the temperature rise is only $\sim 5 \times 10^{-4}$ K. Thus the local heating in STXM is much smaller than that in TEM, for which the computed temperature rise under normal imaging conditions is a few degrees Kelvin (Egerton *et al.*, 2004).

4.2. What is the role of the interface in preventing spread of damage between the layers?

While the capability to selectively pattern into PMMA/PAN bilayers has been demonstrated repeatedly, it is puzzling why this works. As Fig. 7 indicates, the range of 'damage transport' resulting in line broadening in the copolymer systems exceeds the thickness of the combined bilayer system. The bonds are not highly aligned (there is no NEXAFS polarization dependence) and thus there is no reason to expect the primary products of the X-ray absorption (photoelectrons, radicals and ions from the first bond-breaking event) to be preferentially directed in the plane of the layer. Even if that was the case, the secondary scattering and chemical reaction events would rapidly erase any initial directional preference. Thus the electrons and radicals/ions should leave the site of the X-ray absorption, which is at the carbon atom of the C═O or C≡N group, with roughly an isotropic angular distribution. Given that expectation, why doesn't the damage generated in one layer spread to the adjacent layer?

The high degree of photon energy selectivity in the PMMA/PAN bilayer, where the X-rays pass through both materials simultaneously, indicates that, even though the thickness of each film (20–40 nm) is much smaller than the range of radical migration in these materials (100–200 nm), the interface between the two layers forms an effective barrier to damage migration, isolating the damage within the separate films. Transmission electron microscopy was used to exclude the possibility of a physical gap between the layers of a bilayer film by viewing the cross section of the bilayer interface. The two layers were in intimate contact (<1 nm). More plausible is the possibility that reactive migrating species are physically trapped in the potential energy well present at the interface between two incompatible polymers. Finally, it may be possible that small amounts of impurities including low-molecular-weight oligomers were extruded from either or both layers during the spin-coating and drying/annealing process, and were chemically trapping migrating reactive species. Note that there is no spectroscopic evidence for the latter situation: discontinuous impurities at anything more than 2–3 nm thickness would be detected in the images. A continuous layer could be a little thicker (perhaps up to 5–6 nm), but ultimately would show up as a change in the C 1*s* spectra. If interface chemistry is involved, spatial separation alone may not be sufficient for chemically selective damage and patterning on the same region of the bilayer sample. Further analysis of the interface regarding the morphology and composition is needed to understand the role of the interface in quenching the damage spread. This will also help design more advanced systems for chemically selective patterning or lithography.

Although further work is needed to improve spatial resolution and chemical contrast, already this level of chemically selective patterning with STXM allows systematic exploration of potential advantages over other forms of lithography, and provides a platform to explore possible applications. The added value of this technique is chemical selectivity through the use of tuned monochromated synchrotron X-rays. Obvious disadvantages include limited access to focused synchrotron light, expense, and limited spatial resolution. With appropriately prepared layered samples, this technique will allow selective modification of a specific component in a multi-polymer layered system or other multi-component systems. Attributes of possible interest for exploitation include: chemical selectivity, high gradient and contrast patterning, and direct writing of submicrometer patterns on polymer photoresists *etc.* While the ease of tuning, high brightness and highly monochromatic character of the STXM is well suited for method development and demonstrations, practical implementation of this chemically specific lithography will most

likely be carried out using laser plasma or X-ray laser sources which are tuned to the chemically specific energies, combined with full-field X-ray exposure systems, through a suitable mask. A concerted effort is currently under way to develop practical laser-based full-field soft X-ray microscope systems (http://euverc.colostate.edu; http://www.jmar.com), which could be suitable systems in which to implement practical applications of the phenomena we have demonstrated.

Further work to develop multilayer systems, in particular a trilayer system which will allow 'full color' reproduction at the submicrometer scale, is now under investigation. This requires finding a third polymer which has strong absorption at an energy different from the characteristic absorption lines of the PAN and PMMA components, and limited absorption at the PAN and PMMA characteristic energies. In addition, a method of fabricating the trilayer so that each layer is thin and uniform, with minimal mixing of the layers, must be developed. Currently a variety of possible combinations of polymers, solvents and sequence for spin-coating are being explored. Furthermore, an exposure optimization program has been developed which can predict the conditions (photon energies, layer thicknesses, ordering and exposure times) which provide best contrast in any given multilayer system, given knowledge of the absorption spectrum and the critical dose.

In order to improve the spatial resolution of the patterning, it is necessary to understand the origin of the damage spreading, which we currently hypothesize as being associated with radical migration. Preliminary experiments have shown that radical quenchers have some line-narrowing effect, but their influence is relatively minor. A possible explanation is that core-excitation-induced radiation damage leads to a fast cascade process and rapid radical/ion migration and associated chemical and physical changes, which cannot be controlled by a low concentration of radical quenchers. Further exploration of this issue is required.

This research was supported by NSERC (Canada), the Canadian Foundation for Innovation, and the Canada Research Chair Program. X-ray microscopy was carried out at the Advanced Light Source (supported by DoE under contract DE-AC03-76SF00098). We thank David Kilcoyne for expert maintenance of STXM532, Marcia West for superb ultramicrotomy, and Daniel Hernandez-Cruz for assistance with operating the STXM.

References

Ade, H. (1998). *Experimental Methods in the Physical Sciences*, Vol. 32, pp. 225–262. New York: Academic Press.
Ade, H. & Urquhart, S. G. (2002). *Chemical Applications of Synchrotron Radiation*, pp. 1091–1153. River Edge, NJ: World Scientific.
Bauer, E. (2001). *J. Electron Spectrosc. Relat. Phenom.* **114–116**, 975–987.
Beetz, T. & Jacobsen, C. (2003). *J. Synchrotron Rad.* **10**, 280–283.
Cadet, J., Douki, T., Gasparutto, D. & Ravanat, J. L. (2005). *Rad. Phys. Chem.* **72**, 293–299.
Cazaux, J. (1997). *J. Microsc.* **188**, 106–124.
Cerrina, F. (2000). *J. Phys. D*, **33**, R103–R116.
Cherezov, V., Riedl, K. M. & Caffrey, M. (2002). *J. Synchrotron Rad.* **9**, 333–341.
Coffey, T., Urquhart, S. G. & Ade, H. (2002). *J. Electron Spectrosc.* **122**, 65–78.
Egerton, R. F., Li, P. & Malac, M. (2004). *Micron*, **35**, 399–409.
Ekpenyong, K. I. & Okonkwo, R. O. (1983). *J. Chem. Educ.* **60**, 429–430.
Guo, L. J. (2004). *J. Phys. D*, **37**, R123–R141.
Henke, B. L., Gullikson, E. M. & Davis, J. C. (1993). *Atom. Data Nucl. Data Tables*, **54**, 181–342.
Hitchcock, A. P., Morin, C., Heng, Y. M., Cornelius, R. M. & Brash, J. L. (2002). *J. Biomater. Sci. Polym. Ed.* **13**, 919–938.
Jacobsen, C., Wirick, S., Flynn, G. & Zimba, C. (2000). *J. Microsc.* **197**, 173–184.
Joers, J. M., Fong, P. M. & Gore, J. C. (2006). *Phys. Med. Biol.* **51**, N23–N30.
Kilcoyne, A. L. D., Tyliszczak, T., Steele, W. F., Fakra, S., Hitchcock, P., Franck, K., Anderson, E., Harteneck, B., Rightor, E. G., Mitchell, G. E., Hitchcock, A. P., Yang, L., Warwick, T. & Ade, H. (2003). *J. Synchrotron Rad.* **10**, 125–136.
Koprinarov, I. N., Hitchcock, A. P., Li, W. H., Heng, Y. M. & Stöver, H. D. H. (2001). *Macromolecules*, **34**, 4424–4429.
Melngailis, J., Mondelli, A. A., Berry III, I. L. & Mohondro, R. (1998). *J. Vac. Sci. Technol. B*, **16**, 927–957.
Morin, C., Hitchcock, A. P., Cornelius, R. M., Brash, J. L., Urquhart, S. G., Scholl, A. & Doran, A. (2004). *J. Electron Spectrosc.* **137–140**, 785–794.
Osetsky, Y. N. & Bacon, D. J. (2003). *Nucl. Instrum. Methods Phys. Res. B*, **202**, 31–43.
Pease, R. L. (2003). *IEEE Trans. Nucl. Sci.* **50**, 539–551.
Rightor, E. G., Hitchcock, A. P., Ade, H., Leapman, R. D., Urquhart, S. G., Smith, A. P., Mitchell, G., Fischer, D., Shin, H. J. & Warwick, T. (1997). *J. Phys. Chem. B*, **101**, 1950–1961.
Sagstuen, E., Sanderud, A. & Hole, E. O. (2004). *Rad. Res.* **162**, 112–119.
Sanche, L. (2002). *Mass Spectrom. Rev.* **21**, 349–369.
Stöhr, J. (1992). *NEXAFS Spectroscopy*, *Springer Tracts in Surface Science 25*, p. 245. Berlin: Springer.
Stulen, R. H. & Sweeney, D. W. (1999). *IEEE J. Quant. Electron.* **35**, 694–699.
Trachenko, K. (2004). *J. Phys. Condens. Matter*, **16**, R1491–R1515.
Tseng, A. A., Chen, K., Chen, C. D. & Ma, K. J. (2003). *IEEE Trans. Electron. Pack. Manuf.* **26**, 141–149.
Tseng, A. A., Notargiacomo, A. & Chen, T. P. (2005). *J. Vac. Sci. Technol. B*, **23**, 877–894.
Wang, J., Morin, C., Li, L., Hitchcock, A. P., Scholl, A. & Doran, A. (2007). *J. Electron. Spectrosc. Relat. Phenom.* Submitted.
Warwick, T., Ade, H., Kilcoyne, A. L. D., Kritscher, M., Tylisczcak, T., Fakra, S., Hitchcock, A. P., Hitchcock, P. & Padmore, H. A. (2002). *J. Synchrotron Rad.* **9**, 254–257.
Weik, M., Ravelli, R. G. B., Kryger, G., McSweeney, S., Raves, M. L., Harel, M., Gros, P., Silmani, I., Kroon, J. & Sussman, J. L. (2000). *Proc. Natl. Acad. Sci.* **97**, 623–628.
Zhang, X., Jacobsen, C., Lindaas, S. & Williams, S. (1995). *J. Vac. Sci. Technol. B*, **13**, 1477–1483.

Chapter 7

Chemically selective soft X-ray patterning of trilayer polymer films

This chapter presents experimental results of chemically selective soft X-ray patterning of trilayer polymer films, such as PMMA/PPC/PAN and PMMA/PEC/PAN. A simulation program was developed to predict the patterning results with semi-quantitative accuracy.

*Reprinted with permission from the Journal of Physical Chemistry C 111 (**2007**) 16330-16338, Jian Wang, Harald D. H. Stöver, and Adam P. Hitchcock, "Chemically Selective Soft X-ray Direct-Write Patterning of Multilayer Polymer Films", Copyright 2007, American Chemical Society.*

The author of this thesis prepared all the samples for this publication, performed all the STXM experiments (in collaboration with Prof. A. P. Hitchcock), analyzed all the STXM data, developed the simulation program, and wrote the publication with assistance in later stages by Prof. A. P. Hitchcock and Prof. H. D. H. Stöver.

16330 *J. Phys. Chem. C* **2007,** *111,* 16330−16338

Chemically Selective Soft X-ray Direct-Write Patterning of Multilayer Polymer Films

Jian Wang, Harald D. H. Stöver, and Adam P. Hitchcock*

Department of Chemistry and Brockhouse Institute for Materials Research, McMaster University, Hamilton, Ontario, Canada L8S 4M1

Received: April 2, 2007; In Final Form: July 4, 2007

Chemically selective soft X-ray direct-write patterning of trilayer polymer films was performed in a scanning transmission X-ray microscope, extending recent pioneering work on bilayer polymer films. Two trilayer polymer systems were examined: PMMA/PPC/PAN and PMMA/PEC/PAN, where PMMA = poly(methyl methacrylate), PPC = poly(propylene carbonate), PAN = polyacrylonitrile, and PEC = poly(ethylene carbonate). Each polymer layer was selectively patterned by exposure at its characteristic absorption energy: 288.45 eV for PMMA, 290.40 eV for PPC (PEC), and 286.80 eV for PAN. The patterns were visualized by imaging at these same energies. For the PMMA/PPC/PAN trilayer, highly selective patterning was achieved for the PAN and PPC layers, while the selectivity for the PMMA layer was poor. This was significantly improved by replacing PPC with PEC. The trilayer patterning process was simulated from the X-ray absorption spectra of the polymers, the layer order and thicknesses, and the critical doses for damage of each polymer. The simulations give semiquantitative predictions of the experimental contrast, and are a useful tool to find exposure times that optimize pattern contrast. Methods to improve patterning selectivity are discussed. Full color pattern reproduction with ∼150 nm spatial resolution is demonstrated with several high-resolution patterns created in the PMMA/PEC/PAN trilayer film.

1. Introduction

Selective control of chemical reactions has always been a fundamental goal of chemistry. In order to achieve it, photochemistry is especially efficient since the resonant character of photoabsorption can be used to selectively initiate a reaction in a specific target species. The cross sections for soft X-ray (100−1000 eV) absorption are large and lead to significant chemical modification. Since the near-edge X-ray absorption fine structure (NEXAFS) spectra[1] of many species have intense resonances at unique energies, these have great potential as a basis for chemically selective photochemistry. However, secondary processes associated with photoabsorption, such as radical/ion generation and spreading, have deteriorated this selectivity by transferring energy and damage from the initial absorption species to adjacent species which do not absorb the primary radiation. Recently we surmounted this problem and demonstrated chemically selective direct-write patterning using monochromated soft X-rays[2] in a scanning transmission X-ray microscope (STXM).[3,4] The key is to use a layered polymer system, where the interface, through a mechanism as yet incompletely understood, acts as a barrier to transfer of the radiation damage between layers. As a result, we successfully demonstrated a basic bilayer strategy that allows complex patterns to be selectively transferred to target layers with submicron spatial resolution and high chemical contrast, i.e., patterning one layer without damaging the other layer.[2] Without the layer structure, i.e., if the different chemical species were intimately mixed as in a blend, all components are damaged with exposure at any energy, as shown previously.[2]

Here we present the extension of this approach to a trilayer film which allows "full color" pattern reproduction on the submicron scale (∼150 nm line widths). This trilayer consists of three different chemical species that have intense absorption bands at energies where the other two species have weak absorption (orthogonal absorption bands). Specifically, the previously used polyacrylonitrile (PAN) and poly(methyl methacrylate) (PMMA) bilayer components were augmented with a third polymer which has strong absorption at its own unique energy and limited absorption at the PAN and PMMA characteristic energies. The polymers found to be suitable are aliphatic polycarbonates, such as poly(propylene carbonate) (PPC) and poly(ethylene carbonate) (PEC). The chemical structures of PPC, PEC, PMMA, and PAN are given in Scheme 1. In order to guide the optimization of trilayer systems capable of "full color" reproduction, a program to simulate radiation damage in multilayer polymer systems has been developed. It combines key input data (the quantitative NEXAFS spectra, layer thicknesses, layer order, and exposure protocol) to reproduce the experimental observations, and to predict optimum exposure protocols, thereby enabling rational optimization of multilayer systems for chemical patterning using tunable, monochromatic X-rays.

This paper is organized as follows. Section 2 describes experimental methods. Section 3 describes the principles to simulate chemically selective patterning in multilayer polymer films. Section 4 presents the NEXAFS spectra and damage kinetics for PAN, PMMA, PPC, and PEC, and the results from chemically selective patterning of the PMMA/PPC/PAN and PMMA/PEC/PAN trilayers. The two systems are compared with regard to patterning selectivity. Several demonstrations of chemically selective patterning in the PMMA/PEC/PAN trilayer are then presented. We conclude by suggesting methods to further optimize chemical patterning with multiple wavelength monochromated X-rays and possible extensions to other applications.

* Corresponding author. Telephone: (905) 525-9140, ext 24749. Fax: (905) 521-2773. E-mail: aph@mcmaster.ca.

10.1021/jp072570s CCC: $37.00 © 2007 American Chemical Society
Published on Web 10/04/2007

SCHEME 1: Chemical Structures of Poly(methyl methacrylate) (PMMA), Polyacrylonitrile (PAN), Poly(propylene carbonate) (PPC), and Poly(ethylene carbonate) (PEC)

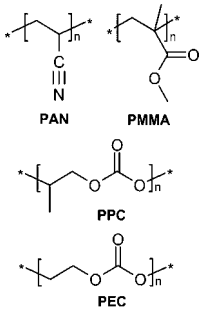

2. Experimental Section

2.1. Sample Preparation. PAN (M_w = 150K) was obtained from Aldrich; PMMA (M_w = 312K) was obtained from Polymer Source Inc.; PPC (M_w = 250K) and PEC (M_w = 150K) were obtained from Empower Materials. All polymers were used without further purification. For NEXAFS spectroscopy and critical dose measurements, free-standing single layer films of each polymer were made according to the same procedure of ref 2. First, a 1 wt % solution of each polymer was prepared in suitable solvents, which were *N*,*N*-dimethylformamide (DMF) for PAN, toluene for PMMA, and 1,4-dioxane for both PPC and PEC. Then a ~50 μL drop of each solution was spun cast (3000 rpm, 30 s) onto freshly peeled, 2.5 cm × 2.5 cm mica surfaces. The room-temperature spun cast PMMA film was used as formed. The PAN, PPC, and PEC single layer films were dried under vacuum at 70 °C for 0.5 h to remove all solvents. Subsequently, all films were cut into 3 mm × 3 mm pieces on the mica surfaces, and then floated onto Milli-Q water. A piece of the polymer film was transferred to a degreased hexacomb grid or a TEM grid and used for STXM measurements after drying again in ambient. The single layer films formed under the above conditions were 30−40 nm thick, according to STXM measurements.

Free-standing trilayer films of PAN (bottom), PPC or PEC (middle), and PMMA (top) were fabricated by spin coating successively, first, PAN from DMF, second, PPC or PEC from 1,4-dioxane, and, third, PMMA from toluene onto the same mica substrate as described above. After each spin coating, the drying condition of each deposited layer was the same as that of the single layer preparation outlined above. The solvents and order of the layers were carefully selected so that the solutions applied on top of an already deposited layer would not dissolve the previously fabricated polymer film. Relative solubility data are summarized in Table 1. Reversing the spin coating sequence for any two of the three polymers will result in a nonuniform microphase-separated film due to redissolution of the already deposited layer, as shown in ref 2. It is rather difficult to find fully orthogonal solvents for these non-cross-linked polymers. Thus, only some layer sequences are viable using the successive spin coating procedure, which we prefer as it gives the most uniform thickness of the layers. The average thickness of the resulting trilayer film was 105(10) nm according to STXM measurements, in close agreement with the value of 120(15) nm determined from the height profile across a scratch through the trilayer film measured by atomic force microscopy (AFM; Quesant Q-scope 350).

2.2. STXM. Experiments were performed at the Advanced Light Source beamline 5.3.2[5] using the polymer scanning transmission X-ray microscope (STXM).[6] The settings of the microscope and the beamline, as well as the procedure for radiation damage studies, were presented elsewhere.[2,7] In brief, a single layer film of each polymer was exposed at 300 eV with an incident photon flux of 1.5−2.5 MHz in the focused ~50 nm diameter X-ray spot. The detector efficiency is 30 ± 10% in the C 1s region,[6,7] and thus the actual incident photon flux is about 3 times larger. A N_2 gas filter (0.7 Torr for a 1 m path) was used to ensure there was negligible higher order radiation, which would result in errors in the quantitative dose−damage evaluation. After a series of exposures at different regions on the polymer film, analysis images were recorded at the characteristic absorption energies for each polymer. In these images, the best contrast between damaged and undamaged regions is displayed. The characteristic absorption energies for the polymers in this work are the strong C 1s → π^* transitions: 286.80(5) eV for PAN, 288.45(5) eV for PMMA, and 290.40-(5) eV for PPC and PEC. The damage rate was evaluated from the dose−damage profile, which plots the damage, expressed as the change in optical density (absorbance) at the characteristic energy, as a function of radiation dose (in units of gray, where 1 Gy = 1 J/kg), determined from the exposure time, incident flux, and absorbance, as outlined elsewhere.[2,7] The dose−damage curve was analyzed assuming first-order kinetics,[2,7−11] i.e., an exponential rise of the damage signal to a maximum value at infinite dose (see eq 3 of ref 2). The fit determines the critical dose of the polymer, i.e., the radiation dose required to attenuate a specific spectroscopic feature to 1/e of the initial intensity. The higher the critical dose, the slower the damage rate.

The chemically selective patterning experiments were performed using the same pattern generation program and procedure as in ref 2. Specifically, the sample is positioned with ~10 nm precision under laser interferometer control[6] to predefined (*x*,*y*) locations and then a fast-acting (~300 μs) in-vacuum piezo shutter is opened for a precise, predefined, position-dependent time interval (usually 50−500 ms) to expose the sample to the focused monochromated soft X-rays. The input files for pattern generation are lists of (*x*, *y*, *t*, *E*) values for each pixel, which are prepared from color-separated images by a routine in aXis 2000.[12] The overall physical size, the pixel density, and thus sampling resolution of the input pattern can be adjusted by changing the image characteristics prior to generating the pattern generation input file. For multicolor (multiphoton energy) patterns, the input files for each color are written sequentially at the appropriate photon energies.

TABLE 1: Solubility of Selected Polymers in Selected Solvents[a]

	solvent		
polymer	DMF	1,4-dioxane	toluene
PAN	+	−	−
PPC	+	+	−
PEC	+	+	−
PMMA	+	+	+

[a] +, soluble; −, insoluble.

3. Simulation of Chemically Selective Patterning in Multilayer Polymer Systems

If quantitative NEXAFS spectra and critical doses for each polymer of a multilayer system are known, it is possible to simulate the chemically selective patterning (or damage) that will result from a defined exposure protocol. For this, it is assumed that (i) first-order damage kinetics apply,[2,7−11] (ii) there

is negligible mass loss in the dose range comparable to the critical dose, and (iii) damage is not transferred between adjacent layers.[2] The total optical density (OD) of a multilayer system at any energy, E, is given by

$$\mathrm{OD}(E) = \sum_i l_i A_i(E) \tag{1}$$

where l_i is the thickness of the ith layer and $A_i(E)$ is the linear absorption coefficient (i.e., OD per nanometer) of component i at photon energy, E. The thickness of each layer is determined by fitting the measured total C 1s spectrum to the linear absorption coefficients of all the components.

For the chemically selective patterning of a target layer, the exposure energy is chosen at its characteristic absorption energy for best patterning selectivity, even though damage to other layers also occurs due to their small photoabsorption at this energy. Thus the simulation is performed by separately computing the radiation damage in each layer with a defined exposure protocol. Specifically, for given energy and exposure time, the remaining OD at the damaged region of a selected layer is calculated according to eq 2, which incorporates both damage kinetics and dose evaluation:[2,7,11]

$$\mathrm{OD}_t = \mathrm{OD}_\infty + C \exp\left[-\frac{I_0(1 - \mathrm{e}^{-\mathrm{OD}})Et}{\epsilon V \rho a_c}\right] \tag{2}$$

where OD_t is the remaining optical density of the exposed region, OD_∞ is the extrapolated optical density after infinite dose, C is a constant, which is equal to the infinite damage ($D_\infty = \mathrm{OD}_0 - \mathrm{OD}_\infty$, where OD_0 is the initial optical density) in the case of negligible mass loss, I_0 is the incident flux (note the incident flux for each successive layer is the flux transmitted through the previous layer), OD is the dynamic optical density of the exposed region during irradiation, which is assigned to OD_0 for simplicity, E is the photon energy, t is the exposure time, ϵ is the detector efficiency, V is the volume of the exposed region (considered to be the volume of a single pixel = 60 nm × 60 nm × l_i), ρ is the polymer density, and a_c is the critical dose of the selected polymer.

The pattern quality is related to the change in OD in the damaged region relative to the undamaged region. There are several ways to define image contrast. The definition of image *contrast* used in this work is

$$\mathrm{contrast} = \frac{\mathrm{OD}_0}{\mathrm{OD}_t} \tag{3}$$

More radiation damage in a given layer means a higher value of the contrast in that layer. Contrast values are always greater than 1, and are independent of layer thickness, within the formalism above. Patterning *selectivity* is then related to the relative contrast in each layer, and can be defined for the purpose of optimization in a pairwise fashion for layers a and b as

$$\mathrm{selectivity(a{:}b)} = S_{\mathrm{ab}} = \frac{\mathrm{contrast(a)}}{\mathrm{contrast(b)}} \tag{4}$$

The contrast is not a linear function of exposure time; thus patterning selectivity varies with exposure time, as well as other aspects of the multilayer system, such as layer order and thickness. The best selectivity would correspond to the greatest differentiation among the pattern contrast in different layers, which can be predicted by consideration of an*optimizer* that simultaneously maximizes all pairwise selectivities. In a trilayer system such an optimizer can be defined as

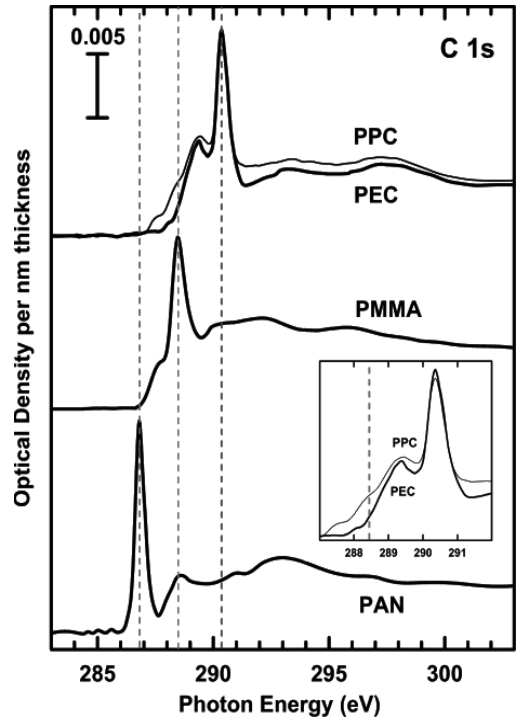

Figure 1. C 1s NEXAFS spectra of PMMA, PAN, PPC (thinner line), and PEC (thicker line). The vertical dashed lines indicate the energies used to create patterns in each species. The inset expands the spectra of PPC and PEC in the energy region used for PMMA patterning.

$$\mathrm{optimizer} = S_{\mathrm{ab}} + S_{\mathrm{ac}} + S_{\mathrm{bc}} \tag{5}$$

The best exposure protocol for chemically selective patterning is that which maximizes the value of this optimizer. ChemLith is an Excel application program developed to simulate chemically selective patterning for multilayer polymer systems within the framework outlined above. Factors that may influence the selectivity, such as layer order, layer thickness, materials (and thus NEXAFS spectra and critical dose), choice of exposure energy, time, and incident flux, can all be analyzed and optimized.

4. Results

4.1. NEXAFS Spectra and Critical Doses for PMMA, PAN, PPC, and PEC. Figure 1 presents the spectra of undamaged PPC, PEC, PAN, and PMMA. Radiation damage of PAN and PMMA causes spectral changes which are readily observed in the C 1s NEXAFS spectra.[2,7] The main change is a decrease of the strong C 1s → π^* transitions. Other spectral changes also occur, including the appearance and growth of a new feature at 285 eV and a decrease in the C 1s continuum intensity. The former signal is associated with C 1s → $\pi^*_{\mathrm{C=C}}$ transitions arising from C=C bonds formed in the damaged polymer backbone. The decreased continuum intensity is associated with mass loss. Since the change of the C 1s → π^* transition intensity is the most sensitive to damage, this signal has been used to evaluate damage and patterning contrast in this study. The quantitative NEXAFS spectra of PPC and PEC are very similar except that the spectrum of PEC has less

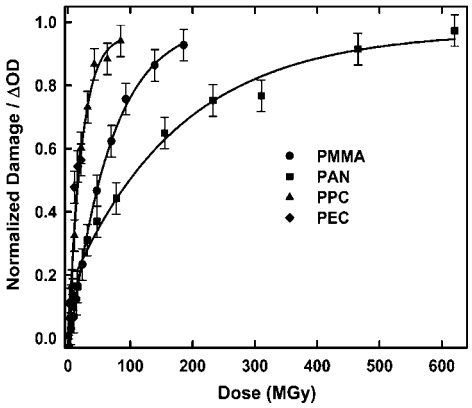

Figure 2. Damage versus dose curves for PMMA, PAN, PPC, and PEC derived from STXM measurements at the C 1s edge. The exposure energy was 300 eV. The damage signal, which is the normalized change in optical density monitored at the characteristic photon energies, tracks the amount of damaged product and thus integrates over possible differences in damage rates for different mechanisms.

absorbance between 287 and 289 eV due to the absence of a methyl group (see insert to Figure 1). Radiation damage to PPC and PEC is also characterized by a substantial decrease of the C 1s $\rightarrow \pi^*_{C=O}$ transition at 290.40 eV. In addition there is considerable mass loss, as evidenced by a decrease in the C 1s continuum intensity with increasing dose.

Figure 2 plots the damage (change of OD at the C 1s $\rightarrow \pi^*$ transition) normalized to infinite damage (D_∞) versus radiation dose for PAN, PMMA, PPC, and PEC, derived from STXM measurements for the pure polymers. All the samples were irradiated at 300 eV in the C 1s continuum for less absorbance variation during radiation damage. The critical dose for soft X-ray damage should be an inherent property of a polymer, and thus the critical dose at the π^* resonance is expected to be the same as that at 300 eV. Note that the dose rate at different energies will vary because of the different absorbance values but this is taken into account in computing dose. The quantitative damage was evaluated from changes in optical density at the characteristic absorption energies (C 1s $\rightarrow \pi^*$ transitions). The damage signal for each species was normalized to the infinite damage level for that species, in order to compare the relative amount of damage created for the same dose. Qualitatively, the relative damage rates are PPC $\approx$ PEC > PMMA > PAN. Quantitative evaluation of the data in Figure 2 by a fit to eq 3 of ref 2 (or a modification of eq 2 in this work) gave critical doses of 150(20) MGy for PAN, 60(10) MGy for PMMA, and 25(5) MGy for PPC and PEC. The critical dose for PMMA determined in this work is consistent with literature values obtained at different irradiation photon energies.[8,11]

4.2. Chemically Selective Patterning for PMMA/PPC/PAN Trilayer. The selective patterning for a bilayer system, PMMA/PAN, has been demonstrated previously[2] with high selectivity and good image contrast. Our goal in this work was to add a third layer to the PMMA/PAN bilayer system, in order to enable full color, chemically sensitive patterning. The choice of the third layer can be rather challenging. The polymer of the third layer should have (i) a chemically distinct absorption feature with a large OD, which is shifted by at least ~1 eV with respect to the other two layers for complete peak separation; (ii) a suitable damage rate in terms of critical dose; and (iii) relatively little absorption at the photon energies used to damage PMMA or PAN. This has led us to explore aliphatic instead of aromatic polymers, since the phenyl components of aromatic polymers are very damage resistant.[7,13,14] Three generic polymer systems were examined as the third layer: aliphatic polyurethane, aliphatic polyurea, and aliphatic polycarbonate. Aliphatic polycarbonates turned out to be the best, since they are commercially available, have high molecular weights, and are soluble in an appropriate solvent for spin coating.

The first trilayer system that was successfully fabricated and patterned was PMMA/PPC/PAN. The notation indicates the ordering of the three layers, with the first mentioned species being the upstream layer (upstream refers to the layer first hit by the incident X-rays). Figure 3a shows ChemLith predictions of the contrast in each layer as a function of exposure time, for the PMMA/PPC/PAN trilayer. The layer thicknesses for the trilayer patterned and analyzed by STXM are 27(3) nm of PMMA, 27(3) nm of PPC, and 36(4) nm of PAN. The top panel of Figure 3a plots the contrast as a function of exposure time created in each of the three layers by irradiation at 288.45 eV. The contrast is defined as in eq 3, and the incident fluxes (I_0) are 2.0, 1.8, and 2.3 MHz at 288.45, 290.40, and 286.80 eV, respectively. Figure 3a shows that while PMMA and PAN are well differentiated (PMMA damage is much higher than PAN damage at most exposure times), this is not the case for PMMA and PPC. In fact, the contrast as a function of exposure time in the PMMA layer is very similar to that created in the PPC layer, even though the PPC is being damaged by an energy different from the energy of its characteristic C 1s $\rightarrow \pi^*_{C=O}$ peak. This predicts that the patterning selectivity of the PMMA layer would be very poor. The middle and bottom panels of Figure 3a present the contrast profiles for selective patterning of the PPC and PAN layers at 290.40 and 286.80 eV, respectively. In contrast to exposure at 288.45 eV, much better selectivity can be seen for these energies in that the contrast generated in PPC by exposure at 290.40 eV is much higher than that in PMMA or PAN, and the contrast generated in PAN by exposure at 286.80 eV is much higher than that in PMMA or PPC.

To verify the quantitative accuracy of the simulations, a series of exposures at variable exposure time were carried out for the same PMMA/PPC/PAN trilayer using the input pattern displayed in Figure 4a. It is a three-color version of the logo of Lawrence Berkeley National Laboratory (LBNL), which is composed of a roof pattern in red, a window pattern in blue, and a tower pattern in green. The red pattern was written into the PMMA layer by exposing at 288.45 eV to selectively damage the ester group; the blue pattern was written into the PPC layer by exposing at 290.40 eV to selectively damage the carbonate group; the green pattern was written into the PAN layer by exposing at 286.80 eV to selectively damage the cyanide group. The incident flux was measured to be 2.0, 1.8, and 2.3 MHz at 288.45, 290.40, and 286.80 eV, respectively. Then LBNL logo patterns were patterned with chemical selectivity into the PMMA/PPC/PAN trilayer with combinations of exposure time selected from 50, 100, and 250 ms at 288.45 eV for the roof pattern; 50, 100, and 200 ms at 290.40 eV for the window pattern; and 100, 200, and 500 ms at 286.80 eV for the tower pattern. For each created logo pattern, the contrast in each layer was extracted from the experimental optical density image at the corresponding characteristic energy based on eq 3. The experimentally determined contrast for each pattern is also plotted in Figure 3a in comparison with the contrast predicted by ChemLith. The results show that the contrasts in the observed patterns are close to the contrast predicted by the simulations at relatively short exposure times, i.e., lower doses. For longer exposure times, some experimental results deviate from the simulations, probably due to errors in the dose−damage model,

16334 *J. Phys. Chem. C, Vol. 111, No. 44, 2007*

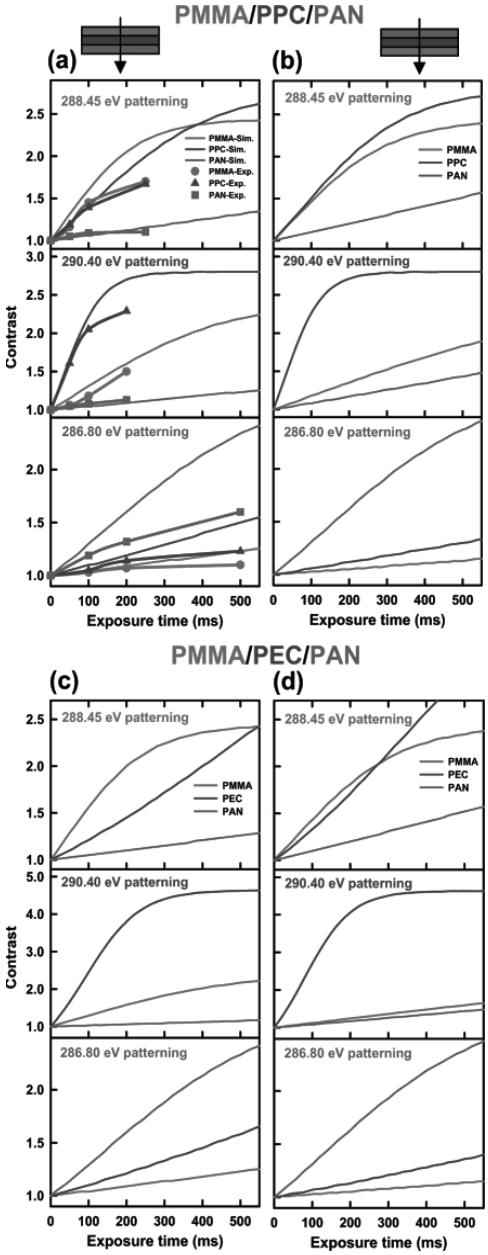

Figure 3. Simulations and experimental results for chemically selective patterning of PMMA/PPC/PAN and PMMA/PEC/PAN trilayers. (a) Predicted contrast (thinner lines) as a function of exposure time for a PMMA/PPC/PAN trilayer with a layer thickness profile as 27/27/36 nm. The top panel shows the contrast as a function of exposure in each of the three layers for exposure at 288.45 eV with $I_0 = 2$ MHz; the middle panel shows the contrast in each of the three layers for exposure at 290.40 eV with $I_0 = 1.78$ MHz; the bottom panel shows the contrast in each of the three layers for exposure at 286.80 eV with $I_0 = 2.25$ MHz. The points and thicker lines plot the experimentally observed contrast as a function of exposure time for selective patterning of each layer under the same incident fluxes. (b) Predicted contrast for the same trilayer system as in (a) but with the PAN layer upstream and thus first exposed to the X-ray beam. (c) Predicted contrast as a function of exposure time for a PMMA/PEC/PAN trilayer with layer thicknesses of 41/46/33 nm under the same exposure energies and I_0 values as (a). (d) Predicted contrast as a function of exposure time for the same trilayer system as (c), but with the PAN layer upstream.

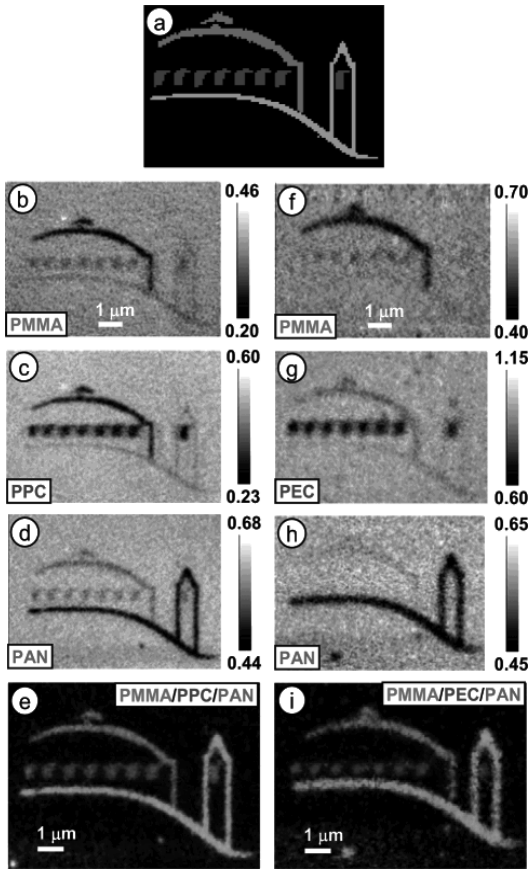

Figure 4. Demonstration of chemically selective patterning of the LBNL logo into PMMA/PPC/PAN and PMMA/PEC/PAN trilayers. (a) Input file, with the roof (red) patterned at 288.45 eV (PMMA), the windows (blue) patterned at 290.40 eV (PPC and PEC), and the tower (green) patterned at 286.80 eV (PAN). (b) Optical density image of the patterned region viewed at 288.45 eV for the PMMA/PPC/PAN trilayer (PMMA absorbs strongest). (c) Optical density image of the pattern region viewed at 290.40 eV for the PMMA/PPC/PAN trilayer (PPC absorbs strongest). (d) Optical density image of the patterned region viewed at 286.80 eV for the PMMA/PPC/PAN trilayer (PAN absorbs strongest). (e) Color-coded composite of the three images after inversion (red, PMMA damage; blue, PPC damage; green, PAN damage). (f) Optical density image of the patterned region viewed at 288.45 eV for the PMMA/PEC/PAN trilayer. (g) Optical density image of the pattern region viewed at 290.40 eV for the PMMA/PEC/PAN trilayer. (h) Optical density image of the patterned region viewed at 286.80 eV for the PMMA/PEC/PAN trilayer. (i) Color-coded composite of the three images after inversion (red, PMMA damage; blue, PEC damage, green; PAN damage). Note the fidelity of creating images in each layer independent of the other two is well demonstrated, but the images are blurred since the microscope was slightly out of focus during the pattern generation step.

such as mass loss and nonlinear behavior. This is especially true for selective patterning at 286.80 eV (PAN damage energy), for which the simulations significantly overestimate the contrast. Further studies are required to clarify the reason for this poor agreement. As predicted by ChemLith, the experimental results show that there is little selectivity between PMMA and PPC for the pattern written at 288.45 eV. The best selectivity for PPC was obtained at 100 ms, which is consistent with the predictions. Also, similar to the predictions, the longer the exposure time for PAN, the better the selectivity will be, but

the improvement was small. In conclusion, the simulations give useful qualitative guidance, but are only semiquantitative with regard to matching experiment.

Parts b, c, and d of Figure 4 present optical density images of the patterns created in the corresponding polymer layers of the PMMA/PPC/PAN trilayer with optimal exposure protocols of 100, 100, and 200 ms at 288.45, 290.40, and 286.80 eV, respectively. Both the radiation damage and the imaging were performed at the same energy. The tower and window patterns were selectively transferred to the PAN and PPC layers, respectively. However, the roof pattern was transferred with only marginal selectivity to the PMMA layer since that same pattern was also created in the PPC layer (Figure 4c). Figure 4e shows a color composite of the three patterned layers, where the individual images have been inverted to produce a black background. The colors of the tower and the windows are green and blue, respectively, indicating good chemical selectivity of patterning at the characteristic energies of the PAN and PPC components. However, the roof is purple, i.e., a nearly equal mixture of red and blue, corresponding to similar damage generated in both the PMMA and PPC layers when the roof pattern was generated at 288.45 eV.

Parameters that influence the patterning results have been explored using ChemLith in order to find ways to improve the patterning selectivity for the PMMA layer. Specifically, layer order and layer thickness have been investigated. Figure 3b presents the predictions of turning the film over so that the X-rays reach the PAN layer first before passing through the PPC and the PMMA layers. ChemLith predicts that the patterning selectivity for writing at 288.45 eV is even worse in this situation, with the PPC layer being damaged even more than the PMMA layer. However, the patterning selectivity for the PPC and PAN layers is further improved compared to the original order of the trilayer. We also explored another PMMA/PPC/PAN trilayer, one with different layer thicknesses due to a different sample preparation (23 nm PMMA, 48 nm PPC, 33 nm PAN). ChemLith predicted that patterning selectivity for all three layers is very similar to that for the system shown in Figure 3a with no improvement in selective patterning of the PMMA layer. This was confirmed by experiment (results not shown). This is not surprising since both the absorbed energy and the mass of material vary linearly with layer thickness, and thus to first order the dose (energy/mass) and thus the pattern contrast (as defined in this work) are independent of layer thickness. The only consequence of varying the thickness of a particular layer is to change the incident flux for the downstream layer(s) so that the relative contrast of the downstream layer(s) might be varied. By this logic, an increase of the PPC layer thickness cannot improve selective patterning of an upstream PMMA layer, especially with respect to the PPC layer. Finally, ChemLith does suggest that the selective patterning of the PMMA layer can be improved by increasing the layer thickness of just the PMMA layer. However, the improvement is very limited even if the layer thickness is doubled. Actually, the absolute linear absorbance of PMMA at 288.45 eV is ~3 times that of PPC (see Figure 1). At the same time, the critical dose of PPC is about 1/3 that of PMMA. Thus these two factors cancel each other, which has the net effect that the damage rate of PMMA and PPC are similar at 288.45 eV. That is why the selective patterning of PMMA is very poor. According to ChemLith, the best strategy to resolve this problem is to find another polymer that preserves the overall characteristics of PPC but has lower absorbance at 288.45 eV or has a larger critical dose.

4.3. Chemically Selective Patterning of a PMMA/PEC/PAN Trilayer. Poly(ethylene carbonate) (PEC), another polycarbonate polymer, was evaluated as a possible replacement for PPC. PEC retains most polymer and radiation damage properties of PPC but has a lower absorbance than PPC at 288.45 eV (see Figure 1) due to fewer C−H and C−C bonds per repeat unit. Figure 3c shows ChemLith simulations for a PMMA/PEC/PAN trilayer film, consisting of 41 nm PMMA, 46 nm PEC, and 33 nm PAN. The top panel of Figure 3c plots the contrast in each component as a function of exposure time for irradiation at 288.45 eV. Comparison to Figure 3a shows that the selective patterning of the PMMA layer should be significantly improved since the PMMA contrast is much higher than the PEC contrast, for the same exposure. The middle and bottom panels of Figure 3c represent the contrast as a function of exposure time for selective patterning of the PEC layer at 290.40 eV and the PAN layer at 286.80 eV. Once again, better patterning selectivity for the PEC layer and comparable selectivity for the PAN layer are predicted, compared to the PMMA/PPC/PAN trilayer. Figure 3d presents the predicted contrast (exposure) curves for the same PMMA/PEC/PAN trilayer system turned over to expose the PAN layer first. As found from examination of Figure 3b, the patterning selectivity becomes much worse for patterning at 288.45 eV, with very little difference in the contrast in the PMMA versus the PEC layer. Thus PMMA upstream is the preferred layer ordering even though the opposite layer ordering gives increased selectivity for the PEC and PAN layers.

To verify the above predictions, chemically selective patterning in the PMMA/PEC/PAN trilayer has been carried out, again using the LBNL logo as a test pattern. The exposure conditions (I_0 and dwell) for each polymer layer were the same as those used to pattern the PMMA/PPC/PAN trilayer. Parts f, g, and h of Figure 4 present optical density images of patterns created in PMMA, PEC, and PAN layers by exposure at 288.45, 290.40, and 286.80 eV, respectively. As shown in these images, all patterns were very selectively transferred to each corresponding polymer layer. The microscope was a little out of focus when the pattern generation was carried out, and thus the component maps and color composite (Figure 4i) are less sharp than the pattern in Figure 4e. In the composite map the colors are essentially pure red, pure blue, and pure green for each part of the logo pattern, indicating very good patterning selectivity.

Two other patterns were selectively written in the PMMA/PEC/PAN trilayer, with the results shown in Figure 5. The pattern in Figure 5a is composed of three circles with partial overlap to produce the seven major colors of the RGB color model. The right lower corner inset is the input image. The red, blue, and green patterns (circles) were selectively written into the PMMA, PEC, and PAN layers. The exposures were 125 ms/pixel for the PMMA and PEC layers and 250 ms/pixel for the PAN layer under the normal beamline conditions and the same microscope settings as before. Note that the exposure time needs to be adjusted when the incident flux deviates significantly from the previous values. Alternatively, entrance and exit slit sizes can be adjusted to give a similar incident flux. The generated color composite image (Figure 5a) clearly shows three circles with all seven colors well resolved, indicating high selectivity of the patterning. The point spacing used to write the pattern was a little too sparse, and thus the individual colors are slightly mottled relative to an optimum write. The pattern in Figure 5b shows a three-color version of the logo of McMaster University. The input pattern is shown. The same exposure conditions as those of the pattern in Figure 5a have been used, but a different color coding was used, i.e., PMMA

16336 *J. Phys. Chem. C, Vol. 111, No. 44, 2007*

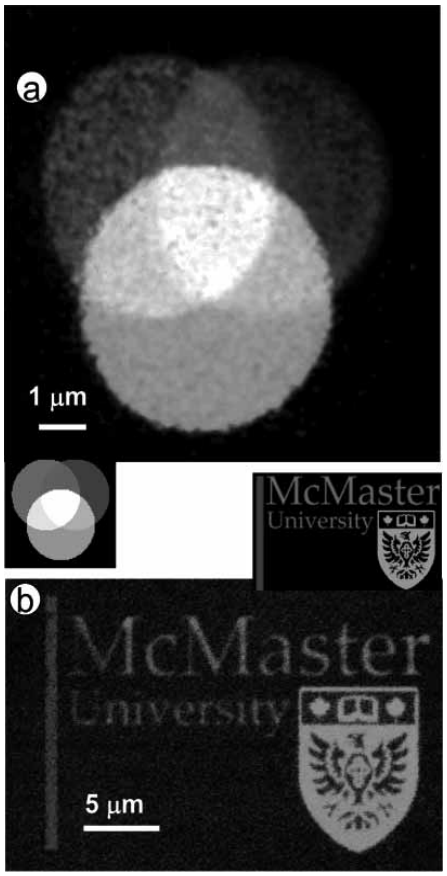

Figure 5. Chemically selective patterning of a PMMA/PEC/PAN trilayer. (a) RGB color circles (red, PMMA damage; blue, PEC damage; green, PAN damage). (b) Logo for McMaster University (red, PEC damage; blue, PMMA damage; green, PAN damage). The input is shown as inserts.

damage in blue, PEC damage in red, and PAN damage in green. Not only the correct colors but also the details of the pattern are clearly reproduced in the final composite image.

In order to demonstrate the layer order effect experimentally, a very simple pattern has been used, i.e., drawing one line in each polymer layer. To ensure that the lines are visible, the exposure time was increased to 250 ms/pixel for the PMMA and PEC layers, and 500 ms/pixel for the PAN layer, under the same beamline conditions and microscope settings. Figure 6a presents images of lines generated in the PMMA, PEC, and PAN layers with exposures at 288.45, 290.40, and 286.80 eV, respectively, for the original order of the trilayer; i.e., PMMA was upstream and thus received X-rays first. Figure 6b shows the results of the same line exposure protocol after the trilayer was turned over in the sample mount so that the PAN layer was upstream. Comparison of Figure 6a and Figure 6b shows that, in the reversed structure, the patterning selectivity for the PMMA layer at 288.45 eV is much worse since a strongly damaged line also appeared in the PEC layer at the same physical position, but the patterning selectivity for the PEC layer at 290.40 eV is greatly improved, as only the PEC layer was highly damaged at this energy. These phenomena are reflected in the color composite images in terms of a more purple color for the PMMA line and a more blue color for the PEC line in the composite image of the reverse order in Figure 6b.

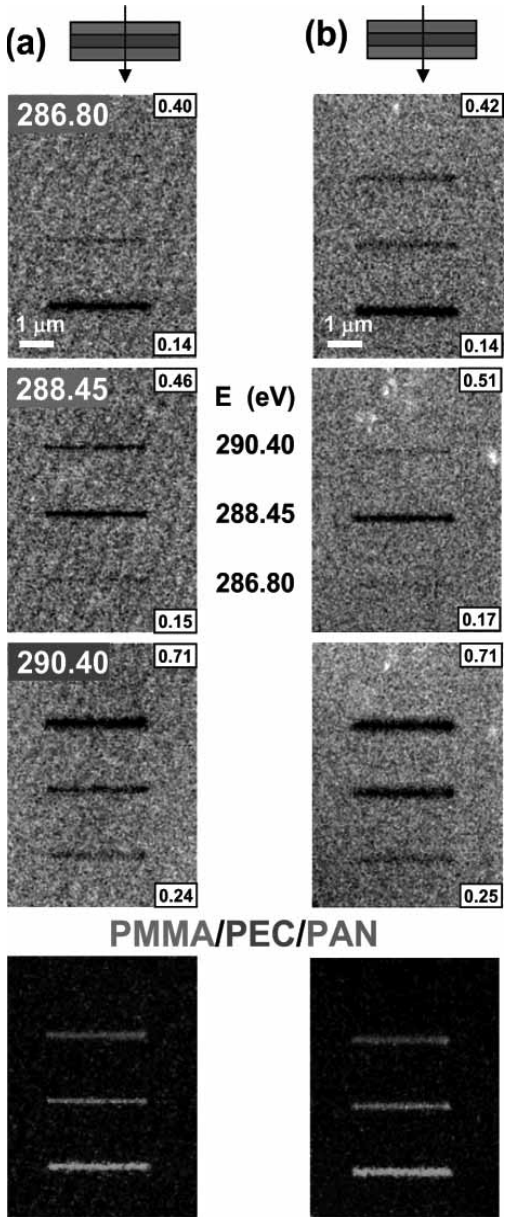

Figure 6. Comparison of chemically selective patterning of a PMMA/PEC/PAN trilayer and its reverse. (a) From top to bottom, optical density images of lines generated by exposure at 288.45, 290.40, and 286.80 eV, respectively, with the PMMA layer upstream; the color-coded composite image of the three patterned layers is shown at the bottom (red, PMMA damage; blue, PEC damage; green, PAN damage). (b) As for (a) but with the layer structure reversed so that the PAN layer is upstream.

Figure 6 shows that the width of the single-write lines with optimal focus and exposure is ~200 nm, as reported earlier.[2] This is surprising since many other applications of the STXM clearly show that the beam spot is less than 50 nm (for the zone plate used in this work the diffraction limited resolution is 42 nm)[15] and the position of the sample relative to the beam is interferometrically controlled to be stable at the 10 nm level.[6] Apparently, there is spreading of the radiation damage by some as yet not fully understood mechanism which broadens the lines.

Different aspects of radiation damage mechanisms were discussed in ref 2. In addition, Figure 6 shows that the damage line widths are different among these three polymers even though the extent of damage (relative to the critical dose for each species) was similar for each of them. The order of the line widths is PEC < PAN < PMMA. The difference is probably due to differences in damage mechanisms, damage propagation, and polymer chain reactions in these species. Further improvement in the spatial resolution of chemical patterning might be achieved by adding inhibitors to the polymer films to quench the radicals/ions produced by the X-rays.[16] Another approach could be to use very short exposures and then reveal the selective damage by chemical amplification.[17,18]

5. Discussion

Chemically selective patterning of trilayer polymer systems by tunable monochromated X-rays has been developed. This allows "full color" reproduction at the submicron scale. The simulation program (ChemLith) is able to provide semiquantitative predictions which were found to be useful in designing and optimizing multilayer systems for chemically selective patterning. Further improvements in chemical selectivity and spatial resolution would make this approach more powerful and thus potentially more useful. Both the NEXAFS spectroscopy and the critical dose for candidate polymers need to be considered simultaneously to improve patterning selectivity. Improvements in modeling the pattern contrast generation physics are necessary in order to further improve the quantitative accuracy of ChemLith. One important modification would be to take into account the time dependence of the optical density of the exposed region during radiation damage, especially at the characteristic energies. At present (eq 2) the sample OD is considered to be fixed during the exposure when the radiation dose is lower than or comparable to the critical dose, but in fact it does change since the spectrum changes due to the radiation damage. A further factor that needs to be included is mass loss, which is a significant factor for PMMA, PPC, and PEC. Both the damage to the functional groups and the mass loss follow the same first-order damage kinetics as are assumed in this work.[2,7−11,19] The strategies described here for chemically selective patterning of trilayer polymer systems are considered generally applicable for the development of polymer systems with even more layers, though finding suitable candidate polymers may be a challenge, as much for chemical compatibility reasons as for the specifics of X-ray absorption spectra and critical dose properties.

In order to make reproducible patterning, a number of factors need to be considered, including film uniformity, accuracy of energy scales, microscope focus quality, higher order light, point spacing in the pattern, etc. Variation in the thin film thickness in the area the pattern is written may be one important source of differences between the experimental and the simulated results. This would introduce irregularities in the pattern, which would not be present in the simulation, since it assumes that the layer thicknesses are uniform. If one included a film thickness map to the input of ChemLith, the simulations could be further improved. The accuracy of the photon energy influences the patterning selectivity since the best results are obtained when the energy corresponds to the maximum of the characteristic NEXAFS peaks. Energy scale errors as small as 0.1 eV will influence the patterning results. The focus quality is also important, not just to the sharpness of the patterns but, even more critically, to the rate of pattern generation. When the pattern is generated with the beam out of focus, blurred patterns (e.g., Figure 4f−i) or even no pattern can result. Below 120 nm, the point spacing in the pattern generation has relatively little influence on the patterning results. For example, the pattern of Figure 5a was generated twice, first using a point spacing of 67 nm and second using a point spacing of 101 nm. The outcomes were very similar (results not shown), which is a direct consequence of the damage spreading effect.

In summary, multilayer polymer structures combined with selected energy irradiation provide chemically selective patterning of polymers and direct-write patterning at the submicron scale. This work complements other efforts in soft X-ray lithography such as soft X-ray patterning of polymer thin films[8,20] and self-assembled monolayers (SAMs).[21−23] The latter examples involved simple patterns such as square pads, and there was no manipulation of the photon energy or exposure protocol to control and optimize the radiation damage. Patterning with tuned soft X-rays, as in this work, exploits differential spectrochemical sensitivity and thereby provides "added value" relative to single energy or broad band X-ray lithography. In addition to the direct-write capability and good spatial resolution, potential applications of this approach may be found in advanced device fabrication and development, which usually involve multilayer and multicomponent structures, or require multilayer resists[24,25] in the lithography stage. Other applications of this technique may be found in radiation modification of materials such as SAMs and nanoparticles for specific purposes such as tailored modification of functional groups and physicochemical properties, e.g., hydrophilic/hydrophobic patterning of a surface, and other types of nanofabrication involving radiation-induced reactions. The principles and examples presented in this work are expected to stimulate further research and possibly lead to practical applications of this novel technique.

Acknowledgment. This research is supported by NSERC (Canada), the Canadian Foundation for Innovation (CFI), and the Canada Research Chair Program. We thank Tolek Tyliszczak for writing the pattern generation component of STXM_control with which these patterns were written. We thank David Kilcoyne for expert maintenance of STXM5.3.2 and Daniel Hernandez-Cruz for assistance with operating the STXM. Construction and operation of the STXM5.3.2 microscope is supported by NSF DMR-9975694, DOE DE-FG02-98ER45737, Dow Chemical, NSERC, and CFI. The Advanced Light Source is supported by the Director, Office of Energy Research, Office of Basic Energy Sciences, Materials Sciences Division of the U.S. Department of Energy, under Contract No. DE-AC03-76SF00098.

References and Notes

(1) Stöhr, J. *NEXAFS Spectroscopy*; Springer Tracts in Surface Science 25; Springer: Berlin, 1992.

(2) Wang, J.; Stöver, H. D. H.; Hitchcock, A. P.; Tyliszczak, T. *J. Synchrotron Radiat.* **2007**, *14*, 181.

(3) Ade, H. In *Experimental Methods in the Physical Sciences*; Samson, J. A. R., Ederer, D. L., Eds.; Academic Press: New York, 1998; Vol. 32, p 225.

(4) Ade, H.; Urquhart, S. G. In *Chemical Applications of Synchrotron Radiation*; Sham, T. K., Ed.; World Scientific Publishing: River Edge, NJ, 2002.

(5) Warwick, T.; Ade, H.; Kilcoyne, D.; Kritscher, M.; Tyliszczak, T.; Fakra, S.; Hitchcock, A.; Hitchcock, P.; Padmore, H. *J. Synchrotron Radiat.* **2002**, *9*, 254.

(6) Kilcoyne, A. L. D.; Tyliszczak, T.; Steele, F.; Fakra, S.; Hitchcock, P.; Franck, K.; Anderson, E.; Harteneck, B.; Rightor, E. G.; Mitchell, G. E.; Hitchcock, A. P.; Yang, L.; Warwick, T.; Ade, H. *J. Synchrotron Radiat.* **2003**, *10*, 125.

(7) Wang, J.; Morin, C.; Li, L.; Hitchcock, A. P.; Scholl, A.; Doran, A. *J. Electron Spectrosc. Relat. Phenom.* **2007**, in press.

(8) Zhang, X.; Jacobsen, C.; Lindaas, S.; Williams, S. *J. Vac. Sci. Technol., B* **1995**, *13*, 1477.

(9) Rightor, E. G.; Hitchcock, A. P.; Ade, H.; Leapman, R. D.; Urquhart, S. G.; Smith, A. P.; Mitchell, G.; Fischer, D.; Shin, H. J.; Warwick, T. *J. Phys. Chem. B* **1997**, *101*, 1950.

(10) Beetz, T.; Jacobsen, C. *J. Synchrotron Radiat.* **2002**, *10*, 280.

(11) Coffey, T.; Urquhart, S. G.; Ade, H. *J. Electron Spectrosc. Relat. Phenom.* **2002**, *122*, 65.

(12) aXis2000 is an application written in Interactive Data Language. It is available free for noncommercial applications at http://unicorn.mcmaster.ca/aXis2000.html.

(13) Egerton, R. F.; Li, P.; Malac, M. *Micron* **2004**, *35*, 399.

(14) Frey, S.; Rong, H.-T.; Heister, K.; Yang, Y.-J.; Buck, M.; Zharnikov, M. *Langmuir* **2002**, *18*, 3142.

(15) Attwood, D. *Soft X-rays and Extreme Ultraviolet Radiation, Principles and Applications*; Cambridge University Press: Cambridge, U.K., 2000.

(16) Rabek, J. F. *Photostabilization of Polymers: Principles and Applications*; Elsevier: Oxford, England, 1990.

(17) Ito, H.; Willson, C. G. *Polym. Eng. Sci.* **1983**, *23*, 1012.

(18) Nakano, A.; Okamoto, K.; Yamamoto, Y.; Kozawa, T.; Tagawa, S.; Kai, T.; Nemoto, H. *Jpn. J. Appl. Phys.* **2005**, *44*, 5832.

(19) Richter, A. G.; Guico, R.; Shull, K.; Wang, J. *Macromolecules* **2006**, *39*, 1545.

(20) Choi, J.; Manohara, H. M.; Morikawa, E.; Sprunger, P. T.; Dowben, P. A.; Palto, S. P. *Appl. Phys. Lett.* **2000**, *76*, 381.

(21) La, Y.-H.; Jung, Y. J.; Kim, H. J.; Kang, T.-H.; Ihm, K.; Kim, K.-J.; Kim, B.; Park, J. W. *Langmuir* **2003**, *19*, 4390.

(22) Klauser, R.; Huang, M.-L.; Wang, S.-C.; Chen, C.-H.; Chuang, T. J.; Terfort, A.; Zharnikov, M. *Langmuir* **2004**, *20*, 2050.

(23) Klauser, R.; Chen, C.-H.; Huang, M.-L.; Wang, S.-C.; Chuang, T. J.; Zharnikov, M. *J. Electron Spectrosc. Relat. Phenom.* **2005**, *144−147*, 393.

(24) Berreman, D. W.; Bjorkholm, J. E.; Becker, M.; Eichner, L.; Freeman, R. R.; Jewell, T. E.; Mansfield, W. M.; MacDowell, A. A.; O'Malley, M. L.; Raab, E. L.; Silfvast, W. T.; Szeto, L. H.; Tennant, D. M.; Waskiewicz, W. K.; White, D. L.; Windt, D. L.; Wood, O. R., II. *Appl. Phys. Lett.* **1990**, *56*, 2180.

(25) Rooks, M. J.; Eugster, C. C.; del Alamo, J. A.; Snider, G. L.; Hu, E. L. *J. Vac. Sci. Technol., B* **1991**, *9*, 2856.

Chapter 8

Summary and future work

This chapter summarizes the work of this thesis, and highlights the major original contributions of this thesis. In addition, suggestions are provided for future studies of radiation chemistry studies with soft X-rays.

8.1 Summary

NEXAFS spectroscopy at different core edges, i.e. C 1s, N 1s and O 1s, was used to study the radiation chemistry of selected polymers, including poly(methyl methacrylate) (PMMA), polyacrylonitrile (PAN), poly(ethyl cyanoacrylate) (PECA), poly(propylene carbonate) (PPC), poly(ethylene carbonate) (PEC), polyethylene terephthalate (PET), polystyrene (PS), and fibrinogen (Fg) in a STXM. The results show that radiation chemistry is quite diverse among these polymers. Specifically, the observed radiation damage can be classified into three categories: (i) chemical change without mass loss, such as PAN, PET and PS, (ii) chemical change with small mass loss, such as PMMA, PECA, Fg and (iii) chemical change with large mass loss, such as PPC and PEC. NEXAFS spectroscopy provides abundant information with respect to polymer radiation damage. The chemical change is characterized by attenuation, or development and growth, of specific NEXAFS features associated with different functional groups. The destruction of functional groups involves bond dissociation, transformation, elimination etc. A common phenomenon of damage to these polymers is the development and growth of the signal around 285.1 eV associated with the creation of C=C double bonds. This is

believed due to dehydrogenation in the polymer backbone, thus it is a common process in polymer damage. Mass loss was often observed for non-aromatic polymers. Mass loss is generally caused by main chain scission, elimination of small fragments or side chains, etc. Furthermore, damage to functional groups which are part of the polymer backbone results in relatively large mass loss due to main chain scission, such as the large mass loss in polylactide (PLA) (Appendix A) compared to PMMA. The damage to functional groups changes depending on the immediate chemical environment. For instance, C≡N groups in PAN mainly undergo reduction or transformation whereas some of them are eliminated as mass loss in PECA. The ester groups in non-aromatic polymers are radiation sensitive and susceptible to destruction and elimination, whereas they are stabilized when attached to phenyl rings.

Not only radiation chemistry, but also damage rate is rather different among the polymers studied in this work. The damage rate is represented by the critical dose, which is determined by the quantitative methodology developed in this thesis. The quantitative results show that the order of radiation resistance for these polymers is PS > PET > Fg > PAN > PECA ≈ PMMA > PPC ~ PEC. Aromatic polymers, such as PS and PET, are much more damage resistant than non-aromatic polymers, such as PAN and PEC, with 3- to 60-fold larger critical doses. The phenyl ring in PS is the most radiation resistant, about three times less probable to be damaged than the ester group directly attached to a phenyl ring in PET. The damage rate of protein (e.g. Fg) is between that of typical aromatic and non-aromatic polymers. This is consistent with the complicated chemical composition of a protein. Although non-aromatic polymers are generally radiation sensitive, they still

exhibit a variety of damage rates, which are closely related to their chemical structures and radiation chemistry. Chemical environment is also significant to the damage rate of a functional group. For instance, C≡N groups in PAN are about two times more radiation resistant than those in PECA. The ester groups attached to phenyl rings are about seven times more stable than those in non-aromatic polymers. Apart from these, sample environment and technique specificity have shown minor influence on the critical dose as demonstrated by comparable dose-damage results obtained in both STXM and X-PEEM.

The soft X-ray damage studies of this thesis provide useful guidelines for meaningful soft X-ray spectromicroscopy of radiation sensitive materials. They also contribute to improved understanding of the fundamentals of the radiation chemistry and damage kinetics of polymers. A potential application of these studies was explored in this thesis, i.e. chemically selective soft X-ray direct-write patterning by STXM. Chemically selective damage was initially investigated in four different polymer systems: a PMMA/PAN bilayer film, a PMMA-*blend*-PAN micro phase-separated film, a poly(MMA-*co*-AN) copolymer film and a PECA homopolymer film. A high level of chemically selective damage was only achieved for the PMMA/PAN bilayer, i.e. irradiation at 288.45 eV selectively removed the carbonyl group from PMMA while irradiation at 286.80 eV selectively reduced the nitrile group of PAN. In the last two homogenous polymer systems similar amounts of damage to the nitrile and carbonyl groups occurred during irradiation at either 286.80 or 288.45 eV. This is attributed to damage spread between the C≡N and C=O groups probably via electrons and radical/ionic processes, aided by their close spatial proximity. Although the overall

thickness of the bilayer sample is about 70 nm (much smaller than the lateral damage spreading which is as large as 300 nm), the interface between the layers appears to effectively block the transfer of damage between the two layers. The interface was investigated to show no physical gap or measurable impurities. The damage spread was proved not to be caused by sample heating since this is negligible for the X-ray irradiation used.

Chemically selective patterning was demonstrated for the first time in the PMMA/PAN bilayer and extended to trilayer polymer films in order to achieve full color pattern reproduction. Two trilayer polymer systems were successfully fabricated - PMMA/PPC/PAN and PMMA/PEC/PAN. Each polymer layer was selectively patterned by exposure at its characteristic absorption energy: 288.45 eV for PMMA, 290.40 eV for PPC (PEC) and 286.80 eV for PAN. For the PMMA/PPC/PAN trilayer, highly selective patterning was achieved for the PAN and PPC layers, while the selectivity for the PMMA layer was poor. This was significantly improved by replacing PPC with PEC. A simulation program was developed to predict the patterning results with input of the X-ray absorption spectra of the polymers, the layer order and thicknesses, the critical dose of each polymer etc. The simulations generated semi-quantitative predictions of the experimental contrast, and are a useful tool to find exposure times that optimize pattern contrast and to guide the improvement directions. Full color pattern reproduction with ~ 150 nm spatial resolution was demonstrated with several high resolution multi-wavelength patterns created in the PMMA/PEC/PAN trilayer film.

8.2 Original contributions of this thesis

Based on the specific experimental observations, results and conclusions, the major original contributions of this thesis are:

- Quantitative methodologies for critical dose determination in STXM and X-PEEM were developed and optimized.
- A quantitative approach was developed for dose evaluation of variable optical density during exposure in STXM. This approach is important to accuracy for damage with mass loss and damage at NEXAFS features. The better fits of the dose – damage data using this approach helped to support the concept that radiation processes can generally be described with first order kinetics.
- Discovery of the interface effect of the layered polymer films, i.e. the interface effectively blocking damage transport between different layers.
- Chemically selective soft X-ray direct-write patterning was achieved in layered polymer films for the first time. A spatial resolution of ~ 150 nm in the patterning is the best achieved to date.
- A simulation program was developed to predict the radiation damage and patterning contrast and shown to have semi-quantitative accuracy.

8.3 Future work

8.3.1 Understanding the polymer interface effect

The polymer-polymer interface that has been shown to be effective to block damage propagation still needs further investigation to understand how it blocks damage

spread. Although TEM and STXM of cross-sections of the bilayer was used to study the interface, it would be better to use non-destructive technique to study the polymer interface with respect to the morphology to check if there is a physical gap or an intimate contact. Neutron reflection appears to be an excellent candidate technique [BHH98]. It determines the composition variation normal to the surface of the polymer films, with accuracy on a sub-nanometer length scale and without modification to the sample. Thus it can determine the thickness of the interface. X-ray reflectivity [RGS&06] is another possible technique to use to provide this information.

The chemical composition of the interface may be important to the interface effect. It may be possible that small amounts of impurities were localized at the interface from either or both layers during the spin coating and drying/annealing process, and these impurities are chemically trapping reactive species, such as radicals and ions and thus preventing them from migrating across the interface. Although NEXAFS spectroscopy does not show impurities, the sensitivity may not be enough. Further analysis of the composition of the interface is needed with higher sensitivity techniques, such as X-ray Photoelectron Spectroscopy (XPS) depth profiling and Secondary Ion Mass Spectrometry (SIMS).

Another possibility is the potential energy well of the interface that blocks the reactive migrating species, especially positive ions. A major cause of a potential energy barrier could be an electric field built up at the interface due to more emission of electrons from one layer to the other as a function of photon energy during radiation damage [C97]. As a result, the side of the interface with more radiation damage could become positively

charged, while the other side would be negatively charged. To check this hypothesis in a bilayer structure, an external electric field could be applied to the sample to counteract the hypothesized interface electric field so that damage spread can cross the interface. Reversing the external field polarity might result in better blocking of the damage spread. Another approach to interfere with possible interface charging may be to apply a conductive coating at the interface.

The damage spread is mainly lateral for a bilayer sample. If the interface is placed perpendicular to the film, whether the damage in one phase is easily transferred to the other phase will help to understand the interface effect and the damage mechanism. Such a scenario can be found in the PMMA-*blend*-PAN micro phase-separated film (see Chapter 6). Radiation damage experiments at the interface can be conveniently carried out by drawing line damage in perpendicular and in close proximity parallel to a boundary in the polymer blend. If the damage spread is blocked at the interface, it means the interface is effective in any direction of the damage transport. If the damage spread is not effectively blocked by the interface, it means a high enough concentration of migrating reactive species is able to overcome the interface. The capacity of the interface effect can also be measured in a bilayer structure when one of the layers is selectively damaged with increased dose to high enough values. Then one would check if there is a threshold dose which destroys the interface.

8.3.2 Understanding radiation damage mechanisms

Soft X-ray damage involves two successive stages, the primary and secondary

processes. The primary processes include photoabsorption and subsequent decay of the core holes by the Auger process [C95a, C97]. The consequence of the Auger process is to generate singly charged or doubly charged parent ions. The latter is more dissociative than the former. As a result there should be a large difference in the damage rate. An approach to verify this is to quantify the damage rate in terms of critical dose in the pre-edge and in the post-edge. X-ray irradiation in the pre-edge region mainly results in single ionization, while irradiation in the post-edge yields double or higher levels of ionization. Experiments to test this mechanism have been carried out for hexaphenylbenzene by STXM, but further clarification is needed to remove side effects, such as carbon contamination and non-uniform sample thickness.

The secondary processes of soft X-ray damage involve the generation of free radicals and ions as a consequence of bond dissociation. A direct approach to reduce radiation damage could be to add radical inhibitors to the sample to see if the damage rate is slowed or damage spread is reduced. Preliminary inhibiting experiments have been carried out by STXM and show very limited effects of the inhibitor. A possible explanation is that core excitation induced radiation damage leads to a fast cascade process and rapid radical/ion migration and associated chemical and physical changes, which is hard to control with a low concentration of radical inhibitors. Further investigation is needed.

Soft X-ray damage involves loss of a large number of electrons in the surface(s) of the sample, resulting in surface charging. If those electrons could be compensated promptly, the radiation damage may be slowed. Conductive coatings, including metal (e.g.

Au) and carbon, have been applied to polymer surfaces to see if polymers can be protected via removing surface charging and possible heating. However, the experiments attempted to date have been unsuccessful, due to damage of the polymer sample during sputtering coating. A coating method that does not damage the sample is needed to further investigate this approach.

The soft X-ray damage mechanism is speculated to be similar to that of electron beam damage. A comparison between these two kinds of damage via STXM and Transmission Electron Microscopy (TEM) would thus help to understand radiation damage mechanisms. Experiments have been carried out to damage PET using the two techniques with consistent results [HDJ&07]. A recent measurement gained more insights to the radiation damage kinetics and chemistry with respect to these two techniques. Another publication is under preparation.

8.3.3 Anti-contamination in STXM

One problem in current generation STXM microscopes is sample contamination from X-ray induced photodeposition of a carbonaceous contaminant layer. The possible sources of the contaminants are lubricants from the mechanical stages as well as fingerprints and organic species from frequent use of STXM for organic and biological samples. These contaminants generally have no influence on routine STXM measurements because the radiation dose is very low for typical exposure times of a few milliseconds per pixel. However, it can be a serious problem when high radiation dose with exposure time of a few seconds per pixel is required e.g. in order to study radiation

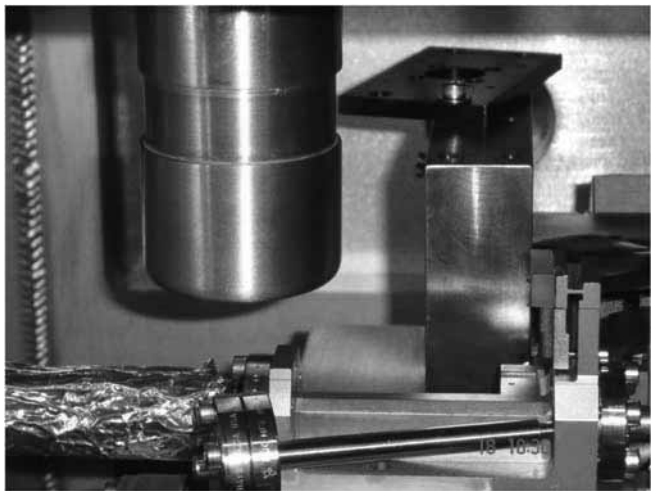

Figure 8.1 Photograph of the in-vacuum liquid nitrogen cold trap. (Courtesy of Danielle Covelli and Dr. Stephen Urquhart, University of Saskatchewan)

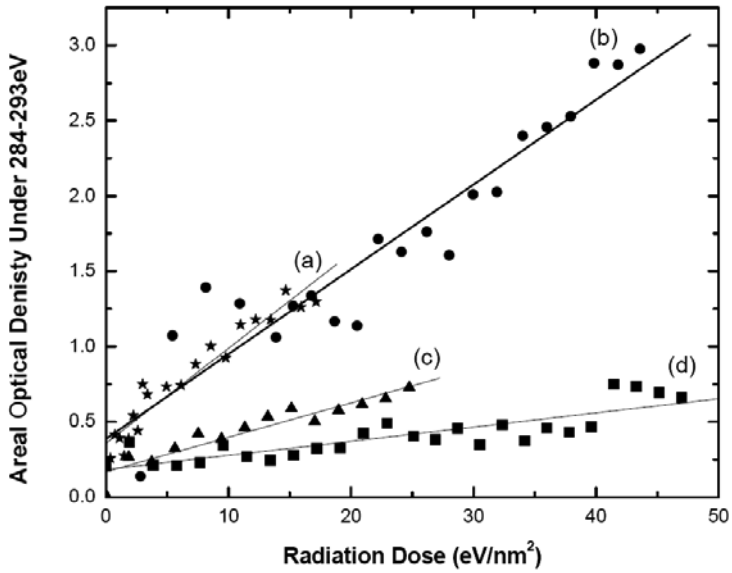

Figure 8.2 Plots of the integrated areal optical density of carbon as a function of radiation exposure, (a) ambient temperature and active pumping, (b) ambient temperature and helium atmosphere, (c) liquid nitrogen cooled and active pumping, (d) liquid nitrogen cooled and helium atmosphere. (Courtesy of Danielle Covelli and Dr. Stephen Urquhart, University of Saskatchewan)

damage of some aromatic polymers, to analyze materials that contain low concentrations, or if one wishes to do extended time measurements involving correlation of the STXM

signal with variation of the sample properties (e.g. chemical reactions, magnetic dynamics, stress, temperature etc). In order to reduce this carbon contamination, an in-vacuum liquid nitrogen cold trap (**Figure 8.1)** was designed and tested in the polymer STXM at ALS beamline 5.3.2 (unpublished results from collaborators, Danielle Covelli and Dr. Stephen Urquhart, University of Saskatchewan). This cold trap showed a significant decrease in the rate of contamination in this microscope, as shown in **Figure 8.2**.

Another approach is to protect the sample by encapsulating it into a cell which is made by two or three Si_3N_4 windows, as shown in **Figure 8.3**. **Fig. 8.3a** shows a polymer film is spin coated (or solvent casting) onto a Si_3N_4 window, then it is sealed by two more windows. The empty space in front of and behind the sample is free of organic contaminants and oxygen when this device is fabricated in a helium environment. Then during STXM measurements, there will be no photodeposition at the focal point on the sample. The photodeposition would be negligible on the front and back Si_3N_4 windows

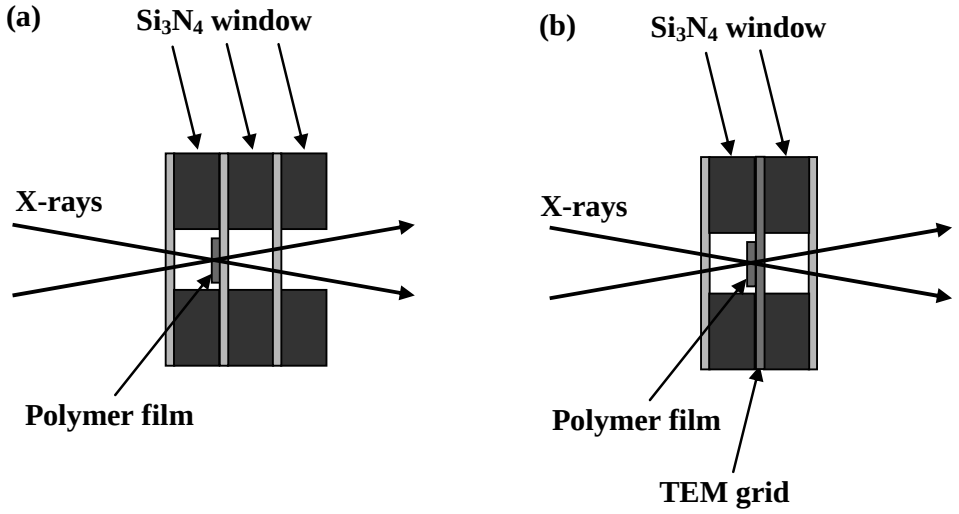

Figure 8.3 Schemes to protect polymer films from photodeposition, (a) a polymer film is spin coated (or solvent casting) on a Si_3N_4 window, then sealed by two more windows, (b) a polymer film is placed on a TEM grid, then sealed by two Si_3N_4 windows.

because the X-rays are defocused there and the energy density is too low to result in observable photodeposition. Similarly, **Figure 8.3b** presents the scheme to protect a polymer film on a TEM grid. These anti-contamination schemes are currently under test.

8.3.4 Further improvement of chemical patterning in multi-layer polymer films

More studies of multi-layer polymer films are necessary in order to further improve the patterning selectivity. With the help of the simulation program, **ChemLith**, many factors, such as layer order, layer thickness, layer materials, choice of exposure energy, time and incident flux, can be systematically varied to improve the patterning results. Some promising directions include: optimization of the PMMA layer thickness; replacement of the PEC layer with an analogue of higher critical dose or even lower absorption at 288.45 eV while retaining other properties of PEC; etc.

The best spatial resolution of patterning is about 150 nm, much larger than the beam spot size of ~ 30 nm. This is probably due to damage spreading via radicals and ions, and associated chemical reactions, such as depolymerization and fragmentation. The patterning spatial resolution was confirmed by multiple-pass exposures at the same region with a registration error smaller than 10 nm. Further improvement of spatial resolution might be achieved by adding inhibitors to the polymer films to quench the radicals/ions to reduce damage spread. Another approach could be chemical amplification [IW83, NOY&05] combined with very short exposures. Furthermore, I note the lateral spreading of damage is quite different for different polymers, so polymers with better spatial resolution capability should be used for patterning applications.

8.3.5 Further improvement of simulations

Improvements in the simulation program are necessary in order to further improve the quantitative accuracy of **ChemLith**. One important modification would be to take into account the time dependence of the optical density of the exposed region during radiation damage using equation 3.3, especially at the characteristic energies. At present the sample OD is simply treated as fixed during exposure, but in fact it does change since the spectrum changes due to the radiation damage. Thus the actual dose rate is decreasing during exposure, resulting in lower experimental contrast compared to predictions. Another factor that needs to be included is mass loss, which is a significant factor for PPC and PEC. Another improvement to **ChemLith** is to add a film thickness map to the input.

ChemLith assumes no inter-layer damage transfer across the interface. In reality, it is possible that there is a small portion of damage transferred between adjacent layers. This may contribute to part of the deviation between **ChemLith** results and experiments. Future improvements to **ChemLith** with capability to simulate the damage transfer across the interface are important to increase its accuracy.

8.3.6 Extension to more organic materials

As shown in Chapter 1 there is extensive literature dealing with soft X-ray damage to different kinds of organic materials. However, currently these studies have focused mainly on polymers although a protein was investigated in this thesis. The radiation damage studies in X-PEEM reported in this thesis are pioneering. So it would be interesting to extend these studies to other organic materials. Small organic molecules

should be involatile in order to be suitable for STXM and X-PEEM damage measurements. Small biochemical molecules, including amino acids, DNA components such as nucleobases and nucleotides, appear to fulfil the requirement and are studied increasingly by other techniques. Other synthetic polymers are also worth studying so that a larger library of radiation damage studies can be created. For instance, aromatic polycarbonate, polyurethane and polyurea are good candidates in order to compare with non-aromatic counterparts which have been studied in this work. Biopolymers, including proteins, deoxyribonucleic acid (DNA), ribonucleic acid (RNA), polysaccharides, polylipids, etc. are important to life sciences. STXM damage studies of these biopolymers can provide damage information at the molecular level, and may achieve chemically selective damage to some extent. So does the X-PEEM damage of these materials. These studies should be of great importance to understand more complicated radiation damage to biological materials and species.

8.3.7 Potential applications

Potential applications of this work have been discussed throughout the thesis in a number of directions. For details, one can refer to sections 4.4 (page 153-154), 6.4.2 (page 192-193), and 7.5 (page 202).

References

The reference code is formulated from the first letter of the last name of the first three authors, followed by the year of publication. If a reference has more than three authors, the initials are followed by an ampersand. If two references have the same author-year code, a sequence letter is added after the year for each publication.

[A91] B.K. Agarwal, *X-Ray Spectroscopy: an Introduction*, Springer Series in Optical Sciences Vol. 15, Springer-Verlag, Berlin, Heidelberg, **1991**.

[A98] E.L. Alpen, *Radiation Biophysics*, Academic Press, San Diego, California, **1998**.

[A99] D. Attwood, *Soft X-Rays and Extreme Ultraviolet Radiation: Principles and Application*, Cambridge University Press, **1999**.

[A01] J.S. Amstock, *Handbook of Adhesives and Sealants in Construction*, McGraw-Hill, New York, **2001**.

[AFY04a] K. Akamatsu, K. Fujii and A. Yokoya, *Int. J. Radiat. Biol.* 80 (**2004**) 849-853.

[AFY04b] K. Akamatsu, K. Fujii and A. Yokoya, *Radiat. Res.* 161 (**2004**) 442-450.

[AHE&95] E.T. Ada, L. Hanley, S. Etchin, J. Melngailis, W.J. Dressick, M-S. Chen and J.M. Calvert, *J. Vac. Sci. Technol. B* 13 (**1995**) 2189-2196.

[AHP&06] M.G. Anderson, T. Haraszti, G.E. Petersen, S. Wirick, C. Jacobsen, S.W.M. John and M. Grunze, *Micron* 37 (**2006**) 689-698.

[APD&99] S. Anders, H.A. Padmore, R.M. Duarte, T. Renner, T. Stammler, A.

Scholl, M.R. Scheinfein, J. Stöhr, L. Séve and B. Sinkovic, *Rev. Sci. Instrum*. 70 (**1999**) 3973-3981.

[ARF&96] D.E. Alexander, L.E. Rehn, K. Farrell and R.E. Stoller, *J. Nucl. Mater.* 228 (**1996**) 68-76.

[ASE98] H. Ade, in: J.A.R. Samson, D.L. Ederer (Eds.), *Experimental Methods in the Physical Sciences*, Vol. 32, Academic Press, New York, **1998**.

[AUT02] H. Ade and S.G. Urquhart, in: T.K. Sham (Ed.), *Chemical Applications of Synchrotron Radiation*, World Scientific Publishing, Singapore, **2002**.

[AXIS] *aXis2000* is a freeware program written in Interactive Data Language, and is available at http://unicorn.mcmaster.ca/aXis2000.html.

[AZC92] H. Ade, X. Zhang, S. Cameron, C. Costello, J. Kirz and S. Williams, *Science* 258 (**1992**) 972-975.

[B46] J.P. Blewett, *Phys. Rev.* 69 (**1946**) 87-95.

[B00a] A. Bhattacharya, *Prog. Polym. Sci.* 25 (**2000**) 371-401.

[B00b] W.P. Burmeister, *Acta Cryst. D* 56 (**1994**) 328-341.

[B01] E. Bauer, *J. Electron Spectrosc. Relat. Phenom.* 114-116 (**2001**) 975-987.

[BAA&06] H. Bluhm, K. Andersson, T. Araki, K. Benzerara, G.E. Brown, J.J. Dynes, S. Ghosal, M.K. Gilles, H.-Ch. Hansen, J.C. Hemminger, A.P. Hitchcock, G. Ketteler, A.L.D. Kilcoyne, E. Kneedler, J.R. Lawrence, G.G. Leppard, J. Majzlam, B.S. Mun, S.C.B. Myneni, A. Nilsson, H. Ogasawara, D.F. Ogletree, K. Pecher, M. Salmeron, D.K. Shuh, B. Tonner, T. Tyliszczak, T. Warwick and T.H. Yoon, *J. Electron Spectrosc. Relat. Phenom.* 150

(**2006**) 86-104.

[BC63] R.O. Bolt and J.G. Carroll, *Radiation Effects on Organic Materials*, Academic Press, **1963**.

[BFB&00] M. Bässler, R. Fink, C. Buchberger, P. Väterlein, M. Jung and E. Umbach, *Langmuir* 16 (2000) 6674-6681.

[BGC&07] D. Borek, S.L. Ginell, M. Cymborowski, W. Minor and Z. Otwinowski, *J. Synchrotron Rad.* 14 (**2007**) 24-33.

[BHH98] D.G. Bucknall and J.S. Higgins, in: H. Hommel (Ed.), *Polymers and Surfaces. A Versatile Combination*, Research Signpost, Trivandrun, India, **1998**.

[BJ76] T.L. Blundell and L.N. Johnson, *Protein Crystallography*, Academic, **1976**.

[BJ02] T. Beetz and C. Jacobsen, *J. Synchrotron Rad.* 10 (**2002**) 280-283.

[BLW&04] J.A. Brandes, C. Lee, S. Wakeham, M. Peterson, C. Jacobsen, S. Wirick and G. Cody, *Mar. Chem.* 92 (**2004**) 107-121.

[BO02] D.J. Bacon and Y.N. Osetsky, *Int. Mater. Rev.* 47 (**2002**) 233-241.

[BPM01] R.A. Britten, L.J. Peters and D. Murray, *Radiat. Res.* 156 (**2001**) 125-135.

[BRA&89] C. Buckley, H. Rarback, R. Alforque, D. Shu, H. Ade, S. Hellman, N. Iskander, J. Kirz, S. Lindaas, I. McNulty, M. Oversluizen, E. Tang, D. Attwood, R. DiGennaro, M. Howells, C. Jacobsen, Y. Vladimirsky, S. Rothman, D. Kern and D. Sayre, *Rev. Sci. Instrum.* 60 (**1989**) 2444-2447.

[BW99] M. Born and E. Wolf, *Principles of Optics*, Cambridge University Press, **1999**.

[BZW94] M.J. Boack, Y. Zhou and S.D. Worley, *J. Chem. Phys.* 100 (**1994**) 8392-8398.

[C81] F. J. Campbell, *Rad. Phys. Chem.* 18 (**1981**) 109-123.

[C83] J.E. Coggle, *Biological Effects of Radiation*, Taylor & Francis, **1983**.

[C95a] J. Cazaux, *Microsc. Microanal. Microstruct.* 6 (**1995**) 345-362.

[C95b] J. Cazaux, *Ultramicroscopy* 60 (**1995**) 411-425.

[C97] J. Cazaux, *J. Microsc.* 188 (**1997**) 106-124.

[C98] N.E.A. Crompton, *Acta Oncol.* 37 (**1998**) 129-142.

[CCS&05] Z. Cai, P. Cloutier, L. Sanche and D. Hunting, *Radiat. Res.* 164 (**2005**) 173-179.

[CCV&95] K.D. Childs, B.A. Carlson, L.A. Vanier, J.F. Moulder, D.F. Paul, W.F. Stickle, D.G. Watson and C.L. Hedberg, *Handbook of Auger Electron Spectroscopy*, Physical Electronics, Eden Prairie, MN, **1995**.

[CDG&05] J. Cadet, T. Douki, D. Gasparutto and J.-L. Ravanat, *Rad. Phys. Chem.* 72 (**2005**) 293-299.

[CDS&06] L-L. Chua, M. Dipankar, S. Sivaramakrishnan, X. Gao, D. Qi, A.T.S. Wee and P.K.H. Ho, *Langmuir* 22 (**2006**) 8587-8594.

[CMM&00] J. Choi, H.M. Manohara, E. Morikawa, P.T. Sprunger, P.A. Dowben and S.P. Palto, *Appl. Phys. Lett.* 76 (**2000**) 381-383.

[CRC02] V. Cherezov, K.M. Riedl and M. Caffrey, *J. Synchrotron Rad.* 9 (**2002**) 333-341.

[CS91] R.L. Clough and S.W. Shalaby, *Radiation Effects on Polymers*, ACS

Symposium Series 475, **1991**.

[CS02] C. Claeys and E. Simoen, *Radiation Effects in Advanced Semiconductor Materials and Devices*, Springer-Verlag, **2002**.

[CSN&04] S.J. Collis, J.M. Schwaninger, A.J. Ntambi, T.W. Keller, W.G. Nelson, L.E. Dillehay and T.L. DeWeese, *J. Biol. Chem.* 279 (**2004**) 49624-49632.

[CSS&98] D. Choudhary, M. Srivastava, A. Sarma and R.K. Kale, *Radiat. Environ. Biophys.* 37 (**1998**) 177-185.

[CU04] R.R. Cooney and S.G. Urquhart, *J. Phys. Chem. B* 108 (**2004**) 18185-18191.

[CUA02] T. Coffey, S.G. Urquhart and H. Ade, *J. Electron Spectrosc. Relat. Phenom.* 122 (**2002**) 65-78.

[CW86] C.Z. Chen and D.E. Watt, *Int. J. Radiat. Biol.* 49 (**1986**) 131-142.

[DAU03] O. Dhez, H. Ade and S.G. Urquhart, *J. Electron Spectrosc. Relat. Phenom.* 128 (**2003**) 85-96. (http://www.physics.ncsu.edu/stxm/polymerspectro/)

[DCL&98] G. De Stasio, M. Capozi, G.F. Lorusso, P.A. Baudat, T.C. Droubay, P. Perfetti, G. Margaritondo and B.P. Tonner, *Rev. Sci. Instrum.* 69 (**1998**) 2062-2066.

[DGP&98] G. De Stasio, B. Gilbert, L. Perfetti, O. Fauchoux, A. Valiquer, T. Nelson, M. Capozi, P.A. Baudat, F. Cerrina, Z. Chen, P. Perfetti, B.P. Tonner and G. Margaritondo, *Rev. Sci. Instrum.* 69 (**1998**) 3106-3108.

[DRH&02] Y. Dabin, G. Rostaing, O. Hignette, A. Rommeveaux and A.K. Freund, *Proc. SPIE* 4782 (**2002**) 235-245.

[DSA00] J. Dahm-Daphi, C. Sab and W. Alberti, *Int. J. Radiat. Biol.* 76 (**2000**) 67-75.

[DSW&98] R. Devanathan, K.E. Sickafus, W.J. Weber and M. Nastasi, *J. Nucl. Mater.* 253 (**1998**) 113-119.

[EGL&47] F.R. Elder, A.M. Gurewitsch, R.V. Langmuir and H.C. Pollock, *Phys. Rev.* 71 (**1947**) 829-830.

[EKR&91] W. Engel, M.E. Kordesch, H.H. Rotermund, S. Kubala, and A. von Oertzen, *Ultramicroscopy* 36 (**1991**) 148-153.

[ELM04] R.F. Egerton, P. Li and M. Malac, *Micron* 35 (**2004**) 399-409.

[FAM&03] K. Fujii, K. Akamatsu, Y. Muramatsu and A. Yokoya, *Nucl. Instr. Meth. Phys. Res. B* 199 (**2003**) 249-254.

[FBB&92] G.F. Foster, C.J. Buckley, P.M. Bennett and R.E. Burge, *Rev. Sci. Instrum.* 63 (**1992**) 599-600.

[FMG&95] H. Frohlich, M. Le Maire, F. Guillot, M. Tronc, J.M. Cosset and C. Le Sech, *Nucl. Instr. Meth. Phys. Res. B* 105 (**1995**) 314-317.

[FPW&02] J. Feng, H. Padmore, D.H. Wei, S. Anders, Y. Wu, A. Scholl and D. Robin, *Rev. Sci. Instrum.* 73 (**2002**) 1514-1517.

[FRH&02] S. Frey, H.-T. Rong, K. Heister, Y.-J. Yang, M. Buck and M. Zharnikov, *Langmuir* 18 (**2002)** 3142-3150.

[FTA&02] B. Fayard, A. Touati, F. Abel, M.A. H. du Penhoat, I. Despiney-Bailly, F. Gobert, M. Ricoul, A. L'Hoir, M.F. Politis, M.A. Hill, D.L. Stevens, L. Sabatier, E. Sage, D.T. Goodhead and A. Chetioui, *Radiat. Res.* 157

(**2002**), 128-140.

[FTO&96] H. Fujisaki, S. Takahashi, H. Ohzeki, K. Sugisaki, H. Kondo, H. Nagata, H. Kato and S. Ishiwata, *J. Micros.* 182 (**1996**) 79-83.

[FVA&07] E. Fioravanti, F.M.D. Vellieux, P. Amara, D. Madern and M. Weik, *J. Synchrotron Rad.* 14 (**2007**) 84-91.

[FWU&97] R. Fink, M.R. Weiss, E. Umbach, D. Preikszas, H. Rose, R. Spehr, P. Hartel, W. Engel, R. Degenhardt, R. Wichtendahl, H. Kuhlenbeck, W. Erlebach, K. Ihmann, R. Schlögl, H.-J. Freund, A.M. Bradshaw, G. Lilienkamp, Th. Schmidt, E. Bauer and G. Benner, *J. Electron Spectrosc. Relat. Phenom.* 84 (**1997**) 231-250.

[G74] D.T. Grubb, *J. Mater. Sci.* 9 (**1974**) 1715-1716.

[GBK&02] J.-J. Gallet, F. Bournel, S. Kubsky, G. Dufour, F. Rochet and F. Sirotti, *J. Electron Spectrosc. Relat. Phenom.* 122 (**2002**) 285-295.

[GKG&02] S. Günther, B. Kaulich, L. Gregoratti and M. Kiskinova, *Prog. Surf. Sci.* 70 (**2002**) 187-260.

[GN94] A. Gonzalez and C. Nave, *Acta Cryst. D* 50 (**1994**) 874-877.

[GS97] E.F. Garman and T.R. Schneider, *J. Appl. Crystallogr.* 29 (**1997**) 211-237.

[GTG&07] A. Glišović, J. Thieme, P. Guttman and T. Salditt, *Int. J. Biol. Macromole.* 40 (**2007**) 87-95.

[H94] K. Hieda, *Int. J. Radiat. Biol.* 66 (**1994**) 561-567.

[H01a] A.P. Hitchcock, *J. Synchrotron Rad.* 8 (**2001**) 66-71.

[H01b] A.P. Hitchcock, *Am. Lab.* 33 (**2001**) 30-36.

[HAN&85] D.M. Hanson, S.L. Anderson, M.C. Nelson, G.P. Williams and N. Lucas, *J. Phys. Chem.* 89 (**1985**) 2235-2237.

[HBC&00] E. Höglund, E. Blomquist, J. Carlsson and B. Stenerlöw, *Int. J. Radiat. Biol.* 76 (**2000**) 539-547.

[HDJ&07] A.P. Hitchcock, J.J. Dynes, G. Johansson, J. Wang and G. Botton, *Micron* (**2007**) in press.

[HGD93] B.L. Henke, E.M. Gullikson and J.C. Davis, *Atom. Data Nucl. Data Tables* 54 (**1993**) 181-342.

[HHA&96] K. Hieda, T. Hirono, A. Azami, M. Suzuki, Y. Furusawa, H. Maezawa, N. Usami, A. Yokoya and K. Kobayashi, *Int. J. Radiat. Biol.* 70 (**1996**) 437-445.

[HHT90] G.R. Harp, Z-L Han and B.P. Tonner, *Phys. Scrip.* T31 (**1990**) 23-27.

[HJW&06] M. Howells, C. Jacobsen and T. Warwick, in: P.W. Hawkes, J.C.H. Spence (Eds.), *Science of Microscopy*, Springer, New York, **2006**.

[HM78] A. Halpern and B. Mütze, *Int. J. Radiat. Biol.* 34 (**1978**) 67-72.

[HMH&02] A.P.Hitchcock, C. Morin, H.M. Heng, R.M. Cornelius and J.L. Brash, *J. Biomater. Sci. Polymer Edn.*, 13 (**2002**) 919-937.

[HMZ&05] A.P.Hitchcock, C. Morin, X. Zhang, T. Araki, J. Dynes, H. Stöver, J. Brash, J.R. Lawrence and G.G. Leppard, *J. Electron Spectrosc. Relat. Phenom.* 144-147 (**2005**) 259-269.

[HRC&01] O. Hignette, G. Rostaing, P. Cloetens, A. Rommeveaux, W. Ludwig and A.K. Freund, *Proc. SPIE* 4499 (**2001**) 105-116.

[HRT&01] L.R. Hutchings, R.W. Richards, R.L. Thompson, A.S. Clough, S. Langridge, *J. Polym. Sci. Part B: Polym. Phys.* 39 (**2001**) 2351-2362.

[HN02] A.P. Hitchcock and J.J. Neville, in: T.K. Sham (Ed.), *Chemical Applications of Synchrotron Radiation,* World Scientific Publishing, Singapore, **2002**.

[HSH&85] J.A. Horsley, J. Stöhr, A.P. Hitchcock, D.C. Newbury, A.L. Johnson and F. Sette, *J. Chem. Phys.* 83 (**1985**) 6099-6107.

[HZG&01] K. Heister, M. Zharnikov, M. Grunze, L.S.O. Johansson and A. Ulman, *Langmuir* 17 (**2001**) 8-11.

[ICT&00] G.E. Ice, J.-S. Chung, J.Z. Tischler, A. Lunt and L. Assoufid, *Rev. Sci. Instrum.* 71 (**2000**) 2635-2639.

[IW83] H. Ito and C.G. Willson, *Polym. Eng. Sci.* 23 (**1983)** 1012-1018.

[JWF&00] C. Jacobsen, S. Wirick, G. Flynn and C. Zimba, *J. Microsc.* 197 (**2000**) 173-184.

[K79] M.O. Krause, *J. Phys. Chem. Ref. Data* 8 (**1979**) 307-327.

[K92] F.F. Komarov, *Ion Beam Modification of Metals*, Gordon and Breach Science, **1992**.

[K01] E.S. Kempner, *J. Pharm. Sci.* 90 (**2001**) 1637-1646.

[K03] M. Kiskinova, *J. Phys. IV* 104 (**2003**) 453-458.

[KAF04] S. Kuwamoto, S. Akiyama and T. Fujisawa, *J. Synchrotron Rad.* 11 (**2004**) 462-468.

[KBC&03] B. Kaulich, D. Bacescu, D. Cocco, J. Susini, M. Salomé, O. Dhez, C.

David, T. Weitkamp, E. DiFabrizio, S. Cabrini, G. Morrison, P. Charalambous, J. Thieme, T. Wilhein, J. Kovac, M. Podnar and M. Kiskinova, *J. Phys. IV* 104 (**2003**) 103-107.

[KCH&05] R. Klauser, C.-H. Chen, M.-L. Huang, S.-C. Wang, T.J. Chuang and M. Zharnikov, *J. Electron Spectrosc. Relat. Phenom.* 144-147 (**2005**) 393-396.

[KHM&02] I.N. Koprinarov, A.P. Hitchcock, C. McCrory and R.F. Childs, *J. Phys. Chem. B* 106 (**2002**) 5358-5364.

[KHW&04] R. Klauser, M-L. Huang, S-C. Wang, C-H. Chen, T.J. Chuang, A. Terfort and M. Zharnikov, *Langmuir* 20 (**2004**) 2050-2053.

[KJH95] J. Kirz, C. Jacobsen and M. Howells, *Q. Rev. Biophys.*, 28 (**1995**) 33-130.

[KOJ&02] K. Kaznacheyev, A. Osanna, C. Jacobsen, O. Plashkevych, O. Vahtras, H. Ågren, V. Carravetta and A.P. Hitchcock, *J. Phys. Chem. B* 106 (**2002**) 3153-3168.

[KPC&03] R. Korde, C. Prince, D. Cunningham, R.E. Vest and E. Gullikson, *Metrologia* 40 (**2003**) S145-S149. Calibrated silicon photodiodes (AXUV-100) were obtained from International Radiation Detectors, 2527 West 237th Street Unit A, Torrance, CA 90505-5243. http://www.ird-inc.com/axuvope.html

[KR85] J. Kirz and H. Rarback, *Rev. Sci. Instrum.* 56 (**1985**) 1-13.

[KT96] J. Kikuma and B.P. Tonner, *J. Electron Spectrosc. Relat. Phenom.* 82 (**1996**) 53-60.

[KTS&03] A.L.D. Kilcoyne, T. Tyliszczak, W.F. Steele, S. Fakra, P. Hitchcock, K.

Franck, E. Anderson, B. Harteneck, E.G. Rightor, G.E. Mitchell, A.P. Hitchcock, L. Yang, T. Warwick and H. Ade, *J. Synchrotron Rad*. 10 **(2003)** 125-136.

[KYP&00] T.K. Kim, X.M. Yang, R.D. Peters, B.H. Sohn and P.F. Nealey, *J. Phys. Chem. B* 104 (**2000**) 7403-7410.

[KWS&98] J. Kikuma, T. Warwick, H.-J. Shin, J. Zhang and B.P. Tonner, *J. Electron Spectrosc. Relat. Phenom.* 94 (**1998**) 271-278.

[L06] L. Li, PhD thesis, *X-ray Spectromicroscopy Study of Protein Adsorption onto a Chemically Patterned Surface*, McMaster University, **2006**.

[LBG&05] A. Locatelli, A. Barinov, L. Gregoratti, L. Aballe, S. Heun and M. Kiskinova, *J. Electron Spectrosc. Relat. Phenom.* 144-147 (**2005**) 361-366.

[LCA01] J.A. LaVerne, Z. Chang and M.S. Araos, *Rad. Phys. Chem.* 60 (**2001**) 253-257.

[LCC&07] R. Lessard, J. Cuny, G. Cooper and A.P. Hitchcock, *Chem. Phys.* 331 (**2007**) 289-303.

[LGB&91] P.E. Laibinis, R.L. Graham, H.A. Biebuyck and G.M. Whitesides, *Science* 254 (**1991**) 981-983.

[LHR&06] L. Li, A.P. Hitchcock, N. Robar, R. Cornelius, J.L. Brash, A. Scholl and A. Doran, *J. Phys. Chem. B* 110 (**2006**) 16763-16773.

[LJK&03] Y-H. La, Y.J. Jung, H.J. Kim, T-H. Kang, K. Ihm, K-J. Kim, B. Kim and J.W. Park, *Langmuir* 19 (**2003**) 4390-4395.

[LTR&06] H-K.S. Leiros, J. Timmins, R.B.G. Ravelli and S.M. McSweeney, *Acta*

Cryst. D62 (**2006**) 125-132.

[M75] F.A. Makhlis, *Radiation Physics and Chemistry of Polymers*, John Wiley & Sons, New York, **1975**.

[M86] A.G. Michette, *Optical Systems for Soft X-rays*, Plenum, London, **1986**.

[M88] G. Margaritondo, *Introduction to Synchrotron Radiation*, Oxford University Press, New York, **1988**.

[M04] C. Morin, PhD thesis, *Soft X-ray Spectromicroscopy of Proteins on Patterned Polymer Films*, McMaster University, **2004**.

[MBL&97] E.L. Montei, V.W. Ballarotto, M.E. Little and M.E. Kordesch, *J. Electron Spectrosc. Relat. Phenom.* 84 (**1997**) 129-136.

[MCR&07] J.E. McGeehan, P. Carpentier, A. Royant, D. Bourgeois and R.B.G. Ravelli, *J. Synchrotron Rad.* 14 (**2007**) 99-108.

[MD89] T.P. Ma and P.V. Dressendorfer, *Ionizing Radiation Effects in MOS Devices and Circuits*, John Wiley & Sons, New York, **1989**.

[MGB&99] M. Magnuson, J.-H. Guo, S.M. Butorin, A. Agui, C. Såthe, J. Nordgren and A.P. Monkman, *J. Chem. Phys.* 111 (**1999**) 4756-4761.

[MHC&04] C. Morin, A.P. Hitchcock, R.M. Cornelius, J.L. Brash, S.G. Urquhart, A. Scholl and A. Doran, *J. Electron Spectrosc. Relat. Phenom.* 137-140 (**2004**) 785-794.

[MHI&02] C. Morin, A.P. Hitchcock, H. Ikeura-Sekiguchi, A. Scholl and A. Doran, *X-ray Photoelectron Emission Microscopy with PEEM-2 on ALS Beamline 7.3.1.1 User Manual*, ALS, **2002**.

[MM85] F.A. Mettler and R.D. Moseley, *Medical Effects of Ionizing Radiation*, Grune & Stratton, Orlando, Florida, **1985**.

[MMB93] G.R. Morrison, in: A.G. Michette, C.J. Buckley (Eds.), *X-ray Science and Technology*, Institute of Physics, London, **1993**.

[MMC&99] H.M. Manohara, E. Morikawa, J. Choi and P.T. Sprunger, *J. Microelectromech. Syst.* 8 (**1999**) 417-422.

[MOW&00] J. Maser, A. Osanna, Y. Wang, C. Jacobsen, J. Kirz, S. Spector, B. Winn, and D. Tennant, *J. Microscopy* 197 (**2000**) 68-79.

[MYY&02] Y. Mori, K. Yamauchi, K. Yamamura, H. Mimura, Y. Sano, A. Saito, K. Ueno, K. Endo, A. Souvorov, M. Yabashi, K. Tamasaku and T. Ishikawa, *Proc. SPIE* 4782 (**2002**) 58-64.

[NOY&05] A. Nakano, K. Okamoto, Y. Yamamoto, T. Kozawa; S. Tagawa, T. Kai and H. Nemoto, *Jap. J. Appl. Phys.* 44 (**2005**) 5832-5835.

[OB03] Y.N. Osetsky and D.J. Bacon, *Nucl. Instru. Meth. Phys. Res. B* 202 (**2003**) 31-43.

[OF01] P.G. O'Shea and H.P. Freund, *Science* 292 (**2001**) 1853-1858.

[OR98] C. Olsen and P.A. Rowntree, *J. Chem. Phys.* 108 (**1998**) 3750-3764.

[P03] R.L. Pease, *IEEE Trans. Nucl. Sci.* 50 (**2003**) 539-551.

[QTM&98] F.M. Quinn, D. Teehan, M. MacDonald, S. Downes and P. Bailey, *J. Synchrotron Rad.* 5 (**1998**) 783-785.

[R81] E. M. Rowe, *Physics Today*, May **1981**, 28-37.

[RCG&02] L. Radu, B. Constantinescu, D. Gazdaru and I. Mihailescu, *Rad. Prot. Dos.*

99 (**2002**) 153-154.

[RDB03] Y. Razskazovskiy, M.G. Debije and W.A. Bernhard, *Radiat. Res.* 159 (**2003**) 663-669.

[RGK&03] M. Richter, A. Gottwald, U. Kroth, A.A. Sorokin, S.V. Bobashev, L.A. Shmaenok, J. Feldhaus, Ch. Gerth, B. Steeg, K. Tiedtke and R. Treusch, *Appl. Phys. Lett.* 83 (**2003**) 2970-2972.

[RGS&06] A.G. Richter, R. Guico, K. Shull and J. Wang, *Macromolecules* 39 (**2006**) 1545-1553.

[RHA&97] E.G. Rightor, A.P. Hitchcock, H. Ade, R.D. Leapman, S.G. Urquhart, A.P. Smith, G. Mitchell, D. Fischer, H.J. Shin and T. Warwick, *J. Phys. Chem. B* 101 (**1997**) 1950-1960.

[RKK&80] H. Rarback, J. Kenney, J. Kirz and X.S. Xie, in: A. Ash (Ed.), *Scanned Image Microscopy*, Academic, London, **1980**.

[RM00] R.G.B. Ravelli and S.M. McSweeney, *Structure* 8 (**2000**) 315-328.

[RMB&99] L.P. Ratliff, R. Minniti, A. Bard, E.W. Bell, J.D. Gillaspy, D. Parks, A.J. Black and G.M. Whitesides, *Appl. Phys. Lett.* 75 (**1999**) 590-592.

[RSF&88] H. Rarback, D. Shu, S.C. Feng, H. Ade, J. Kirz, I. McNulty, D.P. Kern, T.H.P. Chang, Y. Vladimirsky, N. Iskander, D. Attwood, K. McQuaid and S. Rothman, *Rev. Sci. Instrum.* 59 (**1988**) 52-59.

[RSS&98] C. Ruehlicke, D. Schneider, M. Schneider, R.D. DuBois, and R. Balhorn, *Nanotechnology* 9 (**1998**) 251-256.

[S78] W. Schilling, *Hyperfine Interactions*, 4 (**1978**) 636-644.

[S92] J. Stöhr, *NEXAFS Spectroscopy*, Series in Surface Science Vol. 25, Springer, Berlin, **1992**.

[S02] L. Sanche, *Mass Spectrom. Rev.* 21 (**2002**) 349-369.

[SA88] J. Sygusch and M. Allaire, *Acta Cryst. A* 44 (**1988**) 443-448.

[SBC&02] B.M. Sutherland, P.V. Bennett, N. Cintron-Torres, M. Hada, J. Trunk, D. Monteleone, J.C. Sutherland, J. Laval, M. Stanislaus and A. Gewirtz, *J. Radiat. Res.* 43 Suppl. (**2002**) S149-S152.

[SBS&93] G.P. Summers, E.A. Burke, P. Shapiro, S.R. Messenger and R.J. Walters, *IEEE Trans. Nucl. Sci.* 40 (**1993**) 1372-1379.

[SFP&96] K. Seshadri, K. Froyd, A.N. Parikh, D.L. Allara, M.J. Lercel and H.G. Craighead, *J. Phys. Chem.* 100 (**1996**) 15900-15909.

[SGF&02] Th. Schmidt, U. Groh, R. Fink, E. Umbach, O. Schaff, W. Engel, B. Richter, H. Kuhlenbeck, R. Schlögl, H.-J. Freund, A.M. Bradshaw, D. Preikszas, P. Hartel, R. Spehr, H. Rose, G. Lilienkamp, E. Bauer and G. Benner, *Surf. Rev. Lett.* 9 (**2002**) 223-232.

[SHH&07] N. Shimizu, K. Hirata, K. Hasegawa, G. Ueno and M. Yamamoto, *J. Synchrotron Rad.* 14 (**2007)** 4-10.

[SNW&90] S.G. Swarts, G.B. Nelson, C.A. Wallen and K.T. Wheeler, *Radiat. Environ. Biophys.* 29 (**1990**) 93-102.

[SRN&80] G. Schmahl, D. Rudolph, B. Niemann and O. Christ, *Q. Rev. Biophys.* 13 (**1980**) 297-315.

[SS91] A. Singh and J. Silverman, *Radiation Processing of Polymers*, Hanser

Publishers, Oxford University Press, New York, 1991.

[SSH04] E. Sagstuen, A. Sanderud and E.O. Hole, *Radiat. Res.* 162 (**2004**) 112-119.

[SSR&88] D. Shu, D.P. Siddons, H. Rarback and J. Kirz, *Nucl. Instr. Meth. Phys. Res. A* 266 (**1988**) 313-317.

[SSR&98] N. Sartori Blanc, D. Studer, K. Ruhl and J. Dubochet, *J. Micros.* 192 (**1998**) 194-201.

[SZH&05] A. Schoell, Y. Zou, D. Huebner, S.G. Urquhart, T. Schmidt, R. Fink and E. Umbach, *J. Chem. Phys.* 123 (**2005**) 044509.

[SZF&06] A. Shaporenko, M. Zharnikov, P. Feulner and D. Menzel, *J. Phys. Condens. Matter* 18 (**2006**) S1677-S1689.

[T04a] J.E. Turner, *Health Phys.* 86 (**2004**) 228-252.

[T04b] K. Trachenko, *J. Phys. Condens. Matter* 16 (**2004**) R1491-R1515.

[T69] M.W. Thompson, *Defects and Radiation Damage in Metals*, Cambridge Unversity Press, **1969**.

[TAG&01] A.C. Thompson, D.T. Attwood, E.M. Gullikson, M.R. Howells, J. B. Kortright, A.L. Robinson, J. H. Underwood, K-J. Kim, J. Kirz, I. Lindau, P. Pianetta, H. Winick, G.P. Williams, J.H. Scofield and D. Vaughan, *X-ray Data Booklet*, Lawrence Berkeley National Laboratory, **2001**.

[TDD&95] B.P. Tonner, D. Dunham, T. Droubay, J. Kikuma, J. Denlinger, E. Rotenberg and A. Warwick, *J. Electron Spectrosc. Relat. Phenom.* 75 (**1995**) 309-332.

[TH88] B.P. Tonner and G.R. Harp, *Rev. Sci. Instrum.* 59 (**1988**) 853-858.

[THK&92] B.P. Tonner, G.R. Harp, S.F. Koranda and J. Zhang, *Rev. Sci. Instrum.* 63 (**1992**) 564-568.

[TM00] T-Y. Teng and K. Moffat, *J. Synchrotron Rad.* 7 (**2000)** 313-317.

[TPP91] S. Tanuma, C.J. Powell and D.R. Penn, *Surf. Interf. Anal.* 17 (**1991**) 927-939.

[TPP93] S. Tanuma, C.J. Powell and D.R. Penn, *Surf. Interf. Anal.* 21 (**1993**) 165-176.

[TR91] R.M. Tromp and M.C. Reuter, *Ultramicroscopy* 36 (**1991**) 99-106.

[TTM&94] M.C.K. Tinone, K. Tanaka, J. Maruyama, N. Ueno, M. Imamura and N. Matsubayashi, *J. Chem. Phys.* 100 (**1994**) 5988-5995.

[TUM&96] M.C.K. Tinone, N. Ueno, J. Maruyama, K. Kamiya, Y. Harada, T. Sekitani and K. Tanaka, *J. Electron Spectrosc. Relat. Phenom.* 80 (**1996**) 117-120.

[UA02] S.G. Urquhart and H. Ade, *J. Phys. Chem. B* 106 (**2002**) 8531-8538.

[UKM&93] N. Ueno, M. Komada, Y. Morimoto, M.C.K. Tinone, M. Kushida, K. Sugita, K. Honma and K. Tanaka, *Jpn. J. Appl. Phys.* 32 Suppl. (**1993**) 229-231.

[V77] P. Vajda, *Rev. Mod. Phys.* 49 (**1977**) 481-521.

[VKW85] V.E. Viola, K. Kwiatkowski and M. Walker, *Phys. Rev. C* 31 (**1985**) 1550-1552.

[WAH&97] T. Warwick, H. Ade, A.P. Hitchcock, H. Padmore, E.G. Rightor and B.P. Tonner, *J. Electron Spectrosc. Relat. Phenom.* 84 (**1997**) 85-98.

[WAK&02] T. Warwick, H. Ade, D. Kilcoyne, M. Kritscher, T. Tylisczczk, S. Fakra,

A. Hitchcock, P. Hitchcock and H. Padmore, *J. Synchrotron Rad.* 9 (**2002**) 254-257.

[WBH&81] H. Winick, G. Brown, K. Halbach and J. Harris, *Physics Today*, May **1981**, 50-63.

[WCT&05] J. Wang, G. Cooper, D. Tulumello and A.P. Hitchcock, *J. Phys. Chem. A* 109 (**2005**) 10886-10896.

[WFK&98] T. Warwick, K. Franck, J.B. Kortright, G. Meigs, M. Moronne, S. Myneni, E. Rotenberg, S. Seal, W. F. Steele, H. Ade, A. Garcia, S. Cerasari, J. Denlinger, S. Hayakawa, A.P. Hitchcock, T. Tyliszczak, J. Kikuma, E.G. Rightor, H.-J. Shin and B.P. Tonner, *Rev. Sci. Instrum*. 69 (**1998**) 2964-2973.

[WH98] B. Weiland and J. Huttermann, *Int. J. Radiat. Biol.* 74 (**1998**) 341-358.

[WJM&00] Y. Wang, C. Jacobsen, J. Maser and A. Osanna, *J. Microsc.* 197 (**2000**) 80-93.

[WLL&97] R.N. Watts, S. Liang, Z.H. Levine, T.B. Lucatorto, F. Polack and M.R. Scheinfein, *Rev. Sci. Instrum.* 68 (**1997**) 3464-3476.

[WPA98] T. Warwick, H.A. Padmore and H. Ade, *Proc. SPIE*, 3449 (**1998**) 12-18.

[WRK&00] M. Weik, R.B.G. Ravelli, G. Kryger, S. McSweeney, M.L. Raves, M. Harel, P. Gros, I. Silman, J. Kroon, and J.L. Sussman, *Proc. Natl. Acad. Sci.* 97 (**2000**) 623-628.

[WSH&07] J. Wang, H.D.H. Stöver, A.P. Hitchcock and T. Tyliszczak, *J. Synchrotron Rad.* 14 (**2007**) 181-190.

[WVB&05] T.M. Willey, A.L. Vance, T. van Buuren, C. Bostedt, L.J. Terminello and C.S. Fadley, *Surf. Sci.* 576 **(2005**) 188-196.

[XMW97] T.J. Xue, M.A. McKinney and C.A. Wilkie, *Polym. Degrad. Stab.* 58 (**1997**) 193-202.

[YAF&04] A. Yokoya, K. Akamatsu, K. Fujii and M. Ukai, *Int. J. Radiat. Biol.* 80 (**2004**) 833-839.

[YT02] K. Yoshihara and A. Tanaka, *Surf. Interface Anal.* 33 (**2002**) 252-258.

[YWH99] A. Yokoya, R. Watanabe and T. Hara, *J. Radiat. Res.* 40 (**1999**) 145-158.

[ZBF94] M. Zaider, M. Bardash and A. Fung, *Int. J. Radiat. Biol.* 66 (**1994**) 459-465.

[ZFH&00] M. Zharnikov, S. Frey, K. Heister and M. Grunze, *Langmuir* 16 (**2000**) 2697-2705.

[ZFW&04] Y. Zubavichus, O. Fuchs, L. Weinhardt, C. Heske, E. Umbach, J.D. Denlinger and M. Grunze, *Radiat. Res.* 161 (**2004**) 346-358.

[ZJL&95] X. Zhang, C. Jacobsen, S. Lindaas and S. Williams, *J. Vac. Sci. Technol. B* 13 (**1995**) 1477-1483.

[ZZS&04a] Y. Zubavichus, M. Zharnikov, A. Shaporenko and M. Grunze, *J. Electron Spectrosc. Relat. Phenom.* 134 (**2004**) 25-33.

[ZZS&04b] Y. Zubavichus, M. Zharnikov, A. Shaporenko, O. Fuchs, L. Weinhardt, C. Heske, E. Umbach, J.D. Denlinger and M. Grunze, *J. Phys. Chem. A* 108 (**2004**) 4557-4565.

Appendix A

This appendix briefly presents soft X-ray damage to an example of very damage-resistant organic materials, i.e. hexaphenylbenzene, by STXM. This appendix also lists radiation damage results from unpublished work performed in the group, as well as literature values of some polymer materials.

A.1 STXM damage of hexaphenylbenzene (Ph_6Bz)

The C 1s NEXAFS spectra of undamaged and heavily soft X-ray damaged hexaphenylbenzene (Ph_6Bz) are shown in **Figure A.1**. Similar to polystyrene (PS) presented in Chapter 5, radiation damage in Ph_6Bz is characterized by similar spectroscopic changes: a significant decrease of intensity at the 285.1 eV C 1s(C=C) $\rightarrow$ $\pi^*_{C=C}$ transitions associated with damage to the phenyl ring; a simultaneous increase in

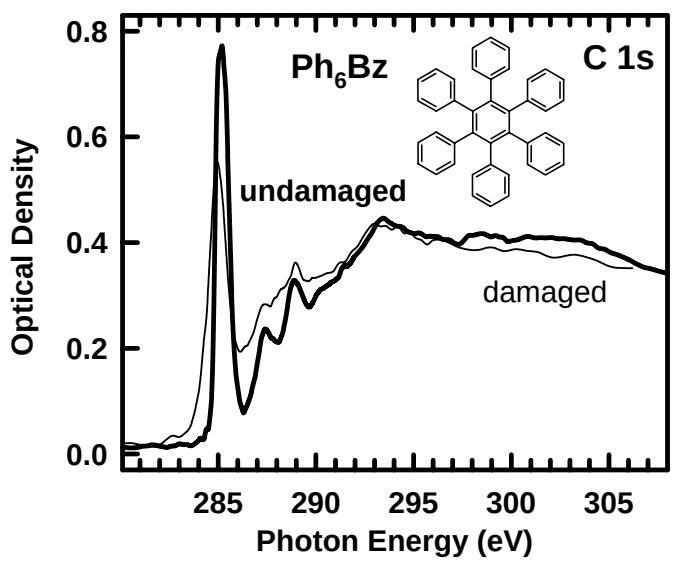

Figure A.1 C 1s NEXAFS spectra of undamaged and radiation damaged Ph_6Bz, the Ph_6Bz structure is shown.

signal at 284.4 eV, attributed to the isolated C=C bonds generated from ring destruction; the destruction of aromatic rings is also indicated by loss of the C 1s → 2π* transition (289 eV) and the double peaked C 1s → $\sigma^*_{C=C}$ continuum features (293, 303 eV), both of which are characteristic of phenyl rings [HSH&85]. The C 1s continuum intensity stays almost constant showing negligible mass loss during radiation damage.

Figure A.2 illustrates the quantitative determination of critical dose for damage of Ph_6Bz at 255 and 320 eV respectively. The damage of Ph_6Bz was monitored at 284.4 eV to track the formation of isolated C=C bonds due to phenyl ring destruction. **Figure A.2a** shows 9 combined images recorded at 284.4 eV with the two damage spots and exposure condition indicated. **Figure A.2b** plots the normalized optical density at 284.4 eV as a function of radiation dose for Ph_6Bz after exposure at 255 and 320 eV respectively. The

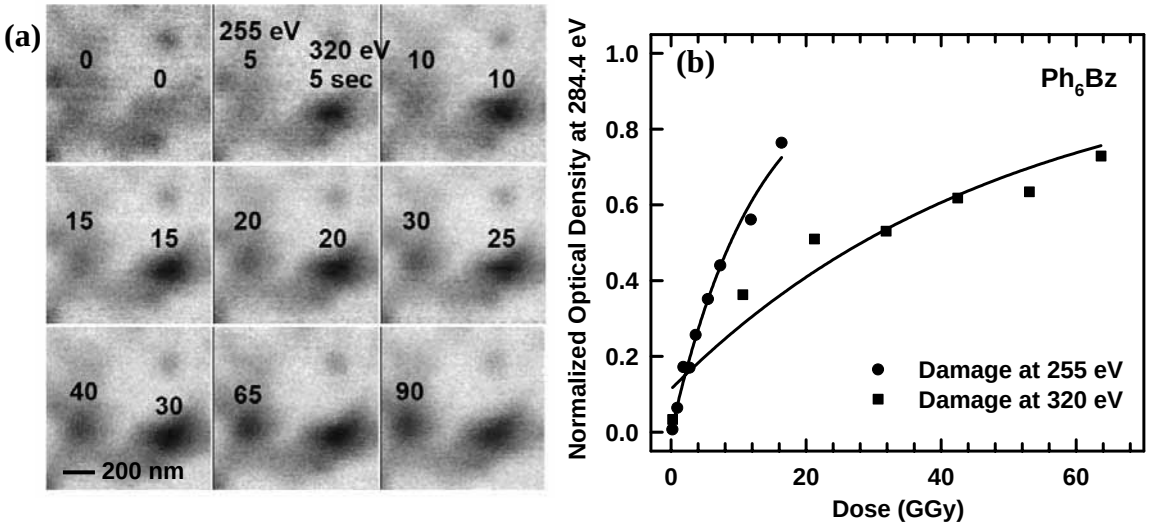

Figure A.2 STXM damage of Ph_6Bz. (a) Two spots on an initially undamaged Ph_6Bz crystal sample by exposure at 255 and 320 eV respectively with the indicated per-pixel dwell times; the dose rate is 182 MGy/s at 255 eV, and is 2123 MGy/s at 320 eV; the 9 combined images are all transmission images recorded at 284.4 eV. (b) Plots of the normalized optical density at 284.4 eV as a function of radiation dose for Ph_6Bz after exposure at 255 and 320 eV respectively. (1 GGy = 1000 MGy)

two series of dose versus normalized OD data points were fit to equation 3.4. The final derived critical dose is 13 GGy for damage at 255 eV, and 49 GGy for damage at 320 eV (1 GGy = 1000 MGy). The critical dose derived at 320 eV is larger than that at 255 eV, probably due to the carbon contamination in STXM as high radiation doses (exposure times) were used. Nevertheless, the critical dose of Ph_6Bz is very high compared to other organic materials presented in this thesis.

A.2 Unpublished radiation damage results and literature results

Table A.1 Photon energies used to damage and quantify soft X-ray damage rate and determined critical dose from unpublished work and from literature

Polymer	Damage energy (eV)	C=C damage		C=O damage		Mass loss	
		Energy (eV)	Critical dose (MGy)	Energy (eV)	Critical dose (MGy)	Energy (eV)	Critical dose (MGy)
Coronene	285	285	> 1000	---	---	---	---
PLA	300	---	---	288.7	52	300	?
Nafion- Dry	390	---	---	---	---	510	15
Nafion- Wet	300	---	---	---	---	683-710	35
Literature							
Nylon 6*	315	---	---	288.2	329	315	114
PC*	315	---	---	290.4	77	---	---
PES*	315	---	---	288.6	72	315	113
PET*	315	---	---	288.2	2545	315	6790
PMMA - unbaked#	317	285	11	288.5	50	317	8
PMMA - baked at 150°C#	317	285	12	288.5	13	317	8
PMMA - baked at 200°C#	317	285	9	288.5	15	317	9
PMMA at 298 K$	525	---	---	531.5	18	528-529.5; 538.5-540	35
PMMA at 113 K$	525	---	---	531.5	13	528-529.5; 538.5-540	597
PMMA*	315	---	---	288.5	69	315	47
PPO*	315	---	---	---	---	315	69
PU*	315	---	---	289.9	96	---	---
PVMK*	315	---	---	286.6	229	315	200

*: Ref. [CUA02]; #: Ref. [ZJL&95]; $: Ref. [BJ02].
PLA: polylactide; PC: poly(bisphenol-A-carbonate); PES: poly(ethylene succinate); PET: poly(ethylene terephthalate); PMMA: poly(methyl methacrylate); PPO: poly(propylene oxide); PU: polyurethane; PVMK: polyvinylmethylketone.

Appendix B

This appendix lists publications, and conference presentations and contributions.

B.1 Publications (journal articles and conference proceedings)

1. A.P. Hitchcock, J.J. Dynes, G. Johansson, J. Wang and G. Botton, Comparison of NEXAFS microscopy and TEM-EELS for studies of soft matter, *Micron* (**2007**) (in press).
2. A.P. Hitchcock, J.J. Dynes, G. Johansson, J. Wang and G. Botton, Comparison of NEXAFS microscopy and TEM-EELS for studies of soft matter, *Proceedings of the Microscopical Society of Canada – 34th Annual General Meeting* (**2007**).
3. J. Wang, C. Morin, L. Li, A. P. Hitchcock, A. Scholl and A. Doran, Radiation damage in soft X-ray microscopy, *J. Electron Spectrosc. Relat. Phenom.* (**2007**) (accepted).
4. J. Wang, H.D.H. Stöver and A.P. Hitchcock, Chemically selective soft X-ray direct-write patterning of multilayer polymer films, *J. Phys. Chem. C* 111 (**2007**) 16330-16338.
5. J. Wang, H.D.H. Stöver, A.P. Hitchcock and T. Tyliszczak, Chemically selective soft X-ray patterning of polymers, *J. Synchrotron Rad.* 14 (**2007**) 181-190.
6. A.P. Hitchcock, J. Wang, D. Hernández-Cruz, H. Stöver, M.-E. Rousseau and M. Pézolet, Soft X-ray spectromicroscopy of polymers and biomaterials: from analysis to synthesis, *Proceedings of the Fifth International Conference on Synchrotron Radiation in Materials Science* (**2006**) 220.

7. J. Wang, G. Cooper, D. Tulumello and A.P. Hitchcock, Inner shell excitation spectroscopy of biphenyl and substituted biphenyls: probing ring-ring delocalization, *J. Phys. Chem. A* 109 (**2005**) 10886-10896.
8. A.P. Hitchcock, J. Wang, G. Botton, R.F. Egerton, Quantitative dose-damage relationships for radiation damage to polymers and molecular compounds in X-ray and electron microscopes, *Microsc. Microanal.* 11(Suppl. 2) (**2005**) 2046-2047.
9. J. Wang, H. Stöver, G. Botton and A.P. Hitchcock, Radiation damage effects in soft X-ray microscopy of polymers, *Proceedings of the Microscopical Society of Canada - 32nd Annual General Meeting* (**2005**) 128-129.

B.2 Conference presentations and contributions

1. J. Wang, A.P. Hitchcock, H.D.H. Stöver and T. Tyliszczak, Poster presentation: *Chemically selective soft X-ray direct-write patterning of multilayer polymers*, The 62nd Annual Congress of the Canadian Association of Physicists, June 17-20, 2007, University of Saskatchewan, Saskatoon, Saskatchewan, Canada.
2. J. Wang, A.P. Hitchcock, H.D.H. Stöver and T. Tyliszczak, Poster presentation: *Chemically selective soft X-ray direct-write patterning of multilayer polymers by Scanning Transmission X-ray Microscopy*, The 10th CLS Annual Users' Meeting, June 15-17, 2007, University of Saskatchewan, Saskatoon, Saskatchewan, Canada.
3. A.P. Hitchcock, J.J. Dynes, G. Johansson, J. Wang and G. Botton, Oral presentation: *Comparison of NEXAFS microscopy and TEM-EELS for studies of soft matter*, Microscopical Society of Canada - 34th Annual General Meeting, June

12-15, 2007, University of Alberta, Edmonton, Alberta, Canada.

4. A.P. Hitchcock, J. Wang, D. Hernández-Cruz, H. Stöver, M.-E. Rousseau and M. Pézolet, Oral presentation: *Soft X-ray spectromicroscopy of polymers and biomaterials: from analysis to synthesis*, The 5th International Conference on Synchrotron Radiation in Materials Science, July 30-August 2, 2006, Chicago, Illinois, USA.

5. D. Covelli, J. Wang, D. Hernández Cruz, A. Hitchcock and S. Urquhart, Poster presentation: *Design and implementation of an anticontaminator for X-ray microscopy*, The 9th CLS Annual Users' Meeting, June 16-18, 2006, University of Saskatchewan, Saskatoon, Saskatchewan, Canada.

6. J. Wang, A.P. Hitchcock, H.D.H. Stöver, D. Hernández Cruz and T. Tyliszczak, Poster presentation: *Chemically selective soft X-ray lithography*, Materials Research Society 2006 Spring Meeting, April 17-21, 2006, San Francisco, California, USA.

7. A.P. Hitchcock, J. Wang, L. Li, J. Stewart-Ornstein, H. Stöver, J. Brash and D. Guay, Poster presentation: *Materials research with soft X-ray scanning transmission X-ray microscopy (STXM)*, The 8th CLS Annual Users' Meeting, November 18-20, 2005, University of Saskatchewan, Saskatoon, Saskatchewan, Canada.

8. A. Hitchcock, J. Wang, H. Stöver and T. Tyliszczak, Oral presentation: *Novel uses of STXM: b. Chemically Selective X-ray Lithography*, 2005 ALS Users' Meeting, October 20-22, 2005, Advanced Light Source, Lawrence Berkeley National

Laboratory, Berkeley, CA, USA.

9. A.P. Hitchcock, J. Wang, G.A. Botton and R.F. Egerton, Poster presentation: *Quantitative dose-damage relationships for radiation damage to polymers and molecular compounds in X-ray and electron microscopes*, Microscopy & Microanalysis 2005 meeting, July 31-August 4, 2005, Honolulu, Hawaii, USA.

10. A. Hitchcock, J. Wang, G. Botton and R. Egerton, Poster presentation: *Radiation Damage in X-ray and Electron Microscopes*, Enhanced Data Generated by Electrons 2005 Grundlsee Workshop, May 1-5, 2005, Grundlsee, Austria.

11. J. Wang, G. Cooper, D. Tulumello and A.P. Hitchcock, Poster presentation: *Inner Shell Excitation Spectroscopy of Biphenyl and Substituted Biphenyls*, Canadian Society for Chemistry - 88th Canadian Chemistry Conference and Exhibition, May 28-June 1, 2005, Saskatoon, Saskatchewan, Canada.

12. J. Wang, H. Stöver, G. Botton and A.P. Hitchcock, Poster presentation: *Radiation Damage Effects in Soft X-ray Microscopy of Polymers*, Microscopical Society of Canada - 32nd Annual General Meeting, May 18-20, 2005, McMaster University, Hamilton, Ontario, Canada.

Appendix C

This appendix lists all the software packages used for this thesis.

1. Xis2000

aXis2000 is a freeware program written in Interactive Data Language (IDL) by Adam Hitchcock, and it is available from http://unicorn.mcmaster.ca/aXis2000.html. It was used for the spectromicroscopy data analysis: images, stack and spectral analyses.

2. BAN

BAN is a general purpose data analysis DOS program produced and distributed by Dr. Tolek Tyliszczak (ALS). In some case, it was used for fitting spectral peaks. It is complementary to aXis2000 for spectrum analysis.

3. ISIS Draw2.4

ISIS Draw 2.4, from MDL Information Systems, Inc., is a program which specializes in two dimensional drawings of small molecules and polymers.

4. Microsoft Office, versions 2000, XP and 2003

Word and PowerPoint were used to write reports and prepare oral and poster presentations. Excel was used for dose-damage data analysis, **ChemLith** simulations, regression analysis, cataloguing samples and making graphical representations.

5. NoteTab

Note Tab, by Fookes Software, is a text and HTML editor. It was used to format spectral files in order to use them in various software.

6. PaintShop Pro, version 4 and 5

PaintShop Pro, from JASC Incorporated, was used to edit images for presentations and pattern generation. Images for presentation were either screen saved from the aXis2000 software, pasted from constructed figures in PowerPoint, or read from other image formats from aXis2000 and other software.

7. Q-Analysis

Q-Analysis is the software provided by the Quesant Instrument Corporation for the acquisition and processing of AFM images obtained with the Q-Scope 350 AFM.

8. Sigma Plot 6.0

Sigma Plot 6.0 (by Jandel Scientific) was used for graphical representations and regression analysis.

9. STXM_Control

This software was initially written by Dr. Tolek Tyliszczak and Peter Hitchcock, and extensively further developed from 2002-2006 by Dr. Tyliszczak, especially the pattern generation function. It controls the beamline (slit sizes and monochromator) and the STXM microscope, and acquires the data at STXM 5.3.2.

10. X-PEEM software packages

The software packages are used for operating the X-PEEM at the ALS. Except for Image Pro 4.0, the commercial camera software, the X-PEEM programs were written by various members of the PEEM2 team.